Geological and geotechnical characterisation, preliminary design, and numerical modelling of underwater roundabouts in the Suðuroy Tunnel

;

Cristian Tebaldi



Delft University of Technology

TU Delft

Geological and geotechnical characterisation, preliminary design, and numerical modelling of underwater roundabouts in the Suðuroy Tunnel

by

Cristian Tebaldi

to obtain the degree of Master of Science

at the Delft University of Technology,

to be defended publicly on Wednesday August 27, 2025 at 14:00 AM.

Student number:	5861691	
Project duration:	April 16, 2024 – August 27, 2025	
Thesis committee:	Dr. ir. W. (Wout) Broere,	TU Delft, supervisor
	Dr. ir. DJM. (Dominique) Ngan-Tillard,	TU Delft
	Dr. P. (Paula) Rulff,	TU Delft
	N. (Nghia) Trinh	SINTEF

Cover:	A.I.-generated image inspired by the Eysturoy underwater roundabout (Faroe Islands).
Style:	TU Delft Report Style, with modifications by Daan Zwaneveld

An electronic version of this thesis is available at http://repository.tudelft.nl/.

TU Delft

This thesis is dedicated
to my grandmother
Annamaria

Abstract

Underwater road tunnels have become critical infrastructure in Norway and, more recently, in the Faroe Islands. Initially excavated to bypass fjords, they later developed to replace ferry services across longer marine straits. The 24 km-long Suðuroy Tunnel will be the longest underwater fixed link in the archipelago and among the longest worldwide. Due to its exceptional length and prolonged poorly lit driving conditions, special safety measures are planned, including two large equal-design caverns functioning as U-turn roundabouts for emergency vehicle evacuation. This study examined the feasibility of excavating these underground widenings within the geological and geotechnical context of the site, primarily composed of sub-horizontal basaltic lava flow cores interbedded with lava breccias and volcaniclastic sandstones. To address knowledge gaps in local lithostratigraphy, rock strength, deformability, and in-situ stress conditions, geological and geomechanical characterisation was carried out using desk studies and field mapping. Preliminary cavern geometries were defined for numerical modelling, with two design solutions emerging: one with a central pillar and one full-span cavern without internal supports.

Continuum-based simulations explored various cavern sizes. Within basaltic flow core units, the stress regime was mostly moderate, with maximum principal stress less than half the uniaxial compressive strength. Tensile stresses reached 80–85% of the rock's tensile strength, and displacements remained under 4.5 mm, suggesting cavern excavation feasibility. The ratio of horizontal to vertical in-situ stress had a greater influence on stability than rock mass parameters such as Young's modulus, Poisson's ratio, or compressive strength. Caverns in both planned positions along the alignment showed similar stress and displacement responses and comparable geomechanical behaviour across the two sites. Simulations involving lava breccia and volcaniclastic sandstone indicated higher instability risks: breccia exhibited potential for spalling and damage accumulation, while sandstone approached the onset of failure. Based on modelling results, two optimal cavern configurations were proposed: (i) a 20-m outer radius with a 4-m central pillar, and (ii) an 18-m radius full-span excavation without support.

This study advances understanding of large-scale underground widenings designed for road roundabouts. It also highlights the need for more site-specific data on stress fields and rock mass strength for the current project, as the models primarily relied on desk-based estimates. Complementary approaches, such as combining continuum modelling with discrete element methods and incorporating structural reinforcement, would provide further insight into brittle failure mechanisms and help evaluate the full feasibility and improvement of such cavern excavations.

Aknowledgments

There are truly many people I wish to thank for making this project possible.
First and foremost, my sincere thanks go to my thesis committee: Prof. Wout, Prof. Dominique, and Prof. Paula, for their valuable guidance, the expertise they generously shared with me, and their patience throughout the development of this long project—as well as for their careful reading of a rather...elaborate report.

My gratitude also extends to the research association SINTEF and in particular the "Berg og geoteknikk" team, for the incredible support and warm welcome they offered me. In particular, I owe a huge thank you to Nghia, for the time he dedicated to helping me—whether it was navigating the complexities of the numerical model code or teaching me how to properly conduct a rock mass quality assessment on the outskirts of Trondheim. I would also like to thank Prof. Eivind Grøv, without whom this thesis project opportunity would not have been possible. A special thank you goes to the company P/F Suðuroytunnel, and in particular to Mr. Teitur Samuelson and Mr. Einar Brimnes, for giving me the opportunity to spend a week of fieldwork in the truly unique—geologically and otherwise—setting of the Faroe Islands.

I am truly grateful to my family for always supporting the choices I've made over the past few years, even when those choices meant living far apart—with all the distance and technical challenges that came with the video calls. A special thanks goes to Massimo, who, in every sense, became an extended member of my family for a few months, and without whom I might not have even been able to begin this academic journey.

Thank you to all the friends I had the pleasure of sharing this Master's journey with. To those who spent time with me at the university in Delft (and especially at Doerak)—how could I forget the intense exam sessions we endured together, followed by weeks of...assignment writing! And to those who also shared the daily routine with me, as I often took over (or held hostage) the kitchen at home. Thanks as well to everyone I shared my Trondheim experience with—Norwegians, fellow Italians, or neighbouring French. A special thought goes to all my friends back home. During my Master's years, we didn't see each other as often as before, but—as the saying goes—quality matters more than quantity, and I'm convinced that every time I managed to come back, I spent truly meaningful time with you. And whether that time was spent up on the altopiano, the quality was even higher!

A final, heartfelt thank you also goes to the Faroese community. The kindness, trust, and generosity of the local people greatly helped me to successfully complete my field mapping campaign during the difficult days of the transport strike.

Contents

Abstract ii

Aknowledgments iii

1 Introduction and project framework 1

1.1 Problem contextualisation . . . 2
1.2 Geological setting . . . 6
1.3 Underground widenings . . . 8
1.4 Numerical modelling . . . 13
1.4.1 Continuum approach . . . 13
1.4.2 Discontinuum approach . . . 14
1.5 Project outline . . . 16

2 Faroe Islands geology: an overview 19

2.1 The igneous nature of the Faroe Islands . . . 20
2.2 Faroe Islands stratigraphy . . . 24
2.2.1 Beinisvørð Formation . . . 26
2.2.2 Prestfjall and Hvannhagi Formations . . . 27
2.2.3 Malinstindur Formation . . . 27
2.2.4 Sneis Formation . . . 29
2.2.5 Enni Formation . . . 29
2.2.6 Post-magmatic evolution . . . 30
2.3 Total geological history approach . . . 31

3 Engineering geology for particular site 34

3.1 Geological and geophysical surveys overview . . . 35
3.2 Main lithostratigraphic features . . . 37
3.2.1 Bathymetry . . . 37
3.2.2 A-Horizon . . . 39
3.2.3 B-Horizon . . . 40
3.2.4 Sandstone below C-Reflector . . . 42
3.2.5 C-Reflector . . . 43

3.2.6 Sneis Formation . . . 43
3.2.7 Sandur Beds basal boundary . . . 44
3.2.8 Queen Sandstone layer . . . 45
3.2.9 Intra-flows lithostratigraphic overview . . . 45
3.3 In-situ stresses . . . 47
3.3.1 Rock stress origin and main regional trends in the Faroe Islands . . . 47
3.3.2 Boreholes' structural data . . . 49
3.3.3 Caverns favourable orientation . . . 51
3.3.4 Horizontal and in-situ stresses magnitude . . . 51
3.3.5 Theoretical models outcomes . . . 53

4 Geophysical properties for particular site 55
4.1 Rock elastic properties . . . 56
4.2 Rock electrical properties . . . 60
4.2.1 Basics of rocks petrophysics . . . 60
4.2.2 Single conductivity component and Archie's laws . . . 63
4.2.3 Second conductivity component . . . 65
4.3 Groundwater origin and saturation estimation on permeable layers . . . 66
4.3.1 Suðuroy core logs electric properties . . . 66
4.3.2 Saturation estimation . . . 68
4.4 Required hydraulic conductivity . . . 73

5 Field mapping 78
5.1 Outcrops identification . . . 79
5.2 Field testing methodology at the outcrops . . . 85
5.2.1 Outcrop sections mapping sheet . . . 87
5.2.2 Stereonets . . . 90
5.2.3 Rose diagrams . . . 91
5.2.4 Schmidt Hammer . . . 91
5.3 Field mapping campaign results . . . 93
5.3.1 Rock mass quality assessment . . . 93
5.3.2 Discontinuities orientation . . . 102
5.3.3 Longitudinal section . . . 105
5.3.4 Structural data . . . 108
5.3.5 Rock mass strength . . . 110
5.3.6 Rock mass deformability . . . 114

6 Cavern design guidelines 116

6.1 Tunnel . . . 117
6.2 Connection . . . 119
6.3 Roundabout . . . 121
6.3.1 Roundabout design guidelines . . . 121
6.3.2 Cavern structural stability considerations . . . 125
6.4 Parametric design . . . 126

7 Numerical modelling approach 130
7.1 Model domain . . . 131
7.2 Meshing . . . 131
7.3 Materials . . . 133
7.4 In–situ and boundary conditions . . . 135
7.5 Constitutive models . . . 137
7.5.1 Mohr–Coulomb . . . 137
7.5.2 Hoek–Brown . . . 138
7.5.3 Hoek–Brown to Mohr–Coulomb fitting . . . 138
7.6 Drill and blast sequential excavation stages . . . 140
7.7 Numerical simulations plan . . . 143
7.7.1 First round . . . 143
7.7.2 Second round . . . 144

8 Numerical modelling results 150
8.1 First simulations round . . . 151
8.2 Proposed final geometries . . . 162
8.3 Second simulations round . . . 165
8.3.1 Local sensitivity analysis . . . 165
8.3.2 Global sensitivity analysis . . . 168
8.3.3 Numerical model response with different geotechnical units . . . 173
8.3.4 Discussion on potential failure mechanisms . . . 178
8.3.5 Disturbance factor . . . 181
8.4 Suggested structural reinforcements . . . 182

9 Conclusions and recommendations 185
9.1 Main findings and developments . . . 186
9.2 Tackling research gaps . . . 188
9.3 Limitations and possibilities . . . 191
9.3.1 Limitations . . . 191
9.3.2 Possibilities . . . 192
9.4 Social impact . . . 193

References **194**

A Appendix A: Engineering geology for particular site **204**
A.1 Jarðfeingi boreholes: Skúvoy-1 204
A.2 Seismic surveys data processing: Line O1 224
A.3 Faroe Islands seabed bathymetry 227
A.4 Main lithostratigraphic units 229

B Appendix B: Geophysical properties for particular site **234**
B.1 Glyvursnes-1 log parameters 234

C Appendix C: Field mapping **236**
C.1 Field Mapping reference objects 236
C.2 Outcrop mapping: Streymoy 1 (Section 2) 238
C.3 Q and GSI estimates per outcrop sections 251

D Appendix D: Cavern design guidelines **255**
D.1 Tunnel design specifics 255
D.2 Grasshopper architectures 257

E Appendix E: Numerical modelling approach **258**
E.1 Mesh nodes and tetrahedra 258
E.2 HB-MC fitting methods 260

F Appendix F: Numerical modelling results **265**
F.1 Relevant numerical simulations overview 265
F.2 Using the Rock Support Chart and the Revised Support Chart for the Faroe Islands 272

List of Figures

Fig. 1.1: Estimated travel time differences to and from the capital, Tórshavn, comparing the former ferry-based transportation system with travel after the introduction of subsea tunnels. Modified from Connect 3 Million (2024). Data source: Landsverk (2019). 2

Fig. 1.2: The Faroe Islands' tunnel network currently comprises 23 operational tunnels, including 4 underwater. Operational tunnels are shown in purple and planned tunnels in yellow. The proposed Suðuroy Tunnel is intended to connect the southern island of Suðuroy with Sandoy. Note that the alignment of this tunnel shown in the image reflects an earlier conceptual design, which differs from the final proposed alignment. Adapted from Visit Faroe Islands (n.d.). 3

Fig. 1.3: The three initial proposed alignments of the Suðuroy Tunnel. Option 2 has been selected as the final choice and is therefore the focus of the current project. Along this alignment, the indicative locations of the planned roundabouts are labelled as Cavern 1 and Cavern 2. Modified from Holter et al. (2021). 5

Fig. 1.4: The three formations comprising the Faroe Islands Basalt Group (FIBG) and their representative facies, along with the underlying Lopra Formation, which consists of intruded volcaniclastic lithologies. Adapted from Passey and Jolley (2009). 6

Fig. 1.5: Overview of roundabouts and cavern elements in road tunnels across Norway and the Faroe Islands. Topographical conditions have driven the adoption of these solutions in particular in the Arctic city of Tromsø and the fjord region in south-west Norway. In 2020, an underwater roundabout was also opened in the Faroe Islands with the inauguration of the Eysturoy Tunnel. Modified from Yarmolin (2020). 8

Fig. 1.6: (a) The three-arm roundabout at the end of the Breivika Tunnel in Tromsø—one of the first of its kind ever constructed. (b) One of the three caverns excavated along the 24.5 km Lærdal Tunnel, designed to break the monotony of driving through the use of non-invasive lighting effects and to offer safe resting spots. Image (a) adapted from Troms County Municipality (2025). . 10

Fig. 1.7: General recommended modelling approach based on the Q-value score of the rock mass. Reproduced from Barton (2022). 14
Fig. 1.8: Image-based project overview diagram. The approach integrates desk studies, analysis of previous projects, field mapping, and uncertainty characterisation to address research gaps related to the local geology. In addition, a review of current guidelines and the use of CAD software will support the development of a reliable set of preliminary designs. Numerical simulations will build on these contributions using FLAC3D software, and the evaluation of results will help answer the project's main research question. Notably, Python is compatible as programming language with all software tools used in the project. 16

Fig. 2.1: The Faroe Islands archipelago from an aerial view. 20
Fig. 2.2: The North Atlantic Igneous Province (NAIP), with the Faroe Islands archipelago situated within a vast complex of subaerial and submarine volcanic flows, most of which are now submerged. Adapted from Kender et al. (2021). . . . 21
Fig. 2.3: Simple and compound lava flows: main features and average size scale. Reproduced from Passey and Jolley (2009). 22
Fig. 2.4: Comparison between (a) ʻaʻā and (b) pāhoehoe lava flows. In the first, typical clinkers are visible at the top of the still-molten flow, while in the latter, the characteristic structure of overlapping folds is clearly identifiable. Images from Cressler (2007) and Cressler (2011). 23
Fig. 2.5: Comparison of different basalt types found across the Faroe Islands. (a) Aphyric basalts exhibit a fine-grained, uniform matrix with an almost complete absence of visible phenocrysts. (b) Plagioclase-phyric basalts are distinguished by embedded white plagioclase crystals that are larger than the surrounding matrix. (c) Olivine basalts, rarely observed in Faroese outcrops, typically display a darker matrix and plagioclase minerals. 24
Fig. 2.6: Exposed stratigraphic units across the Faroe Islands archipelago, along with the names of the most relevant geological sites, the average thickness of the three basalt formations (Beinidsvørð, Malinstindur and Enni), and the stratigraphic intervals covered by the three deep boreholes: Lopra-1/1A, Vestmanna-1, and Gyvursnes-1. The locations of the three boreholes are also marked on the map with star symbols. Adapted from Szöőr et al. (2005) and Olavsdottir et al. (2021). 25
Fig. 2.7: Columnar basalt formations near Tvøroyri, Suðuroy Island. 26
Fig. 2.8: A mesolite mineral formation within a Malinstindur basalt flow observed in an outcrop on Suðuroy Island. 28

Fig. 2.9: Range of average dip angles for the three basalt sequences in the Faroe Islands. Adapted from Walker et al. (2010). 30
Fig. 2.10: Fookes model for basic igneous volcanic environments. Reproduced from Fookes et al. (2000) 32

Fig. 3.1: Location and details of the six deep boreholes drilled by Jarðfeingi. Data retrieved from Petersen et al. (2022). Background map from https://mapy.com. 36
Fig. 3.2: Bathymetric profile between Sandoy and Suðuroy in proximity of the Suðuroy Tunnel alignment. 38
Fig. 3.3: Identification of the A-Horizon, cropping out at the Kolaratangi coal seam west of Hvalba. Background map from https://mapy.com. 39
Fig. 3.4: Undrilled stratigraphic interval between the Skúvoy-1 and Sandvík-1 boreholes along Suðuroy Fjord (Suðuroyarfjørður), where Cavern 2 is expected to be excavated. Adapted from Petersen et al. (2022). 40
Fig. 3.5: Depth migrated seismic profile (NE to SW from left to right) in Line-L from Jarðfeingi seismic surveys with the four interpreted reflections and the most pronounced peg leg multiples (pink lines). Modified from Petersen et al. (2022). 41
Fig. 3.6: Four main reflectors identification within the Line-O1 velocity model. Modified from Petersen (2020) 42
Fig. 3.7: Stratigraphic correlations of the upper Malinstindur and Enni sedimentary and brecciated units across four deep boreholes in Sandoy and Skúvoy (Søltuvík-2, Sandur-1, Skarvanes-1, and Skúvoy-1). For each sequence, the depth is shown on the left and the thickness on the right. 46
Fig. 3.8: The two major regional rift events and their localisation w.r.t. the Faroe Islands archipelago. 48
Fig. 3.9: Orientation of fjords along the islands of Sandoy and Suðuroy, along with the estimated orientations of regional major and minor principal stresses according to Walker et al. (2010). 49
Fig. 3.10: Rose diagrams along the stratigraphic intervals of the Enni (a–d) and Malinstindur (e,f) basalts, in or near the units where the two caverns are expected to be excavated. Tunnel alignment orientation is indicated with the red segment. The diagrams are adapted from Petersen et al. (2022). 50
Fig. 3.11: Development of the horizontal-to-vertical stress ratio w.r.t. variations in excavation depth and average deformation elastic modulus. The two cavern depths are indicated by the horizontal dotted lines, and the corresponding k-values are shown for a deformation modulus of 35 GPa, a suitable value for the elastic modulus under isotropic material assumption. 53

Fig. 4.1: Distribution of physical properties with lithology and depth in Glyvursnes-1 deep borehole. Reproduced from Waagstein and Andersen (2004). 57
Fig. 4.2: Flow top facies and morphology can vary significantly between flows, being classified either as (a) volcaniclastic conglomerate or (b) as retaining the morphological characteristics of the underlying flow core. In the latter case, a higher degree of weathering results in mechanical weakening and discolouration. Photo (a) taken at the National Museum of the Faroe Islands. 58
Fig. 4.3: Illustration of Archie's equations. The diagram on the left shows how the formation factor (m) decreases as porosity rises in a fully water-saturated rock. The diagram on the right depicts how the resistivity index (n) drops as water saturation increases in a rock that is only partially saturated. Reproduced from Schön (2015). 63
Fig. 4.4: Schematic representation of a well within a porous and permeable formation, illustrating the formulas used to determine the degree of saturation in both the undisturbed (S_w) and invaded (S_{x0}) zones by inverting Archie's second law. Reproduced from Schön (2015). 64
Fig. 4.5: Parallel conductor circuit for the pore fluid composed of water and clay. Adapted from Schön (2015). 65
Fig. 4.6: Preliminary groundwater model of the Faroe Islands. The underground piezometric height h_2 can reach values up to 20 times higher than the piezometric height h_1 above the sea level. Adapted from Ólavsdóttir and Eidesgaard (2023). 68
Fig. 4.7: Evolution of the saturation index (S_w) by varying the porosity of the sedimentary and brecciated units assuming mixed fresh-brackish water presence along Søltuvík-2 (a), Sandur-1 (b), Skarvanes-1 (d), Sandvík-1 (e) and saltwater presence in Skúvoy-1 (c). 71
Fig. 4.8: Simplified model of a water flow through a permeable layer in contact with the tunnel and cavern excavation. Δh represents the head loss , R the contact surface width between cavern and permeable layer, z the layer thickness, L the distance between layer outcrops in seabed and the contact with the cavern, α the layer dip angle. 74
Fig. 4.9: Optimal and maximum allowable hydraulic conductivities outcomes w.r.t. reference values from literature (Freeze and Cherry, 1979) for sandstone and permeable basalt lithologies. 75

Fig. 5.1: Outcrops Streymoy 1 and Streymoy 2 localisation w.r.t. the Suðuroy Tunnel alignment. Background map from https://mapy.com. 79
Fig. 5.2: Outcrops (a) Streymoy 1 and (b) Streymoy 2 overview and their subdivision in sections. 80

Fig. 5.3: Outcrops Sandoy 1, Sandoy 2 and Sandoy 3 localisation w.r.t. the Suðuroy Tunnel alignment. Background map from https://mapy.com. 81
Fig. 5.4: Outcrops (a) Sandoy 1, (b) Sandoy 2, and (c) Sandoy 3 overview and their subdivision in sections. 82
Fig. 5.5: Outcrops (a) Sandoy 4 and (b) Sandoy 5 overview. Field mapping was finally not performed in these outcrops. Photograph (a) by Bartal Højgaard (2015). 83
Fig. 5.6: Outcrops Suduroy 1 and Suduroy 2 localisation w.r.t. the Suðuroy Tunnel alignment. Background map from https://mapy.com. 83
Fig. 5.7: Outcrops (a) Suduroy 1 and (b) Suduroy 2 overview and their subdivision in sections. 84
Fig. 5.8: Site investigation plan and goals from each outcrop analysis. 86
Fig. 5.9: Example of (a) Q-System and (b) GSI mapping sheets evaluating rock mass quality in an outcrop section during the FM campaign. 89
Fig. 5.10: Representation through Schmidt and Wulff projections, the first for the surfaces conservation, the second for angles conservation. Retreived from Caudal (2021). 90
Fig. 5.11: Geotechnical units characterising the Streymoy 2 outcrop (section 3 in the image), namely the lava flow core (Unit 1) and the lava flow top (Unit 2). . 94
Fig. 5.12: Comparison between a tight, stiff joint in the Suduroy 1 outcrop (a) and a widely spaced, disintegrated rock-filled joint in Suduroy 2 (b). 96
Fig. 5.13: Geotechnical units characterising the Sandoy 2 outcrop (section 2 in the image), namely the lava flow core (Unit 1) and the volcaniclastic sandstone (Unit 2). 98
Fig. 5.14: Different degrees of weathering along the analysed sandstone unit, with disintegrated rock along jointing paths (a) and moderately fresh to discoloured conditions with tight joints (b). 98
Fig. 5.15: Stereonets for Enni lava core units of outcrops Streymoy 1 (a), Sandoy 1 (b), Sandoy 2 (c), and Sandoy 3 (d). 103
Fig. 5.16: Stereonet for Enni sandstone unit of outcrop Sandoy 2. 104
Fig. 5.17: Stereonets for Malinstindur lava core units of outcrops Suduroy 1 (a) and Suduroy 2 (b). 104
Fig. 5.18: Longitudinal cross section w.r.t. the Suðuroy Tunnel alignment. Background map from https://mapy.com. 106
Fig. 5.19: Longitudinal cross section of the Sandoy-Suðuroy sea strait, with the tunnel alignment and the two cavern locations specified, alongside with the main units highlighted, namely Basalt Formations, sedimentary and brecciated main units and horizons. 107

Fig. 5.20: Rose diagram for the island of Streymoy, based on data collected in this project (left) in comparison with the work of Ziska (2012) in Streymoy and Eysturoy (right). Adapted from Ziska (2012). 108
Fig. 5.21: Rose diagram for the island of Sandoy, based on data collected in this project. 109
Fig. 5.22: Rose diagram for the island of Suðuroy, based on data collected in this project (left) in comparison with the work of Ziska (2012) in the same island (right). Adapted from Ziska (2012). 109
Fig. 5.23: Proceq® OS8000 N-type hammer, the model used during the site investigation. Retrieved from Screening Eagle (n.d.). 110
Fig. 5.24: UCS values estimated from Schmidt Hammer measurements on the Streymoy 1 outcrop using the selected correlations (results for the entire outcrop). . . 111
Fig. 5.25: Typical average values and strength ranges in uniaxial compression for common rock types. The dark grey boxes illustrate the ranges as reported by Johnson and DeGraff (1988). Adapted from Schön (2015). 112

Fig. 6.1: Schematic tunnel profile with its main elements (a), and geometric dimensions for T9.5–T14.0 tunnel profiles (b), with measurements varying for each individual profile. Adapted from Statens Vegvesen (2024b) 118
Fig. 6.2: Roundabout branch measurements in Oppdal (a), Dombås (b), and Otta (c) along the E6 high-communication road. Satellite images are modified from https://www.google.com/maps. 119
Fig. 6.3: Sketch of the connection element and its dimensions. The first 10 m are integrated into the tunnel section, while the last 20 m represent the connection block itself. The upper width of the element varies slightly depending on the external radius of the roundabout. in order to ensure a joint that is as smooth and cornerless as possible. 120
Fig. 6.4: Outer diameter of roundabout versus driving area width for three vehicle categories. Adapted from Figure 4.1.2.1—1 in Statens Vegvesen (2024a). . . 121
Fig. 6.5: Visibility requirements in roundabout design in Norway: Requirement 1 ensures that drivers approaching the roundabout (black eye point) have a reasonable unobstructed view of vehicles already circulating within it. Requirement 2 addresses the need for clear forward visibility when already in the roundabout (red eye point) and approaching another entry arm. Adapted from Figures 4.1.2.5—1, 4.1.2.7—1, and 4.1.2.7—2 in Statens Vegvesen (2024a). 122
Fig. 6.6: Trigonometric relationships to estimate the maximum allowable pillar radius (r_{max}), given the roundabout's external radius (R_r) and the corresponding lane width (w), for the "road train" vehicle category. 123
Fig. 6.7: Maximum pillar radius corresponding to the cavern's external radius. . . 124

Fig. 6.8: Design principles for underground openings in rocks at varying stress levels and stress directions, with the candidate cross sections for this project highlighted. Adapted from Selmer-Olsen and Broch (1978). 125
Fig. 6.9: Non-pillar (a) and pillar (b) output geometries in Rhino Grasshopper and their respective variables. 126

Fig. 7.1: Pillar geometry model mesh, with the finest tetrahedra elements sized 0.1 m (100 mm) and the largest up to 10 m. 132
Fig. 7.2: Sediment cover thickness in the seabed along the Sandoy-Suðuroy area. The majority of the deposits have been located between Sandoy and Skúvoy in an area bypassed by the proposed tunnel alignment. However, another relevant deposit is visible slightly southern of Cavern 1 proposed location. Adapted from Petersen (2023). 133
Fig. 7.3: Overview of thickness distribution among basaltic units, sediment or sedimentary units and seawater at (a) Cavern 1 and (b) Cavern 2. 134
Fig. 7.4: Representation of the model's boundary conditions in terms of imposed constraints. 136
Fig. 7.5: Mohr-Coulomb domain used to define the non-associated flow rule in FLAC. When an elastic guess violates the composite yield function it can fall either into Domain 1 or Domain 2. Adapted from Itasca Consulting Group (2017). 137
Fig. 7.6: Assumption of circular tunnel in an elastoplastic rock mass subject to hydrostatic initial stress field—p_0 (a), σ_0 (b)—and a tunnel support pressure—p_i (a), σ_A (b)—from (a) Sofianos and Nomikos (2006) and (b) Jimenez et al. (2008). Adapted from Sofianos and Nomikos (2006) and Jimenez et al. (2008). . . . 139
Fig. 7.7: Excavation blocks in a pillar (a) and non-pillar (b) input geometry. The stages of excavation are as follows: 6 blocks for the tunnel section (blue), 4 blocks for the connection (light blue to dark green), and between 3 to 6 blocks (or couple of blocks) for the roundabout (yellow to dark red). 141
Fig. 7.8: Average mechanical ratio evolution during the excavation stages of a cavern with arbitrary outer (R) and pillar (r) radius. Each subsequent excavation step is executed once the system's equilibrium drops below a predefined threshold. The first peak appears significantly higher than the subsequent ones, as all six tunnel blocks were excavated in a single step, causing increased instability. 142

Fig. 8.1: Characteristic regions of peak stress and displacement localisation along (a) non-pillar and (b) pillar geometries. 151
Fig. 8.2: Evolution of major principal peak stress for different pillar radii along each R-series. 154

Fig. 8.3: Stress distribution and magnitude evolution in the pillar element core and edges by varying its radius from 0.5 to 2.5 m. The reference geometry series is R = 26 m. 155
Fig. 8.4: Evolution of minor principal peak stress for different pillar radii along each R-series. 157
Fig. 8.5: Extension and magnitude range of tensional areas in (a) pillar and (b) non-pillar excavations. The reference geometries are the R = 26 m, r = 0 m and r = 4 m, respectively. 158
Fig. 8.6: Evolution of translational displacements for different pillar radii along each R-series. 159
Fig. 8.7: Normalised major principal stresses from the first simulations round w.r.t. to the uniaxial compressive strength characterising the Enni lava core continuum. 163
Fig. 8.8: Final selected geometries related to the underwater roundabout: one configuration including (a) the central pillar and (b) one without. 164
Fig. 8.9: Local sensitivity results for major principal stress outcomes in (a) pillar and (b) non-pillar geometries. 166
Fig. 8.10: Local sensitivity results for minor principal stress outcomes in (a) pillar and (b) non-pillar geometries. 167
Fig. 8.11: Local sensitivity results for displacement outcomes in (a) pillar and (b) non-pillar geometries. 168
Fig. 8.12: Major principal stress contour plots for global sensitivity analysis in (a) pillar and (b) non-pillar geometries. 170
Fig. 8.13: Minor principal stress contour plots for global sensitivity analysis in (a) pillar and (b) non-pillar geometries. 171
Fig. 8.14: Displacement contour plots for global sensitivity analysis in (a) pillar and (b) non-pillar geometries. 172
Fig. 8.15: (a) Comparison of peak major principal stress (σ_1) responses for the three materials for Cavern 1 and Cavern 2 (pillar geometry). For each material group, the stress coordinates of the material point with the highest σ_1 in (b) Cavern 1 and (c) Cavern 2 models are shown in the σ_3–σ_1 and σ_n–τ spaces relative to the HB failure envelopes for the three materials. 174
Fig. 8.16: (a) Comparison of peak major principal stress (σ_1) responses for the three materials for Cavern 1 and Cavern 2 (non-pillar geometry). For each material group, the stress coordinates of the material point with the highest σ_1 in (b) Cavern 1 and (c) Cavern 2 models are shown in the σ_3–σ_1 and σ_n–τ spaces relative to the HB failure envelopes for the three materials. 175
Fig. 8.17: Comparison of peak minor principal stress (σ_3) responses for the three material groups for (a) pillar and (b) non-pillar geometries. 176

Fig. 8.18: Comparison of peak displacement responses for the three material groups for (a) pillar and (b) non-pillar geometries. 176
Fig. 8.19: Tangential stress accumulation at the excavation boundary in the numerical model, potentially triggering failure by spalling (a), and a documented case of spalling at the Baihetan Hydropower Station in China (b). Image (b) reproduced from Wang et al. (2023). 178
Fig. 8.20: Large-magnitude displacements mobilised in the non-pillar cavern and connection rooftops characterised by sandstone material (a), and the extent of collapse damage caused by block failure in the top arch of a main powerhouse excavation (b). Image (b) adapted from Xiao et al. (2024). 179
Fig. 8.21: Comparison between (a) stress-controlled and (b) displacement-controlled failure modes in rock pillars. Reproduced from Esterhuizen et al. (2011). . . 180
Fig. 8.22: Shear zone represented by a thin sedimentary unit sandwiched by massive basalt flows. Reproduced from Zou et al. (2024). 180
Fig. 8.23: Percentage changes in major and minor stresses and displacement with varying disturbance factor (D) in both (a) pillar and (b) non-pillar geometries, assuming lava core properties from the Enni Formation. 182

Fig. A.1: Bathymetric profile of the Faroe Islands, with the depth range limited to 0 to -150 m a.s.l. to better highlight the trenches and underwater dunes on the oceanic plateau where the archipelago is located. Data retrieved from Umhvørvisstovan (2024) 228
Fig. A.2: A-Horizon layer bedding. 230
Fig. A.3: B-Horizon layer bedding (Hypothesis 1). 230
Fig. A.4: B-Horizon layer bedding (Hypothesis 2). 231
Fig. A.5: Sandstone below C-Reflector layer bedding. 231
Fig. A.6: C-Reflector layer bedding.. 232
Fig. A.7: Sneis Formation layer bedding. 232
Fig. A.8: Sandur Beds Base layer bedding. 233
Fig. A.9: Queen Sandstone layer bedding. 233

Fig. C.1: Reference objects used during the site investigation: (a) the bicycle for large size objects, (b) the bag for intermediate objects, (c) the highlighter for detailed pictures. 237

Fig. E.1: Number of nodes in the domain meshes from the first simulations round geometries. 258
Fig. E.2: Number of tetrahedra elements in the domain meshes from the first simulations round geometries. 259

Fig. E.3: Hoek–Brow linearisation graphical procedure in order to obtain the equivalent Mohr–Coulomb parameters described by Jimenez et al. (2008). 262

Fig. F.1: Overview of major principal stresses (calculated by volumetric averaging) in the R = 18 m cavern excavation. 266
Fig. F.2: Overview of major principal stresses tensors in the R = 18 m cavern excavation. 266
Fig. F.3: Overview of minor principal stresses (calculated by volumetric averaging) in the R = 18 m cavern excavation. 267
Fig. F.4: Overview of minor principal stresses tensors in the R = 18 m cavern excavation. 267
Fig. F.5: Overview of translational displacements in the R = 18 m cavern excavation. 268
Fig. F.6: Mechanical ratio average evolution in the R = 18 m cavern excavation. . . 268
Fig. F.7: Overview of major principal stresses (calculated by volumetric averaging) in the R = 20 m, r = 4 m cavern excavation. 269
Fig. F.8: Overview of major principal stresses tensors in the R = 20 m, r = 4 m cavern excavation. 269
Fig. F.9: Overview of minor principal stresses (calculated by volumetric averaging) in the R = 20 m, r = 4 m cavern excavation. 270
Fig. F.10: Overview of minor principal stresses tensors in the R = 20 m, r = 4 m cavern excavation. 270
Fig. F.11: Overview of translational displacements in the R = 20 m, r = 4 m cavern excavation. 271
Fig. F.12: Mechanical ratio average evolution in the R = 20 m, r = 4.0 m cavern excavation. 271
Fig. F.13: Employment of RSC for Cavern 1 structural supports. 276
Fig. F.14: Employment of RSC for Cavern 2 structural supports. 277
Fig. F.15: Employment of Revised Support Chart for Cavern 1 and Cavern 2 structural supports. 280

List of Tables

Tab. 1.1: Summary of general information about the selected roundabout and cavern elements reviewed in this study. 9

Tab. 1.2: Geological setting, site investigations, support and safeguarding measures for the four reviewed roundabouts and cavern elements. 11

Tab. 3.1: A-Horizon bedding plane orientation and dip. 40

Tab. 3.2: B-Horizon bedding plane orientation and dip (hypothesis 1 and 2). 42

Tab. 3.3: Sandstone below C-Reflector bedding plane orientation and dip. 43

Tab. 3.4: C-Reflector bedding plane orientation and dip. 43

Tab. 3.5: Sneis Formation bedding plane orientation and dip. 44

Tab. 3.6: Sandur Beds basal boundary bedding plane orientation and dip. 45

Tab. 3.7: Queen Sandstone bedding plane orientation and dip. 45

Tab. 3.8: Estimated k-values using the models of (a) Terzaghi and Richart (1952)—with both the 10^{th} and 50^{th} percentiles of Poisson's ratios—and (b) Sheorey (1994), for the two caverns, based on their specific depths and the mechanical properties of the surrounding geology. 54

Tab. 4.1: Calculated mean (μ) and standard deviation (σ) of the elastic properties for the (a) Upper and (b) Middle basalt formation material groups. From left to right, the illustrated physical properties are material density (ρ), P-wave velocity (V_p), and the ratio of P-wave to S-wave velocities (V_p/V_s). The corresponding Young's modulus (E) and Poisson's ratio (ν) are shown in the last two columns. Physical property data are reported from Waagstein and Andersen (2004). 59

Tab. 4.2: Calculated 50^{th} (mean) and 5^{th} percentiles of the elastic properties—Young's modulus (E) and Poisson's ratio (ν)—for (a) Upper and (b) Middle Basalt Formation material groups. 59

Tab. 4.3: Electrical properties of the main geolgical units along the Sandoy–Suðuroy stratigraphy. Values from Schön (2015). 61

Tab. 4.4: Electrical properties of common rock-forming minerals in the basalt matrix of the Faroe Islands. Values from Schön (2015). 62

Tab. 4.5: Electrical properties of common minerals precipitated in the stratigraphic units of the Faroe Islands. Values from Schön (2015). 62
Tab. 4.6: Electrical properties for different water types. Values from Schön (2015). . 62
Tab. 4.7: Averaged SPR measurements (in Ω) of sedimentary and brecciated flow-top units within the (a) Enni and (b) Malinstindur Formations, estimated from measurements along the drilled cores of Søltuvík-2, Sandur-1, Skúvoy-1, Skarvanes-1 and Sandvík-1 performed by Jarðfeingi (Petersen et al., 2022). 67
Tab. 4.8: Calculated resistivities (in Ω·m) of sedimentary and brecciated flow-top units within the (a) Enni and (b) Malinstindur Formations, estimated from their respective average SPR. 70

Tab. 5.1: Instrumentation utilised during the field mapping campaign for rock mass quality and strength evaluation. 85
Tab. 5.2: Basaltic core characterisation at outcrops Streymoy 1 and Streymoy 2. . . 94
Tab. 5.3: Basaltic core characterisation at outcrops Sandoy 1, Sandoy 2, and Sandoy 3. 95
Tab. 5.4: Basaltic core characterisation at outcrops *Suduroy 1* and *Suduroy 2*. 97
Tab. 5.5: Volcaniclastic sandstone characterisation at outcrop Sandoy 2. 99
Tab. 5.6: Basaltic flow top characterisation at outcrop *Streymoy 2*. 100
Tab. 5.7: Selected Q- (a) and GSI (b) value ranges and averages (in brackets) to characterise the Enni and Malinstindur stratigraphic units of lava core, lava flow top and volcaniclastic sandstone. 101
Tab. 5.8: Stereonet results for Enni basaltic cores showing mean resultant dip directions and dip angles compared to literature data. 103
Tab. 5.9: Stereonet results for Malinstindur lava core units showing mean resultant dip directions and dip angles compared to literature data. 105
Tab. 5.10: Schmidt Hammer rebound number (R_N) mean, mode and median along the five Streymoy 1 outcrop sections. 111
Tab. 5.11: UCS values from SINTEF laboratory tests of Faroe Islands basalt samples. 112
Tab. 5.12: Selected UCS ranges defined by the 5^{th}, 50^{th} (mean), and 95^{th} percentiles for the numerical model inputs. 113
Tab. 5.13: Rock mass deformability empirical relationships outcomes for Enni (a) and Malinstindur (b) geotechnical units. 115

Tab. 6.1: Length of the driving curve L as a function of the driving curve radius $R_r - w/2$. Adapted from Table 4.1.2.7—1 in Statens Vegvesen (2024a). . . . 123
Tab. 6.2: Variables and parameters for pillar and non-pillar geometries in Rhino® Grasshopper. 127

Tab. 7.1: Model domain size in relation of the cavern external radius R. Note that the z-interval is kept constant regardless of the cavern excavation size 131
Tab. 7.2: Displacement boundary conditions overview. 135
Tab. 7.3: Results from the HB-MC selected fitting methods given the average HB parameters and typical Q-parameters and average UCS values of Enni and Malinstindur lava cores. 140
Tab. 7.4: Mechanical properties characterising the rock mass for the first simulation round. 144
Tab. 7.5: Low and high bound of the four parameters to perform the local sensitivity analysis, alongside with the baseline scenario inputs. 145
Tab. 7.6: Parameter levels used for the global sensitivity analysis. Note that the Young's modulus and Poisson's ratio do not have levels higher than the baseline scenario, since the focus is on studying the model response with weaker and brittle-like (i.e., lower percentiles) mechanical properties. . . . 146
Tab. 7.7: Average properties of the three main material groups, corresponding to the (a) Enni and (b) Malinstindur Formations, representing the input for the simulations set related to material characterisation. 148

Tab. 8.1: Support specifications for pillar and non-pillar geometries across the various geotechnical units, as per NGI handbook (Norwegian Geotechnical Institute, 2015). 184
Tab. 8.2: Support specifications for pillar and non-pillar geometries across the various geotechnical units, as per revised rock support classification for the Faroese context. 184

Tab. C.1: (a) Q- and (b) GSI estimated values for Enni basalt cores along outcrop sections. 252
Tab. C.2: (a) Q- and (b) GSI estimated values for Malinstindur basalt cores along outcrop sections. 253
Tab. C.3: (a) Q- and (b) GSI estimated values for the volcaniclastic sandstone unit along outcrop sections. 253
Tab. C.4: (a) Q- and (b) GSI estimated values for flow top unit along outcrop sections. 254

Tab. D.1: Geometric measurements (in metres) for the different tunnel profiles. Adapted from Statens Vegvesen (2024b) 256
Tab. D.2: Tunnel cross-sectional data for the different tunnel profiles, including both theoretical blasted profile and normal profile. Adapted from Statens Vegvesen (2024b) 256

1

Introduction and project framework

Ilt er at byggja borð fyri báru

It's difficult to build a boat plank against the wave

The Faroe Islands (Føroyar in the native language) comprise an archipelago of 18 major islands located in the North Atlantic Ocean, approximately 580 km west of the Norwegian coast, 330 km north of Scotland, and 450 km south-east of Iceland. Characterised by a highly variable and unpredictable climate, these islands experience wind speeds of up to 110 km/h during adverse weather conditions, while average wave heights along the western coast, exposed to the open Atlantic, often exceed 10 metres (Niclasen and Simonsen, 2012). These challenging environmental conditions, combined with the need to reduce travel times between the islands (Fig. 1.1), led to a reevaluation of the existing ferry transportation system in the last decades. Efforts then shifted towards the construction of fixed links through underwater tunnels, facilitated by the quite favourable geological and geotechnical conditions across the archipelago.

1.1 Problem contextualisation

The Faroe Islands' first subsea link, the Vágar Tunnel, opened in 2002, connecting the capital city Tórshavn with Vágar Airport—the archipelago's only operative airport—over a nearly 5 km underwater crossing. ts success was followed by the opening of three additional tunnels (Fig. 1.2): Norðoy (2003), Eysturoy (2020), and Sandoy (2023). The inland tunnel network has been contemporarily upgraded, leading to a total combined length of 66 km (Samuelsen and Grøv, 2018). The only major subsea link yet unbuilt is the Suðuroy Tunnel, which plans to connect the islands of Suðuroy and Sandoy (Fig. 1.2).

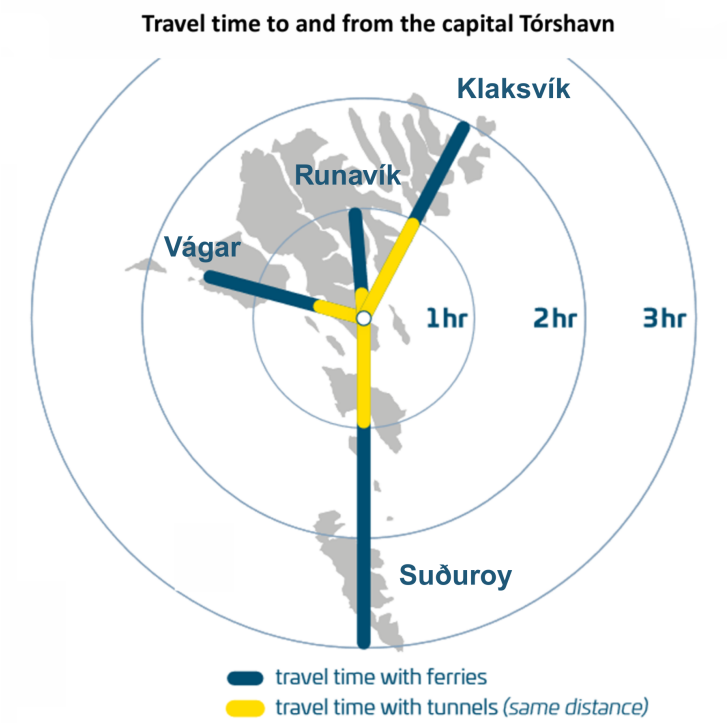


Figure 1.1: Estimated travel time differences to and from the capital, Tórshavn, comparing the former ferry-based transportation system with travel after the introduction of subsea tunnels. Modified from Connect 3 Million (2024). Data source: Landsverk (2019).

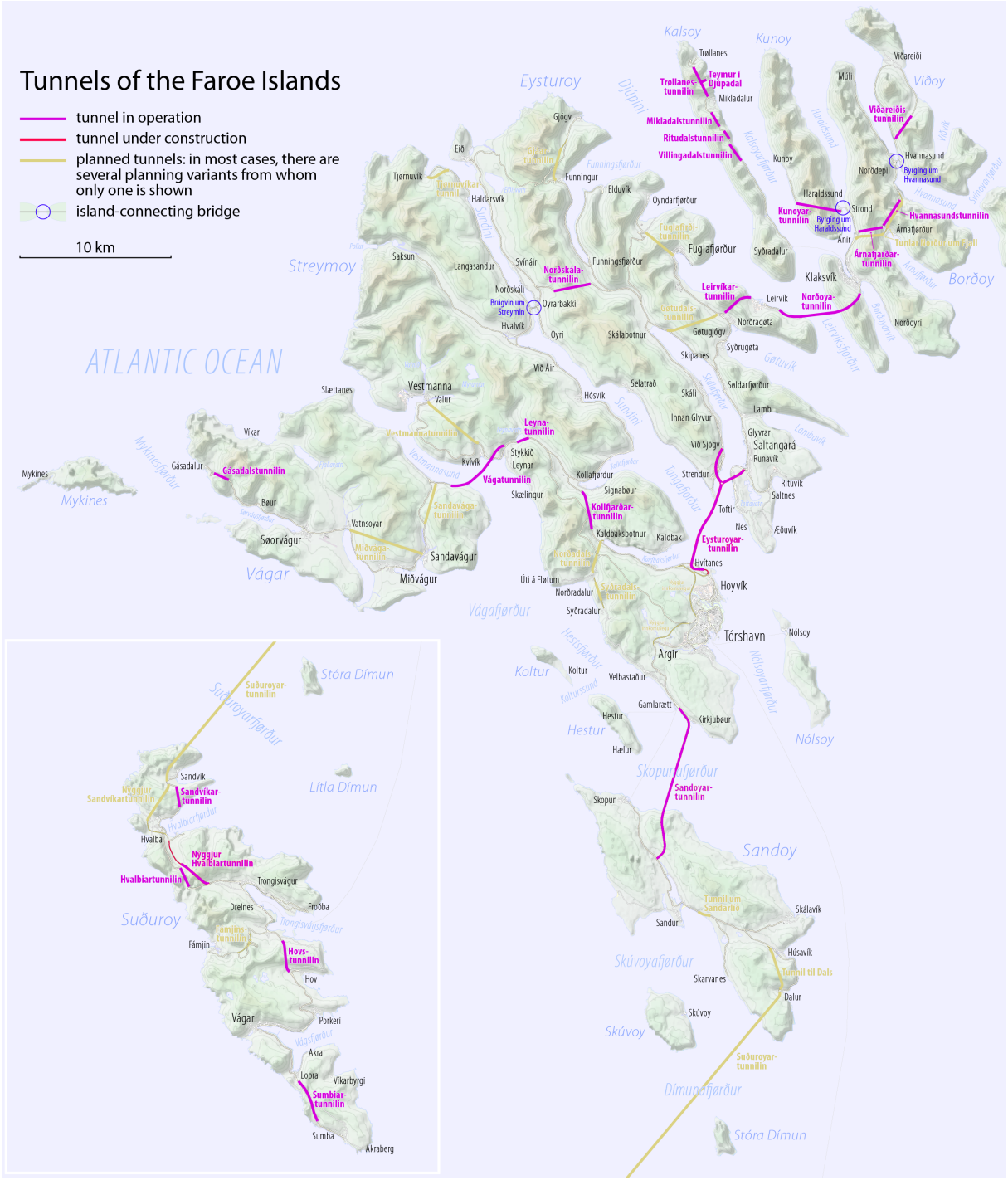


Figure 1.2: The Faroe Islands' tunnel network currently comprises 23 operational tunnels, including 4 underwater. Operational tunnels are shown in purple and planned tunnels in yellow. The proposed Suðuroy Tunnel is intended to connect the southern island of Suðuroy with Sandoy. Note that the alignment of this tunnel shown in the image reflects an earlier conceptual design, which differs from the final proposed alignment. Adapted from Visit Faroe Islands (n.d.).

Three alignment options were considered for the Suðuroy Tunnel (Fig. 1.3): via Skúvoy with two shorter tunnels and a surface intermediate break in the island (Option 1), a single tunnel running under Skúvoy (Option 3), or by completely bypassing the island (Option 2). Option 2 was ultimately selected and is the reference alignment for this project. It specifically proposes a 24 km tunnel from north of Skarvanes (Sandoy) to near Sandvík (Suðuroy).

Due to its length, the tunnel presents challenges such as extended evacuation times and driver distraction or drowsiness caused by the poor lighting environment. To address these issues, two caverns, referred to as Cavern 1 and Cavern 2, will be excavated at one-third and two-thirds of the tunnel alignment from the Sandoy portal, at estimated depths of ~130 m and ~150 m, respectively. These widened sections will primarily function as U-turn roundabouts, enabling even large vehicles to reverse direction easily in emergencies, and secondarily as features that break the monotony of driving and allow short stops when strictly necessary.

At the client's request, the two caverns must share the same design. Accordingly, the objective of this thesis project is to develop the realisation of these tunnel elements through: (1) an engineering geological and geotechnical characterisation of the local site; (2) a preliminary structural design of the two caverns; (3) numerical modelling and stability analysis of their excavation process.

The introduction and approach to these three aspects are presented in the following sections, along with the associated research gaps and questions that this project aims to address.

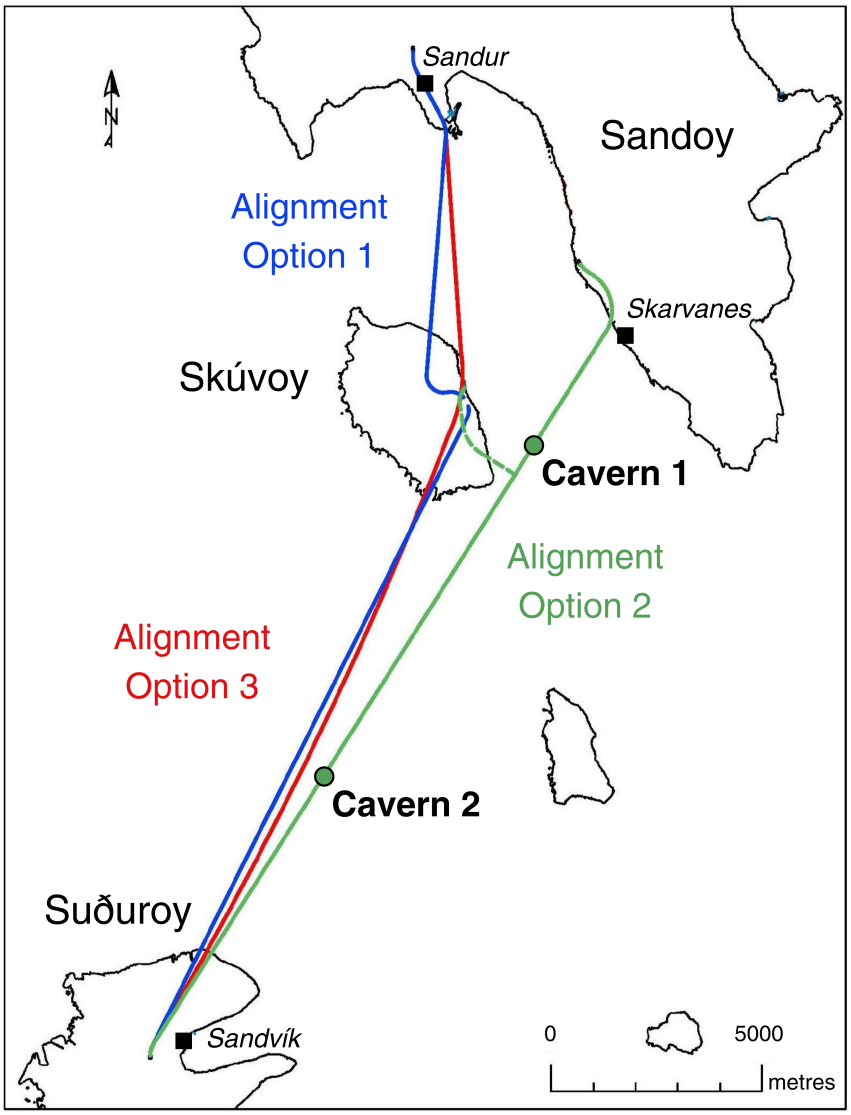


Figure 1.3: The three initial proposed alignments of the Suðuroy Tunnel. Option 2 has been selected as the final choice and is therefore the focus of the current project. Along this alignment, the indicative locations of the planned roundabouts are labelled as Cavern 1 and Cavern 2. Modified from Holter et al. (2021).

1.2 Geological setting

The Faroe Islands originated during rifting events preceding and accompanying the Mid-Atlantic Ridge development. Their lithostratigraphic nomenclature was standardised through the revision performed by Passey and Jolley (2009), replacing earlier schemes (Rasmussen and Noe-Nygaard, 1970; Waagstein, 1988), and clarifying the volcanic and sedimentary sequences.

The stratigraphy is dominated by basalt flows subdivided into three principal formations (Fig. 1.4), each reflecting distinct magmatic phases and depositional settings. Overlying the basal *Lopra Formation*, the *Beinisvørð Formation* comprises extensive tabular basalts from voluminous flood volcanism. Overlying it, the *Malinstindur Formation* represents a second major effusive phase with similarly thick tabular flows. The uppermost *Enni Formation* exhibits more complex facies, including hyaloclastites, indicating lava-water interaction and possible marine or fluvial influence at the time of emplacement.

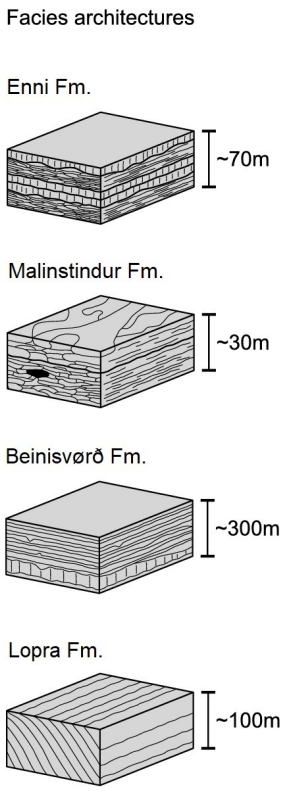


Figure 1.4: The three formations comprising the Faroe Islands Basalt Group (FIBG) and their representative facies, along with the underlying Lopra Formation, which consists of intruded volcaniclastic lithologies. Adapted from Passey and Jolley (2009).

Interbedded sedimentary layers record eruptive quiescence, while widespread dykes and sills—particularly near formation boundaries—highlight intrusive activity emplaced along the structural discontinuities and influencing the mechanical evolution of the volcanic sequence.

Insights into the physical properties of the basalt formations have been derived from deep borehole investigations and seismic surveys. Three deep boreholes across the Faroe Islands, supervised by the Geological Survey of Denmark and Greenland (GEUS), yielded key geophysical logs and seismic data (Mavko et al., 2004; Waagstein and Andersen, 2004; Japsen and Waagstein, 2005), defining average mechanical and petrophysical properties for each main formation (i.e., density, seismic velocities, gamma ray, and neutron porosity). In the Sandoy–Suðuroy region, marine seismic surveys data (Petersen, 2020; Petersen, 2023) and Jarðfeingi-managed boreholes (Petersen et al., 2022) provided

detailed stratigraphic insights.

Structural interpretations of the volcanic sequences and tectonic evolution were presented by Walker et al. (2010). In addition, a notable study by Ziska (2012) mapped fractures and dykes across ~70% of the islands surface using aerial and satellite imagery, identifying regional fracture and dyke trends across major islands and formations. Jarðfeingi also analysed core samples to assess fracture orientation and frequency (Petersen et al., 2022).

Despite the considerable progress in characterising the geological setting at both regional and local scales, several knowledge gaps persist in the Suðuroy Tunnel location. Particularly, in-situ stress measurements are currently unavailable for the proposed tunnel excavation area. Structural data coverage is also incomplete: the work of Ziska (2012) provided no results for Sandoy Island, and an approximately 400 m interval in the stratigraphy along the tunnel alignment remains unlogged, only partly compensated by previous project data reported by Petersen et al. (2022). Lastly, rock mass quality has yet to be evaluated in the target area.

These gaps raise the following research questions:

Q 1.1 What rock mass fracture orientation and quality are expected at the depth where the caverns will be excavated?

Q 1.2 Beyond rock mass parameters, what other factors—such as in-situ stresses, water seepage, and rock-environment interactions—affect tunnel cavern construction and long-term performance in this area?

Q 1.3 Which vertical and horizontal variability in the rock mass is expected at the cavern locations?

To achieve the three sub-questions, a combined desk study and field mapping campaign is planned. The desk study covers a review of relevant literature, analysis of previous site investigations, and examination of datasets from other projects conducted within the Faroe Islands archipelago—whether solid geological correlations with the current project area would be identified. Beyond conventional geotechnical data, the study also incorporates geophysical information, focusing on the seismic and electrical properties of the rock mass as initial indicators. The field mapping aims to fill the remaining data gaps through rock mass characterisation using the Geological Strength Index (*GSI*, Marinos and Hoek, 2000) and the *Q-system* (Barton et al., 1974) methods, along with structural measurements (joint orientations) and evaluations

of rock strength and deformability at selected outcrops around the planned excavation zone.

1.3 Underground widenings

Underground roundabouts and cavern excavations in road tunnels are well-established in Norway (Fig. 1.5). The city of Tromsø, situated around a steep, rocky island, pioneered these facilities construction to redirect tunnel traffic and ensure quick links among various neighbourhoods.



Figure 1.5: Overview of roundabouts and cavern elements in road tunnels across Norway and the Faroe Islands. Topographical conditions have driven the adoption of these solutions in particular in the Arctic city of Tromsø and the fjord region in south-west Norway. In 2020, an underwater roundabout was also opened in the Faroe Islands with the inauguration of the Eysturoy Tunnel. Modified from Yarmolin (2020).

Early works in this site revealed slope failures due to loosening along rock fractures. In particular, experience from the Sentrumstangenten project—Breivika (Fig. 1.6a) and Blå Tunnels—emphasised the need for immediate permanent bolting after ensuring site safety (Høien, 2006). The construction of roundabout elements within tunnels later expanded to the fjord region

of southwestern Norway, where topographical conditions similar to those in Tromsø can be found.

Meanwhile, long tunnel projects such as Lærdal (mountain tunnel, Fig. 1.6b) and Ryfast (subsea tunnel) started incorporating cavern excavations along the alignment, equipped with special lighting to mitigate driver monotony. In the case of the Lærdal Tunnel, these widened sections also serve as safe stopping areas for vehicles. In 2020, the world's first underwater roundabout opened in the Faroe Islands' Eysturoy Tunnel. Nicknamed the "jellyfish roundabout", it links Tórshavn with the towns of Strendur and Runavík, reducing their mutual travel time significantly.

The current review considers three underground roundabout case studies, namely the Steinberg Tunnel, Karmøy Tunnel, and Eysturoy Tunnel. Additionally, the Lærdal Tunnel widening element is selected as a large-span cavern reference. Their basic pieces of information (location, excavation technique, opening year, outer and pillar diameters for roundabout elements) are summarised in Tab. 1.1.

Table 1.1: Summary of general information about the selected roundabout and cavern elements reviewed in this study.

Tunnel name (Localisation)	***Excavation technique***	***Opening year***	***Outer radius***	***Pillar radius***
Steinberg Tun. (Trondheim, NO)	Drill & blast	2006	20 m	9.5 m
T-Connection (Haugesund, NO)	Drill & blast	2011	28 m	7.0 m
Eysturoy Tun. (Tangafjørður, FO)	Drill & blast	2020	19 m	5.0 m
Lærdal Tun. (Lærdal–Aurland, NO)	Drill & blast	2000	15 m	—

The review further covers geological setting, site investigations (particularly related to the roundabout/widening), and adopted support and safeguarding measures (Tab. 1.2).

Geologically, the Eysturoy Roundabout, located within the *Malinstindur* (Middle) *Basalt Formation*, offers the most relevant comparison due to its similar lithology. Quite good rock quality is present there, especially when compared to the greenstone encountered in Steinberg Tunnel. However, basalt failures may occur more suddenly than, for example, in the gneiss observed in the Lærdal Tunnel.



(a)



(b)

Figure 1.6: (a) The three-arm roundabout at the end of the Breivika Tunnel in Tromsø—one of the first of its kind ever constructed. (b) One of the three caverns excavated along the 24.5 km Lærdal Tunnel, designed to break the monotony of driving through the use of non-invasive lighting effects and to offer safe resting spots. Image (a) adapted from Troms County Municipality (2025).

Table 1.2: Geological setting, site investigations, support and safeguarding measures for the four reviewed roundabouts and cavern elements.

	Geological setting	***Preliminary investigations***	***Supports & Safeguarding***
Steinberg	Predominantly greenstone from Cambro-Silurian Caledonian orogeny[1]. Occurrences of greenschist and sections of granodioritic rock with a pillow-like structure[1]. Minor weak and fractured zones in eastern section of the roundabout[2]. Approx. 40 m rock overburden[1].	Surface engineering geological mapping[1]. Analysis of existing maps and aerial photos[1]. Boreholes to bedrock[1]. laboratory testing of rock samples[1].	Fully grouted 6 m combination bolts[2]. Approx. 10 cm shotcrete[2]. Additional reinforcement in SE roundabout section[2]. Combination Rock (CT) bolts for immediate stabilisation and corrosion protection.
T-Connection	Metamorphic igneous rocks, mainly phyllite with significant structural variation[3]. Good quality granitic gneiss[3]. Approx. 60 m rock overburden[3].	Data from the previous Statpipe project[3]. Systematic core drilling ahead of tunnel face[3]. Four-stage seismic surveys (one after the alignment changed)[3]. Final investigation round specifically focussed on roundabout geology[3].	Short and split drilling rounds[3]. 6 m CT bolts in suspension, 4 m CT bolts in rock pillars[3]. Systematic shotcrete[3].
Eysturoy	Varying basalt horizons, no significant weakness zones identified[4]. Excavated 72 m below sea level, approx. 50 m of them of rock cover.	Stress measurements prior to excavation[4].	Avoided simultaneous rock removal on both pillar sides to prevent deformation and fractures[5]. Staged installation of supports for stability and load-bearing capacity[4].
Lærdal	Precambrian gneisses, generally few joints, but major fault zones present[6]. Localised high stress anisotropy[6] and rock stress relief phenomena[7]. Relevant water ingress; up to 1500 m of rock cover[6].	Engineering geological surveying of the area above and around the alignment[7]. Geotechnical classification according to the *Q*-system[7]. No core drilling or stress measurements performed prior to construction, interpretations from similar projects.	Scaling of loose rock[8]. Pre-excavation grouting. Systematic rock bolts, fibre-reinforced shotcrete, additional concrete lining in fractured zones[8]. Specialised ventilation systems used during blasting[8].

[1] Rambøll Norge AS (2007) [2] Høien (2006) [3] Stumo (2016) [4] Samuelsen and Grøv (2018)
[5] The Guardian (2024) [6] Norwegian Tunnelling Society (2022) [7] Blindheim (2003) [8] Statens Vegvesen (2000)

The feasibility of large spans is promising, as demonstrated by existing widenings with radii exceeding 20 m (e.g., the T-Connection), provided that appropriate support systems and pillar dimensions are implemented. Notably, pillar supports have never been required for roundabout branches, even in weaker zones such as the eastern section of the Steinberg Roundabout.

Investigations varied significantly across the four case studies, ranging from desk-based investigations to core drilling ahead of the tunnel face. However, the underwater setting of the current project will limit the direct application of many inland investigation methods. Support systems—including bolt type and length, as well as shotcrete thickness—must indeed be adapted to site-specific conditions. Although structural supports will not be explicitly modelled in simulations for this project, design recommendations will be provided. As in the Eysturoy Roundabout, the central pillar will need to be excavated in stages, with one side completed per blasting phase. Regarding safeguarding measures, given that the Suðuroy Tunnel's length (~24 km) is comparable to that of the Lærdal Tunnel, specialised ventilation during blasting operations will also be required.

Norwegian guidelines have been adopted across all four projects, including that in the Faroe Islands. At present, the primary national reference for tunnel design is Handbook N500–*Vegtunneler* ("Road Tunnels", Statens Vegvesen, 2024b). Roundabout dimensioning and lane widening follow Handbook N100–*Veg-og-Gateutforming* ("Road and Street Design", Statens Vegvesen, 2024a), specifically Section 4.1.2 *Rundkjøringer* ("Roundabouts"). Both handbooks are issued by the Norwegian Public Roads Administration (*Statens Vegvesen*). In addition, for large spans and caverns, the Norwegian Rock Caverns guidelines are also applied (Norwegian Tunnelling Society, 2016).

> In the Suðuroy Tunnel, the planned roundabouts are primarily intended to facilitate turning by large vehicles rather than to control traffic. They may also serve secondarily to reduce driver monotony and provide brief rest areas. Accordingly, further evaluation is needed to assess the applicability of existing designs under differing conditions, including alternative geometrical parameters scale beyond those of Norwegian and Faroese precedents.

Achieving the absence of prior cases involving similar infrastructure in terms of both context and functionality, the following research questions emerge:

Q 2.1 How do the geometrical parameters of cavern excavation affect tunnel stability and design functionality?

Q 2.2 How will the different purposes of the Suðuroy caverns influence their design compared to the Eysturoy Roundabout and other existing ones?

To address the existing gaps, a parametric design approach is adopted by synthesising current roundabout and cavern guidelines. Key parameters and variables are then identified based on the relevance of excavation elements to the aforementioned functionalities and structural stability (Q 2.1). The resulting geometries, intended for use as inputs in numerical models, are developed using the CAD software Rhino® and its integrated tool Grasshopper, provided by the host organisation. During this process, design decisions will determine whether modifications to existing geometries are required (Q 2.2).

1.4 Numerical modelling

Despite significant progress in recent decades in developing analytical solutions for cavern stability in collapse mechanisms (Fraldi and Guarracino, 2009; Fraldi and Guarracino, 2010; Gharsallaoui et al., 2020), face stability (Mihalis et al., 2009; Qarmout et al., 2022), and displacements (Zhang et al., 2022), numerical methods remain the widest approach in tunnelling engineering practice. Tunnel and cavern simulations are typically categorised into continuum and discontinuum models. The former treat rock masses as continuous media using methods such as the Finite Element Method (FEM), Finite Difference Method (FDM), and Finite Volume Method (FVM). The latter models rock as discrete blocks, better capturing mechanical behaviour dominated by discontinuities.

1.4.1 Continuum approach

The Finite Element Method (FEM) is the predominant technique for modelling large-span caverns in Norway (Norwegian Tunnelling Society, 2016). It relies on the assumption of continuum behaviour at scales larger than rock discontinuities (Carranza-Torres, 2021), which allows the use of standard failure criteria such as Mohr–Coulomb (Duncan and Chang, 1970) and the generalised Hoek–Brown criterion (Brown and Hoek, 1980; Hoek and Brown, 1997). Commercial implementations in software, such as the Hoek–Brown PAC (Pan and Hudson, 1988; Shah, 1992; Carter et al., 1993), are also widely applied. The Hoek–Brown criterion was

later revised with the introduction of the disturbance factor D (Hoek et al., 2002).

Finite Difference (FDM) and Finite Volume (FVM) methods offer alternative continuum formulations. FDM discretises differential equations via nodal grids, often in dynamic simulations, while FVM conserves fluxes across control volumes to compute averaged field values. As continuum methods, they cannot capture randomly distributed discontinuities, necessitating field monitoring (e.g., stress sensors) for calibration and validation (Trinh and Jonsson, 2013).

1.4.2 Discontinuum approach

Discrete Element Methods (DEM) model discontinuous media by representing interacting bodies through explicit contacts. As noted by Cundall and Hart (1993), a method qualifies as DEM if it permits finite displacements and rotations of discrete elements (including separation) and can autonomously detect and form contacts. A notable application of DEM in large spans modelling is the Gjøvik Olympic Cavern in Norway, an impressive 62 m wide excavation analysed with rock mass software specifically designed for discontinuum systems (Barton et al., 1994). DEM modelling requires appropriate constitutive laws for jointed rock masses. According to Barton (2022), three main shear strength criteria are commonly used to characterise rock joints: (i) the Mohr–Coulomb criterion, (ii) its low-stress adaptation by Patton (1966), and (iii) the Barton–Bandis empirical model (Barton and Choubey, 1977).

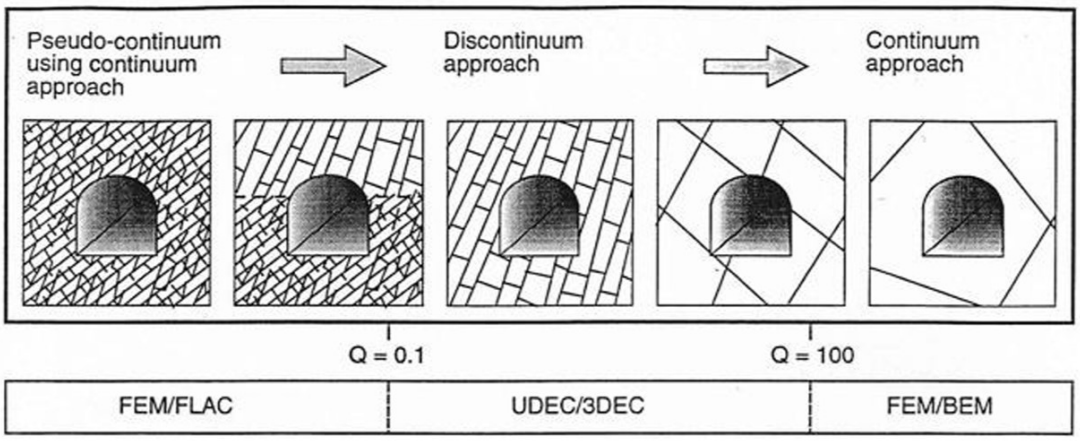


Figure 1.7: General recommended modelling approach based on the Q-value score of the rock mass. Reproduced from Barton (2022).

The choice between continuum and discontinuum modelling in tunnel and cavern design is largely debated. As a guideline, Fig. 1.7 suggests appropriate methods for five schematic rock

mass types, based on *Q*-values—consistent with the *Q-system* classification that will be applied during the field mapping campaign of this project. Due to in-house software constraints, this study employs FLAC3D (v 6.0), a FVM tool widely used in tunnelling and mining expertise that has already shown to deliver high predictive accuracy (Trinh et al., 2021).

Given the new context for cavern excavation, reflected in site-specific failure criteria parameters, elastoplastic material properties, and in-situ and boundary stress and displacement conditions, it is clear that a specific numerical model is required to assess the suitability and structural reliability of the proposed geometries.

From which, the **main research question** of the project is formulated:

To what extent can an underwater road tunnel widening be excavated given the specific in-situ stresses field, rock layer typology and orientation of the Suðuroy Tunnel, both including and excluding a central rock pillar?

In addition, the other questions related to the numerical modelling section are:

Q 3.1 How do stresses and displacements vary with changes in cavern geometry, and where are the most critical stress conditions located within the excavation?

Q 3.2 How do rock mass quality, lithostratigraphic variability, and blasting methodology (disturbance factor) affect the model response and the design of cavern size?

The main research question is addressed through a series of numerical simulations with various input geometries, in which the key geometrical parameters are systematically modified. The continuum is characterised by average mechanical properties and failure criterion parameters. The resulting stress and displacement fields are then analysed to evaluate the geometries' performances.

Sub-question Q 3.1 is explored by examining both peak stress and displacement magnitude and localisation, as well as the evolution of these variables along the entire excavation contour across the various simulations. Finally, a targeted set of simulations is planned to investigate the cavern excavation response with respect to the main geotechnical units identified in the area, thereby tackling sub-question Q 3.2. Additionally, also in connection with sub-question Q 1.3, spatial variability in geological and geotechnical conditions is introduced. The impact of rock

mass quality is assessed through sensitivity analyses on elastoplastic and failure parameters whose characterisation remains uncertain even after the desk study and field mapping.

1.5 Project outline

The thesis project is structured around the three main lines of investigation: the review and integration of the excavation site's geological, lithostratigraphic, and geotechnical parameters; the development of preliminary design approaches tailored to the cavern geometries; and the numerical analysis of the excavation geometries in terms of their stability (Fig. 1.8). The thematic threads are developed across seven chapters (excluding the introuction and

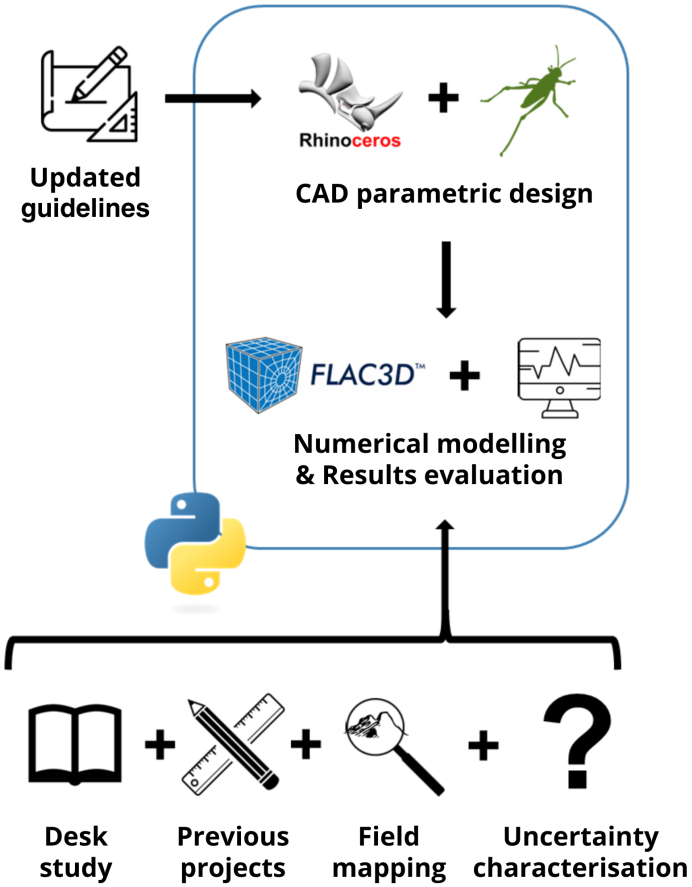


Figure 1.8: Image-based project overview diagram. The approach integrates desk studies, analysis of previous projects, field mapping, and uncertainty characterisation to address research gaps related to the local geology. In addition, a review of current guidelines and the use of CAD software will support the development of a reliable set of preliminary designs. Numerical simulations will build on these contributions using FLAC3D software, and the evaluation of results will help answer the project's main research question. Notably, Python is compatible as programming language with all software tools used in the project.

the conclusions), designed to follow the logical progression of the project. While the topics naturally interrelate and overlap throughout the study, each chapter is specifically dedicated to one of the main themes for clarity.

Note: the entire workflow of preliminary design and simulation tools is implemented with Python-based programs, ensuring an integrated computational framework within a unique programming language.

- **Chapter 1**, the present chapter, introduces the research problem and outlines the key questions to be addressed throughout the course of the project itself.
- **Chapter 2** provides an overview of the stratigraphy of the Faroe Islands, highlighting the different geological phases and the resulting transitions from older to more recent units. The chapter concludes with a discussion of the Total Geological Approach proposed by Fookes et al. (2000), offering a review of past and recent tectonic activity, geological context, and relevant case studies to anticipate potential geohazards and geotechnical challenges in the proposed tunnel excavation area (Q 1.1, Q 1.2).
- **Chapter 3** adopts an engineering geology perspective of the excavation site. Following a brief illustration of existing site investigation relevant data, the chapter is divided into two main sections. The first characterises the bedding and orientation of key geological layers, forming the basis for a longitudinal cross-section of the area. The second conducts a detailed analysis of the likely orientation and relative magnitude of in-situ stresses at the cavern locations, acknowledging the current lack of direct instrumentation data and the unfeasibility of acquiring such data during the planned field mapping campaign (Q 1.1, Q 1.3).
- **Chapter 4** investigates the rock masses from a geophysical perspective by examining their seismic and electrical properties. The seismic properties are related to the rocks' elastic characteristics, while the electrical properties are analysed to assess the potential presence and magnitude of water inflow into the excavation. This assessment considers factors such as rock porosity, saturation index, and hydraulic conductivity, given the project's underwater context (Q 1.2, Q 1.3).
- **Chapter 5** details the field mapping activities carried out during the study, in collaboration with the host company. It outlines the rationale, planning, methodologies, and key findings, presenting them as a complement or a validation of the preceding desk-based engineering geological, geotechnical, and geophysical analyses (Q 1.1, Q 1.3).
- **Chapter 6** tackles the preliminary design of the two caverns. It examines the latest applicable design standards according to Norwegian guidelines and integrates the functional requirements of the roundabout with the structural demands of a large-span underground

excavation. The result is a set of reliable preliminary design proposals to be used in the subsequent numerical modelling (Q 2.1, Q 2.2).

- **Chapter 7** presents the rationale for developing the numerical model by explaining the methodologies and modelling strategies adopted to address the core research question and the related sub-questions concerning numerical modelling in the project (Q 3.1, Q 3.2).
- **Chapter 8** presents the numerical results, beginning with simulations that address the main research question of the project while simultaneously identifying the optimal geometries for the final design. This is followed by an analysis of the simulation results aimed at assessing the impact of uncertain parameters on the principal stress and displacement outcomes. The chapter concludes with a brief section on the proposed structural reinforcements for the excavation (Q 2.1, Q 3.1, Q 3.2).
- **Chapter 9** concludes the project by highlighting the main findings of the study. It also addresses the research gaps and emphasises the strengths, limitations, and potential directions for future work. Additionally, the chapter underscores the project's relevance in terms of its social impact.

This chapter-by-chapter arrangement facilitates a clear and focused investigation, ensuring that each aspect of the project is thoroughly examined and effectively linked to the overall research goals.

2

Faroe Islands geology: an overview

Bundin er bátleysur maður

A boatless man is tied up

Shaped over millions of years by weathering and glacial erosion, the Faroe Islands are characterised by a distinctive mountainous landscape, carved into steep cliffs and deep fjords. Due to frequent and strong oceanic winds, woody vegetation is almost entirely absent, while vast stretches of grass often hide the dark and volcanic rocky core of these islands, which is mostly revealed along the steep cliffs in the coastline or the inland waterfalls and stream beds.

2.1 The igneous nature of the Faroe Islands

Tectonically, the Faroe Islands (Fig. 2.1) are the emerging portion of a larger oceanic plateau located between the Eurasian Plate and the Mid-Atlantic Ridge (Fookes et al., 2000). They formed as a result of intense magmatic activity during the Palaeogene period—approximately 63.1 Ma (Waagstein et al., 2002) to 54.8 Ma (Ziska, 2012)—which, unlike in neighbouring Iceland, is no longer active. The entire archipelago consists of flood basalts, collocating the Faroe Islands within the larger geological North Atlantic Igneous Province (NAIP), which also includes the British Palaeogene Igneous Province, parts of the eastern Greenland coastline, the island of Jan Mayen, and Iceland (Fig. 2.2). When focusing specifically on the Faroese basalts, they are referred to as the Faroe Islands Basalt Group (FIBG).



Figure 2.1: The Faroe Islands archipelago from an aerial view.

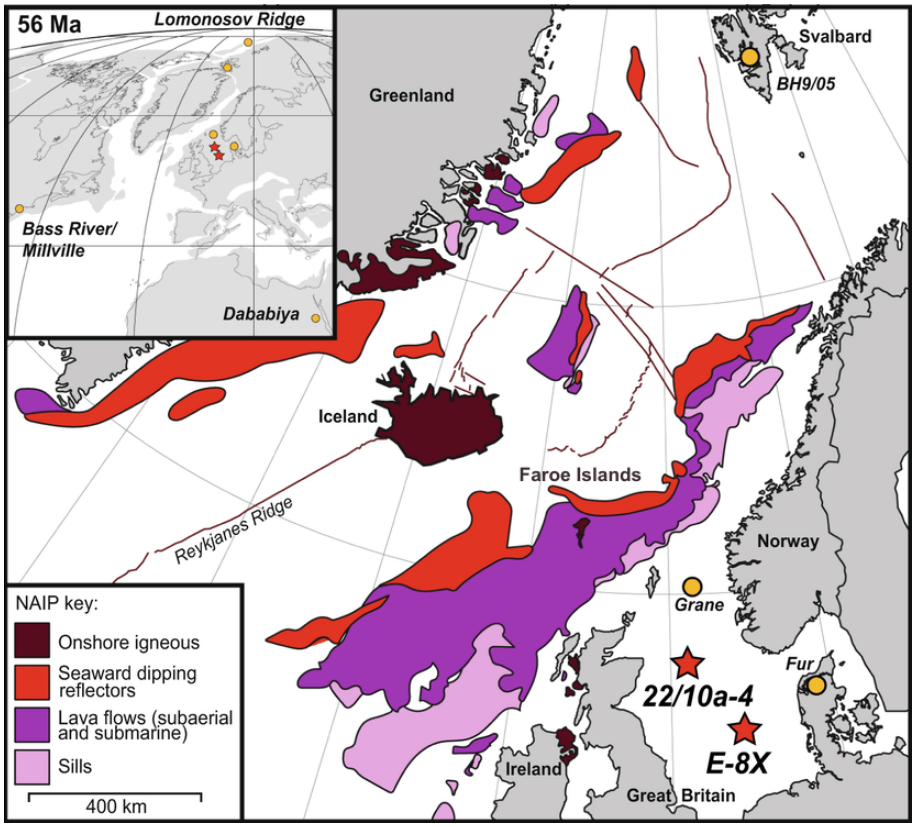


Figure 2.2: The North Atlantic Igneous Province (NAIP), with the Faroe Islands archipelago situated within a vast complex of subaerial and submarine volcanic flows, most of which are now submerged. Adapted from Kender et al. (2021).

Most of the volcanic activity in the Faroe involved subaerial lava flows, meaning they interacted with the atmosphere rather than with seawater. In fact, during the Palaeocene, the FIBG was emplaced at or around sea-level (Walker et al., 2011a). A fundamental unit of lava, surrounded by a chilled crust, is referred to as a flow lobe. Depending on the duration and consistency of magmatic activity, one or multiple flow lobes can form either a simple lava flow or a compound lava flow (Fig. 2.3; Walker, 1971). In the latter case, flow lobes often overlap. Individual lava flows are distinguished by weathering surfaces and/or volcaniclastic lithologies, developed when sufficient time between flows allows for significant sediment deposition.

For subaerial magmatic effusive activity, two main types of mafic (i.e., low-silica) lava flows have been identified by examining the terminal tongues of the flows: *'a'ā* and *pāhoehoe*.

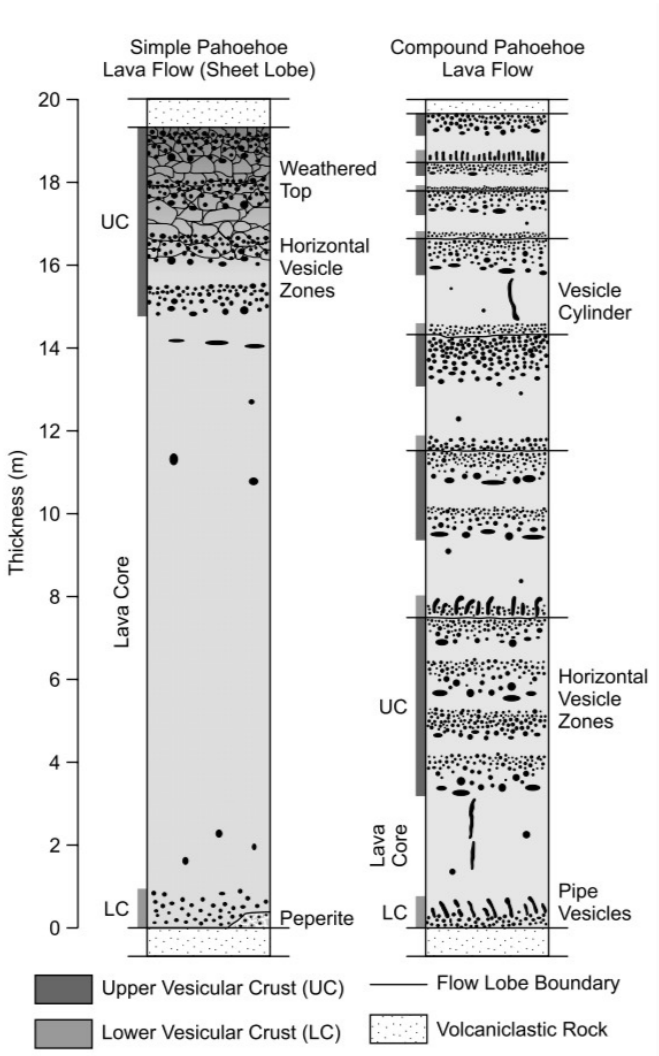


Figure 2.3: Simple and compound lava flows: main features and average size scale. Reproduced from Passey and Jolley (2009).

'A'ā lava (Fig. 2.4a) is highly viscous and non-plastic, which prevents cracks in the crust from healing. These flows display a distinctive structure, with clinkers present at both the top and the base, comprising between 15% and 65% of the total flow thickness. The clinkers move as a thick layer above the molten lava, effectively sandwiching the dense, massive core of the flow. *Pāhoehoe* lava (Fig. 2.4b), in contrast, features a thin, light-coloured, and smooth crust with a wrinkled surface, often characterised by small, tight folds as the result of small lava lobes that break through the crust, solidifying into irregular shapes in response to the surrounding topography. *Pāhoehoe* flows also contain numerous pores, ranging in size from tiny voids to several centimetres and often filled with light-coloured secondary minerals.



(a) (b)

Figure 2.4: Comparison between (a) ʻaʻā and (b) pāhoehoe lava flows. In the first, typical clinkers are visible at the top of the still-molten flow, while in the latter, the characteristic structure of overlapping folds is clearly identifiable. Images from Cressler (2007) and Cressler (2011).

When solidifying underwater, a third type of flow—known as pillow lava—forms as a result of rapid extrusion, cooling, and solidification. Pillow lavas are rarely encountered in the Faroese stratigraphy.

In petrological terms, Faroese basalts are classified as tholeiitic lava flows—low in alkali content (sodium, potassium) but rich in iron and magnesium—which commonly originate from mid-ocean ridges, continental rift zones, and oceanic islands. Based on their texture and the size of crystals within the matrix, three tholeiitic basalts groups can be classified within the Faroese stratigraphy.

The first group consists of aphyric basalts (Fig. 2.5a), characterised by an extremely fine-grained (aphanitic) groundmass, with only small minerals present. The second group includes plagioclase-phyric basalts (Fig. 2.5b), characterised by a variety of porphyritic textures with eye-visible white minerals embedded in a finer-grained matrix. When crystals grow to several times the size of the surrounding matrix, they are commonly referred to as phenocrysts. Lastly, the third group comprises olivine-phyric basalts (Fig. 2.5c), distinguished by small (<5 mm), typically stout phenocrysts, which can vary on a local scale (Passey and Jolley, 2009).

In this volcanic igneous setting, minerals such as zeolites, quartz, and calcite are spread across the archipelago. These minerals, often appearing as light-coloured crystals, were not part of the original basaltic lava. Instead, they precipitated later from hot water through cracks, pores and extensional shear veins inside the basaltic bedrock (National Museum of the Faroe Islands, n.d.; Walker et al., 2010).



(a)

(b)

(c) .

Figure 2.5: Comparison of different basalt types found across the Faroe Islands. (a) Aphyric basalts exhibit a fine-grained, uniform matrix with an almost complete absence of visible phenocrysts. (b) Plagioclase-phyric basalts are distinguished by embedded white plagioclase crystals that are larger than the surrounding matrix. (c) Olivine basalts, rarely observed in Faroese outcrops, typically display a darker matrix and plagioclase minerals.

2.2 Faroe Islands stratigraphy

The first large scale explorations of the Faroese underground lithology involved drilling three deep boreholes at their respective locations: *Lopra*-1/1A—conducted in two stages (1981 and 1996)—on Suðuroy Island, *Vestmanna*-1 (1980) and *Glyvursnes*-1 (2002) on Streymoy Island (Fig. 2.6). The primary objective was to capture the entire Faroese basalt lithostratigraphic sequence, reaching and penetrating the pre-volcanic basal layer; this goal has never been fully achieved. Nevertheless, the initial boundary of the lava basalt layer was identified and designated as the *Lopra Formation*, marking a distinct geological transition from the overlying lithologies (Fig. 2.6).

These three deep boreholes enabled the identification of three main stratigraphic sequences overlying the *Lopra Formation*, previously only partly exposed along the archipelago. In accordance to the nomenclature revision by Passey and Jolley (2009) these sequences, from

oldest to youngest, are referred to as *Beinisvørð*, *Malinstindur*, and *Enni Formations* (Fig. 2.6).

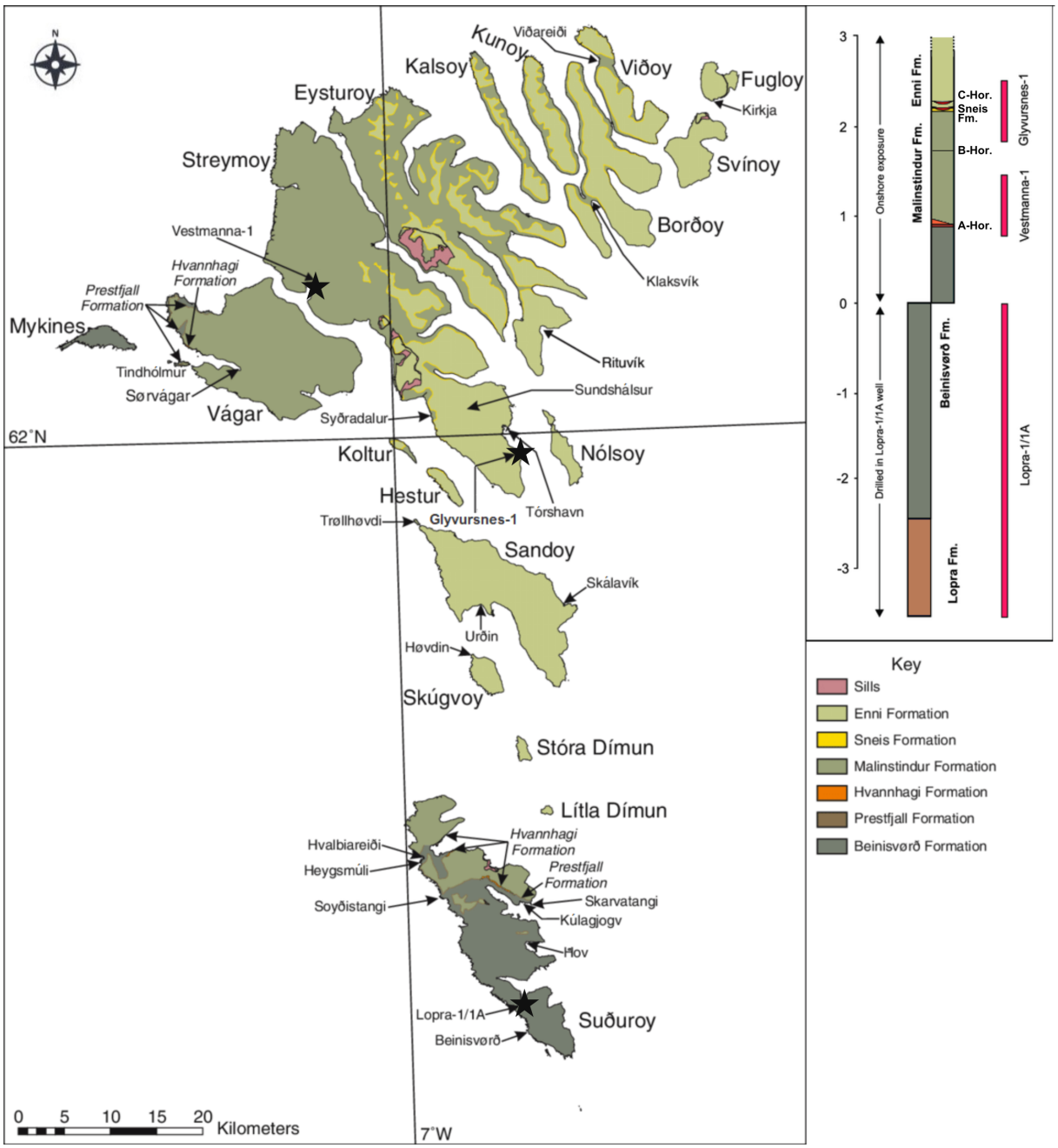


Figure 2.6: Exposed stratigraphic units across the Faroe Islands archipelago, along with the names of the most relevant geological sites, the average thickness of the three basalt formations (Beinidsvørð, Malinstindur and Enni), and the stratigraphic intervals covered by the three deep boreholes: Lopra-1/1A, Vestmanna-1, and Gyvursnes-1. The locations of the three boreholes are also marked on the map with star symbols. Adapted from Szöőr et al. (2005) and Olavsdottir et al. (2021).

Rasmussen and Noe-Nygaard (1970) previously referred to them as the Lower, Middle, and Upper Basalt Formations—a nomenclature still commonly used in many sources. The overall lava flows

sequence is frequently interrupted by sedimentary units of varying thicknesses, ranging from a few tens of centimetres to several meters, as well as by morphological changes occurring either suddenly or gradually. In particular, when extensive and recurrent sequences of sedimentary layers are present within the stratigraphy, they are referred to as “beds". This section focuses on the key geological features of the Faroe Islands relevant to the project, providing a more detailed study building on the basic review performed in Section 1.2, Chapter 1.

2.2.1 Beinisvørð Formation

The earliest evidence of volcanic activity in the Faroe Islands consists of lava flows deposited in shallow marine waters, determining the beginning of the *Beinisvørð* (Lower Basalt) *Formation*. At upper levels of the *Lopra*-1/1A well, thick *'a'ā*-type lava flows are encountered. This volcanic episode marks the beginning of continental rifting, which successively led to the opening of the North Atlantic (National Museum of the Faroe Islands, n.d.).



Figure 2.7: Columnar basalt formations near Tvøroyri, Suðuroy Island.

With a total thickness of approximately 3200 m (National Museum of the Faroe Islands, n.d.), the Lower Basalt Formation consists of 36 identified flows. Its morphology is mainly characterised by simple lava flows with a tabular geometry, averaging 20 m in thickness (Waagstein et al.,

1984). Within the exposed upper ~900 m, the first ~700–800 m are predominantly composed of poorly developed prismatic joints, which is commonly observed throughout most of the Faroese igneous stratigraphy. In contrast, the final ~100–200 metres show regular, uniformly spaced hexagonal columns (Passey and Jolley, 2009), particularly within the *Kulagjógv Flow* (Fig. 2.7), cropping out near Tvøroyri (Suðuroy Island).

2.2.2 Prestfjall and Hvannhagi Formations

The first eruptive cycle is interrupted by a relatively long period of quiescence, allowing for significant sedimentary deposition and the origin of the *Prestfjall Formation*, a volcaniclastic conglomerate characterised by two distinct coal seams along its lithology (Passey and Jolley, 2009). This formation was formerly referred to as the "coal-bearing sequence formation" or the "*A-Horizon*" (Rasmussen et al., 1956; Rasmussen and Noe-Nygaard, 1970). The *Prestfjall Formation* exposure is limited, and it primarily outcrops on the island of Suðuroy, relatively near the southern tunnel portal, around the town of Hvalba. In this area, the unconformity varies in thickness between 3 m and 15 m (Rasmussen and Noe-Nygaard, 1970). Within the formation, five to six thin—usually $<$1 m (Rasmussen and Noe-Nygaard, 1970; Passey, 2004)—lithologies have been identified (Passey and Jolley, 2009), including the two coal seams.

A gradual and sequential transition is observed between the *Prestfjall Formation* and the overlying syn-eruption facies (cf. Smith, 1991), known as the *Hvannhagi Formation* (Fig. 2.6). Its distribution across the archipelago is uncertain and confined to topographic depressions in the paleo-landscape (Passey, 2004). In the northern part of Suðuroy Island, near Hvalba, the formation thickness is expected to reach 30 to 40 m. The facies include both pyroclastic (coarse to homogeneous tuffs, lapillistone, conglomerates) and sedimentary (volcaniclastic sandstones and mudstones) lithologies, deposited in a terrestrial environment (Passey, 2004).

2.2.3 Malinstindur Formation

The middle 1250–1350 m of the exposed basalts on the Faroes are known as the *Malistindur* (Middle Basalt) *Formation*, predominantly consisting of *pāhoehoe*, almost exclusively compound lava flow lobes (Passey and Bell, 2007; Passey and Jolley, 2009). Each lava flow is typically about 2 m thick (Rasmussen and Noe-Nygaard, 1970; Waagstein, 1988; Passey and Bell, 2007) and consists of braiding tongues and thin overlapping flow units. These tongues merge and may display parallel small vesicle zones in high concentration in the flow tops, while the core remains liquid for a more extended period. Cylindrical vesicles (or pipes) are also commonly found in a 5–10 cm zone at the base, likely formed by water vapour rising from a wet subsurface

or by internal boiling within the lava. Over time, these vesicles became filled with minerals (Fig. 2.8) such as zeolite, calcite, or clay minerals, with occasional occurrences of montmorillonite. A tunnel project investigation in Vágar found that vesicles can account for up to 20% of the pore volume in many cases (Rodrigues et al., 2002), offering potential flow paths for the groundwater. Where weathered, the tops of the flows often exhibit a characteristic red colouration.



Figure 2.8: A mesolite mineral formation within a Malinstindur basalt flow observed in an outcrop on Suðuroy Island.

The *Malistindur Formation* originated in an initial phase characterised by a high production of volcanic ash, lapilli, and volcanic bombs, followed by a second phase marked by continuous lava production (National Museum of the Faroe Islands, n.d.). This phase coincides with the initiation of sea-floor spreading in the North Atlantic rift system. As a result, sedimentary deposits are largely absent especially in the lower interval of the formation (Passey and Jolley, 2009). Three main basalt textures are identified within the Middle Formation. The first ~450 m consist of (i) olivine-phyric basalts (Noe-Nygaard and Rasmussen, 1968; Waagstein et al., 1984; Waagstein, 1988), transitioning to (ii) pale-weathering plagioclase basalts (Noe-Nygaard and Rasmussen, 1968; Rasmussen and Noe-Nygaard, 1970), and further to the upper (iii) brown-weathering aphyric to olivine-phyric basalts (Noe-Nygaard and Rasmussen, 1968; Rasmussen and Noe-Nygaard, 1970; Waagstein et al., 1984; Larsen et al., 1999). Toward the top of the formation, interlava lithologies become more frequent, including reddened volcaniclastic beds of sandstone and mudstone (Passey, 2004), which are rarely more than a few metres thick

(Passey and Jolley, 2009).

2.2.4 Sneis Formation

The *Sneis Formation* consists of an eroded, brown-weathered lava flow sequence that caps the Middle Basalt Formation. It is uniformly present across the Faroe (Passey and Jolley, 2009) and is typically overlain by a volcaniclastic sandstone series, commonly referred to as the *Sund Beds*, followed by multiple conglomerate beds (Rasmussen and Noe-Nygaard, 1970), which may be either cemented or display protrusions of coarse sand and boulders (Passey, 2004). The *Sneis Formation* reaches a maximum thickness of 30 m gradually decreasing to just 1 m moving southward across the archipelago until Sandoy (Passey and Jolley, 2009). Here, thin sandstone facies replace the thicker conglomerates found beneath the northern islands (Passey, 2009). Slightly above lies the so-called *C-Horizon* (Passey, 2009), a shallow intrusive group of layers—therefore not flows—comprising brown-weathered, aphyric to olivine-phyric basalts (Rasmussen and Noe-Nygaard, 1970; Passey and Jolley, 2009).

2.2.5 Enni Formation

The upper ~900 m of the Faroese succession are once again dominated by rhythmic lava production. The individual *pāhoehoe* flows are thinner, consisting of a mixture of both compound flows—tens of metres thick—and simple (sheet lobe) flows 15 m thick on average (Passey and Bell, 2007; Passey and Jolley, 2009). This lava facies connects to the starting of the sea-floor spreading active phase in the North Atlantic, occurring partly in a subaerial environment and partly in shallow sea or under abundant surface water.

A first clear chromatic and textural distinction is evident in the *Enni* (Upper Basalt) *Formation* between a first basalt sequence of brown weathering, aphyric to olivine-phyric and a second pale weathering, plagioclase-phyric to aphyric. A strong horizontal foliation and defined flow lobes are displayed in the former, with large plagioclase within the matrix. Instead, less defined flow lobes and strong weathering and erosion processes characterise the latter (Passey and Jolley, 2009). A total of 29 flows have been identified in the lower section of the *Enni Formation*, while the uppermost ~300 m have not yet been fully logged according to Passey and Jolley (2009). Several interlava lithologies are observed throughout the stratigraphy, mainly consisting of volcaniclastic sandstone and mudstone, with occasional conglomerates. The most significant layers in terms of thickness—exceeding 50 cm—are found beneath the single flows. In contrast, sediment thickness decreases within the compound flow sequences. Similar to the *Malinstindur Formation*, numerous beds are formed by the close accumulation of sedimentary sequences

over time.

Intrusions such as dykes are widespread across all the Faroese lithostratigraphy, where the intruded basalt often resists erosion better than surrounding rock, forming prominent linear features that resemble stone fences. However, post-solidification movements along the original fractures and the development of parallel cracks can locally reduce erosion resistance, leading to dyke degradation and the formation of ravines or fissures, resembling those in non-intruded fractures (National Museum of the Faroe Islands, n.d.).

2.2.6 Post-magmatic evolution

The lavas exhibit an overall progradational stacking pattern, reaching a true vertical thickness on the order of kilometres, which suggests that a comparable scale of subsidence occurred during the eruption period—a process with which most of the deformation structures on the archipelago are associated (Geoffroy et al., 1994; Ellis et al., 2009; Passey, 2009). Consequently, a progressive flattening of bedding planes is observed from the oldest (~8°–6°) to the youngest basalts (~3°–1° in the *Enni Formation*, see Fig. 2.9). This geometry suggests regional-scale tilting due to fold growth in coincidence with the emplacement of the Faroe Islands Basalt Group (Doré et al., 2008; Walker et al., 2010; Walker et al., 2011b).

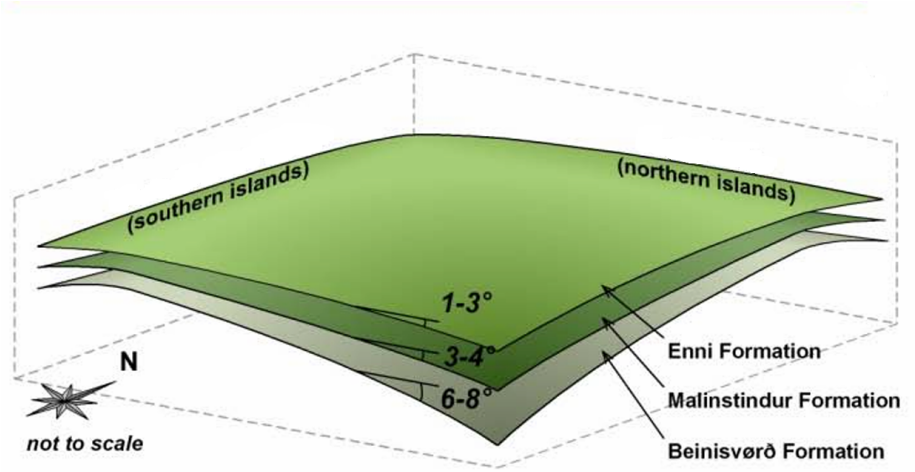


Figure 2.9: Range of average dip angles for the three basalt sequences in the Faroe Islands. Adapted from Walker et al. (2010).

It is estimated that 200–300 additional metres of the *Enni Formation* flows have been eroded over the years (Waagstein et al., 2002). Although there is clear evidence of only two glaciations

in the Faroes, the actual number is likely between six and ten, based on findings from NW Europe (National Museum of the Faroe Islands, n.d.). Ice has transformed the original basalt plateau—once characterised by flood plains and low relief—into a rugged landscape of deep valleys, fjords, and steep mountain ridges. Ice flows have loosened material and transformed the original V-shaped valleys into wider U-shaped ones. As the glaciers advanced, material frozen to their bases carved striations into the underlying rock, ground rocks into fine powder, and polished exposed surfaces. Enormous volumes of material have been eroded and deposited as thick layers of sand and clay on the seafloor of newly formed fjords and sea straits separating the islands and partially washed away in a second instance. Overall, glacial erosion appears to be the dominant process in shaping the present-day Faroese landscape.

2.3 Total geological history approach

The initial elementary data, combined with a well-established lithological overview, enable the anticipation of certain geological features of the region using the total geological history model approach proposed by Fookes et al. (2000). This approach aids to offer a preliminary feature which is a valuable foundation for planning ground investigations and provide essential information for developing subsequent site-specific models. The study focuses on the Sandoy–Suðuroy area (~25×15 km), the planned site for tunnel excavation. Here, the most appropriate geological model is the igneous-basic volcanics (Fig. 2.10).

Although basaltic lava flows generally present relatively limited risks during blasting, their complex stratigraphy often includes mechanically weak features such as intra-flow sedimentary units and breccias or conglomerates at the flow top and base. Their characterisation should be therefore carefully included in site investigations and parameter assessments. Given that the Faroese lava flows exhibit a mean dip of approximately 3° (Rodrigues et al., 2002) and with a typical range between 1° and 8° (Waagstein et al., 2002), any weak layers intersecting the tunnel are likely to persist along the alignment for tens of metres. This could potentially compromise excavation stability—a concern also highlighted by Holter et al. (2021). Additionally, localised mechanical weaknesses within the basalt may also arise from irregular lava flow structures or pyroclastic interbeds. Stratigraphic core logging—via onshore, offshore, and preferably inclined boreholes as well—remains the most reliable method for identifying such hazards.

Given the underwater alignment of the Suðuroy Tunnel and the potential for localised high groundwater flow along drainage features typical of igneous formations, particular attention must be paid to permeability conditions—especially in the deepest fjord sections, where uncontrolled inflows could pose critical risks (Samuelsen and Grøv, 2018). In general, underwater

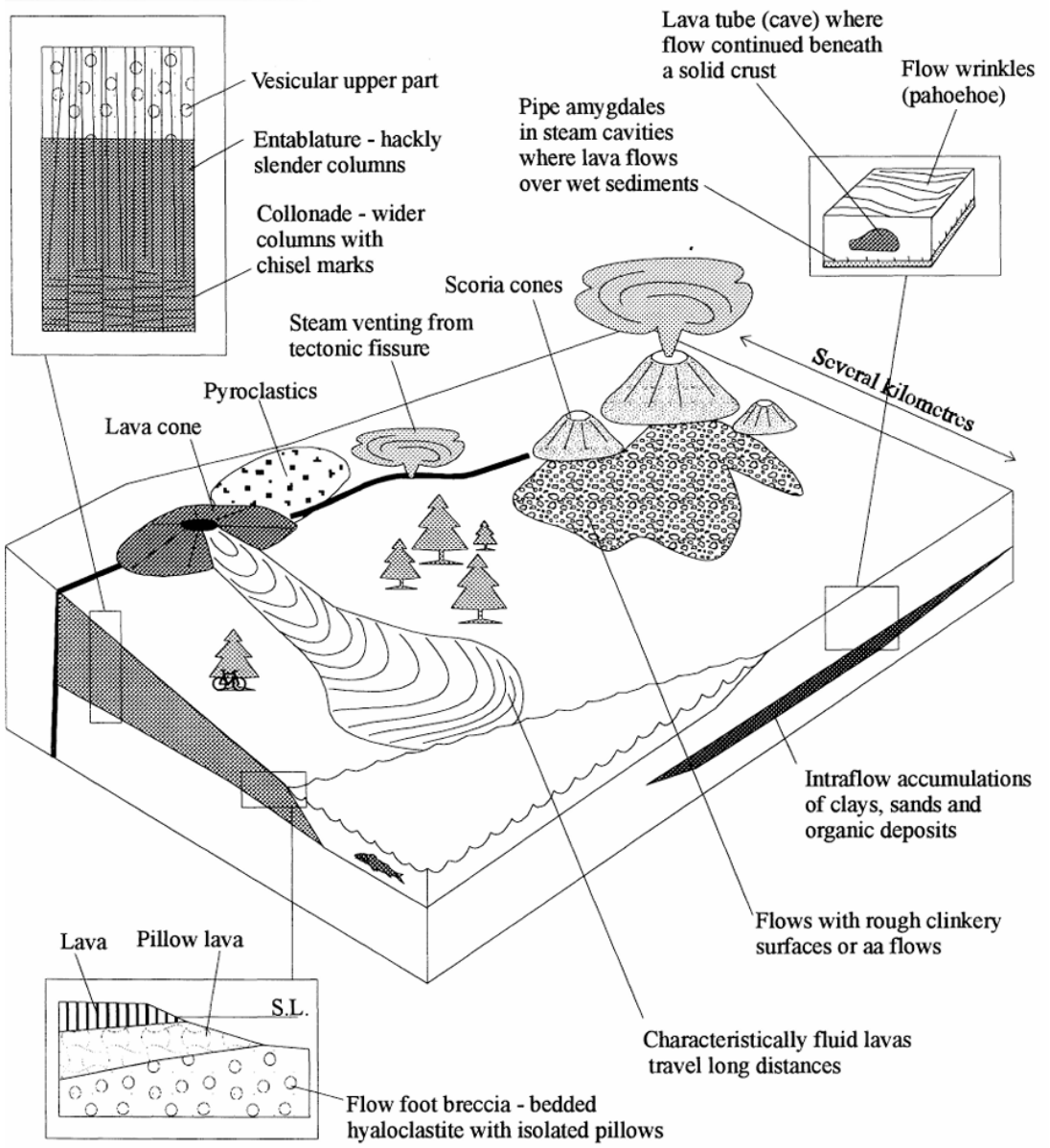


Figure 2.10: Fookes model for basic igneous volcanic environments. Reproduced from Fookes et al. (2000)

tunnelling inherently involves higher uncertainty and hazard levels. In the absence of direct permeability measurements (e.g., laboratory or in-situ testing), geophysical methods can help assess the degree of fracturing in rock masses and the presence of electrically conductive fluids, thereby drafting a preliminary inflow assessment. Notably, the previous Vágar Tunnel project (2002) demonstrated controlled water ingress well below design thresholds (Rodrigues et al., 2002). Nevertheless, the potential for encountering highly permeable zones remains and must be anticipated.

Reactive silica phases (e.g., quartz, chert, volcanic glass) represent a potential hazard due to alkali–silica reactions (ASR), which may be triggered by water ingress and result in expansive gel formation, cracking, and long-term concrete degradation. Water can also activate swelling clays (e.g., montmorillonite, halloysite) along tunnel alignments, as documented in a recent Suðuroy Island project—though involving different lithostratigraphic units than the Suðuroy Tunnel. Tunnel. Core testing remains an effective method for assessing these risks, which remain overall likely to some extent but not the primary hazard in the area of interest.

Regarding potential seismic activity and faulting, the Faroese tectonic history over the past 60 million years has been shaped by two major rifting phases. The first phase led to the formation of the *Beininsvørð Formation* (*Munkegrunnar Ridge*), followed by the development of the *Malinstindur* and *Enni Formations* (*Fugloy Ridge*). Although rift-related fractures are widespread due to crustal extension, no active faults or significant displacements have been identified in the area, and seismic hazard is to be considered almost inexistent.

Total Geological History – Conclusions

While generally stable, basaltic lava flows contain weak layers (e.g., sediments, breccias) that may persist several metres along the Suðuroy Tunnel alignment and affect the excavation stability. Groundwater inflow is indeed to be accounted given the subsea nature of the project, especially in the deepest fjord sections; geophysical methods can assist in preliminary assessments where direct permeability measurements are lacking. Reactive silica and swelling clays can also present long-term durability risks, therefore requiring core testing. Despite past rifting, no active faults have been identified in the area, and seismic risk is minimal.

3

Engineering geology for particular site

Blindur er bókleysur maður

Blind is the bookless man

Following a general overview of the Faroe Islands' geology, a detailed desk study is needed to examine the lithostratigraphic sequences along the project area. The primary goal is to support a longitudinal section of the approximately 24-kilometre tunnel alignment, building on previous work by Jarðfeingi and NGI. The first part of this chapter expands on these efforts, focusing specifically on the planned cavern locations.

Due to the lack of instrumentation and prior in-situ stress measurements, the second part addresses this aspect through desk-based analysis. While absolute stress magnitudes remain difficult to determine, the orientation of principal stresses and the ratio between vertical and horizontal components can still be estimated using structural data (e.g., rose diagrams) and theoretical models from the literature.

3.1 Geological and geophysical surveys overview

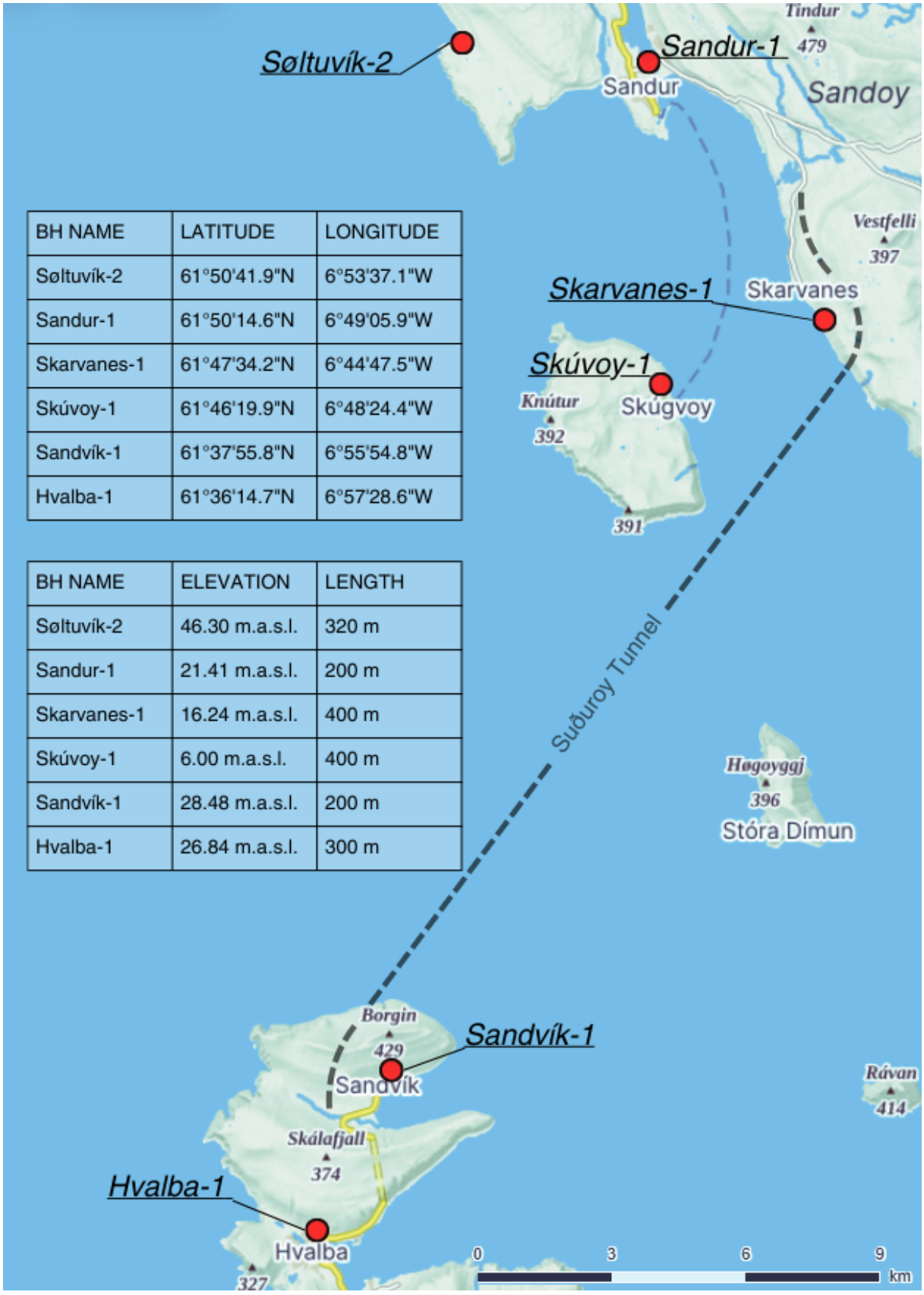
Six deep onshore boreholes drilled by Jarðfeingi (Fig. 3.1) provide the primary geological data for the excavation site, with cores reaching lengths up to 400 m (Petersen et al., 2022). Three boreholes on Sandoy Island, aligned NW–SE between Søltuvík and Skarvanes, support all three proposed tunnel alignments (see Fig. 1.3). One borehole was drilled in Skúvoy, and two on Suðuroy near Sandvík and Hvalba. An illustration of borehole *Skúvoy*-1, representative of those analysed in this study, is provided in Appendix A.1.

Lithological core logging indicates that basalt dominates the stratigraphy, occurring in three main lava core textures: (i) aphyric, (ii) fine-grained feldspar-phyric, and (iii) coarse-grained feldspar-phyric basalt. Substantial morphological and textural variation is identifiable in the flow top and base as volcanic breccia or conglomerate. Core stone and saprolitic bole facies—products of post-eruption weathering—are identified only in the *Hvalba*-1 borehole. The secondary lithology consists of sand–claystone layers ($\leq$10 cm to 2–3 m thick), with sandstone being more common.

Borehole stratigraphy is supported by rough fracture logs and high-resolution core imagery, and no laboratory samples were collected. Given the boreholes density and distribution, (Fig. 3.1), the 3-point method for determining layers bedding appears feasible between Sandoy and Skúvoy, while only 2D profiling seems possible near Suðuroy. This highlights the need for supplementary data in the latter area, such as outcrop orientations or information from other site investigations.

Additional columns were added to the composite logs to incorporate supplementary measurements: caliper, gamma ray, single-point resistance (*SPR*), temperature, fracture density, and structural data. In particular, the structural data will be used to estimate in-situ stress orientations, while *SPR* data will serve as the basis for geophysical analyses in the following chapter.

As a second key contribution, 19 high-resolution 2D seismic profiles, ideally oriented perpendicular to the basalt flow strike (Petersen, 2020), are presented alongside derived velocity models. These models provide detailed velocity data for the upper ~100 m below the seabed, facilitating the layers dipping, the discontinuities, and to some extent the physical-mechanical properties. Depth-migrated profiles further enhance subsurface imaging by using peg-leg multiples to provide information on stratigraphy, acoustic impedance contrasts, and structural geometry. Together, these data improve the accuracy of delineating the base and thickness of potential sedimentary basins. An example of the seismic data processing is provided in Appendix A.2, featuring Line O1 from the surveys (reported in Petersen, 2020).



BH NAME	LATITUDE	LONGITUDE
Søltuvík-2	61°50'41.9"N	6°53'37.1"W
Sandur-1	61°50'14.6"N	6°49'05.9"W
Skarvanes-1	61°47'34.2"N	6°44'47.5"W
Skúvoy-1	61°46'19.9"N	6°48'24.4"W
Sandvík-1	61°37'55.8"N	6°55'54.8"W
Hvalba-1	61°36'14.7"N	6°57'28.6"W

BH NAME	ELEVATION	LENGTH
Søltuvík-2	46.30 m.a.s.l.	320 m
Sandur-1	21.41 m.a.s.l.	200 m
Skarvanes-1	16.24 m.a.s.l.	400 m
Skúvoy-1	6.00 m.a.s.l.	400 m
Sandvík-1	28.48 m.a.s.l.	200 m
Hvalba-1	26.84 m.a.s.l.	300 m

Figure 3.1: Location and details of the six deep boreholes drilled by Jarðfeingi. Data retrieved from Petersen et al. (2022). Background map from https://mapy.com.

3.2 Main lithostratigraphic features

Following an overview of the available dataset from the Sandoy–Suðuroy area, the structural attitudes (strike and dip) of key stratigraphic units—horizons and sedimentary features—are estimated. This analysis forms the basis for a longitudinal stratigraphic section covering the Suðuroy Tunnel alignment.

3.2.1 Bathymetry

Publicly available bathymetric data for the area, including the 50 m grid dataset from Føroyakort (Umhvørvisstovan, 2024), offer a general overview but lack the resolution required for detailed profiling along the tunnel alignment. In this study, 10 m contour lines are used to approximate the seabed in the longitudinal section (Fig. 3.2). A higher-resolution overview of the archipelago bathymetry is provided in Appendix A.3.

Bathymetric data indicate that a maximum depth of approximately 50 m below sea level is reached in the Skúvoy Fjord (*Skúvoyarfjørður*), with localised shallows likely caused by sedimentation or subaqueous dunes, as analysed by Petersen (2023). In contrast, the Suðuroy Fjord (*Suðuroyarfjørður*) reaches depths of approximately 80–90 m. The sparse spacing of isobaths suggests low slope gradients, consistent with the sub-continental setting of the Faroe Islands, which sit on an oceanic plateau.

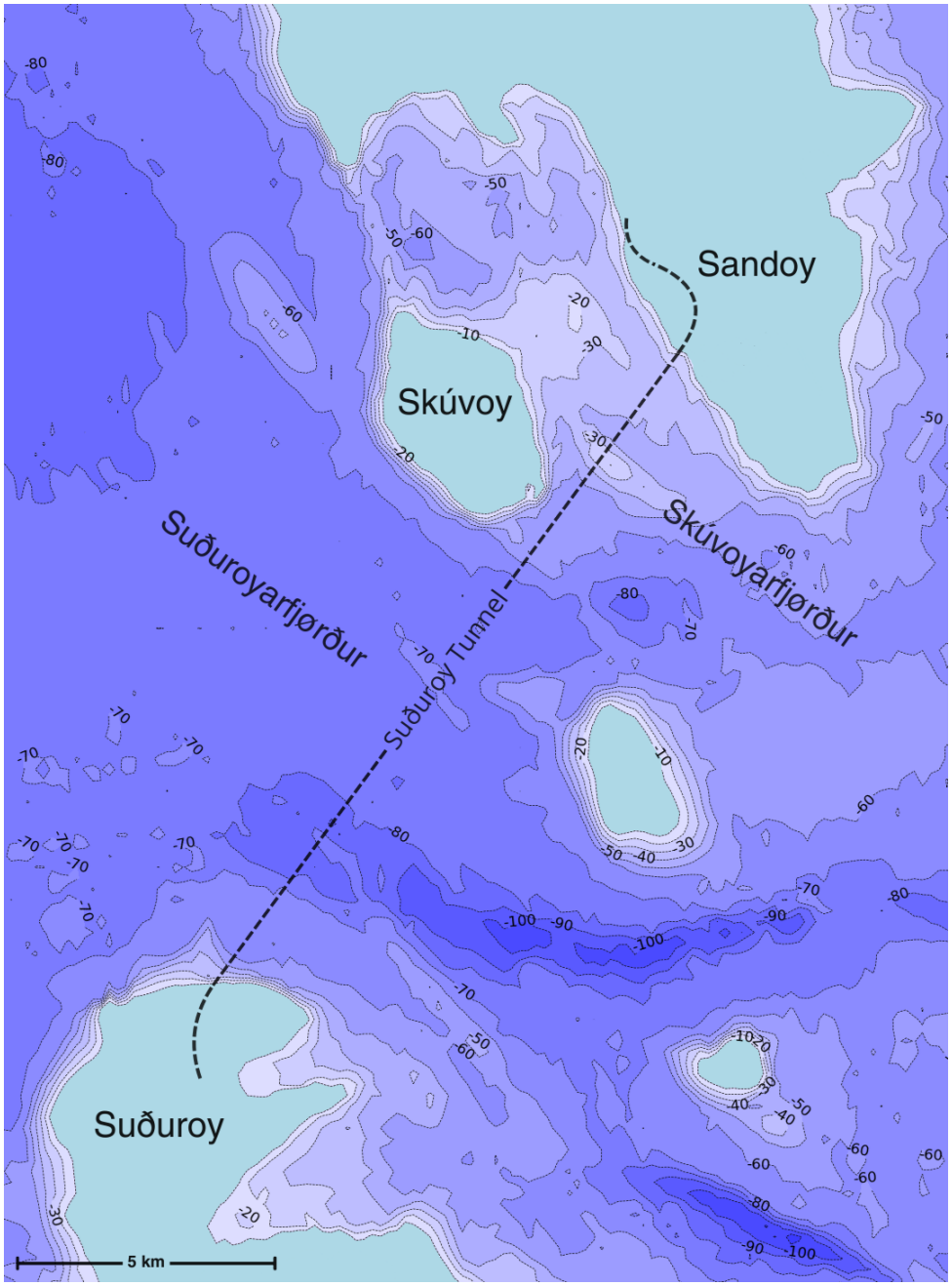


Figure 3.2: Bathymetric profile between Sandoy and Suðuroy in proximity of the Suðuroy Tunnel alignment.

3.2.2 A-Horizon

The former *A-Horizon*, now *Beinidsvørð–Malinstindur Unconformity* (BMU, Passey and Jolley, 2009), marks the basal boundary of the *Prestfjall Formation* and was first identified in coal mines near Hvalba in Suðuroy (Rasmussen and Noe-Nygaard, 1970). Despite the updated terminology, the original designation remains prevalent in literature and is thus retained here for clarity in labelling.

The *A-Horizon* is absent in the *Hvalba*-1 borehole, as drilling began below its expected stratigraphic level within the Lower Basalt Formation. The *Prestfjall Formation* dips NNE–NE, consistent with the underlying *Beininsvørð Formation*, which exhibits average dip angles of 1°–4° according to Waagstein (1988) and 6°–8° according to Walker et al. (2010) across the Faroe Islands. Examination of the *Sandvík*-1 borehole reveals a 2 m volcaniclastic sandstone at -145 m a.s.l., marking a sedimentary break, but without any overlying coal, thereby excluding correlation with the *A-Horizon*.

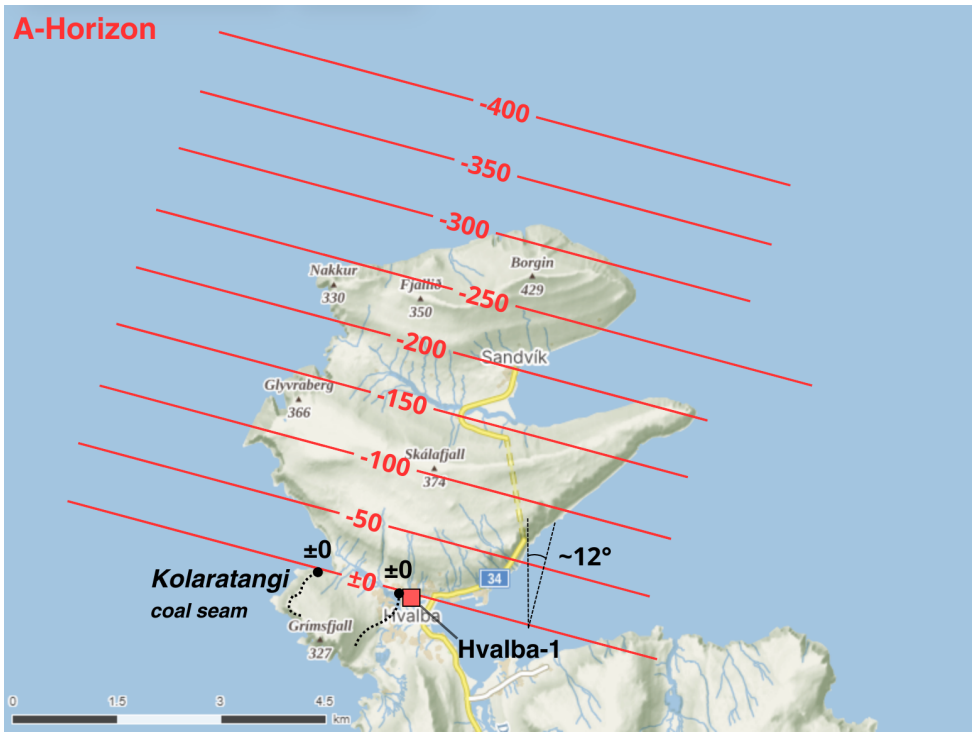


Figure 3.3: Identification of the A-Horizon, cropping out at the Kolaratangi coal seam west of Hvalba. Background map from https://mapy.com.

This supports a refined dip estimate of 2.9°–4.0° for the *Prestfjall Formation*, validating NGI's previously proposed value of 3.3° (Holter et al., 2021). In the absence of direct *A-Horizon* data

from boreholes, dip direction is estimated by connecting two coal seam outcrops at 0 m a.s.l.—at *Kolrabjørg* and near Hvalba—indicating a 12° dip direction (Fig. 3.3), consistent with Passey and Jolley (2009). Based on these estimations (Tab. 3.1), the Suðuroy Tunnel is unlikely to intersect the Lower Basalt Formation at planned cavern locations, where its upper boundary lies considerably deeper.

Table 3.1: A-Horizon bedding plane orientation and dip.

Stratigraphic unit	Estimated dip direction	Estimated dip angle
A-Horizon	12°	3.3°

3.2.3 B-Horizon

A marked textural contrast between pale- and brown-weathering basalts defines the first major discontinuity in the *Malinstindur* basalt series, known as the B-Horizon (Rasmussen and Noe-Nygaard, 1970). This transition, expected to intersect the tunnel alignment, may be progressive and therefore span several meters. Its exact location remains uncertain due to absence of stratigraphic data within a ~400 m undrilled section across the six boreholes (Petersen et al., 2022; Fig. 3.4).

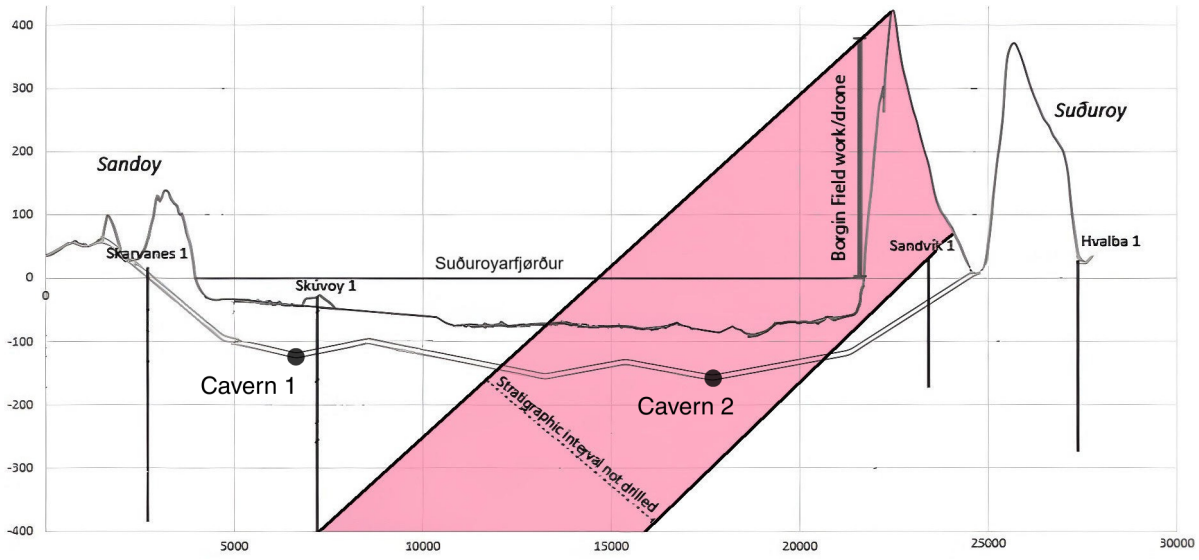


Figure 3.4: Undrilled stratigraphic interval between the Skúvoy-1 and Sandvík-1 boreholes along Suðuroy Fjord (Suðuroyarfjørður), where Cavern 2 is expected to be excavated. Adapted from Petersen et al. (2022).

One hypothesis associates the horizon with the aforementioned -145 m a.s.l. deep sandstone layer observed in the *Sandvík*-1 borehole, below which a clear lightening of basalt colouration appears in core images. However, poor resolution limits data reliability, and dip direction and angle cannot be directly measured. A conservative dip angle of 2.2° is adopted based on literature (Rasmussen and Noe-Nygaard, 1970; Waagstein, 1988), representing a minimal estimate, therefore maximising the layer-tunnel contact length (Tab. 7.2). Assuming correlation with the *Malinstindur Formation*, dip direction insights are planned to be gained from stereonets of outcrops in north Suðuroy collected during field campaigns (Fig. A.3).

A second hypothesis relies on marine seismic surveys identifying four principal discontinuities—the *A*-, *B*-, *C*-, and *D-Reflectors*—along the Sandoy–Suðuroy strait (Petersen, 2020). Peg-leg multiples, formed by acoustic impedance contrasts, appear prominently along the Line-L profile (Fig. 3.5), reflecting fine-grained interbedded sedimentary sequences. Velocity models from Line-O1 seismic data (Fig. 3.6) confirm these four discontinuities, evidenced by distinct velocity shifts. The *B-Reflector*, at depths of −100 to −700 m a.s.l., is the strongest candidate for matching the *B-Horizon*.

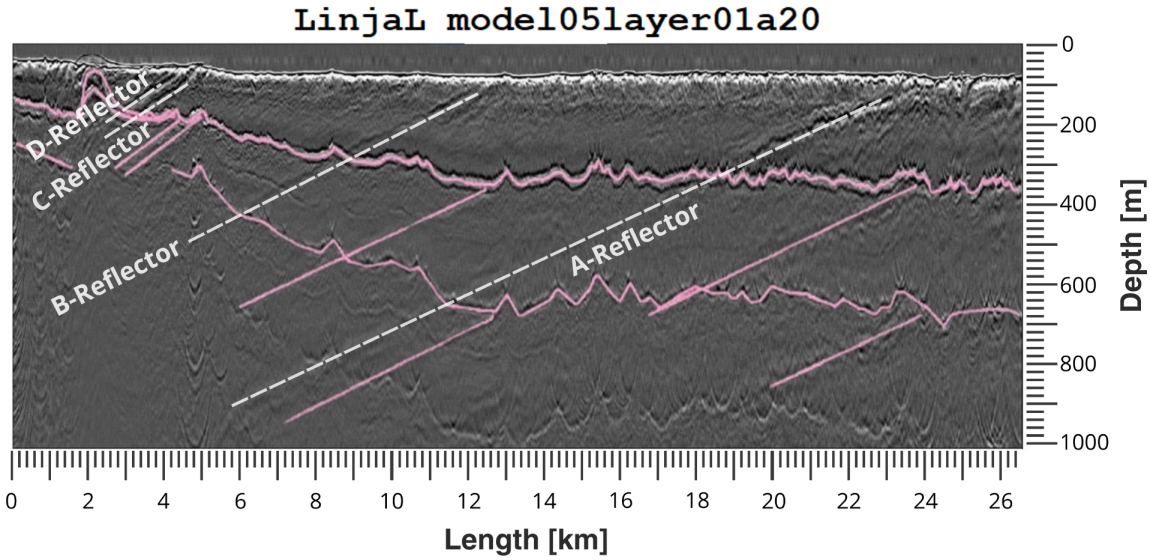


Figure 3.5: Depth migrated seismic profile (NE to SW from left to right) in Line-L from Jarðfeingi seismic surveys with the four interpreted reflections and the most pronounced peg leg multiples (pink lines). Modified from Petersen et al. (2022).

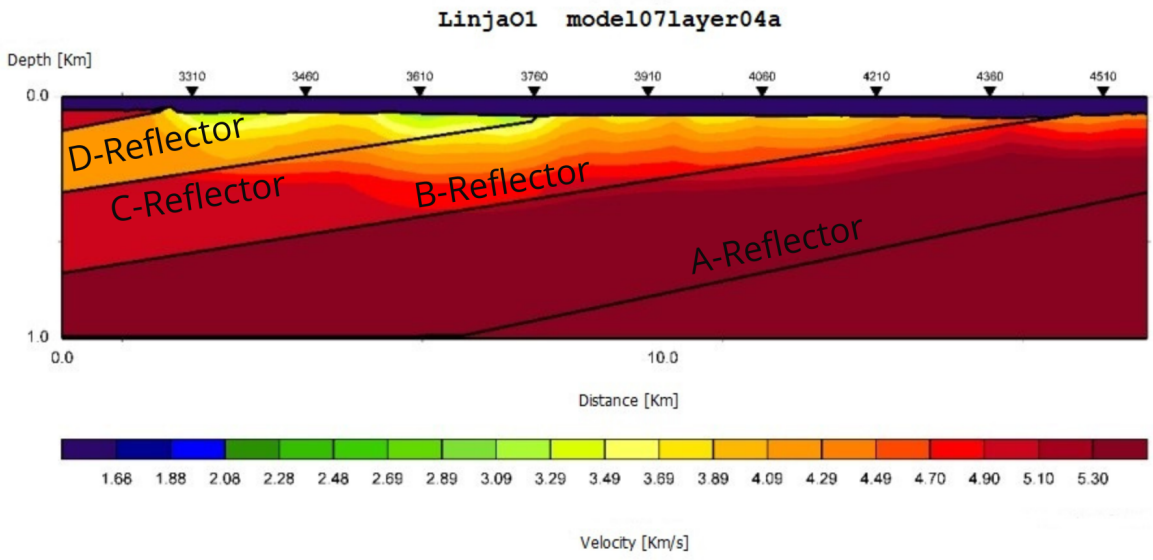


Figure 3.6: Four main reflectors identification within the Line-O1 velocity model. Modified from Petersen (2020)

While seismic surveys provide only 2D imagery, the coincident discontinuity in Lines-O1 and -L allows calculation of a plane dipping with an angle of 2.9° and direction of 11° (Tab. 7.2). The layer is expected to crop out along the seabed approximately 3.5 km north of Suðuroy's coast and deepen by about 450 m a.s.l. as it approaches Skúvoy Island (Fig. A.4). Its thickness remains unrecorded, as the stratigraphic unit lies below the maximum depth reached by the *Skúvoy*-1 core.

Table 3.2: B-Horizon bedding plane orientation and dip (hypothesis 1 and 2).

Stratigraphic unit	Estimated dip direction	Estimated dip angle
B-Horizon – hyp. 1	?	2.2° [1]
B-Horizon – hyp. 2	11°	2.9°

[1] Value adopted from literature (Rasmussen and Noe-Nygaard, 1970; Waagstein, 1988).

3.2.4 Sandstone below C-Reflector

A <1 m-thick sandstone layer between the *B*- and *C-Reflectors* (marine seismic discontinuities) is consistently observed in the *Skúvoy*-1, *Søltuvík*-2, and *Skarvanes*-1 boreholes (Fig. A.5). Application of the three-point method indicates a notable dip direction change relative to the underlying *B-Reflector* (Tab. 3.3).

Table 3.3: Sandstone below C-Reflector bedding plane orientation and dip.

Stratigraphic unit	Estimated dip direction	Estimated dip angle
Sandstone below *C-Reflector*	83°	1.8°

3.2.5 C-Reflector

The aforementioned *C-Reflector* is a sedimentary unit within the upper *Malinstindur Formation* but below the transition to the *Enni Formation*. Therefore, it should not be correlated with the *Sneis Formation* to avoid misinterpretation, although it may correspond to its lowermost part, also referred to as the *Malinstindur–Sneis Unconformity* (MSU, Passey and Jolley, 2009; Petersen et al., 2022). Initially recognised through seismic data (Fig. 3.5; Fig. 3.6), it was later confirmed in the *Skúvoy*-1, *Søltuvík*-2, and *Skarvanes*-1 cores with a thickness of 1.5–1.8 m. Its orientation, calculated using the 3-point rule (Fig. A.6), closely matches the underlying volcaniclastic sandstone unit, indicating stratigraphic continuity (Tab. 3.4).

Table 3.4: C-Reflector bedding plane orientation and dip.

Stratigraphic unit	Estimated dip direction	Estimated dip angle
C-Reflector	79°	1.9°

3.2.6 Sneis Formation

In all four boreholes on Sandoy and Skúvoy, interlava lithologies become increasingly frequent above this level, indicating a gradual geological transition. However, the Upper–Middle Basalt boundary remains poorly defined. The *Sneis Formation*, expected below Sandoy as a thin (<1 m) sandstone layer (Passey and Jolley, 2009), has an uncertain depth in the boreholes. The so-called *C-Horizon*, previously associated with the *Sneis*, has proven to be miscorrelated with the 10–15 m thick *Høvdhamarin Flow*, situated ~100 m a.s.l. near Sandur and ~120–130 m above the true MSU (Passey and Jolley, 2009).

The brecciated top flow (1.0–8.0 m) and overlying sandstone (0.25–0.40 m) in *Søltuvík*-2 and *Skúvoy*-1 are interpreted as the *Sneis Formation* and its underlying, moderately weathered flow top, marking the transition from *Malinstindur* to *Enni*. A three-point plane, including *Skarvanes*-1, supports this interpretation, aligning with the 0.70 m sandstone at -127.5 m in *Sandur*-1 (Fig. A.7). Although the underlying breccia is absent in *Sandur*-1 and *Skarvanes*-

1, it likely reflects prolonged subaerial exposure of the *Malinstindur* upper boundary or a more explosive eruption phase rather than intrusive emplacement, indicating a hiatus in lava deposition before *Enni* volcanism. The estimated dip angle is moderately lower than that of the underlying lithostratigraphic units (Tab. 3.5).

Alternative correlations of the *Sneis* proved inconsistent. The first, based on a sandstone layer in *Søltuvík*-2 (-36.5 m a.s.l.), *Sandur*-1 (-127.5 m a.s.l.), and *Skarvanes*-1 (-170.5 m a.s.l.), conflicts with three-point plane analysis, which would place this layer cropping out on Skúvoy—unsupported by field evidence. A second hypothesis links the shallower (-1.5 m a.s.l.) sandstone in *Søltuvík*-2 with *Skúvoy*-1, closer to the known outcrop, but this implies the formation crops out near Sandur, contradicting geological maps that show only *Enni Formation* basalts (see Fig. 2.6, Chapter 2). Therefore, the deeper volcaniclastic sandstone at -36.5 m a.s.l. in *Søltuvík*-2 is considered the most likely *Sneis* marker.

Table 3.5: Sneis Formation bedding plane orientation and dip.

Stratigraphic unit	Estimated dip direction	Estimated dip angle
Sneis Formation	75°	0.8°

Overall, the transition between the *Malinstindur* and *Enni* formations appears more complex than a single horizon. Instead, it likely includes a stratigraphic interval starting from the MSU (*C-Reflector*) to the upper boundary of the *Sneis*, also referred to as the *Sneis–Enni Unconformity* (SEU, Passey and Jolley, 2009).

3.2.7 Sandur Beds basal boundary

A ~30 m-thick group of volcaniclastic sandstone sequences, referred to as the *Sandur Beds* (Petersen et al., 2022), is strongly correlated in thickness and spacing between the *Sandur*-1 and *Skarvanes*-1 boreholes, and has been seismically confirmed within the Sandoy–Skúvoy basin (Petersen, 2020). The base of these beds is logged at -2.5 m a.s.l. in *Skúvoy*-1 as well (Petersen et al., 2022; Fig. A.8). Three-point method analysis suggests the base reaches 0 m a.s.l. at the western Sandur cliffs, although no outcrop has been observed there, implying the formation is likely confined to the Sandoy–Skúvoy Basin. The beds show a very low dip and NEE strike and therefore good continuity with the *Sneis Formation* (Tab. 3.6).

Table 3.6: Sandur Beds basal boundary bedding plane orientation and dip.

Stratigraphic unit	Estimated dip direction	Estimated dip angle
Sandur Beds basal boundary	55°	1.1°

3.2.8 Queen Sandstone layer

A prominent ~2 m-thick volcaniclastic sandstone unit, informally named the *Queen Sandstone* in honor of Queen Margrethe II of Denmark, crops out west of Sandur. The same unit is identified in the *Sandur*-1 and *Skarvanes*-1 boreholes at -18 and -46 m a.s.l., respectively (Fig. A.9), enabling estimation of bedding dip and direction (Tab. 3.7). This unit is expected to appear shortly after the northern tunnel portal in Sandoy during excavation. Core logs indicate the presence of one or two additional sandstone layers between the base of the *Sandur Beds* and the *Queen Sandstone*, as well as two intra-bed brecciated flow tops (the latter observed in *Skarvanes*-1). However, the dip and orientation of these layers cannot be evaluated due to the lack of a third core or structural data. Nonetheless, given the minimal differences in dip (<0.5°) and orientation (<10°) between the *Queen Sandstone* and the basal boundary, similar structural parameters are inferred for the adjacent units. This assumption is also applied—albeit less robustly—to the 6.3 m weathered flow top above *Sandur*-1 for the purposes of longitudinal-sectional modelling.

Table 3.7: Queen Sandstone bedding plane orientation and dip.

Stratigraphic unit	Estimated dip direction	Estimated dip angle
Queen Sandstone	63°	1.4°

3.2.9 Intra-flows lithostratigraphic overview

In conclusion, this study provides an overview of correlations among sedimentary and brecciated units in the *Søltuvík*-2, *Sandur*-1, *Skarvanes*-1, and *Skúvoy*-1 boreholes, shown in Fig. 3.7. The focus is on the *Enni* and upper *Malinstindur* units, where most discontinuities between lava flows occur. A key observation is the slight change in apparent dip between the *C-Reflector* and *Sneis Formation*, marking a shift in dip and/or strike of the layers and thus the transition from the Middle to Upper Basalt Formation. Despite this, stratigraphic continuity is maintained across the Sandoy–Suðuroy area, with all lithostratigraphic units showing gentle bedding consistent with regional trends.

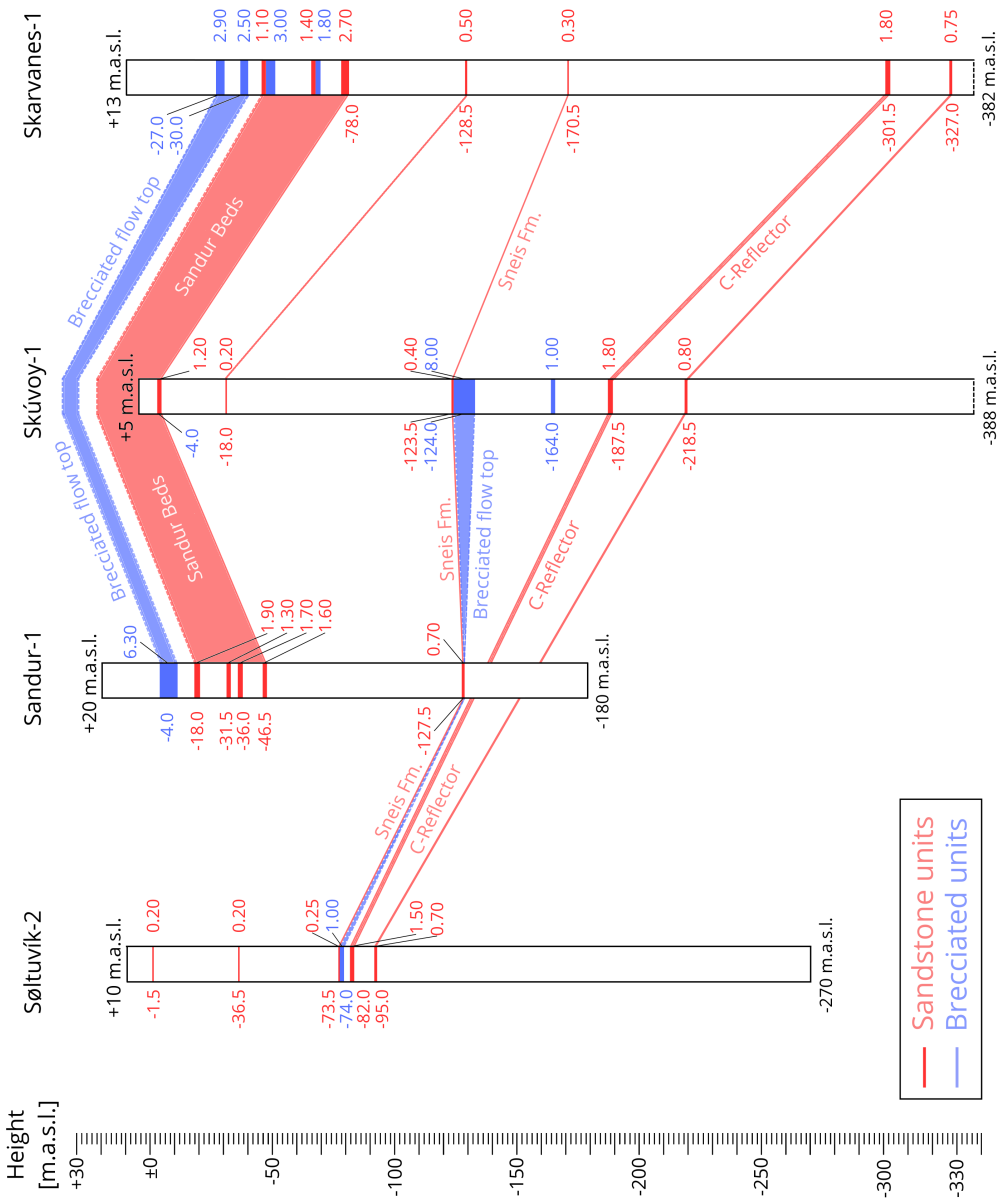


Figure 3.7: Stratigraphic correlations of the upper Malinstindur and Enni sedimentary and brecciated units across four deep boreholes in Sandoy and Skúvoy (Søltuvík-2, Sandur-1, Skarvanes-1, and Skúvoy-1). For each sequence, the depth is shown on the left and the thickness on the right.

Main lithostratigraphic features – Conclusions

The seabed along the Sandoy–Suðuroy alignment ranges in depth from approximately 50 m to 90 m, with gentle gradients consistent with the Faroese sub-continental plateau setting. Integration of lithostratigraphic core logs, seismic velocity models, and migrated seismic profiles enabled the identification of seven main stratigraphic units within the *Malinstindur* and *Enni* basalt formations. These units form the structural basis for constructing a longitudinal section of the tunnel alignment, as presented in the following chapters. A notable change in strike direction—from NNE in the lower *Malinstindur* to NEE–E in the upper *Malinstindur* and *Enni* units—is observed, accompanied by a slight dip variation beginning in the *Enni* formation.

This analysis is subject to several limitations. Bathymetric data are of low spatial resolution. Borehole coverage is either incomplete or of low resolution in some areas, and key stratigraphic horizons such as the *A-* and *B-Horizons* are not directly intersected, necessitating indirect inference from seismic data and literature. Seismic interpretation is based only on 2D profiles, limiting both spatial resolution and the ability to validate the continuity of identified reflectors. Furthermore, the use of average values from literature in the absence of direct measurements introduces inherent uncertainty into local depth predictions.

3.3 In-situ stresses

After characterising the key lithostratigraphic units, the second part of the chapter focuses on addressing in-situ stress orientations and, possibly, their relative magnitudes in the project area. Due to the absence of direct stress measurements (as outlined in Section 2.2, Chapter 1), stress characterisation is based on literature data, morphological and topological analyses, and established theoretical models.

3.3.1 Rock stress origin and main regional trends in the Faroe Islands

Local rock stress generally arises from four primary sources: (i) gravity, (ii) tectonic forces, (iii) residual stress (retained post-deformation), and (iv) topographic stress, reflecting surface morphology. In valleys and narrow fjords, stress often aligns with valley sides and concentrates at the base. Thus, stress orientation estimation requires the integration of tectonic and

topographic indicators, as desk-based methods alone may be insufficient.

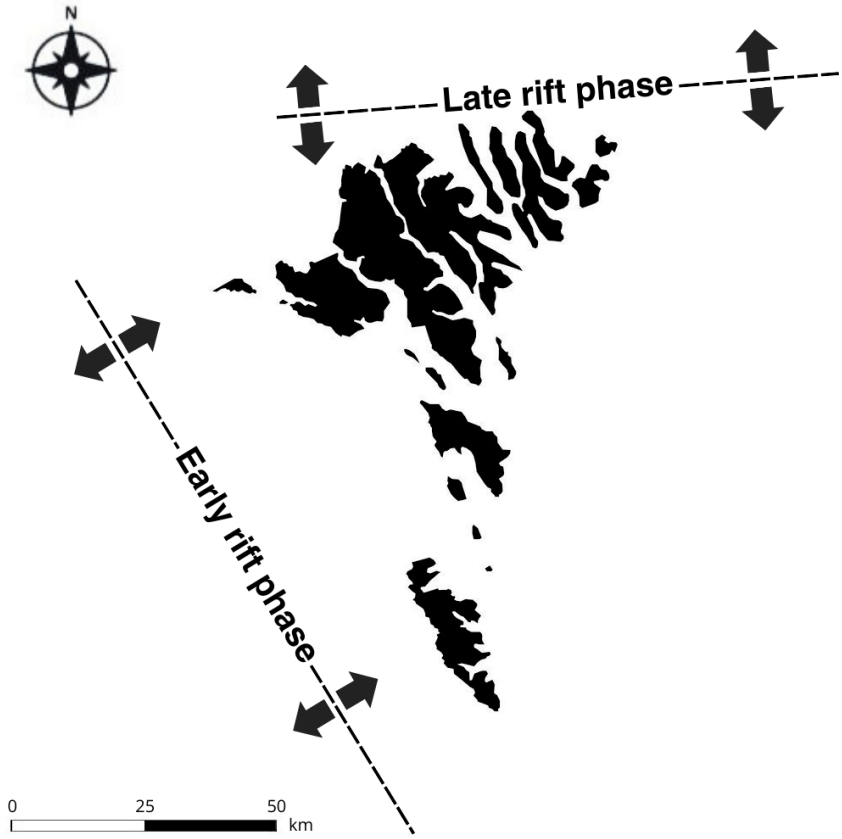


Figure 3.8: The two major regional rift events and their localisation w.r.t. the Faroe Islands archipelago.

Structural data suggest a five-phase anticlockwise shift in the Faroese regional extension vector (NE–SW to NW–SE), with the first two phases impacting the majority of the basalt sequence. The first stage, originated west of the Faroese Platform, involved NW–SE to NNW–SSE rifting and formed the *Beinisvørð Formation*. The second phase, to the north, was dominated by E–W to ENE–WSW extension, linked to the *Malinstindur* and *Enni Formations* (Fig. 3.8).

Su and Stephansson (1999) demonstrated through numerical analyses that the principal stress aligns with the orientation of the faults locally. However, the trend strongly diverges with distance, from which a good practice is to combine numerical observations with topographic indicators.

Fractures across the archipelago show a shift in minimum stress direction between the two tectonic events. Rasmussen and Noe-Nygaard (1970) documented a NW–SE fault predating the origin of the *Malinstindur*, suggesting SW–NE oriented minimum stress during early basalt emplacement. Ziska (2012) found contrasting fracture sets between the *Beinisvørð* and younger formations, though NW–SE fractures in *Malinstindur* basalts on Vágoy and Suðuroy hint at reactivation of older faults. This implies that *Beinisvørð*-aligned stresses may extend into shallower strata southern in the Sandoy–Suðuroy strait.

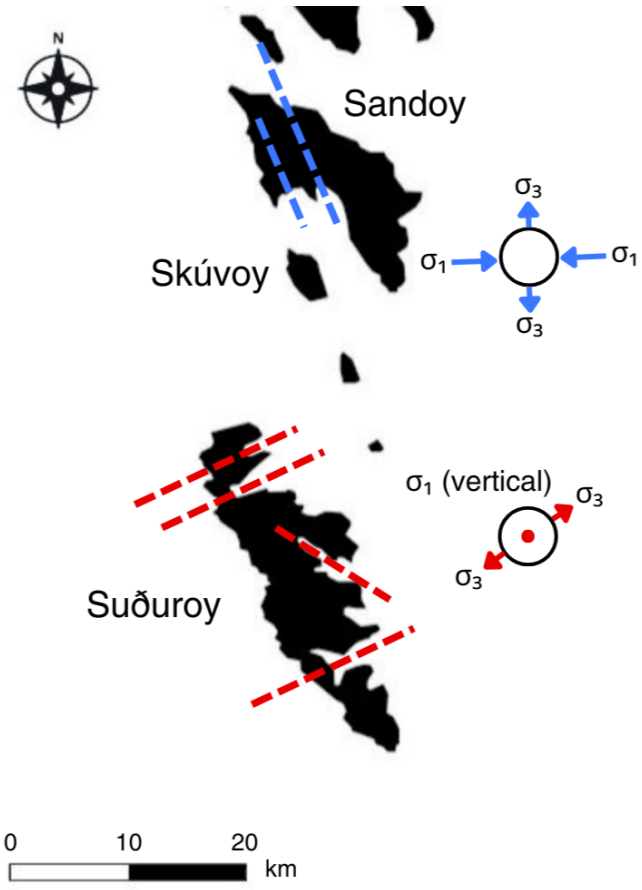


Figure 3.9: Orientation of fjords along the islands of Sandoy and Suðuroy, along with the estimated orientations of regional major and minor principal stresses according to Walker et al. (2010).

The younger *Malinstindur* and *Enni* Formations show dominant E–W fractures, indicating a N–S minimum stress during their formation. This likely reflects stress trend conditions while approaching Sandoy.

Topographic analysis supports this interpretation, as the orientations of fjords on Suðuroy differ from those on the northern islands (Fig. 3.9), reflecting distinct underlying fault and fracture trends (Rodrigues et al., 2002). Dykes, which typically intrude perpendicular to the minimum stress direction, would provide another useful indicator for confirming these assumptions.

3.3.2 Boreholes' structural data

To assess the validity of the estimated regional stress trend derived from tectonic and topographic considerations at the Sandoy–Suðuroy scale, structural data from Jarðfeingi boreholes (Petersen et al., 2022) are used. These data are presented as rose diagrams, each summarising a 50 m core interval with 10° strike bins per petal.

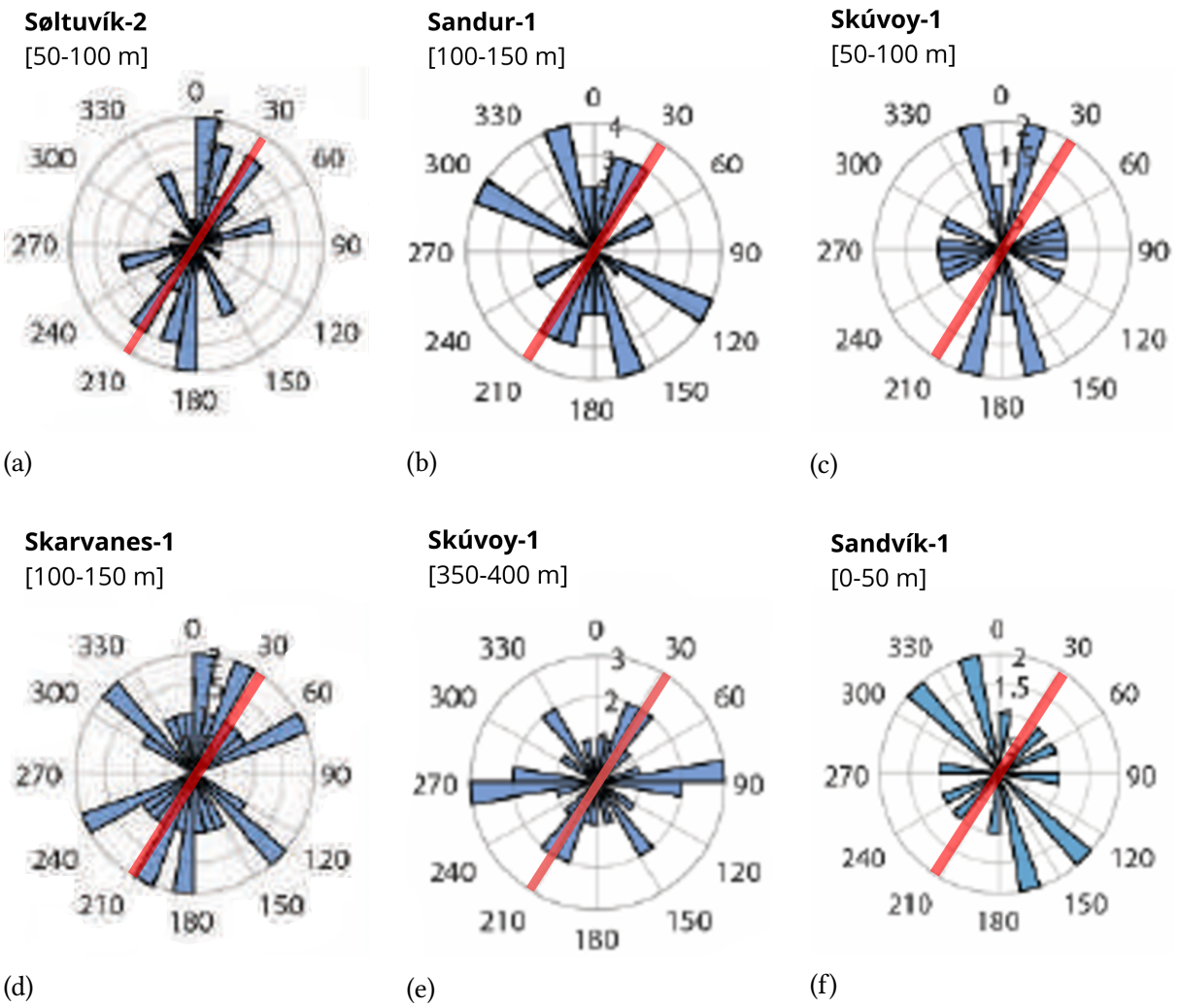


Figure 3.10: Rose diagrams along the stratigraphic intervals of the Enni (a–d) and Malinstindur (e,f) basalts, in or near the units where the two caverns are expected to be excavated. Tunnel alignment orientation is indicated with the red segment. The diagrams are adapted from Petersen et al. (2022).

The analysis focuses on stratigraphic sections corresponding to planned excavation sites: the *Sandur Beds–Sneis Formation* interval for Cavern 1, and the undrilled closeness of the *B-Horizon* (Hypothesis 2) for Cavern 2 (Fig. 3.4). As such, fracture orientation at Cavern 1 appears quite well supported by data, whereas for Cavern 2 it can only be inferred.

Fig. 3.10 collects selected rose diagrams, with the tunnel alignment orientation shown in red. The first four diagrams (Fig. 3.10a–d) are linked to the *Enni Formation* (Cavern 1), while the last two (Fig. 3.10e–f) are associated with the *Malinstindur* basalts adjacent to the undrilled section (Cavern 2). Substantial heterogeneity in fracture orientations across the *Enni Formation* indicates variability among individual lava flows, despite their formation during the same tectonic episode. The *Enni Formation* exhibits substantial heterogeneity in fracture orientations, indicating variability among individual lava flows, despite their formation during the same

tectonic episode. However, quite consistent trends in fracture density within the ranges of 0°–30° and 180°–210° suggest a dominant NNE–SSW direction for σ_1. This differs from the regional E–W trend, possibly due to stress reorientation at this site, located approximately 70 km from the rifting source (Fig. 3.8). In summary, despite a slight NNE–SSW fractures local trend, within the *Enni Formation* flows local estimation of σ_1 and σ_3 is quite complicated by high structural heterogeneity. For the *Malinstindur* basalts, the limited number of rose diagram indicate a potential shift in σ_1 from E–W to NNW–SSE with depth (Fig. 3.10e–f), although the data set is considered insufficient for conclusive interpretations of the stress orientation.

3.3.3 Caverns favourable orientation

To evaluate whether the estimated stress conditions support aligning the cavern orientation with the tunnel axis, the practical guidelines by Selmer-Olsen and Broch (1978) is referenced. The guidelines emphasise the role of major discontinuities in optimising underground opening orientation to minimise instability and overbreak. For shallow to intermediate depths, openings should align with the bisector of the largest angle between dominant joint sets, including bedding or foliation. At greater depths, alignment should deviate 15°–30° from the horizontal projection of the major principal stress for optimal stability.

Rose diagrams and inferred stress orientations (Fig. 3.10) indicate generally unfavourable conditions in the *Enni Formation*, with improved—though uncertain—conditions in the *Malinstindur* basalts. According to this, higher consideration should be given to stability in Cavern 1 and tunnel segments within the Upper Basalt flows. Note how a circular cavern base, appropriate for a roundabout, would offer neutral response to stress anisotropy. However, roundabout branch excavations, lacking radial symmetry, may still be susceptible to stress-induced instability.

3.3.4 Horizontal and in-situ stresses magnitude

After assessing the local orientation of principal stresses, it is essential to establish an estimation of their relative magnitudes. A common approach is to calculate the vertical stress as its purely gravitational component and then determine the horizontal stress via the horizontal-to-vertical stress ratio k (Eq. 3.1).

$$k = \frac{\sigma_h}{\sigma_v} \tag{3.1}$$

The early model from Terzaghi and Richart (1952) links k to Poisson's ratio (Eq. 3.2), but this

assumption is not always proven to be accurate, especially at shallow depths where k tends to be higher (Brown and Hoek, 1978; Herget, 1988).

$$k = \frac{\nu}{1 - \nu} \tag{3.2}$$

To improve the estimation in such conditions, Sheorey (1994) proposed an elasto-static model that considers Earth's layered structure and thermal stresses. It provides a simplified equation to estimate a reasonable basis of the k value as a function of depth z and average elastic horizontal modulus E_h (Eq. 3.3). The model divides the Earth into 12 spherical layers (6 within the crust, 6 within the mantle), assigning each a specific E_h and unit weight. The uppermost crustal layer, has already a thickness of 5 km, enough to fully include the caverns excavation. From this perspective, the model appears to be significantly oversized for the specific application.

$$k = 0.25 + 7 \cdot E_h \left(0.001 + \frac{1}{z}\right) \tag{3.3}$$

Despite capturing large-scale trends, Sheorey (1994) acknowledges that the model fails to explain anomalies such as vertical stress exceeding the overburden, unusually high horizontal stresses, or unequal horizontal stresses—likely due to local geological features. Field measurements are therefore recommended, but they are unavailable for this project. Open-source tools like the World Stress Map (WSM; available at https://www.world-stress-map.org) provide localised stress data from tens of thousands of geotechnical projects worldwide and represent a valuable resource for integrating in-situ data with theoretical models. However, all these open sources lack coverage for the Faroe Islands.

Moreover, characterising the horizontal elastic modulus E_h in Sheorey's model is essential, as basalts can exhibit a wide range of values. For the top layer, Sheorey (1994) suggests $E_h \approx 50$ GPa, which may not represent the in-situ mechanical properties. Considering available estimates of in-situ moduli (discussed in detail in the following chapters) and the potential anisotropy between vertical and horizontal elasticity, multiple E_h values in the 10–100 GPa range are tested at fixed depths for Caverns 1 and 2 (Fig. 3.11). By instead considering the assumption of near-isotropic material behaviour within this range, a value of 35 GPa is appropriate for in-situ conditions, as it aligns with the vertical deformation modulus of basalt flows.

From Fig. 3.11 a wide range of k values, from ~1 to over 6, is obtained across the full E_h range while considering the two caverns depth. The related k ratios to the elastic modulus of 35 GPa are pointed and reported in the plot.

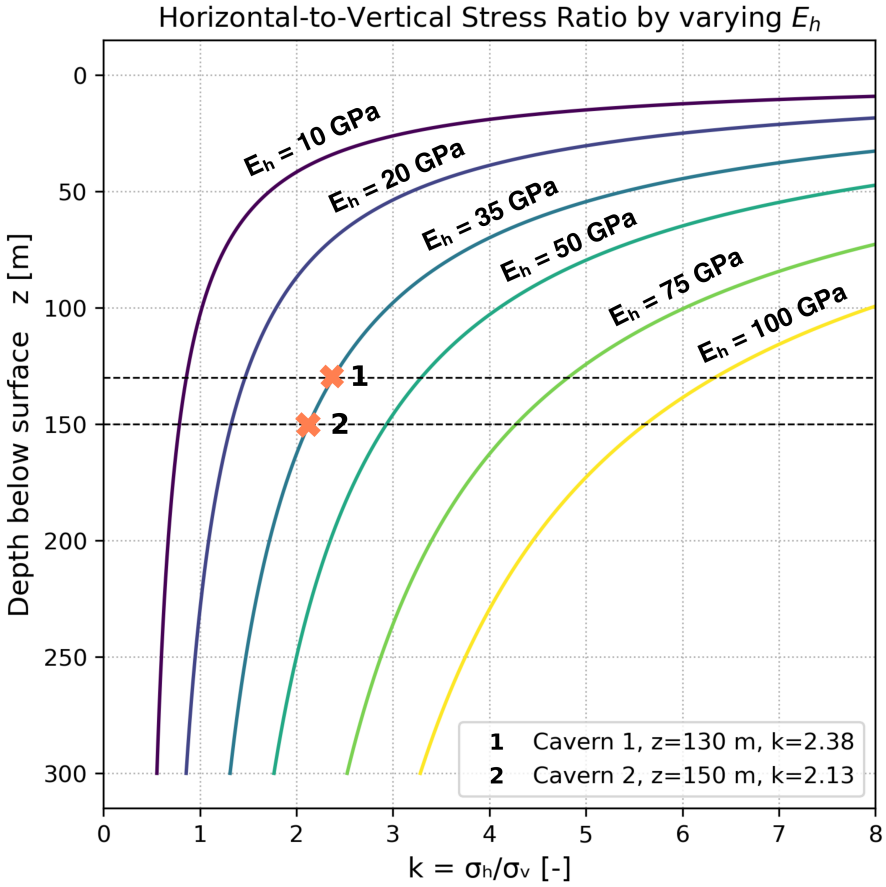


Figure 3.11: Development of the horizontal-to-vertical stress ratio w.r.t. variations in excavation depth and average deformation elastic modulus. The two cavern depths are indicated by the horizontal dotted lines, and the corresponding k-values are shown for a deformation modulus of 35 GPa, a suitable value for the elastic modulus under isotropic material assumption.

3.3.5 Theoretical models outcomes

The horizontal stress and k-ratio inputs are derived from both the Terzaghi and Richart (1952) formulation and the model by Sheorey (1994). The former depends only on Poisson's ratio, reliably estimated from seismic logs across basalt units. Sheorey's model assumes a constant volumetric weight of $\gamma = 27\,\mathrm{kN/m^3}$ to represent upper crustal conditions, a value considered reasonable for this application as well.

Despite the use of established equations, calculated k values vary from 0.3 to 2.3 (Tab. 3.8), highlighting the uncertainty inherent in in-situ stress prediction, especially at shallow depths. The absence of direct measurements and wide theoretical variability therefore suggests a sensitivity analysis on k as the best approach.

Table 3.8: Estimated k-values using the models of (a) Terzaghi and Richart (1952)—with both the 10th and 50th percentiles of Poisson's ratios—and (b) Sheorey (1994), for the two caverns, based on their specific depths and the mechanical properties of the surrounding geology.

Cavern #	ν_{05} **[-]**	ν_{50} **[-]**	k_{05} **(Terzaghi & Richart) [-]**	k_{50} **(Terzaghi & Richart) [-]**
Cavern 1	0.228	0.284	0.3	0.4
Cavern 2	0.234	0.277	0.3	0.4

(a)

Cavern #	z **[m]**	E_h **[GPa]**	k **(Sheorey) [-]**
Cavern 1	130	35	2.3
Cavern 2	150	35	2.1

(b)

Four k values are selected in agreement with the company supervisor: 0.5, 1.0, 1.5, and 2.5. Lower values (e.g., 0.5–1.0) are more consistent with vertical σ_1 in *Malinstindur* basalts, while $>$1.0 values (e.g., 1.5–2.5) suit the horizontal σ_1 orientations expected in *Enni* basalts (refer to Fig. 3.9).

In-situ stresses – Conclusions

Regional rifting in the study area caused a progressive anticlockwise rotation of in-situ principal stress directions—from NE–SW in *Beinidsvørð* to NW–SE in the *Malinstindur* and *Enni Formations*. Structural data from boreholes reveal high fracture orientation heterogeneity within the *Enni Formation*, diverging from regional trends and complicating local stress assessments. When compared to the tunnel alignment, inferred stress orientations indicate generally unfavourable conditions for Cavern 1 stability, with slightly more favourable yet still uncertain conditions for Cavern 2.

Estimates of the horizontal-to-vertical stress ratio (k) from theoretical models vary widely (0.3–2.3), and the lack of direct stress measurements in the area further reduces confidence in stress predictions. Excavation design should therefore account for anisotropic stress fields and local structural variability, with circular cavern bases recommended to improve stability under uncertain or rotating stresses orientation. Sensitivity analysis is considered the most reliable method for defining in-situ stress input in numerical simulations, with a k range of 0.5–2.5 identified as appropriate.

4

Geophysical properties for particular site

Eingin toyggir seg longri, enn armarnir røkka

None reaches further than his arms reach

To assess geotechnical parameters that are not always obtainable through laboratory tests, site investigations, or borehole data, related disciplines with classical geotechnics can provide valuable insights. The Faroe Islands, located in a region with significant oil and gas potential, were the focus of extensive research in the early 2000s aimed at identifying hydrocarbon reservoirs and characterising the basalt formations to be drilled. The outcomes of these studies are not always directly applicable to geotechnical engineering, but can offer valuable information when conventional geotechnical data is limited. This chapter reviews and reinterprets existing geophysical analyses conducted in the Faroe Islands, focusing both on the overall lithostratigraphic sequence and specifically on the Sandoy–Suðuroy area. These analyses are examined from a geotechnical perspective. The results include estimates of the elastic properties of key units identified in borehole core logs and an assessment of potential high-permeability zones along the tunnel alignment, which could pose risks of water intrusion during excavation in the two planned cavern sections, either from the sea or from subsurface freshwater aquifers.

4.1 Rock elastic properties

Sonic logging allows extrapolation of rock physical properties at depth and has been employed in the Faroes to characterise lithologies in boreholes *Lopra*-1/A, *Vestmanna*-1, and *Glyvursnes*-1 (see Fig. 2.6, Chapter 2). Data published by the Geological Survey of Denmark and Greenland (GEUS; Mavko et al., 2004; Waagstein and Andersen, 2004; Japsen and Waagstein, 2005) hold great relevance into the igneous succession down to the basal *Lopra Formation* (Passey and Jolley, 2009).

GEUS reports physical parameters such as density (ρ), P-waves velocity (V_p), S-waves velocity (V_s), and V_p/V_s ratios. From a seismic source, P-waves (compressional) cause material particles to move in the direction of wave propagation, while S-waves (shear) cause particle motion to occur perpendicular to that direction. From the aforementioned physical properties, elastic moduli—Young's modulus (E) and Poisson's ratio (ν)—can be derived, assuming elastic behaviour.

$$\nu = \frac{1}{2} \cdot \frac{(V_\mathrm{p}/V_\mathrm{s})^2 - 2}{(V_\mathrm{p}/V_\mathrm{s})^2 - 1} \tag{4.1a}$$

$$E = \rho \cdot V_\mathrm{p}^2 \cdot \frac{(1+\nu)\cdot(1-2\nu)}{1-\nu} \tag{4.1b}$$

Note that these correlations hold under ideal elasticity, therefore E and ν may be overestimated. To address this, a design-based approach assumes Gaussian distributions and incorporates both mean and 5$^{\text{th}}$ percentile values for modelling. Uncertainty propagation is estimated using the quadrature method (Eq. 4.2), with standard deviation increasing with the number of input parameters.

$$\sigma_f = \sqrt{\left(\frac{\partial f}{\partial x_1}\sigma_{x_1}\right)^2 + \left(\frac{\partial f}{\partial x_2}\sigma_{x_2}\right)^2 + \cdots + \left(\frac{\partial f}{\partial x_n}\sigma_{x_n}\right)^2} \tag{4.2}$$

As widely discussed in Section 2.2, Chapter 2, the stratigraphy from three deep boreholes reveals alternating basalt flows and interlava layers, leading to high heterogeneity in physical properties as well. GEUS addressed this by categorising the sequences into six macro-units: (i) lava core, (ii) lava crust, (iii) top lava breccia, (iv) sediment, (v) basal lava breccia, and (vi) basal lava zone. GEUS also reports the mean and standard deviation of the aforementioned physical parameters for each of these macro-units.

Glyvursnes-1 (Fig. 4.1) intersects the Upper (*Enni*) and upper Middle (*Malinstindur*) basalts, while *Vestmanna*-1 penetrates the deeper sections of the *Malinstindur Formation.* Data for Cavern 1, located within the *Enni* basalts, are derived from *Glyvursnes*-1. For Cavern 2, which is likely situated in the upper to middle *Malinstindur* basalts (see Chapter 3, Section 3.2), *Glyvursnes*-1 is also appropriate, as it provides coverage of the upper ~350 m of the Middle Basalt Formation.

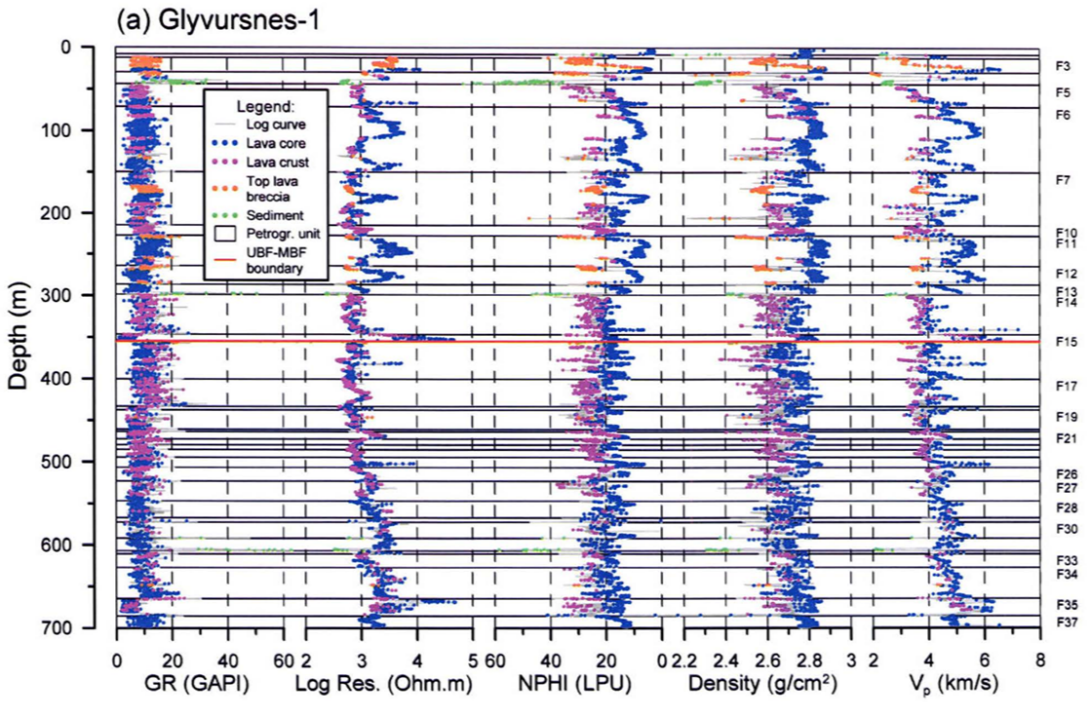


Figure 4.1: Distribution of physical properties with lithology and depth in Glyvursnes-1 deep borehole. Reproduced from Waagstein and Andersen (2004).

Using average properties across full formations ensures a robust approach despite spatial uncertainties. Therefore, although geographically distant, *Glyvursnes*-1 remains a reasonable dataset for estimating E and ν. Empirical correlations based on field rock mass quality assessment methodologies for E will be additionally used for comparison in the next chapter.

Among the six macro-groups identified by GEUS, only four were confirmed through core log stratigraphy from the Sandoy, Suðuroy, and Skuvoy boreholes (Petersen et al., 2022). The number of material groups and corresponding input properties for the to-be-developed numerical model is reduced to three:

(i) **Lava Core**: includes both the lava core and crust, as their physical and mechanical

properties are similar and distinguishing the alternation between the two units along the boreholes is difficult. Based on the continuum assumption and the generally stiff interflow jointing (Petersen et al., 2022), the model adopts lava core properties—the predominant unit in thickness—to estimate Young's modulus and Poisson's ratio.

(ii) **Sediment**: groups volcaniclastic sandstone and claystone interbeds (e.g., the *Sandur Beds*), which are typically thin but laterally extensive (Petersen et al., 2022).

(iii) **Lava Breccia**: combines flow basal and top brecciated lava units, where the latter displays lower density and velocity, likely due to higher exposure and weathering. Thus, the model material group conservatively adopts mechanical properties from the weaker, more common flow top breccias. In reality, this material group comprises a wide and complex range of facies and morphologies, most of which are classified as breccia or conglomerate (Fig. 4.2a), although in some cases flow tops may just preserve the lava flow cores morphology but with a way larger degree of weathering (Fig. 4.2b).



(a) (b)

Figure 4.2: Flow top facies and morphology can vary significantly between flows, being classified either as (a) volcaniclastic conglomerate or (b) as retaining the morphological characteristics of the underlying flow core. In the latter case, a higher degree of weathering results in mechanical weakening and discolouration. Photo (a) taken at the National Museum of the Faroe Islands.

Correlation results for the units in the *Enni* and *Malinstindur Formations* are summarised in Tab. 4.1. The variability of elastic parameters is conservatively estimated by evaluating their 5^{th}–50^{th} percentile range, derived from the cumulative distribution function (CDF) under the assumption of a normal distribution. These values are calculated for all three material types within both the Upper and Middle Basalt formations (Tab. 4.2).

Table 4.1: Calculated mean (μ) and standard deviation (σ) of the elastic properties for the (a) Upper and (b) Middle basalt formation material groups. From left to right, the illustrated physical properties are material density (ρ), P-wave velocity (V_p), and the ratio of P-wave to S-wave velocities (V_p/V_s). The corresponding Young's modulus (E) and Poisson's ratio (ν) are shown in the last two columns. Physical property data are reported from Waagstein and Andersen (2004).

Upper Basalt Fm.	ρ [kg/m^3]		V_p [km/s]		V_p/V_s [-]		E [GPa]		ν [–]	
	μ	σ	μ	σ	μ	σ	μ	σ	μ	σ
Lava Core	2790	80	4.17	0.75	1.82	0.10	37.53	16.32	0.284	0.034
Lava Breccia	2580	90	3.99	0.70	1.89	0.14	30.03	10.70	0.306	0.040
Sediment	2330	70	3.26	0.44	1.78	0.21	19.84	3.52	0.269	0.079

(a)

Middle Basalt Fm.	ρ [kg/m^3]		V_p [km/s]		V_p/V_s [-]		E [GPa]		ν [–]	
	μ	σ	μ	σ	μ	σ	μ	σ	μ	σ
Lava Core	2730	70	4.08	0.59	1.80	0.07	35.84	12.09	0.277	0.025
Lava Breccia	2550	70	3.91	0.56	1.85	0.11	29.47	8.56	0.294	0.035
Sediment	2390	50	3.09	0.33	1.78	0.15	18.29	4.00	0.269	0.057

(b)

Table 4.2: Calculated 50$^{\text{th}}$ (mean) and 5$^{\text{th}}$ percentiles of the elastic properties—Young's modulus (E) and Poisson's ratio (ν)—for (a) Upper and (b) Middle Basalt Formation material groups.

Upper Basalt Fm.	E_{50} [GPa]	E_5 [GPa]	ν_{50} [–]	ν_5 [–]
Lava Core	37.53	11.41	0.284	0.228
Lava Breccia	30.03	12.43	0.306	0.240
Sediment	19.84	14.05	0.269	0.139

(a)

Middle Basalt Fm.	E_{50} [GPa]	E_5 [GPa]	ν_{50} [–]	ν_5 [–]
Lava Core	35.84	16.50	0.284	0.228
Lava Breccia	29.47	15.39	0.306	0.240
Sediment	18.29	11.71	0.269	0.139

(b)

Rock elastic properties – Conclusions

Sonic logging data from the *Glyvursnes*-1 borehole have been used to estimate key elastic properties—Young's modulus (E) and Poisson's ratio (ν)—for the materials to be excavated for Cavern 1 and Cavern 2. Calculations are based on empirical relationships involving bulk density, compressional wave velocity, and the compressional to shear wave velocities ratio. The assumption of ideal elastic behaviour holds, which may overestimate stiffness; to mitigate this, statistical treatment using Gaussian distributions and gaining fifth percentile values was applied to improve reliability, account for uncertainty, and provide a conservative approach for numerical simulations. For modelling purposes, the original six lithological macro-units identified by GEUS were adapted at site specific conditions and grouped/selected into three categories: **lava core** (basalt core and crust), **sediment** (volcaniclastic interbeds), and **lava breccia** (weaker flow tops and bases, mostly brecciated). Data from *Glyvursnes*-1 were considered representative of both Cavern 1 (Upper Basalts) and Cavern 2 (Middle Basalts). The results show that lava cores are the stiffest ($E_{50} \approx 36$–37 GPa), sediments are the weakest ($E_{50} \approx 18$–20 GPa), and lava breccias fall in between ($E_{50} \approx 29$–30 GPa); Poisson's ratio ranges from 0.27 to 0.31. These variations reflect the alternating basalt and sediment sequences typical of the Faroese stratigraphy.

4.2 Rock electrical properties

When evaluating the potential water flow through a rock mass or stratigraphic sequence, hydraulic conductivity is the primary parameter considered. However, direct measurements are often impractical, especially across numerous stratigraphic units or large study areas. Consequently, research has focused on correlating water or other fluids inflow or presence with other rock properties, such as electrical resistivity. This section serves as a critical literature background to lay out the fundamentals of how the electrical behaviour of rocks and their inter-porous or inter-fracture fluids can be assessed and interpreted.

4.2.1 Basics of rocks petrophysics

Petrophysics characterises rocks based on two key electrical properties: (i) specific resistivity and (ii) dielectric permittivity (Schön, 2015). Electrical resistivity Γ (in Ω) is described by Ohm's laws (Eq. 4.3) as the ratio of voltage U to electric current I (first law). It is also proportional to

the conductor's length l and inversely proportional to its cross-sectional area A, assuming a cylindrical sample with axial current flow (second law), with the proportionality factor given by the resistivity R.

$$\Gamma = \frac{U}{I} \qquad\qquad \Gamma = R \cdot \frac{l}{A} \tag{4.3}$$

Under an applied electric field $\vec{E}$, the total current in rock comprises conduction (dependent on conductivity C) and displacement (dependent on dielectric permittivity $\vec{\mathcal{E}}$) components.

$$\vec{j} = \vec{j}_{\mathrm{c}} + \vec{j}_{\mathrm{d}} = C\,\vec{E} + \hat{s}\,\frac{\partial \vec{E}}{\partial t} = \left(C + i \cdot \omega \cdot \vec{\mathcal{E}}\right) \cdot \vec{\mathcal{E}} \tag{4.4}$$

Conductivity C (or resistivity R) and dielectric permittivity $\vec{\mathcal{E}}$ in Eq. 4.4 vary based on rock lithology. In the Suðuroy Tunnel stratigraphy, petrophysical parameters are identified for basalt, sandstone, and claystone. While resistivity is influenced by lithology, it can vary by several orders of magnitude within a single rock type (Tab. 4.3) due to variations in porosity and the nature of pore and fracture fillings. In particular, when pores and fractures are air-filled, bulk resistivity increases significantly; vice versa, the presence of conductive fluids leads to lower resistivity values.

Table 4.3: Electrical properties of the main geolgical units along the Sandoy–Suðuroy stratigraphy. Values from Schön (2015).

Lithology	R **[**$\Omega \cdot$ **m]**	ε_r **[–]**
Basalt	1.0×10^3 – 1.0×10^6	4.0 – 11.0
Sandstone	5.0×10^1 – 1.0×10^4	5.0 – 8.0
Clay	1.0×10^1 – 9.0×10^1	5.0 – 13.0

Most rock-forming minerals hold exceptionally high specific resistivity (>10^9 Ω·m, Schön, 2015) and are thus considered insulators. In the Faroese basalts, the igneous bedrock matrix mainly comprises plagioclase and olivine (Noe-Nygaard and Rasmussen, 1968; Waagstein et al., 1984; Waagstein, 1988; Passey and Jolley, 2009). These silicate minerals—such as labradorite, bytownite (plagioclase), augite, and pigeonite (pyroxenes)—typically have resistivity values on the order of 10^8 Ω·m (Tab. 4.4).

Table 4.4: Electrical properties of common rock-forming minerals in the basalt matrix of the Faroe Islands. Values from Schön (2015).

Mineral	R **[**$\Omega \cdot$ **m]**	ε_r **[–]**
Labradorite	6.3×10^8	5.87
Augite	4.8×10^8	6.95

Beyond those formed through lava flow solidification, additional minerals later precipitated under hot water conditions, seeping into the fissures and pores of the basaltic bedrock. The most common among them are quartz, zeolites, and calcite (National Museum of the Faroe Islands, n.d.).

Table 4.5: Electrical properties of common minerals precipitated in the stratigraphic units of the Faroe Islands. Values from Schön (2015).

Mineral	R **[**$\Omega \cdot$ **m]**	ε_r **[–]**
Quartz	2.0×10^{14}	4.50
Zeolite	1.4×10^{12}	5.60
Calcite	9.0×10^{13}	6.35

As shown in Tab. 4.5, typical precipitated minerals within solidified lava are even more resistive than silicates, minimising parallel conductivity paths. This ensures that measurable currents in the Sandoy–Suðuroy lithostratigraphy arise almost exclusively from conductive pore fluids.

In porous or fractured rocks, electrical conduction occurs mainly through ions in the pore water (Schön, 2015), while other fluids such as oil and gas have low conductivity. The resistivity and conductivity of water vary significantly depending on its source—groundwater, seawater, or fossil water (Tab. 4.6).

Table 4.6: Electrical properties for different water types. Values from Schön (2015).

Water type	R **[**$\Omega \cdot$ **m]**
Ground (fresh) water	5–300
Seawater	0.18–0.22
Fossil water	0.7–3.5

4.2.2 Single conductivity component and Archie's laws

Archie's equations (Archie, 1942) relate the resistivity of a fully water-saturated rock (R_0) to the brine resistivity (R_w) through the formation resistivity factor (F). Their validity requires that brine is the only conductive medium.

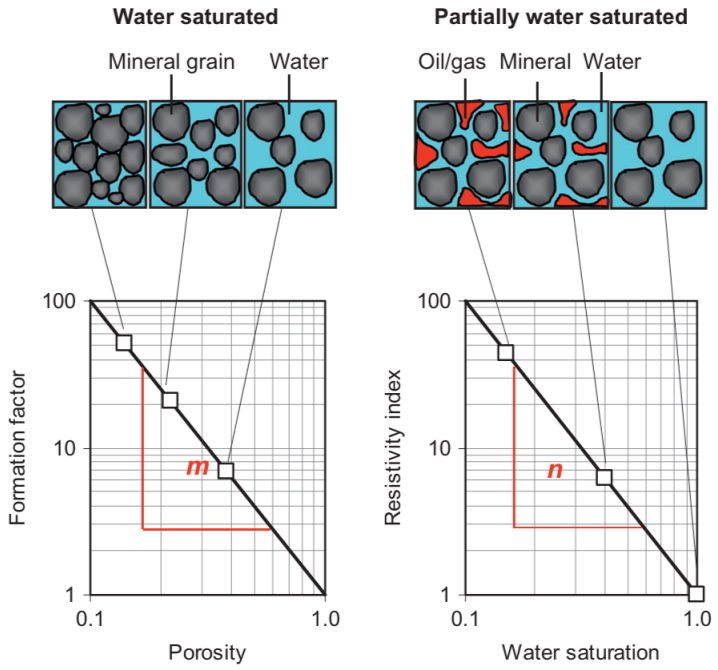


Figure 4.3: Illustration of Archie's equations. The diagram on the left shows how the formation factor (m) decreases as porosity rises in a fully water-saturated rock. The diagram on the right depicts how the resistivity index (n) drops as water saturation increases in a rock that is only partially saturated. Reproduced from Schön (2015).

For such conditions, F varies with porosity (ϕ) through the cementation exponent m (Fig. 4.3). By redefining the equation with the introduction of an additional parameter a the First Archie's Law for fully saturated rocks is obtained (Eq. 4.5). Both a and m empirically aim to represent the complex pore channels geometry with respect to the current flow (Schön, 2015).

$$F = \frac{R_0}{R_\mathrm{w}} = \frac{a}{\phi^m} \tag{4.5}$$

When water saturation decreases within a porous rock, some of the conductive water is replaced by non-conductive fluids such as gas, air, oil, or solid rock minerals. In partially saturated rocks, Archie introduced the resistivity index (IR), defined as the ratio of the resistivity measured

at any given saturation (R_t) to the resistivity of the fully water-saturated rock (R_0). IR also depends on the saturation exponent n (Fig. 4.3), which is determined through laboratory testing, although its typical order of magnitude is around 2, regardless of rock type. These principles form the basis of Archie's Second Law (Eq. 4.6).

$$IR = \frac{R_\mathrm{t}}{R_0} = \frac{1}{S_\mathrm{w}^n} \tag{4.6}$$

By obtaining the specific resistivity R_0 from the first law, the degree of saturation S_w can be calculated by inverting the second law's equation:

$$S_\mathrm{w} = \left(\frac{R_\mathrm{w}}{R_\mathrm{t}} \cdot \frac{1}{\phi^m} \right)^{1/n} \tag{4.7}$$

In borehole proximity, resistivity varies radially due to drilling fluid invasion, separating the so called invaded zone (mud filtrate) from the wider virgin zone (in-situ fluids), as illustrated in a simplified manner in Fig. 4.4.

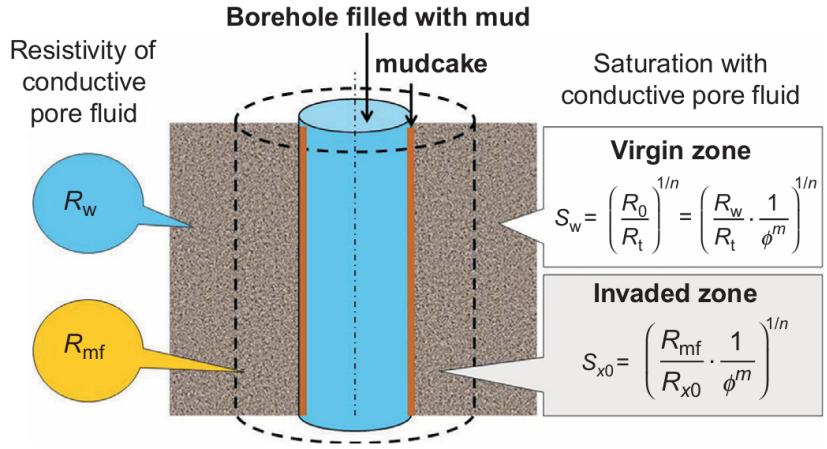


Figure 4.4: Schematic representation of a well within a porous and permeable formation, illustrating the formulas used to determine the degree of saturation in both the undisturbed (S_w) and invaded (S_{x0}) zones by inverting Archie's second law. Reproduced from Schön (2015).

Archie's model assumes that brine is the only conductor and that the rock matrix is non-conductive—a condition met in lithologies referred to as "clean rocks" (Schön, 2015).

4.2.3 Second conductivity component

Natural rocks often contain multiple conductive phases, with clay minerals providing a secondary contribution beyond conductive fluids. In fact, when combined with water, these minerals form shaly formations, introducing an extra conductivity component and causing Archie's Law to overestimate water saturation. To account for this, shaly sand models adopt a parallel conductor approach (Fig. 4.5). A simplified dual-component model was first proposed by Waxman and Smits (1968) and later extended into the Simandoux Equation, which was most recently refined by Bardon and Pied (1969). This equation, solved for S_w, requires the Archie parameters (R_w, ϕ, m), as well as the volume and resistivity of the clay phase.

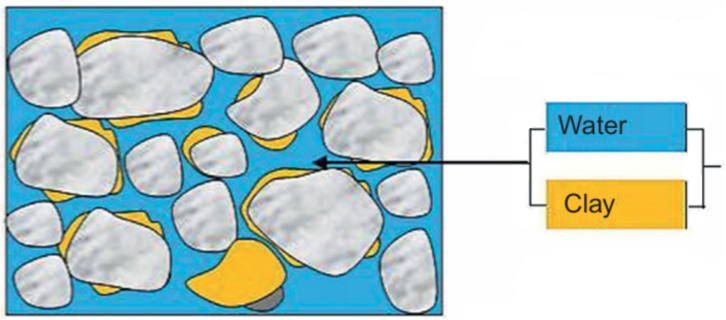


Figure 4.5: Parallel conductor circuit for the pore fluid composed of water and clay. Adapted from Schön (2015).

Although claystone units appear in the borehole logs, they make up only an extremely small portion of the overall lithology and they are rarely encountered near the planned cavern depths (Petersen et al., 2022). Therefore, the water inflow risk assessment can focus exclusively on the behaviour of clean rock.

Rock electric properties – Conclusions

Electrical resistivity and dielectric permittivity are key petrophysical properties for detecting fluid presence and movement in rocks when direct hydraulic measurements are not feasible. In the Faroe Islands, most rock-forming minerals (e.g., labradorite, augite) and precipitated minerals (quartz, zeolite, calcite) are highly resistive, indicating that measurable electrical currents in the Sandoy–Suðuroy lithostratigraphy mainly originate from conductive pore fluids rather than the rock matrix, classifying these units as clean rocks.

Water type strongly affects conductivity, with seawater being highly conductive compared to fresh or fossil waters, which must be considered in geophysical interpretations. Archie's laws (Archie, 1942) provide a theoretical basis for relating rock resistivity to water saturation in clean rocks. Parallel contributions from clay-related conductivity components are unlikely along the analysed lithostratigraphy.

4.3 Groundwater origin and saturation estimation on permeable layers

After reviewing the electrical properties of rocks and the key equations relating resistivity to saturation levels in pores and fractures, these principles are applied to the lithostratigraphy of the project site. The focus is on the most permeable units to assess the likelihood of encountering conductive fluids while excavating these units and their expected saturation levels.

4.3.1 Suðuroy core logs electric properties

Composite logs drilled by Jarðfeingi (Petersen et al., 2022) include a series of additional columns beyond standard lithological descriptions (previously illustrated in Chapter 3, Section 3.1). One of the columns reports electrical and petrographic properties via Single Point Resistance (*SPR*) measurements in Ohm. *SPR* has been measured with the conventional method, therefore between an electrode in a fluid-filled section of the borehole and an electrode at the surface (U.S. Environmental Protection Agency, 2025). *SPR* typically increases with grain size and decreases with higher fracture density or lower dissolved solids, making it a useful tool for identifying lithological changes, water salinity, and permeability.

In Sandoy–Suðuroy boreholes, high *SPR* indicates massive basalt flows; low values mark lava crusts, flow bases, and volcaniclastic units (Petersen et al., 2022). Since brecciated tops and interlava sediments strike roughly parallel to the tunnel alignment, prolonged contact with permeable layers—especially if seawater-connected—could result in significant inflows (Holter et al., 2021). Thus, water ingress must be carefully monitored during excavation.

The caverns, due to their larger blasted surfaces, are especially sensitive to inflow. Cavern 1 is considered the most vulnerable, primarily because of its higher sedimentary frequency within the *Enni Formation*, as supported by both Passey and Jolley (2009) and by Petersen et al. (2022) in his report. Its stratigraphy, between the *Sandur Beds* and *Sneis Formation*, consists

Table 4.7: Averaged SPR measurements (in Ω) of sedimentary and brecciated flow-top units within the (a) Enni and (b) Malinstindur Formations, estimated from measurements along the drilled cores of Søltuvík-2, Sandur-1, Skúvoy-1, Skarvanes-1 and Sandvík-1 performed by Jarðfeingi (Petersen et al., 2022).

Lithological unit	**Søltuvík-2**	**Sandur-1**	**Skúvoy-1**	**Skarvanes-1**
Brecciated flow top (1)	-	170	-	185
Queen Sandstone	-	30	-	40
Brecciated flow top (2)	-	-	-	80
Sandur Beds (1)	-	40	-	-
Sandur Beds (2)	-	40	-	30
Brecciated flow top (3)	-	-	-	70
Sandur Beds base	-	30	N/A	20
Sneis Formation	60	30	10	40
Brecciated flow top (4)	70	-	10	-

(a)

Lithological unit	**Søltuvík-2**	**Sandur-1**	**Skúvoy-1**	**Skarvanes-1**
C-Reflector	35	-	10	30
Sandstone below *C-Reflector*	30	-	9	20
Brecciated crust	-	-	25	-
	Sandvík-1			
B-Horizon (hyp. 1)	45			

(b)

of interbedded sedimentary, brecciated, and basaltic units. Among this interval, *SPR* readings were averaged for thick (>50 cm) sedimentary and brecciated units across boreholes in Sandoy (*Søltuvík*-2, *Sandur*-1, *Skarvanes*-1) and Skúvoy (*Skúvoy*-1), as summarised in Tab. 4.7. The averaging process involved identifying the likely 5^{th} and 95^{th} percentiles of *SPR* values for each target unit, then calculating the mean.

Regarding Cavern 2 stratigraphy, averaged *SPR* were extracted only for a few units in *Søltuvík*-2, *Skúvoy*-1, *Skarvanes*-1, and the *B-Horizon* (Hyp. 1) in *Sandvík*-1 (Tab. 4.7). As a result, *SPR* characterisation for Cavern 2 is not considered feasible, and this study focuses exclusively on Cavern 1.

4.3.2 Saturation estimation

SPR correlates with rock resistivity, allowing fluid estimation via either: (i) empirical value ranges or (ii) mathematical modelling.

As a first empirical approach (Karl-Heinz Wolf, personal communication), fluid presence can be inferred as:

- **0–10** Ω: likely saltwater or saline formation water.
- **30–80** Ω: possible freshwater interaction.
- $>$**200** Ω: negligible fluid flow.

By applying these ranges to the data in Tab. 4.7, most stratigraphic units appear to be in contact with freshwater. Saltwater intrusion or the presence of saline formation water is unlikely, except possibly in *Skúvoy*-1 (average $SPR < 25\ \Omega$ across all units). These reduced resistances may be partly due to the larger borehole diameter (6" vs. 5", Petersen et al., 2022), although this factor alone may not fully explain the low values observed.

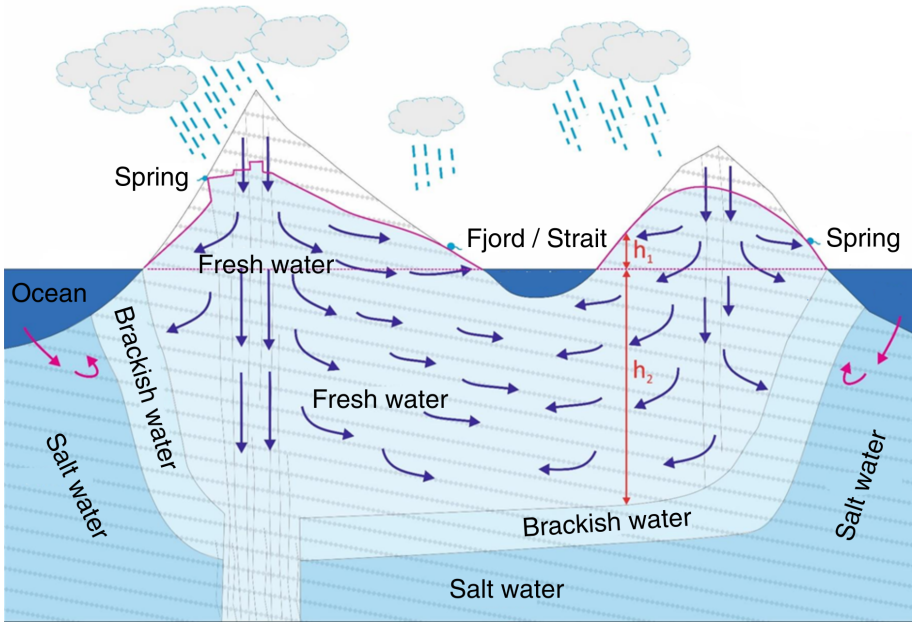


Figure 4.6: Preliminary groundwater model of the Faroe Islands. The underground piezometric height h_2 can reach values up to 20 times higher than the piezometric height h_1 above the sea level. Adapted from Ólavsdóttir and Eidesgaard (2023).

Groundwater dominance beneath the Faroese fjords is supported by past underwater tunnelling

projects, which primarily encountered inland aquifers feeding underground inflows and rarely seawater (Bennett, 2018). A simplified model developed by Jarðfeingi (Fig. 4.6) confirms a fully connected freshwater aquifer network in the archipelago, reaching depths up to 20 times the onshore water table height, suggesting possible artesian conditions (Ólavsdóttir and Eidesgaard, 2023).

After confirming the interaction between the permeable layers and the fluid, and characterising the fluid, the second phase involves estimating the effective resistivity of the target layers. The drilled borehole is modelled as a cylindrical conductor, with each *SPR* measurement representing the resistivity of a small, point-like segment of the geological formation. The stratigraphic unit is thus treated as a series of discrete electrical resistances, each corresponding to an individual *SPR* reading. The total resistance of the layer is calculated by summing these individual values.

$$\Gamma_{\text{eq}} = \Gamma_1 + \Gamma_2 + \cdots + \Gamma_N = \sum_{i=1}^{N} \Gamma_i \tag{4.8}$$

Since the average *SPR* value is known, the equivalent resistance can be calculated by multiplying this value by the total number of measurements N, which can also be expressed as the stratigraphic unit thickness z divided by the measurement frequency f.

$$\sum_{i=1}^{N} \Gamma_i = N \cdot SPR_{\text{avg}} = \frac{z}{\mathrm{f}} \cdot SPR_{\text{avg}} \tag{4.9}$$

By applying Ohm's Second Law and modelling the cased core as an ideal cylinder with height z and cross-sectional area A, the resistivity R can be expressed as follows (Reynolds, 2011):

$$\Gamma_{\text{eq}} = R \cdot \frac{z}{A} = \frac{z}{\mathrm{f}} \cdot SPR_{\text{avg}} \tag{4.10}$$

$$R = \frac{A}{\mathrm{f}} \cdot SPR_{\text{avg}} \tag{4.11}$$

Hence, unit resistivity is demonstrated to be dependent on the average *SPR*, the sampling interval, and the borehole diameter. The corresponding resistivity values are presented in Tab. 4.8.

Table 4.8: Calculated resistivities (in Ω·m) of sedimentary and brecciated flow-top units within the (a) Enni and (b) Malinstindur Formations, estimated from their respective average SPR.

Lithological unit	**Søltuvík-2**	**Sandur-1**	**Skúvoy-1**	**Skarvanes-1**
Brecciated flow top (1)	-	861	-	557
Queen Sandstone	-	152	-	203
Brecciated flow top (2)	-	-	-	405
Sandur Beds (1)	-	203	-	-
Sandur Beds (2)	-	203	-	30
Brecciated flow top (3)	-	-	-	355
Sandur Beds base	-	152	N/A	101
Sneis Formation	304	152	73	203
Brecciated flow top (4)	355	-	73	-

(a)

Lithological unit	**Søltuvík-2**	**Sandur-1**	**Skúvoy-1**	**Skarvanes-1**
C-Reflector	177	-	73	152
Sandstone below *C-Reflector*	152	-	65	101
Brecciated crust	-	-	181	-
	Sandvík-1			
B-Horizon (hyp. 1)	228			

(b)

Following the identification of seawater or freshwater within a stratigraphic layer and its corresponding resistivity, the saturation index (S_w) is estimated using the inverted form of Archie's Second Law (Eq. 4.7). This requires both the layer's specific resistivity and porosity. S_w is firstly evaluated across a full porosity range (0–1) to identify the threshold for full saturation.

A reference water resistivity is assigned to each borehole. Due to the shallow overburden near the sea bottom, a resistivity of 30 Ω·m is assumed—predominantly freshwater with still possibility of minor brackish mixing. An exception is *Skúvoy*-1, where probable seawater contact suggests a lower resistivity of 0.20 Ω·m. Saturation (n) and cementation (m) exponents are both set to 2.0, with $a = 1$, as per Schön (2015).

The plots in Fig. 4.7 show the porosity required for each lithostratigraphic unit to reach full saturation. Based on the resistivity values listed in Tab. 4.8, calculations for freshwater-filled

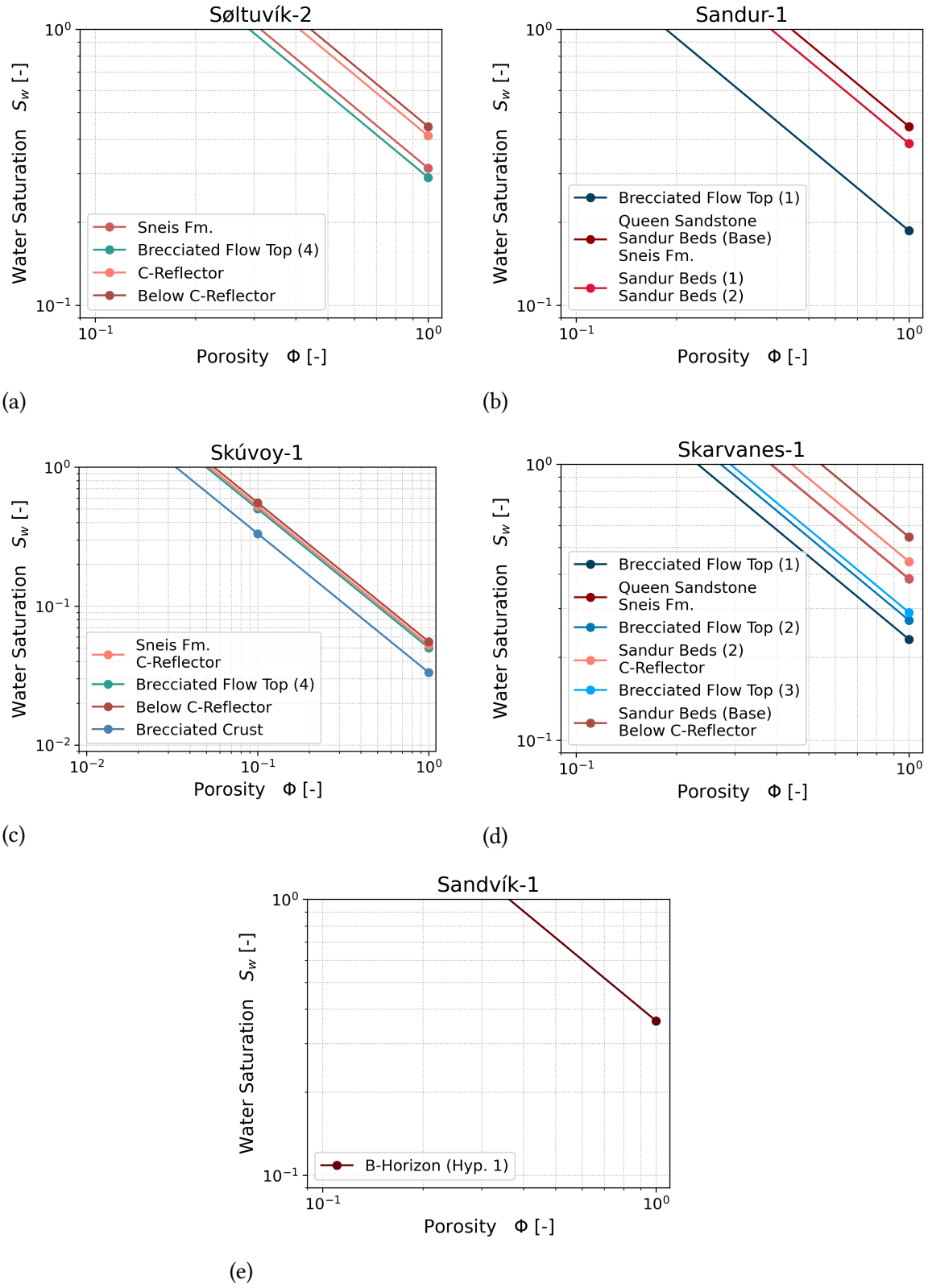


Figure 4.7: Evolution of the saturation index (S_w) by varying the porosity of the sedimentary and brecciated units assuming mixed fresh-brackish water presence along Søltuvík-2 (a), Sandur-1 (b), Skarvanes-1 (d), Sandvík-1 (e) and saltwater presence in Skúvoy-1 (c).

voids indicate that full saturation occurs at porosities below 30–40% for sandstones and below 20–30% for brecciated units (Fig. 4.7a–b, Fig. 4.7d–e). Under saline conditions, the saturation porosity decreases by nearly an order of magnitude, with full saturation reached only below 3% porosity for sandstones and below 2% for breccias (Fig. 4.7c). This means that, given the same porosity, sandstone units are generally more saturated than breccias.

To assess effective saturation along the analysed lithostratigraphic units, porosity values from the plots are compared with Neutron Porosity Index (NPHI) measurements from the *Glyvursnes*-1 log by GEUS (Waagstein and Andersen, 2004). Average NPHI values in the Upper Basalt Formation indicate porosities of 45.7% for sedimentary units and 25.9% for volcaniclastic breccias, suggesting fully or near-fully saturated conditions for both units under freshwater influence (S_w in the 70%–100% range for sandstones, likewise for breccias). In contrast, if seawater or saline formation water is present, saturation is expected to be significantly lower.

Although the results align well with general groundwater models of the Faroe Islands, it is important to remind that since *SPR* logs reflect near-borehole conditions, they may capture the invaded zone properties rather than the formation's intrinsic ones (Fig. 4.4; U.S. Environmental Protection Agency, 2025). Therefore, careful interpretation is required.

Groundwater origin and saturation estimations – Conclusions

The analysis of Single Point Resistance (*SPR*) measurements from the Sandoy–Suðuroy boreholes effectively differentiates lithologies, identifying high-resistance massive basalts and lower-resistance sedimentary and brecciated units associated with increased permeability and the presence of conductive fluids, particularly groundwater. The *Enni Formation* stratigraphic column in proximity of Cavern 1 shows a moderate risk of water inflow due to its sedimentary units-rich nature. *SPR* values likely indicate freshwater contact based on empirical ranges, except for the lower values observed in the *Skúvoy*-1 borehole, which are probably influenced by both the larger borehole diameter compared to all the others and the possible presence of saline fluids. By modelling electrical properties using Ohm's Second Law and Archie's Law, saturation estimates suggest widespread partial to full saturation (70–100%) both for sandstone and breccia units when interacting with freshwater. These findings support existing hydrogeological models of a connected freshwater aquifer system beneath the archipelago, with limited seawater inflow, even under fjord and sea strait settings. The potential influence of the invaded zone on *SPR* measurements, and thus on derived results, cannot be entirely ruled out; therefore, caution is advised when interpreting the data.

4.4 Required hydraulic conductivity

Although the conceptual link between saturation index (S_w) and hydraulic conductivity (K) may seem intuitive, their analytical relationship is complex, particularly under unsaturated conditions. Here, K depends not only on S_w but also on pore structure, texture, and capillarity. The relationship is highly non-linear: K drops sharply as S_w decreases due to increased flow resistance in smaller pores.

Several models (Millington and Quirk, 1961; Brooks, 1965; Mualem, 1976) attempted to capture this behaviour. Yet, estimating K in unsaturated media remains difficult due to its field variability and the cost and complexity of direct measurement. Van Genuchten (1980) proposed a relatively simple closed-form model correlating relative conductivity to effective saturation (S_e), later extended by Van Genuchten and Nielsen (1985) to describe experimental trends across various soils. Despite its simplicity, it involves five parameters, most of which require laboratory test estimation. In the absence of these data, applying the model necessitates strong assumptions, weakening result reliability.

Due to the lack of a solid analytical relationship between saturation degree and hydraulic conductivity, and the significant uncertainties in key parameters, this study focuses on estimating the maximum allowable hydraulic conductivity (K) that satisfies standard tunnel design inflow criteria in the Faroe Islands. A maximum inflow of 20L/min/100m of tunnel is generally accepted for subsea tunnels in the Faroes, while Norwegian projects commonly set this limit at 30L/min/100m (Holter et al., 2021). For the Suðuroy Tunnel, an optimal target of 15L/min/100m has been proposed by NGI to minimise pumping costs (Holter et al., 2021).

Saturated flow in a homogeneous, fully saturated porous medium is assumed to follow Darcy's Law (Darcy, 1856).

$$\frac{Q}{A} = -k \cdot \frac{\Delta h}{\Delta L} \tag{4.12}$$

Optimal (K_{opt}) and maximum (K_{max}) values are estimated based on a simplified cavern model with a circular base and a domed roof, assuming a permeable layer of thickness z and radius R in contact with the cavern, extending from the seafloor to the underground excavation. Under hydrostatic conditions, the head loss Δh is taken as the vertical distance between the seabed and the cavern roof, approximated as 80,m from bathymetric data (Fig. 3.2, Chapter 3). The flow path length L corresponds to the distance between the cavern's contact point and the hypothetical outcrop at the seafloor. It is determined by assigning a 1.0° layer dip (denoted as α), based on desk study outcomes for the sedimentary and brecciated units of the *Enni*

Formation (Section 3.2, Chapter 3). Fig. 4.8 illustrates the schematised model along with all the assumptions.

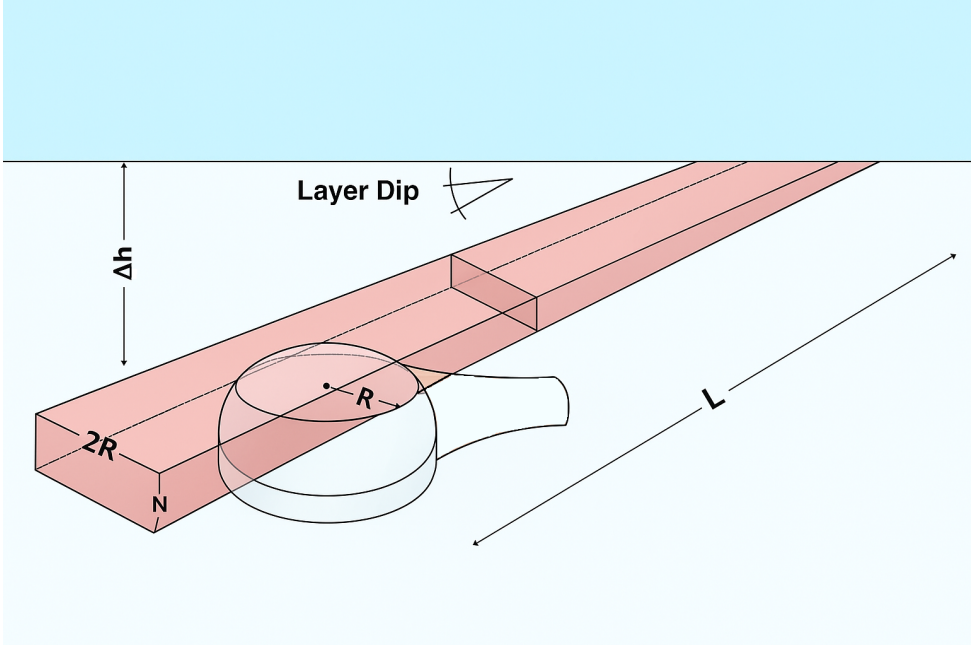


Figure 4.8: Simplified model of a water flow through a permeable layer in contact with the tunnel and cavern excavation. Δh represents the head loss , R the contact surface width between cavern and permeable layer, z the layer thickness, L the distance between layer outcrops in seabed and the contact with the cavern, α the layer dip angle.

Darcy's law is rewritten in terms of hydraulic conductivity K, using:

$$k = K \cdot \frac{\mu}{\rho g} \tag{4.13}$$

Assuming freshwater or saltwater with negligible density difference, $\gamma_w = \rho g = 10\ kN/m^3$ ($10\,000\ N/m^3$) is used. The specific inflow Q_{ref} (in L/min/100m) is converted to volumetric flow Q:

$$Q = Q_{\text{ref}} \cdot 10^{-3} \cdot \frac{1}{60} \cdot \frac{2R}{100} \tag{4.14}$$

By isolating the portion of the layer in contact with the cavern, a cross-section of porous medium is defined, with a width of $2R$ and a height of z. Assuming that the target layer is the only permeable component, continuity of the volumetric flow rate Q can be maintained

between this control cross-section and the surface of the cavern exposed to the permeable lithology—where water inflow is assumed to occur uniformly across the entire exposed surface. Equating Q at these two cross-sections allows the estimation of hydraulic conductivity.

$$K = \frac{Q}{2R \cdot z} \cdot \rho g \cdot \frac{1}{\sin(\alpha)} \tag{4.15}$$

The derived equation shows that, after accounting for the previous assumptions, the relationship is independent of the cavern radius R; thus, the optimal and maximum allowable hydraulic conductivity remain constant regardless of cavern size. This results from the cavern's circular geometry, where the cross-sectional area contribution equals the target layer length over which flow is estimated. Consequently, only the layer thickness z affects the required hydraulic conductivity. In more general cases, a geometric ratio (ranging from 0 to 1) between two geometric variables would appear in the final formulation.

Estimations of K_{opt} and K_{max} are based on the cavern intersecting sandstone or conglomer-

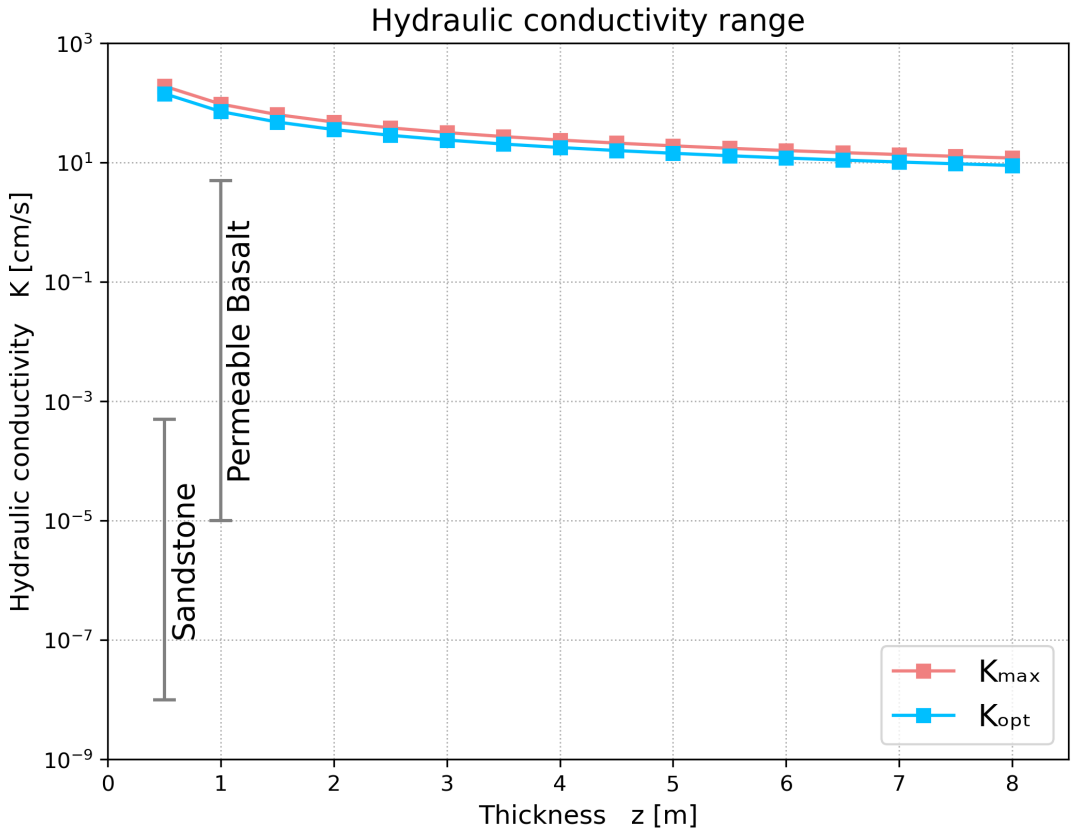


Figure 4.9: Optimal and maximum allowable hydraulic conductivities outcomes w.r.t. reference values from literature (Freeze and Cherry, 1979) for sandstone and permeable basalt lithologies.

ate/breccia units. The layer thickness z varies from 0.5 to ~2.5 m for sandstones and 0.5 to 8.0 m for brecciated flow tops (see Fig. 3.7, Chapter 3), with the latter therefore setting the effective range.

These values are compared with literature data from extensive laboratory and field tests by Freeze and Cherry (1979), focusing on permeable basalts and sandstones. As shown in Fig. 4.9, the estimated conductivity corresponding to the maximum flow rate (Q_{max}) exceeds typical literature values, suggesting that actual inflows during the excavation of Cavern 1 are likely to be lower. Similarly, the identified optimal flow rate (Q_{opt}) cannot be guaranteed, as the estimated permeability ranges fall below this threshold.

It has been assessed that the higher end of the hydraulic conductivity range for permeable basalts is achieved by K_{opt} for thick units ($z > 5$ m) when the dip angle is approximately $\alpha \geq 3°$, and for nearly the entire thickness range ($z \geq 1$ m) when $\alpha \geq 20°$. The magnitude of the first dip is generally higher than local trends but could potentially occur in specific areas; the second, instead, is highly unlikely. Therefore, with respect to general dip trends, the pumping system should be designed to accommodate flows lower than the optimal without increasing costs. For Cavern 2, the dataset remains insufficient to draw definitive conclusions, although no significant changes are expected.

In accordance to the results, no special water inflow control measures seem to be planned. Standard Faroese practice relies on percussive probe drilling and pre-excavation grouting, which seals and strengthens the rock mass in complex conditions (Samuelsen and Grøv, 2018). Continuous ground condition monitoring and excavation adjustment remains important as well. Rock support systems—including cast concrete, sprayed concrete ribs, and linings—incorporate drainage features. Sprayed concrete typically uses a wet mix application made of steel fibres. Corrosion risk is negligible if the thickness exceeds 80 mm and hits at least a strength class of C45 (Samuelsen and Grøv, 2018).

Required hydraulic conductivity – Conclusions

Due to the lack of reliable analytical relationships between saturation degree (S_w) and hydraulic conductivity (K), this study estimated the maximum allowable and optimal hydraulic conductivities ($K_{\max}$ and K_{opt}, respectively) based on inflow limits for subsea tunnels in the Faroe Islands. Assuming saturated flow governed by Darcy's Law (Darcy, 1856), adapted to the site's geology and geometry, a simplified expression for K was derived. This formulation is independent of cavern radius—due to the circular geometry employed—and depends exclusively on the permeable layer thickness.

The calculated values of K_{opt} and K_{max} exceed typical literature values for sandstone and permeable basalt (Freeze and Cherry, 1979) while assuming general local dip angle trends, indicating that actual inflows during Cavern 1 excavation will likely remain below design but also below the optimal threshold, necessitating a site-specific pumping system design. Although data for Cavern 2 are limited, no significant differences from Cavern 1 are expected. Based on these results, standard Faroese inflow control practices for tunnels are considered adequate without additional measures.

5

Field mapping

Betri er at vera fyrivarin, enn eftirsnarur.
It's better to be prepared than swift afterwards.

The initial data collection—including literature review, desk study, and geophysical interpretation—has provided valuable insights into the lithological and mechanical characteristics of the Sandoy–Suðuroy geology. However, critical gaps remain for project-specific requirements and model inputs. While the main basaltic sequences and sedimentary units have been mapped, reliable estimates of dip direction and dip angle for certain lithologies—particularly in the southern Middle Basalt Sequence—are lacking. The available boreholes (Sandvík-1 and Hvalba-1) are insufficient to determine bedding orientations, and the absence of horizontal or marine boreholes leaves much of the central-southern tunnel alignment unexamined.

Moreover, the planned use of Mohr–Coulomb (MC) and Hoek–Brown (HB) failure criteria for numerical modelling introduces significant uncertainties due to limited data. No laboratory tests have been conducted on borehole cores to determine friction angle or cohesion for the MC model. Similarly, key HB parameters—such as Uniaxial Compressive Strength and Geological Strength Index—are entirely unknown at the site. To address these gaps, a comprehensive field mapping campaign has become essential, as agreed upon with Dr. Eivind Grøv, project lead at SINTEF, and the company P/F Suðuroytunnel.

5.1 Outcrops identification

For the field mapping (FM) program, outcrops were selected based on proximity to the project area, geological relevance to the Sandoy–Suðuroy seabed (as indicated by the desk study), and accessibility from Tórshavn. Selection was guided by satellite imagery, Google Street View, literature, and local expertise kindly provided by Bartal Højgaard, geologist at Jarðfeingi. Each outcrop was subdivided into sections based on visible surface differences. Naming followed the format: *Island name + outcrop number – (section number)* for clear geographic reference.

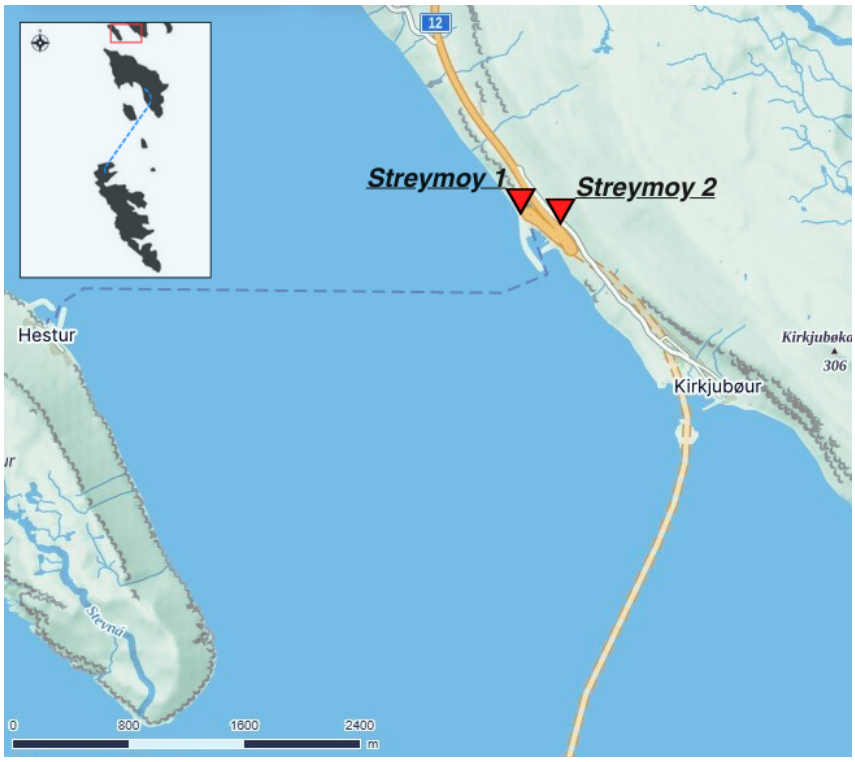
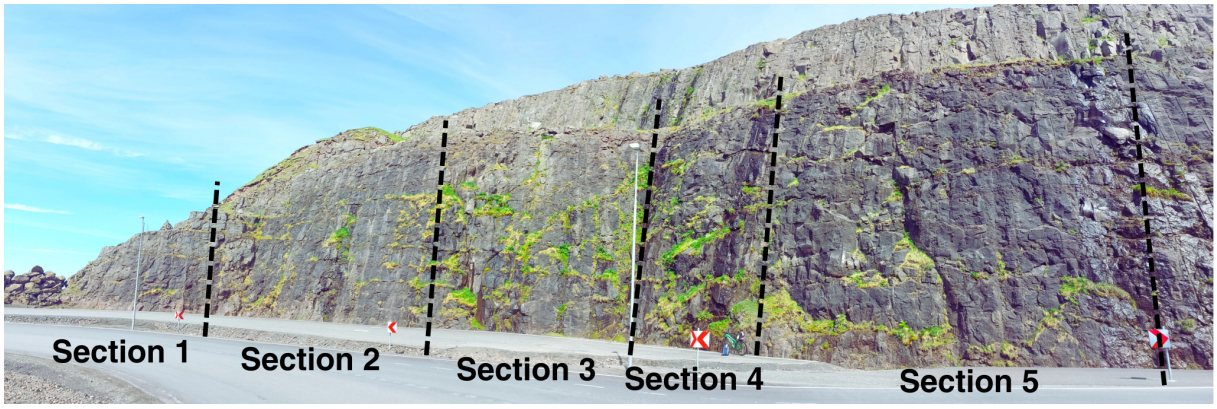
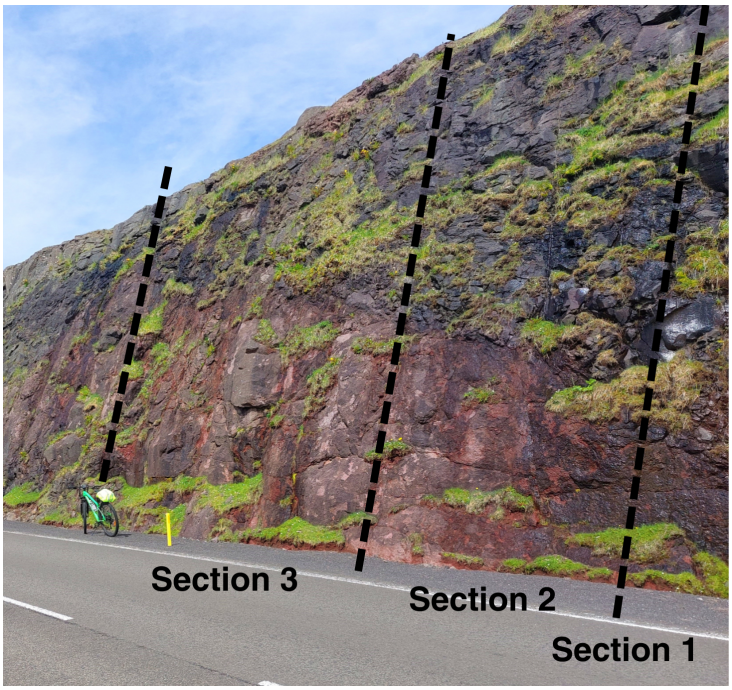


Figure 5.1: Outcrops Streymoy 1 and Streymoy 2 localisation w.r.t. the Suðuroy Tunnel alignment. Background map from https://mapy.com.

Outcrops *Streymoy 1* (Fig. 5.2a) and *Streymoy 2* (Fig. 5.2b), located along Gamlarætt road near the northern Sandoy Tunnel entrance (Fig. 5.1), have been exposed for decades, allowing some vegetation growth along the fractures. *Streymoy 1* lies at sea level near Gamlarætt harbour, spans 75 m in length, and ranges 13–20 m in height. *Streymoy 2* starts at ~30 m a.s.l. and extends for ~200 m, though only three ~10 m-long sections were analysed as representative segments.



(a)



(b)

Figure 5.2: Outcrops (a) Streymoy 1 and (b) Streymoy 2 overview and their subdivision in sections.

The elevation difference between the two outcrops suggests that different basaltic flows are exposed, both belong to the *Enni Formation*. While their distance from the project site limits direct correlation with drill-target lithologies, the outcrops provide relevant qualitative insights such as the variation in basalt textures along distinct flows and a clearly distinguishable weathered flow top at the base of *Streymoy 2*, indicative of a mechanically weaker stratum.

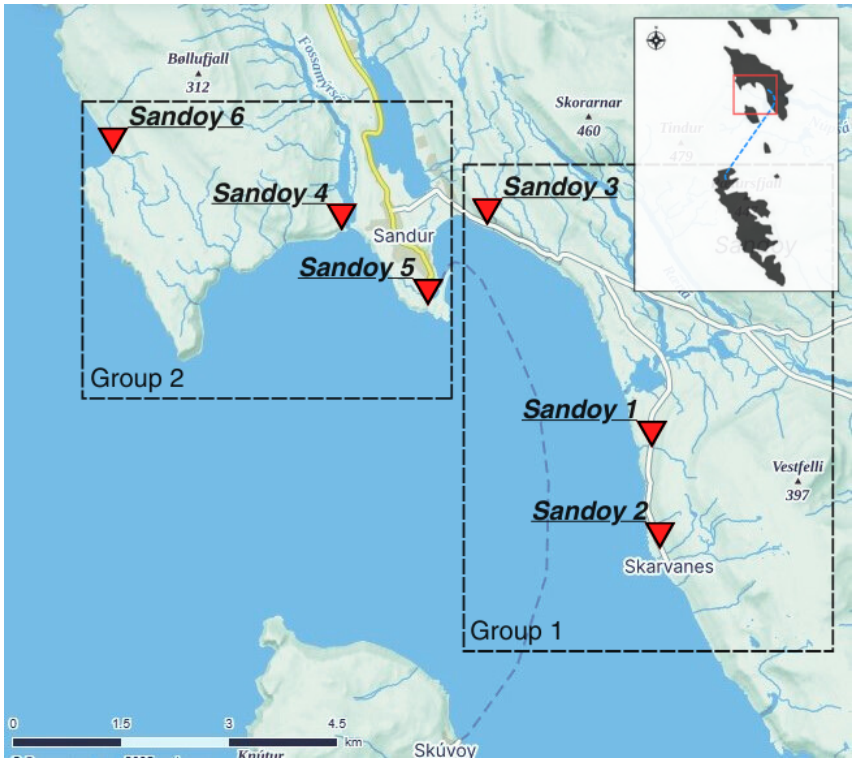
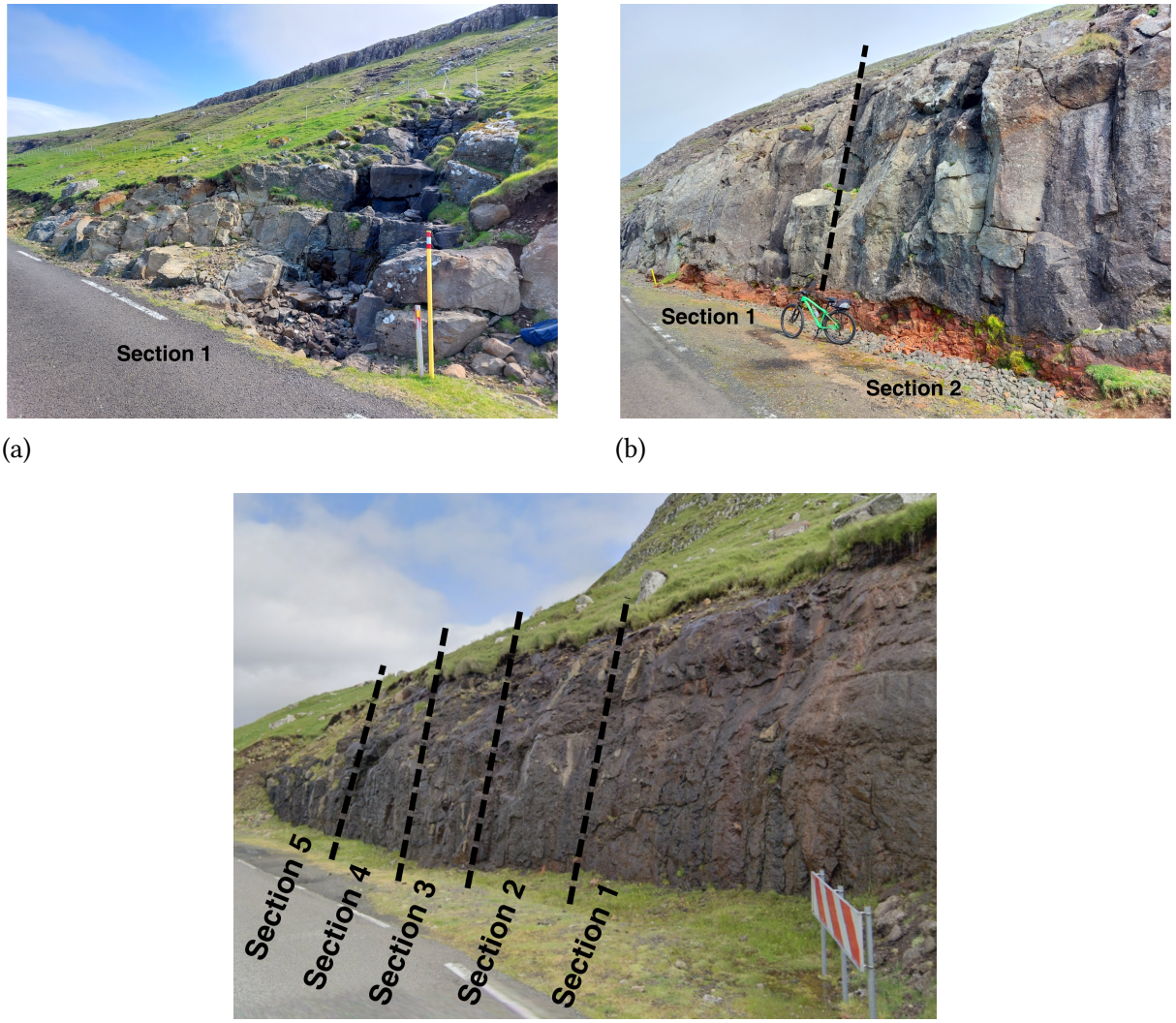


Figure 5.3: Outcrops Sandoy 1, Sandoy 2 and Sandoy 3 localisation w.r.t. the Suðuroy Tunnel alignment. Background map from https://mapy.com.

In Sandoy, two main outcrop groups provide significant insights into the subsurface lithology near the planned northern cavern site. The first group—*Sandoy 1*, *2*, and *3*—is located west of Sandur along the Skarvanes road (Fig. 5.3). From west to east, *Sandoy 3* (Fig. 5.4c) exposes a 55 m roadcut of massive to slightly fractured basalt; *Sandoy 1* (Fig. 5.4a), near the northern portal, shows highly blocky basalt next to a stream bed; and *Sandoy 2* (Fig. 5.4b), a road recess near Skarvanes, features massive basalt with a basal volcaniclastic sandstone layer. These outcrops represent stratigraphically younger flows of the *Enni Formation* compared to those that will be excavated. Although they are located above the tunnel horizon, they remain important for understanding the region's basaltic and sedimentary morphology and characteristics.



(a) (b)

(c)

Figure 5.4: Outcrops (a) Sandoy 1, (b) Sandoy 2, and (c) Sandoy 3 overview and their subdivision in sections.

The second group lies in mid-western Sandoy (Fig. 5.3), beginning with the aforementioned *Queen Margaret sandstone* (here renamed *Sandoy 4*, Fig. 5.5a) introduced in Section 3.1, Chapter 3. Other exposures include a harbour roadcut at Sandur (*Sandoy 5*, Fig. 5.5b) and coastal rocks at Søltuvík (*Sandoy 6*). These span from ~30 m above the presumed *Sneis Formation* to the upper *Sandur Beds*, offering the most representative onshore analogies to the conditions expected at the cavern site.



(a) (b)

Figure 5.5: Outcrops (a) Sandoy 4 and (b) Sandoy 5 overview. Field mapping was finally not performed in these outcrops. Photograph (a) by Bartal Højgaard (2015).

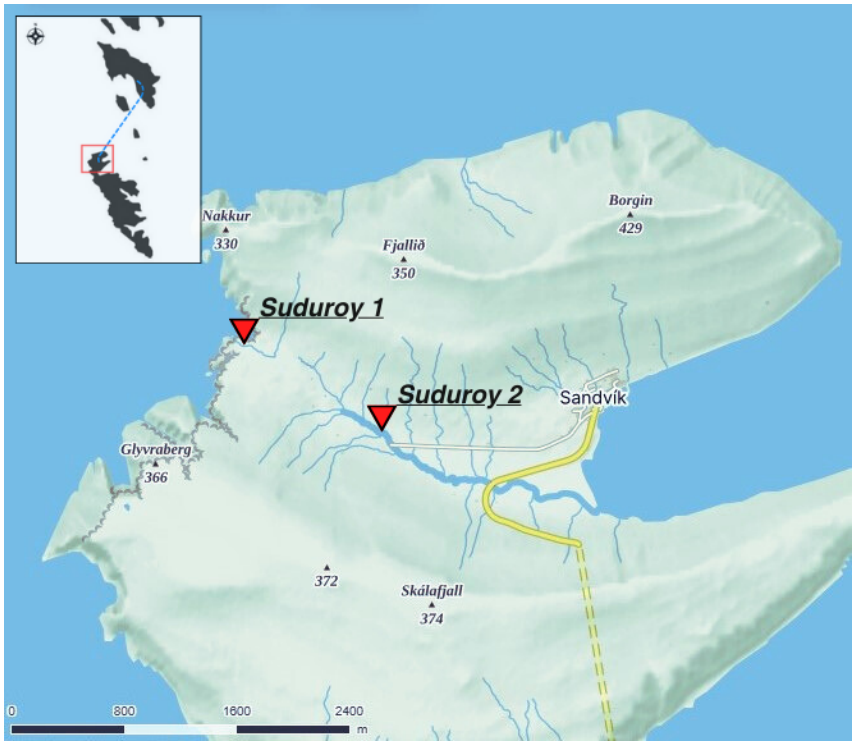


Figure 5.6: Outcrops Suduroy 1 and Suduroy 2 localisation w.r.t. the Suðuroy Tunnel alignment. Background map from https://mapy.com.

Two outcrops west of Sandvík, Suðuroy—designated *Suduroy 1* (Fig. 5.7a) and *Suduroy 2* (Fig. 5.7b)—have been integrated into the FM plan due to sparse borehole data in the southern area of the tunnel alignment (Fig. 5.6) and their likely correlation with unlogged basalt flows. These are the only studied exposures of the *Malinstindur Formation*, making them extremely relevant for assessing rock mass quality and bedding of the Middle Basalt Series and inform Cavern 2 model inputs. *Suduroy 1*, located near the western coast at ~90 m a.s.l., exposes two

massive, homogeneous blocks (~20×15 m and ~15×25 m). *Suduroy 2*, along the Sandviksa stream, features more jointed rock distributed over ~30 m of riverbed.



(a) (b)

Figure 5.7: Outcrops (a) Suduroy 1 and (b) Suduroy 2 overview and their subdivision in sections.

5.2 Field testing methodology at the outcrops

Among each of the 10 identified outcrops, the field mapping (FM) campaign aimed to perform the following measurements and analyses with consequent related outcomes:

1. Rock mass quality assessment using a **mapping sheet**, with evaluations based on the *Q*- and *GSI* systems to derive numerical model parameters and estimate structural reinforcements for the excavation.
2. Measurement of the main joint set orientations, represented on a **stereonet**, and, at the island scale, the implementation of **rose diagrams** to display structural data.
3. Rock mass strength evaluation through **Schmidt Hammer (SH) measurements** and corresponding *UCS* estimations, conducted section-wise or over entire outcrops, supporting model parameter characterisation and reinforcement planning.

Table 5.1: Instrumentation utilised during the field mapping campaign for rock mass quality and strength evaluation.

FM instrumentation
Q-system & GSI mapping sheets
Schmidt Hammer (Proceq® OS8000 N-type hammer)
Knife
Reference objects (bicycle, bag, highlighter)
Compass, camera

A diagram containing plans and goals for each outcrop analysed during the FM is shown in Fig. 5.8. To achieve the aforementioned goals, a basic but essential set of geotechnical and general tools (Tab. 5.1) is required to meet these FM goals.

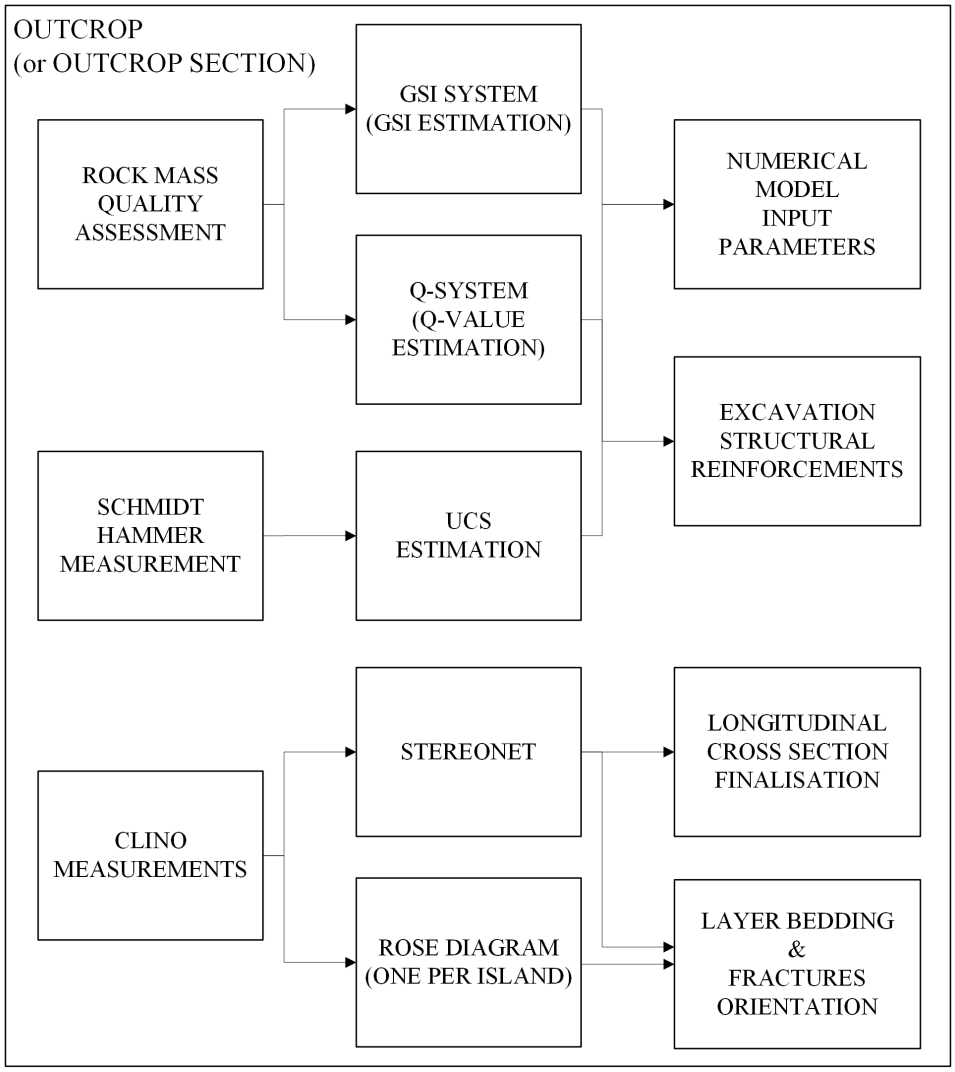


Figure 5.8: Site investigation plan and goals from each outcrop analysis.

5.2.1 Outcrop sections mapping sheet

Outcrop mapping follows a standardised procedure using pre-prepared sheets for each section of the FM campaign. Each sheet contains a sketch showing the front view of the outcrop and an estimated lateral view (the portion extending into the surrounding terrain). These sketches highlight the main joint set orientations, the presence and density of random joints, and the boundaries of geotechnical units. Scale references combine quantitative dimensions with qualitative indicators (e.g., a sketched human silhouette).

Rock mass quality is assessed via both the *Q-system* (Fig. 5.9a) and *Geological Strength Index* (*GSI*, Fig. 5.9b) methods, aligned with NGI handbook guidelines (Norwegian Geotechnical Institute, 2015) and the publication from Marinos and Hoek (2000), respectively. The *Q-system* involves observational and tactile assessments across six parameters: *RQD*, J_n, J_a, J_r, J_w (with a particular attention on the water outflow nature), and *SRF*. For each parameter, a representative value or range is assigned, and the resulting *Q*-value computed accordingly.

The *GSI* provides a disturbance rating (0–100) based on (i) surface conditions and (ii) rock structure. A range (5–10 units wide) is typically quoted as recommended by Marinos and Hoek (2000), with still a representative value selected among this interval for modelling purposes. Although an updated chart exists (Cai et al., 2007), which incorporates less subjective parameters such as the block volume (V_b) and the joint condition factor (J_c), the original chart is preferred in this FM campaign due to its practicality and the lack of high-precision measurement instruments during fieldwork.

Mapping sheets are accompanied by a wide photographic documentation that included overviews for structural assessment and detailed shots for joints and seepage characterisation. Available objects were used for scale in each picture (refer to Appendix C.1).

Outcrop Mapping Sheet - Q-System

Project Name: MSc Thesis – Suduroy Tunnel project

Outcrop coordinates:	Name	Location	Width (B)	Thickness (D)	Height (H)
61°38'08.6"N 6°58'30.2"W	Section 1-1 (TOP to BOTTOM)	Ásmundarstakkur (Suduroy)	10-12 m	10 m	3 m

Nature of the outcrop: Natural
Estimated age: N/A

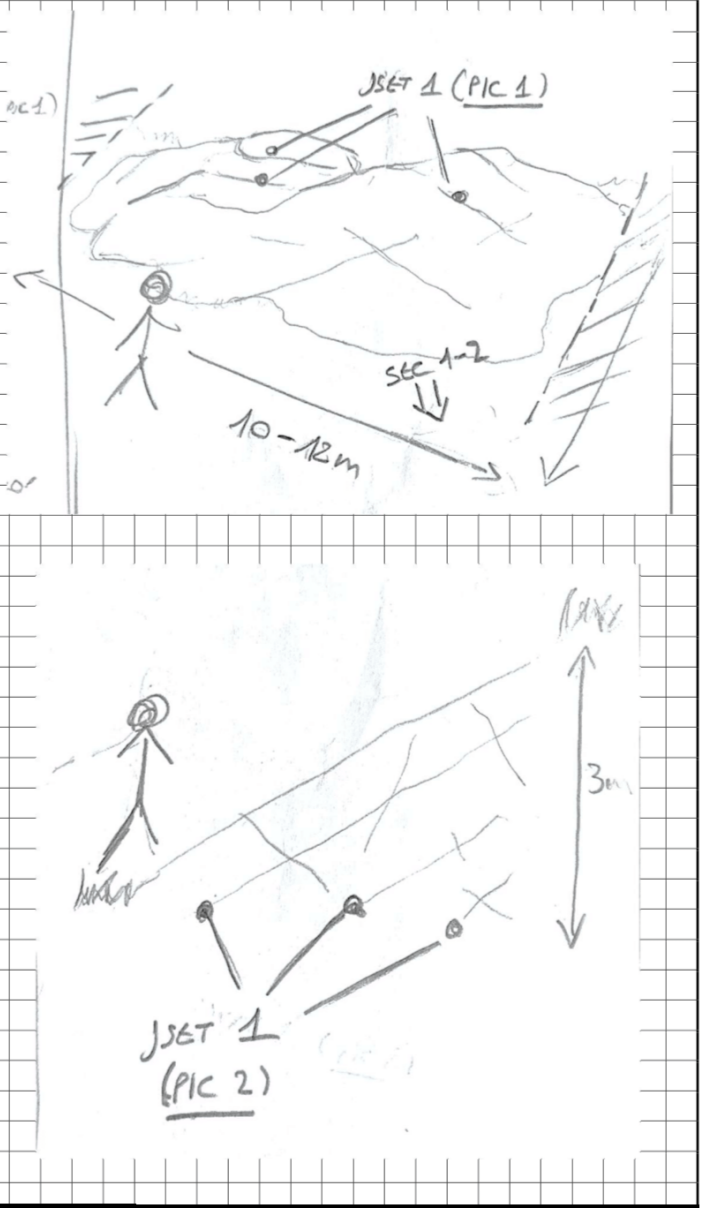
Mapped by: Cristian Tebaldi | Date of Mapping: 25/05/2024

RQD (%)	Jn	Jr (or JRC)	Ja	Jw	SRF
85 - 90	3	4	1	1	2.5

Q-Value = (RQD/Jn) x (Jr/Ja) x (Jw/SRF)

45.30 (RQD = 85)
48.00 (RQD = 90)

Sketch:



Notes:

RQD:
Almost excellent rock mass quality, very uniform configuration with some isolated random joints or 1x1 m blocks or larger (Pic. 1)

Jn:
One main joint set and random joints (Pic. 2)

Jr:
Discontinuous joints and, when present, very rough ones

Ja:
Unaltered joint walls (Pic. 3) with seldom presence of mineral fillings (quartz, calcite, …) (Pic. 4)

Jw:
No presence of water along the section and the outcrop in general

SRF:
The outcrop is situated on the ground surface

(a)

Outcrop Mapping Sheet - GSI

Project Name: MSc Thesis – Suduroy Tunnel project

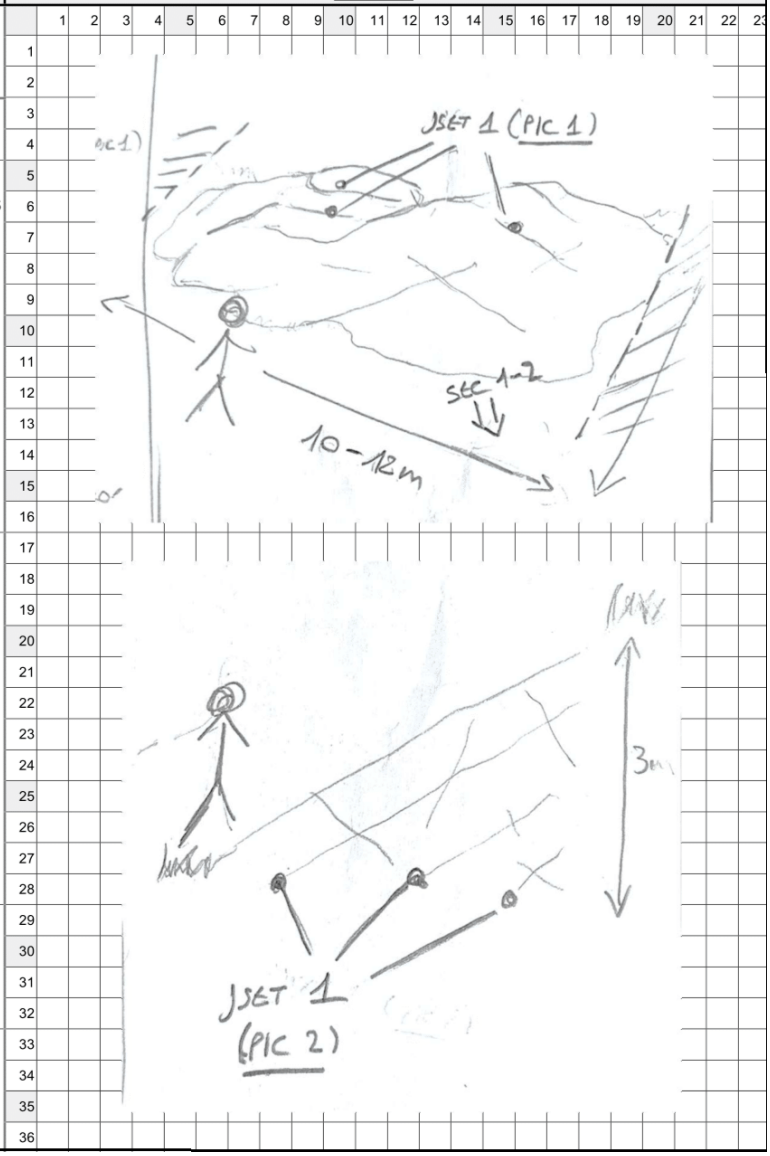
Outcrop coordinates:	Name	Location	Width (B)	Thickness (D)	Height (H)
61°38'08.6"N 6°58'30.2"W	Section 1-1 (TOP to BOTTOM)	Ásmundarstakkur (Suduroy)	10-12 m	10 m	3 m

Nature of the outcrop: Natural
Estimated age: N/A

Mapped by: Cristian Tebaldi | Date of Mapping: 25/05/2024

GSI from	GSI to	Preferred GSI = (the value that best fits as an average for the numerical model)	85
82	87		

Sketch:



Notes:

Structure:
Blocky to intact, with isolated blocks in a massive rock that shows overall widely spaced discontinuities

Surface conditions:
Good, with slightly weathered and very rough surfaces

(b)

Figure 5.9: Example of (a) Q-System and (b) GSI mapping sheets evaluating rock mass quality in an outcrop section during the FM campaign.

5.2.2 Stereonets

Bedrock outcrops offer relevant insights on bedding and joint orientation. Strike and dip are measured using the Clino® app (Petroleum Science) by placing a smartphone on inclined surfaces until compass stabilisation. To ensure accuracy: (i) the smartphone must align with the surface, possibly requiring a rigid support on rough rock, and (ii) measurement points must be undisturbed and unaffected by blasting as most as possible.

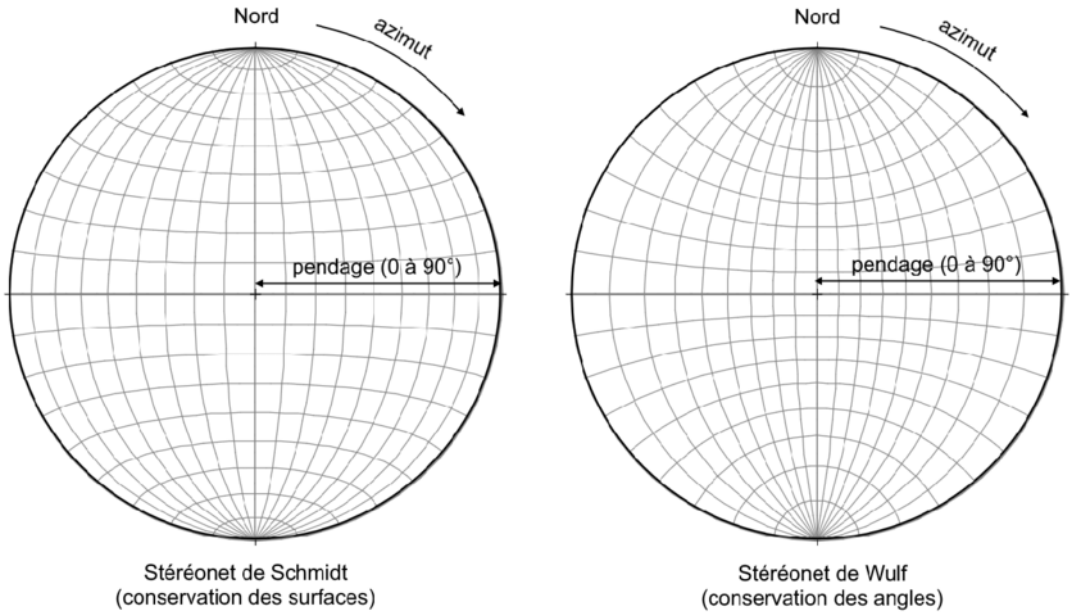


Figure 5.10: Representation through Schmidt and Wulff projections, the first for the surfaces conservation, the second for angles conservation. Retreived from Caudal (2021).

Measurements are then processed and plotted on stereonets using either (i) equal-angle (Wulff) or (ii) equal-area (Schmidt) projections (Fig. 5.10). By maintaining area proportionality, the Schmidt projection is generally more suitable for fracture density and orientation analysis such as this study. The mean resultant plane and its pole are plotted and highlighted along the FM output stereonets, with corresponding dip and strike illustrated in their legend. In addition, outcrop or outcrop section projections also help to identify dominant joint sets and refine/adjust joint number (J_n) values estimated visually during the Q assessment.

5.2.3 Rose diagrams

While stereonets depict plane orientations, fracture frequencies are better visualised with rose diagrams. Previously documented trends are relevant in the Faroese and particularly the Sandoy–Suðuroy context. Notably, Ziska (2012) provided extensive archipelago-wide datasets, while structural logs at 50 m intervals from Sandoy, Skúvoy, and Suðuroy were provided by Petersen et al. (2022) as illustrated in Section 3.3, Chapter 3). However, the rose diagrams of this work cover only limited sectors or highlight peak trends, restricting detailed comparison. Therefore, this scale justifies comparison (Suðuroy) or integration (Sandoy and southern Streymoy) with the highly larger dataset from Ziska (2012), but not with the more localised data provided by Petersen et al. (2022).

5.2.4 Schmidt Hammer

The Schmidt Hammer (SH) rebound test is a standard method for estimating in-situ rock hardness. When the spring-loaded piston impacts the rock surface, it rebounds, and the rebound value R reflects the surface hardness. R can potentially be directly correlated with the Uniaxial Compressive Strength (*UCS*, or σ_{ci}), making the test highly appealing (Culshaw, 2015). Two SH types exist: *N–type* and *L–type*, with their values almost perfectly related (Aydin and Basu, 2005) for $R_L > 30$ and $R_N > 40$ as:

$$R_{\mathrm{N}} = 1.0646\, R_{\mathrm{L}} + 6.3673 \tag{5.1}$$

Many *UCS*–R correlations hold in literature. Among them, those applicable to basaltic rocks are reviewed.

Deere and Miller (1966) and Beverly et al. (1979, in Xu, 1990) suggested identical exponential forms with different coefficients (Eq. 5.2a and Eq. 5.2b, respectively):

$$\sigma_{\mathrm{UCS}} = 9.97 \cdot e^{(0.02 \cdot R_{\mathrm{L}} \cdot \rho)} \tag{5.2a}$$

$$\sigma_{\mathrm{UCS}} = 12.74 \cdot e^{(0.02 \cdot R_{\mathrm{L}} \cdot \rho)} \tag{5.2b}$$

Eq. 5.2a is valid for R_L = 23–59, while any range constraint is specified for Eq. 5.2b

Aufmuth (1973) established a power-law correlation successfully verified for 25 different lithologies:

$$\sigma_{\mathrm{UCS}} = 0.33 \cdot (R_{\mathrm{L}} \cdot \rho)^{1.35} \tag{5.3}$$

Eq. 5.3 is valid for R_L in 10–54 range.

Barton & Choubey (1977, in Gratchev, 2019) proposed a logarithmic relationship using either R_N (Eq. 5.4a) or R_L (Eq. 5.4b), requiring the discard of outliers deviating >7 units from the mean:

$$\log_{10}(\sigma_{ci}) = 0.00088 \cdot \gamma \cdot R_N + 1.01 \tag{5.4a}$$

$$\log_{10}(\sigma_{ci}) = 0.00088 \cdot \gamma \cdot R_L + 1.01 \tag{5.4b}$$

where γ stands for dry unit weight of the rock.

Kahrman (1996, in Yılmaz and Sendır, 2002) provided a versatile correlation for 10 geologies where material density (ρ) is included in the formulation:

$$\sigma_{\mathrm{UCS}} = 0.00045 \cdot (R_{\mathrm{N}} \cdot \rho)^{2.46} \tag{5.5}$$

Yaşar and Erdoğan (2004) derived a free density expression between R_L and *UCS*, with a validity range for R_L of 45–55:

$$\sigma_{\mathrm{UCS}} = 0.0000004 \cdot R_{\mathrm{L}}^{4.29} \tag{5.6}$$

Aydin and Basu (2005) offered additional suggestions for estimating *UCS* via the SH, emphasising its sensitivity in fresh crystalline igneous rocks to microcrack presence and orientation, as failure and deformation in strongly banded materials occur through the coalescence of pre-existing and load-induced microcracks.

ISMR Orange Book (Culshaw, 2015) suggested *N–type* hammers to estimate the *UCS* due to reduced sensitivity to surface irregularities. Since *UCS* depends on microstructural variability, full statistical analysis (mean, mode, range) is advised without discarding readings. Two recommended expressions involving R_L are:

$$\text{UCS} = 1.6 \cdot 10^{-4} \cdot R_L^{3.47} \tag{5.7a}$$

$$\text{UCS} = 1.45 \cdot e^{(0.07 \cdot R_L)} \tag{5.7b}$$

5.3 Field mapping campaign results

Of the 10 identified outcrops, 7 were studied during the campaign, while the remaining 3—Group 2 in Sandoy, refer to Fig. 5.3—could not be examined due to meteorological constraints. No more than 2 geotechnical units were present in each outcrop. Overall, 16 mapping sheets were compiled for outcrops of the *Enni Formation*, and 4 for those of the *Malinstindur Formation*, resulting in 20 estimated *Q*- and *GSI* values or value ranges. Stereonets were plotted for 6 outcrops, with projections made for each geotechnical unit within these outcrops, yielding a total of 7 projections. Schmidt Hammer measurements were only possible at *Streymoy 1*.

5.3.1 Rock mass quality assessment

Enni lava cores

The analysed lava core units belonging to the *Enni Formation* exhibit variable textures and compositions. They are distinguished across the two outcrops in Streymoy (Tab. 5.2) and the three in Sandoy (Tab. 5.3). In outcrop *Streymoy 2*, a distinction is made between the upper lava core (geotechnical Unit 1) and the lower flow top (Unit 2, see Fig. 5.11); only the former is discussed in this section, while the latter is later addressed separately.

In *Streymoy 2*, coarse-grained porphyritic basalt is characteristic of the massive, fresh rock units, while *Streymoy 1* and *Sandoy 3* presents both aphyric and fine-grained porphyritic texture. *Sandoy 1* and *Sandoy 2* are dominated by aphyric basalts. Colour variations reflect both lithological and weathering differences, ranging from blackish-grey (*Streymoy 1*) to pale grey (*Sandoy 2*) in fresher exposures, and shifting to greyish- or reddish-brown in more altered zones (*Streymoy 1* and *Sandoy 3*, respectively).

Weathering intensity ranges from minimal alteration in fresh cores to discolouration along fractures and moderate disintegration, occurring only in isolated, more exposed or eroded sections. Limited weathering is present in *Sandoy 2* and the upper flow unit of *Streymoy 2*, while fracture-related alteration appears in *Streymoy 1*. Extensive surface discolouration characterises *Sandoy 1* and *Sandoy 3*.



Figure 5.11: Geotechnical units characterising the Streymoy 2 outcrop (section 3 in the image), namely the lava flow core (Unit 1) and the lava flow top (Unit 2).

Table 5.2: Basaltic core characterisation at outcrops Streymoy 1 and Streymoy 2.

Property	***Streymoy 1***	***Streymoy 2***
1. Identification	Aphyric to fine-grained porphyritic basalt; colouration from blackish-grey for fresh rock to greyish-brown in weathered areas.	Porphyritic basalt; pale to medium gray.
2. Weathering	Fresh overall; discolouration along fractures.	Massive unit relatively fresh.
3. Discontinuities	One to two main joint sets; crack density increases near top.	One main joint set; additional cracks from blasting; higher fracture density at the base, in contact with the underlying flow top unit.
4. Joint fillings	No major to slightly altered joints with infillings observed	Mostly absent (Section 1) to silty clay coatings (Section 3).
5. Seepage	Rainwater infiltration only; seepage mainly via fractures (secondary permeability).	No relevant seepage observed in the upper basalt unit.

Jointing patterns show variability in orientation, density, and genesis. Two main joint sets are present in most of the *Streymoy 1* outcrop surface, often increasing in density toward the identified flows tops or bases due to erosion or flow boundaries. A single dominant joint set occurs in the upper basalt flow of *Streymoy 2* (excluding its basal flow top unit), in *Sandoy 1* and *Sandoy 3*, accompanied by random fractures, likely induced by blasting (*Streymoy 2*, *Sandoy 3*) and river erosion or weathering (*Sandoy 1*). Discontinuities in *Sandoy 2* are instead widely spaced and show minimal alignment with altered zones.

Table 5.3: Basaltic core characterisation at outcrops Sandoy 1, Sandoy 2, and Sandoy 3.

Property	***Sandoy 1***	***Sandoy 2***	***Sandoy 3***
1. Identification	Aphyric basalt; pale to dark grey.	Fine-grained porphyritic basalt; pale grey to grey.	Aphyric to fine-grained porphyritic basalt; pale grey to reddish-brown.
2. Weathering	Discoloured; moderate weathering due to stream influence.	Fresh rock, minimal weathering.	Moderate to strong discolouration widespread throughout the whole outcrop.
3. Discontinuities	One main joint set; river-induced random joints.	Widely spaced joints, one to two main sets.	One main horizontal joint set; many local blast-induced random cracks
4. Joint fillings	Finely disintegrated rock particles; soil and clay fractions deposited near the stream joints.	No major infillings observed, only few disintegrated rock fillings within cracks unaligned with the main joint sets.	Large presence of crushed rock fragments.
5. Seepage	No major inflow aside from the stream.	No seepage observed.	Rainwater seepage along fractures in Sections 1, 2 and 4.

Joint fillings are mostly absent or consisting of clay-free disintegrated rock in most of the exposed rock masses (*Streymoy 1*, *Streymoy 2*, *Sandoy 2*, and *Sandoy 3*). However, infillings of soil and clay are common in joints that have formed or been widened by surface processes (*Sandoy 1* and Section 3 of *Streymoy 2*).

Water inflow is overall minimal and mainly controlled by secondary permeability along fractures. Rainfall infiltration occurs at almost all outcrops but is limited in volume. Seepage rates are generally low, but particularly pronounced in *Streymoy 1* and *Sandoy 3*. Limited inflow can also be observed in *Sandoy 1* due to the proximity to a stream, but this must be discarded from actual rock mass seepage.

Malinstindur lava cores

The exposed lava core basalts of the *Malinstindur Formation* are found within the two outcrops in Suðuroy (Tab. 5.4). The basalts exhibit textures ranging from aphyric to coarsely porphyritic, and colouration varying from light to dark bluish-grey in fresh samples (*Suduroy 1*) to greyish-, purplish-brown, and pale brownish-orange in weathered states (*Suduroy 2*).

Fresh, unaltered basalt dominates the intact exposures in *Suduroy 1*, whereas moderate to advanced weathering characterises the river-influenced outcrop of *Suduroy 2*, especially near the stream where crack density intensifies.



(a) (b)

Figure 5.12: Comparison between a tight, stiff joint in the Suduroy 1 outcrop (a) and a widely spaced, disintegrated rock-filled joint in Suduroy 2 (b).

Regarding the discontinuities, widely spaced and highly stiff joints define the more intact rock mass, typically arranged in one or at most two main sets with minimal structural degradation (*Suduroy 1*). In contrast, a blocky to very blocky configuration with two to three joint sets

appears in more eroded conditions (*Suduroy 2*), where fracturing is more pervasive.

Joint infilling is almost absent in unaltered rock (Fig. 5.12a), with only sporadic occurrences of quartz or calcite depositions (*Suduroy 1*). In the riverbed erosional context, larger joint openings frequently contain disintegrated material and clay deposited by surface water (*Suduroy 2*, refer to Fig. 5.12b).

No groundwater seepage is recorded at either site. However, moisture from surface runoff is present in the river-adjacent sections of *Suduroy 2*, while dry conditions persist in the undisturbed *Suduroy 1* outcrop.

Table 5.4: Basaltic core characterisation at outcrops *Suduroy 1* and *Suduroy 2*.

Property	***Suduroy 1***	***Suduroy 2***
1. Identification	Fine- to large-grained porphyritic basalt; light to dark bluish-grey colouration.	Aphyric basalt; greyish- or purplish-brown to pale brownish-orange.
2. Weathering	Mostly fresh; minimal weathering	Fully discoloured; moderate to advanced weathering especially near the riverbed
3. Discontinuities	Widely spaced; 1–2 main joint sets; highly stiff.	Very blocky; 2–3 joint sets; increased fracturing near the river stream.
4. Joint fillings	Minimal; occasional quartz and calcite depositions.	Disintegrated rock and river-deposited clay.
5. Seepage	No groundwater observed	No persistent seepage; moisture influence from river proximity.

Volcaniclastic sandstone

At the *Sandoy 2* outcrop, the transition from aphyric basalt (Unit 1) to light brownish-orange volcaniclastic sandstone (Unit 2) is sudden (Fig. 5.13), leading to a marked decline in rock mass quality from the first to the second unit.

The surface layer appears moderately disintegrated (Fig. 5.14a) while deeper sections are discoloured but less fractured (Fig. 5.14b). Nevertheless, fracture density increases substantially in the sandstone with respect to the overlying basalt.

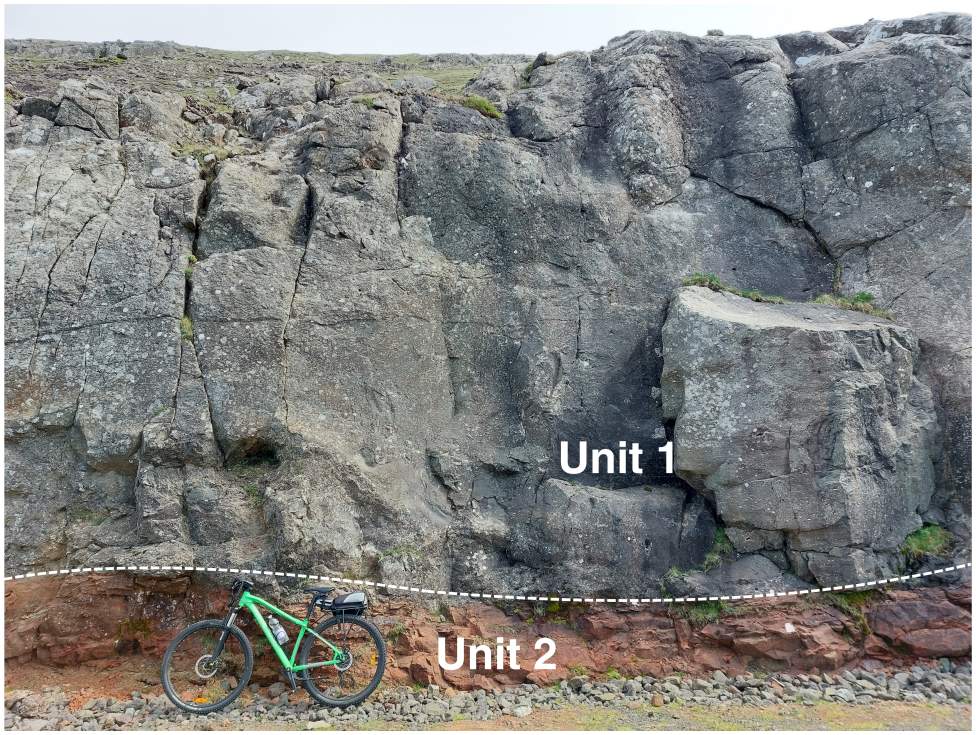


Figure 5.13: Geotechnical units characterising the Sandoy 2 outcrop (section 2 in the image), namely the lava flow core (Unit 1) and the volcaniclastic sandstone (Unit 2).



(a) (b)

Figure 5.14: Different degrees of weathering along the analysed sandstone unit, with disintegrated rock along jointing paths (a) and moderately fresh to discoloured conditions with tight joints (b).

Despite a superficial sugar-cube texture likely caused by blasting, the intact portion of the unit displays two main joint sets. Within these smooth, undulating joints, minor alterations are present, consisting of clay-free, disintegrated rock fillings.

No seepage has been observed throughout the unit.

Table 5.5: Volcaniclastic sandstone characterisation at outcrop Sandoy 2.

Property	***Sandoy 2***
1. Identification	Volcaniclastic sandstone; light brownish-orange colouration.
2. Weathering	Moderately disintegrated surface; deeper sections are highly discoloured but less fractured.
3. Discontinuities	Two main joint sets present in the intact portions of the unit; smooth and undulating surfaces
4. Joint Fillings	Minor alteration with disintegrated rock fillings; no clay present
5. Seepage	No groundwater or seepage observed throughout the unit

Weathered flow top

At the *Streymoy 2* outcrop base (Tab. 5.6) a pale greyish-red basaltic sheet flow top is exposed (Fig. 5.11). Despite significant weathering, the unit, characterised by porphyritic basalt, preserves internal features such as vesicles, phenocrysts, and a homogeneous matrix with consistent characteristics throughout the whole outcrop.

The surface is visibly discoloured and moderately disintegrated, resulting in a rock that is friable and can be carved with modest effort by the knife.

A single dominant joint set is observed, accompanied by random cracking. Joint fillings consist of very fine, clay-free disintegrated particles and surface soil, likely accumulated over decades of the roadcut exposure.

Seepage is observed, particularly in Section 1, and appears to result from both primary rock permeability and secondary permeability through joints—contrary to previously studied intact basalt cores.

Structurally, the flow top displays a steep, undulating profile, with variation in thickness of few meters (clearly visible in Fig. 5.11). These local irregularities, atypical for the low dip Faroese basalt flows, have spatial relevance for underground excavation design due to their potential to induce mechanical anisotropy at the tunnel scale. The basal 50–100 cm of the overlying

basalt flow in the outcrop appears to be affected by this anisotropy, showing increased crack density caused by the local undulations. This phenomenon is also commonly observed in the flow bases described in the core logs from boreholes drilled by Jarðfeingi (Petersen et al., 2022).

Table 5.6: Basaltic flow top characterisation at outcrop *Streymoy 2.*

Property	***Streymoy 2***
1. Identification	Porphyritic basalt with vesicles and phenocrysts; pale greyish-red uniform colouration; homogeneous matrix preserved despite weathering.
2. Weathering	Visibly discoloured and moderately disintegrated surface, where the rock is friable.
3. Discontinuities	One dominant joint set with random secondary cracking; increased crack density in the basal 50–100 cm of the overlying basalt flow due to structural undulations.
4. Joint fillings	Very fine, clay-free disintegrated material and accumulated surface soil.
5. Seepage	Seepage present in Section 1 from both primary permeability and discontinuity-controlled secondary flow paths.

Discussion on resulting Q and GSI values

The examined outcrops has demonstrated generally favourable conditions for blasting operations, in alignment with the geological characteristics commonly observed in the Faroe Islands. The *Q*- and *GSI* scores for each outcrop section are resumed in Appendix C.2.
Although an imbalance exists in the number of analysed outcrops from the *Enni* and *Malinstindur Formations*—five and two, respectively—several insights emerge from the data:

1. An apparent contradictory trend is observed between the *Q*- and *GSI* scores: while the *Enni* basalts display the lowest *GSI* values, the minimum *Q*-values are found within the *Malinstindur* basalts, at *Suduroy 2.* This discrepancy reflects the differing parameters in *Q* versus *GSI* classification methodologies, emphasising their sensitivity to distinct rock mass characteristics. Visual assessments of the natural and unaltered portions of the blasted

outcrops suggest that in general the Middle Basalt Formation holds superior rock mass quality compared to the Upper Basalt Formation.

2. Rock mass properties are characterised by considerable spatial variability, even at scales comparable to those of cavern excavations. As such, caution is advised when deriving averaged properties for use in continuum-based numerical models.

3. The presence of abrupt lithological transitions between sandstone or flow-top layers and overlying basalts suggests possible poor mechanical jointing and a heightened risk of instability and collapses during excavation through such heterogeneous zones.

4. The observed reduction in Q-values across many outcrops is largely influenced by the Strength Reduction Factor (SRF) while describing near-surface exposures. A transition from $SRF = 2.5$ (low stress, near surface, open joints) to $SRF = 1.0$ (moderate depth, favourable stress conditions) is expected in deeper geotechnical contexts.

5. Surface water inflows observed in outcrops are not necessarily indicative of underground conditions, as they are primarily driven by rainfall and surface run-off. Therefore, even after acknowledging that, despite the excavation's subsea location, groundwater flow primarily comes from freshwater contributions (see Chapter 4, Section 4.3), a larger inflow can still be expected at the caverns depth.

Table 5.7: Selected Q- (a) and GSI (b) value ranges and averages (in brackets) to characterise the Enni and Malinstindur stratigraphic units of lava core, lava flow top and volcaniclastic sandstone.

Enni Formation			
Assessment method	***Lava core***	***Lava flow top***	***Sandstone***
Q-System	8–56 (–)	2.33–8 (–)	6.25–6.85 (–)
GSI	50–75 (60)	(37)	37–44 (40)

(a)

Malinstindur Formation			
Assessment method	***Lava core***	***Lava flow top***	***Sandstone***
Q-System	7.5–48 (–)	—	—
GSI	65–85 (70)	—	—

(b)

The selection of representative Q- and GSI ranges has been guided by (i) the geological

proximity and spatial relation to the target excavation zone, and (ii) deviations or alignments from typical values observed across multiple surveyed outcrops. The final selected ranges are presented in Tab. 5.7.

Rock mass quality – Conclusions

Significant spatial variability in rock mass quality is observed across the investigated outcrops. Fresh basalt cores (e.g., *Suduroy 1*, *Sandoy 2*) generally exhibit favourable geotechnical conditions, whereas more weathered units (e.g., *Suduroy 2*, *Streymoy 1*, and *Sandoy 3*) display more pervasive cracking and surface degradation. Flow top and volcaniclastic sandstone units show reduced integrity due to higher degrees of weathering and increased jointing respectively, posing potential stability risks during excavation.

Although the *Enni Formation* generally presents lower *GSI* values for lava cores, the lowest *Q*-values are recorded in the *Malinstindur Formation* (*Suduroy 2*), reflecting methodological differences between the classification systems. Surface seepage is primarily controlled by rainfall and runoff and should not be regarded as representative of deeper conditions. At greater depths, higher *Q*-values are expected due to more favourable stress regimes in the lithostratigraphy. Overall, the pronounced geological heterogeneity observed at tunnel and cavern excavation scales highlights the need for caution when applying averaged parameters in continuum-based numerical models.

5.3.2 Discontinuities orientation

At least ten Clino® measurements were taken and plotted as Schmidt projection for each outcrop from the FM campaign, excluding *Streymoy 2*. Four stereonets correspond to the *Enni Formation* and two to the *Malinstindur Formation* lava cores, and one to the interlava sandstone unit. No data were collected for the weathered flow top basalt unit. Mean dip and strike from the stereonets were compared with literature values to assess alignment and local variability.

The Upper Formation lava core stereonets include *Streymoy 1* (Fig. 5.15a) and *Sandoy 1–3* (Fig. 5.15b–d). Dip angles are generally consistent with the archipelago's sub-horizontal bedding (Tab. 5.8), except for *Sandoy 2*, while strike directions vary and show no preferred orientation—likely due to blasting effects and possibly instrument limitations at low dips. This is clear in *Streymoy 1*, where individual sections differ but combined results are reasonable. *Sandoy 3* best matches the dip direction reported in the literature. All projections show one

dominant joint set, with local variations in *Streymoy 1* and *Sandoy 3*.

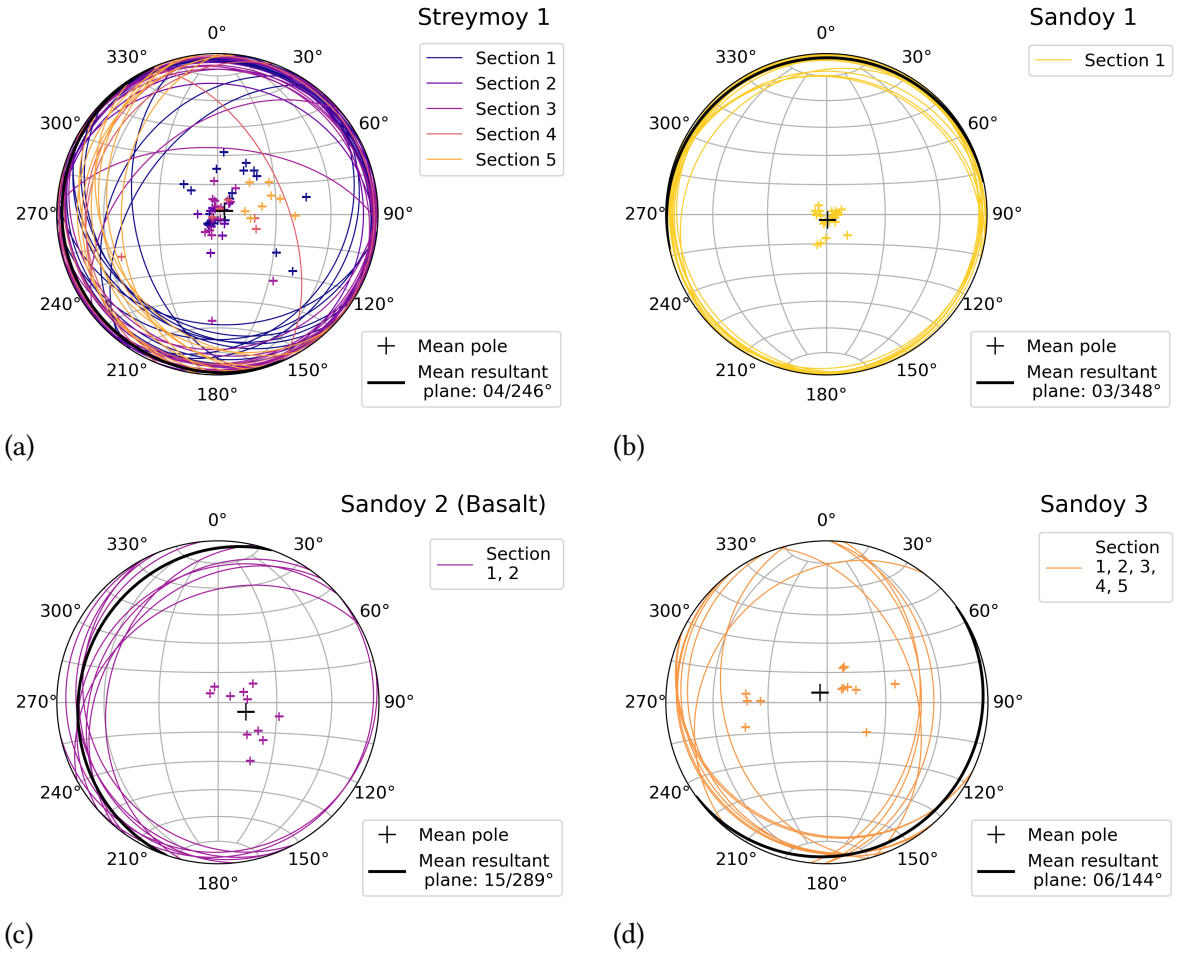


Figure 5.15: Stereonets for Enni lava core units of outcrops Streymoy 1 (a), Sandoy 1 (b), Sandoy 2 (c), and Sandoy 3 (d).

Table 5.8: Stereonet results for Enni basaltic cores showing mean resultant dip directions and dip angles compared to literature data.

Enni Formation	
Outcrop	**Bedding plane**
Streymoy 1	04° / 246°
Sandoy 1	03° / 348°
Sandoy 2	15° / 289°
Sandoy 3	06° / 144°
Literature	1.7°–2.9° / E (~90°), SE (~135°) (Passey and Jolley, 2009) 1.0°–3.0° / — (Walker et al., 2010)

The single stereonet associated with the volcaniclastic sandstone (Fig. 5.16) is considered only partially representative due to the limited exposed thickness in the outcrop. Although a single unit may not capture the regional structural behaviour, a similar strike is observed with the overlying basalt but a slightly lower dip, suggesting overall fair structural continuity between the two lithologies. Other interlava sedimentary layers (e.g., *Sandur Beds*, *Sneis Formation*, *C-Reflector*) may exhibit continuity with the adjacent basalts as well.

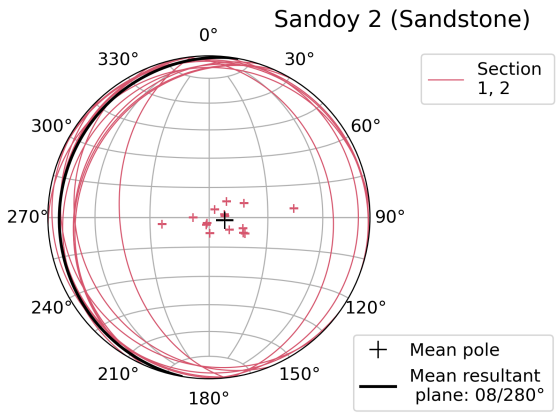
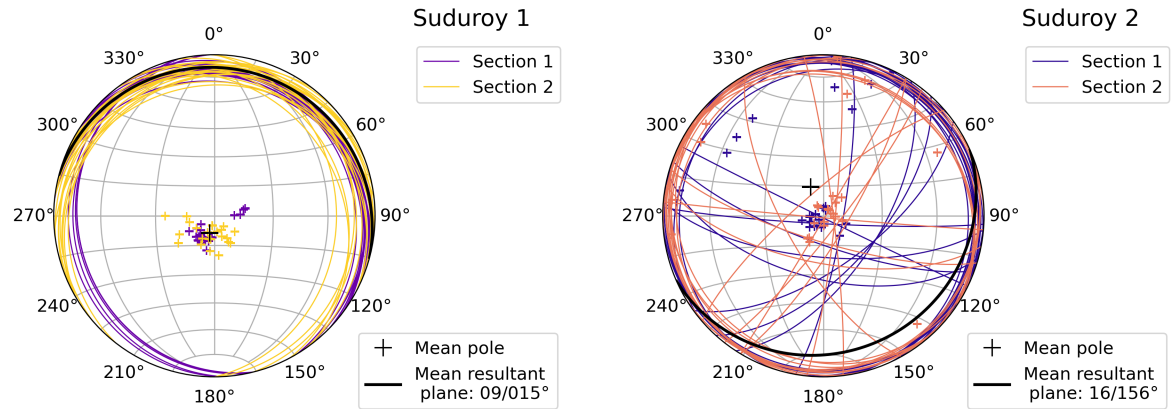


Figure 5.16: Stereonet for Enni sandstone unit of outcrop Sandoy 2.

The two Middle Formation lava core outcrops show marked differences. *Suduroy 1* (Fig. 5.17a) dips NNE with dip angles almost trice those in the literature but remains a reliable reference for local bedding due to its intact nature. *Suduroy 2* (Fig. 5.17b), instead, shows large deviations in mean resultant dip and strike from literature, given the contribution of the 2 (Section 2) to 3 (Section 1) main joint sets. These discrepancies reduce when focusing on the dominant pole cluster, located in the centre of the stereonet.



(a) (b)

Figure 5.17: Stereonets for Malinstindur lava core units of outcrops Suduroy 1 (a) and Suduroy 2 (b).

Table 5.9: Stereonet results for Malinstindur lava core units showing mean resultant dip directions and dip angles compared to literature data.

Malinstindur Formation	
Outcrop	**Bedding plane**
Suduroy 1	09° / 015°
Suduroy 2	16° / 156°
Literature	2.2°–3.9° / NE (~45°), SE (~135°) (Passey and Jolley, 2009) 3.0°–4.0° / — (Walker et al., 2010)

Discontinuities orientation – Conclusions

Stereonet analyses of the *Enni Formation* lave core units confirm generally sub-horizontal bedding and dip angles reasonably consistent with regional trends, with minor deviations attributed to blasting effects or measurement limitations. Dominant joint sets were consistently identified, though local structural complexity is evident especially in *Streymoy 1* and *Sandoy 3*. Although limited, data from volcaniclastic sandstone indicate structural continuity with overlying basalt, supporting conformable interlava sediment interpretation. In the *Malinstindur Formation* lava core units, *Suduroy 1* shows reliable local bedding orientation despite steeper dips compared to literature, while *Suduroy 2* exhibits significant scatter from multiple joint sets, partially resolved while focusing on dominant clusters.

5.3.3 Longitudinal section

The combination of desk study and field mapping contributed to the development of the longitudinal section covering the entire 24 km tunnel (Fig. 5.19), from the northern portal near Skarvanes (Sandoy) to the southern exit near Sandvík (Suðuroy)—left to right along the section. The tunnel initially follows a curvilinear alignment, then transitions into a nearly straight path beneath the sea strait until its exit in Suðuroy (Fig. 5.18). The longitudinal section elevation spans from +400 m a.s.l. to -400 m a.s.l., a sufficient range given the tunnel's maximum depth of approximately -150 m a.s.l.

All three main basalt formations—*Beininsvørð*, *Malinstindur*, and *Enni*—appear within the section. Interlava lithologies (red) and volcanic conglomerates (blue) are shown with exaggerated thickness to allow their visibility. Three horizons (*A*-, *B*-, *Sneis Formation*) are marked; *A*- and *B-Horizons* are colour-coded due to their incompletely logged composition.

From the northern portal, the tunnel descends ~5° over the first 3–3.5 km (Holter et al., 2021), cutting through the basalt-interlava sequences of the Upper Basalt Formation. Key units include the reddish sandstone observed at Oucrop *Sandoy 2*, a 5–6 m brecciated flow top at km 2, and the *Sandur Beds*, in contact with the tunnel for ~1 km—mechanically weak and with possible large water inflows.

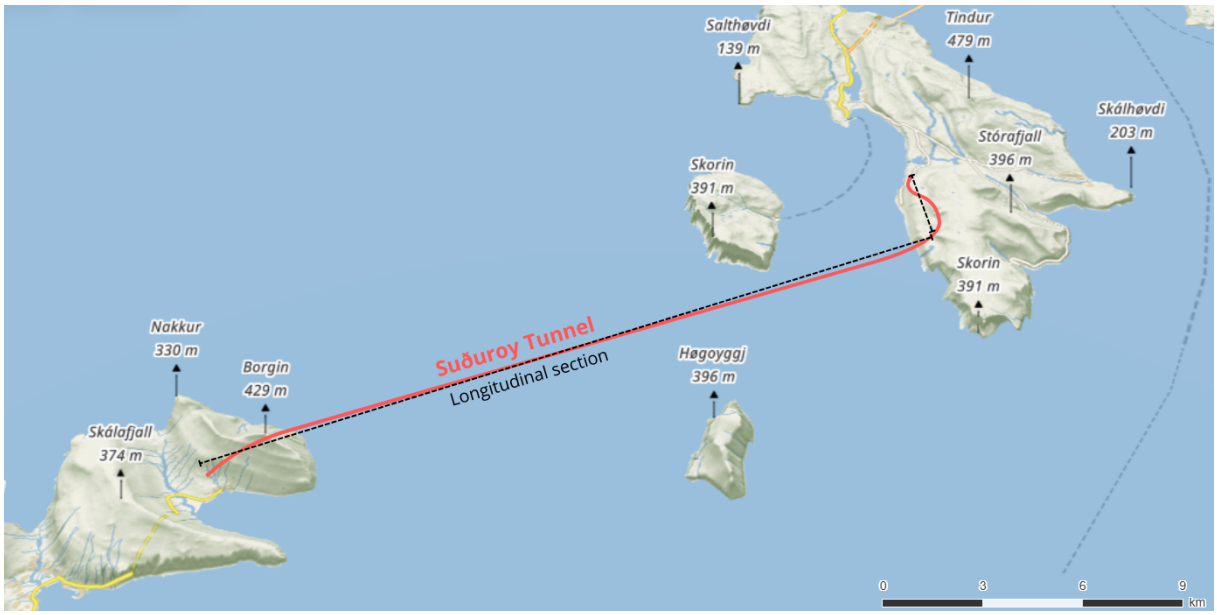


Figure 5.18: Longitudinal cross section w.r.t. the Suðuroy Tunnel alignment. Background map from https://mapy.com.

Around km 4, the tunnel flattens (0.5°–1.0° gradient, Holter et al., 2021) maintaining a regular overburden. It remains in the *Enni Formation* for some more kilometres, with sparse interlava layers. Cavern 1 is planned here. Between km 6–7, a ~20–30 m seabed dune—confirmed as sediment by seismic surveys data (Petersen, 2023)—is encountered.

The boundary between the Upper and Middle Basalt occurs near km 10–11. In the vicinity of Sandoy, the *Sneis Formation* appears as a <1 m thick sandstone layer (Passey and Jolley, 2009). An underlying brecciated basalt unit may be intersected by the tunnel, although it has only been identified in the *Søltuvík*-2 and *Skúvoy*-1 boreholes, so its continuity remains uncertain.

After entering the *Malinstindur Formation*, discontinuities include the ~1.5 m *C-Reflector* volcaniclastic sandstone and a ~2.0 m sand-claystone transition in *Sandvík*-1, which may correspond to the *B-Horizon* (Hypothesis 1, refer to Tab. 7.2, Chapter 3) described by Rasmussen and Noe-Nygaard (1970). Alternatively, the *B-Horizon* might be located closer to the *Enni Formation* (Hypothesis 2, refer to Tab. 7.2, Chapter 3), within the aforementioned undrilled stratigraphy

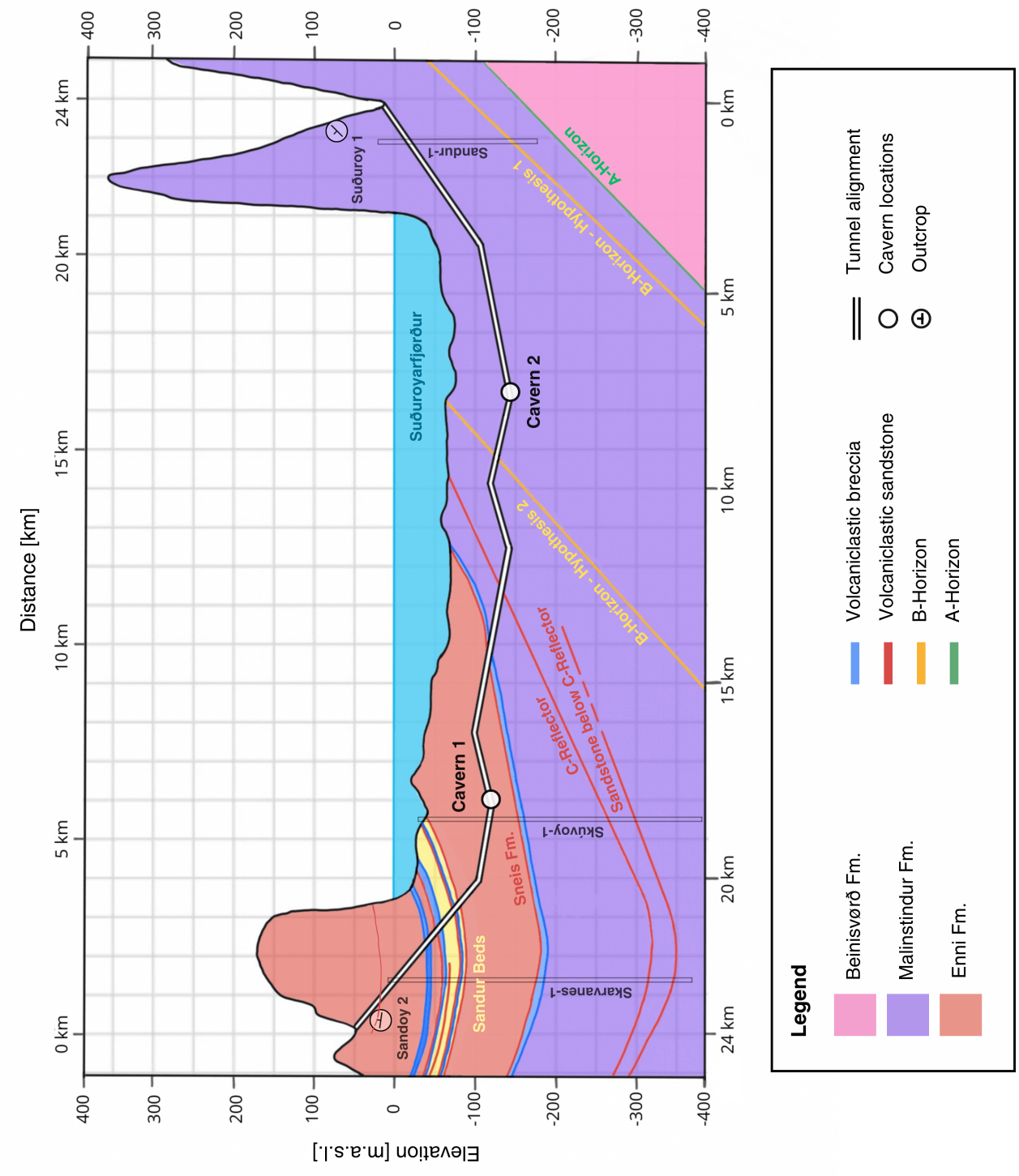


Figure 5.19: Longitudinal cross section of the Sandoy-Suðuroy sea strait, with the tunnel alignment and the two cavern locations specified, alongside with the main units highlighted, namely Basalt Formations, sedimentary and brecciated main units and horizons.

(Fig. 3.4, Chapter 3), potentially corresponding to what seismic data have identified as the *B-Reflector* (Fig. 3.6, Fig. 3.5). This tunnel segment—where Cavern 2 is planned—is flat (1°–1.5°) and reaches a minimal overburden of approximately 50 m.

In the final 4 km, the tunnel rises at 4° (Holter et al., 2021) from −100 m a.s.l. to the surface, exiting in the Sandvík Valley, Suðuroy, maintaining ≥150 m from the *A-Horizon*, therefore avoiding the Lower Basalt Formation. The stratigraphy is overall geologically continuous with no active faults identified in this and previous studies; unit dips are gentle, preserving depositional context between lava flows.

5.3.4 Structural data

Fracture density along the studied outcrops is illustrated using rose diagrams with 10° bins. These diagrams require large datasets to be meaningful; therefore, a single diagram was created for each island by aggregating data from all outcrops. However, data limitations still preclude robust statistical analysis.

Streymoy's rose diagram (Fig. 5.20), based exclusively on *Stremoy 1* outcrop dataset, is skewed westward, with only 5 of 36 bins populated. This pattern partially overlaps with Ziska (2012)—who instead incorporated data from both Streymoy and Eysturoy in his rose diagram—but the correlation is insufficient.

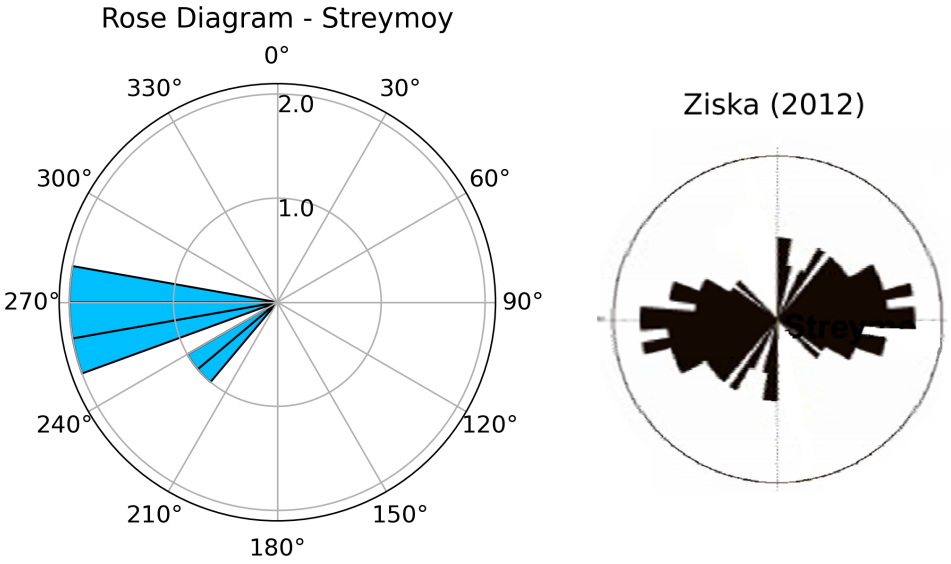


Figure 5.20: Rose diagram for the island of Streymoy, based on data collected in this project (left) in comparison with the work of Ziska (2012) in Streymoy and Eysturoy (right). Adapted from Ziska (2012).

The Sandoy diagram (Fig. 5.21) suggests a dominant E and secondary SW trend. As no previous rose diagrams exist for Sandoy, its inclusion represents one of the secondary aims of this study. Despite limited data, both Sandoy and Streymoy diagrams partially support the E/W fractures' trend identified by Ziska (2012) for the *Enni Formation* basalt flows.

The Suðuroy rosette (Fig. 5.22), arguably the most comprehensive of this study, shows uneven distribution with pronounced SW (partially mirrored) and SE clusters. These fairly correspond to the Suðuroy fracture trends in the *Malinstindur Formation* described by Ziska (2012), where NW–SE is the dominant trend and NE–SW and N–S are secondary ones.

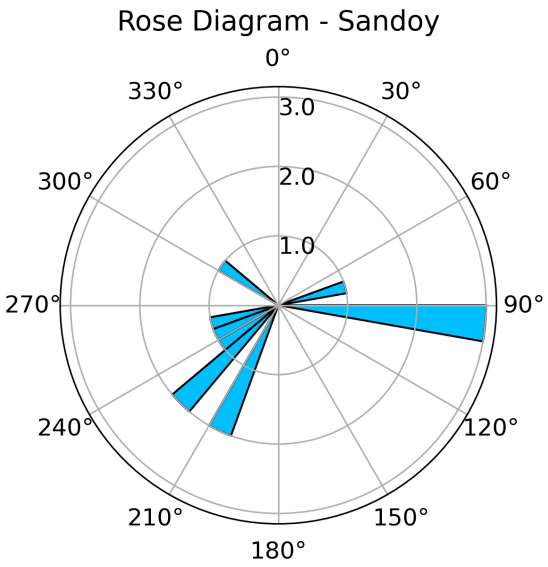


Figure 5.21: Rose diagram for the island of Sandoy, based on data collected in this project.

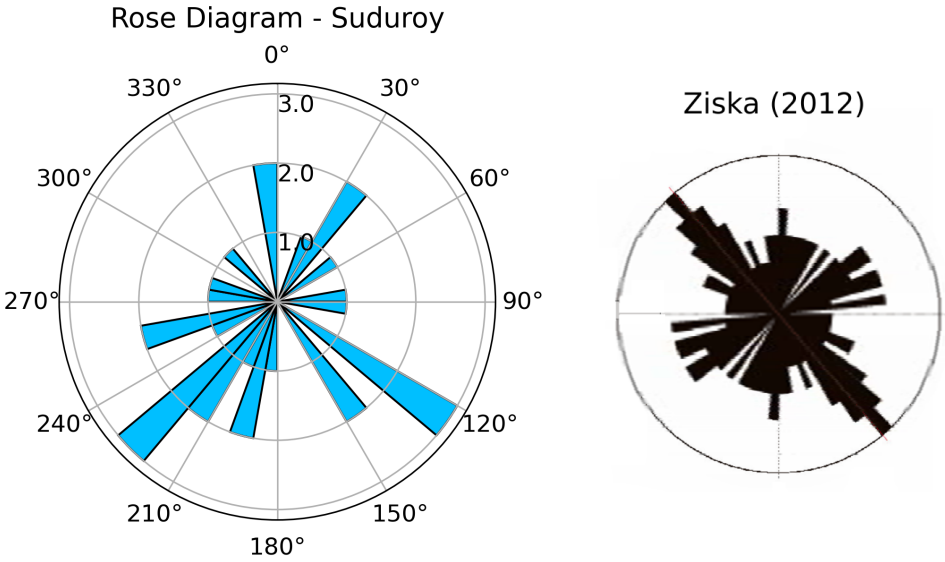


Figure 5.22: Rose diagram for the island of Suðuroy, based on data collected in this project (left) in comparison with the work of Ziska (2012) in the same island (right). Adapted from Ziska (2012).

Structural data – Conclusions

Despite the limited statistical resolution, the three plotted rose diagrams are somewhat consistent with regional fracture trends identified by Ziska (2012)—E–W for Enni basalts in Sandoy and Streymoy, SW–NE for Suðuroy—using a much larger dataset. However, for estimating stress orientations at the cavern sites, it is still preferable to rely on the rose diagrams from Jarðfeingi (Petersen et al., 2022), as they offer greater local accuracy by covering 50 m of stratigraphy each.

5.3.5 Rock mass strength



Figure 5.23: Proceq® OS8000 N-type hammer, the model used during the site investigation. Retrieved from Screening Eagle (n.d.).

Schmidt Hammer (SH) tests were conducted exclusively at the *Streymoy 1* outcrop using a Proceq® OS8000 N-type hammer (Fig. 5.23). Measurement reliability is limited by the blasted origin and prolonged weathered surface of the outcrop. Hammer sound during testing was therefore used as a first qualitative indicator of subsurface areas integrity to discard or validate each single measurement.

Tests focused on basaltic flows, with >50 measurements per section. Mean, median, and mode of the corrected R_N values were reported for each outcrop section (Tab. 5.10) per ISRM guidelines (Culshaw, 2015).

Using the previously selected eight correlations (see Section 5.2.4), *UCS* estimates were derived per outcrop section, including R_N–R_L conversions through Eq. 5.1 when required, although some loss of accuracy is expected due to the measurement range of this project falling below the range of almost perfect correlation reported by Aydin and Basu (2005). Outcrop averaged values are displayed in Fig. 5.24.

Table 5.10: Schmidt Hammer rebound number (R_N) mean, mode and median along the five Streymoy 1 outcrop sections.

# Section	R_N measurements		
	Mean	**Mode**	**Median**
1-1	33	18	34
1-2	30	26	31
1-3	29	29	29
1-4	27	12	25
1-5	26	24	26

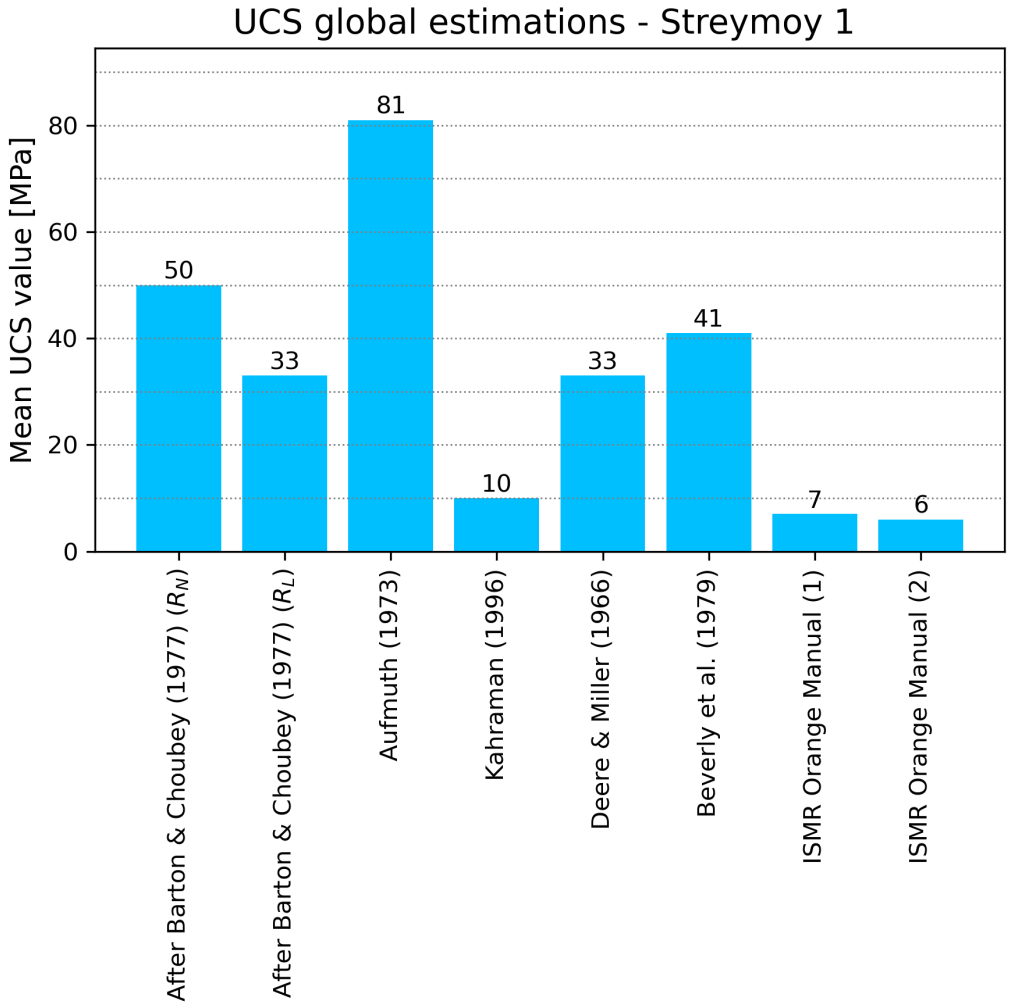


Figure 5.24: UCS values estimated from Schmidt Hammer measurements on the Streymoy 1 outcrop using the selected correlations (results for the entire outcrop).

Results show wide *UCS* variability. Aufmuth (1973) produced the most consistent *UCS* estimates relative to standard ranges for intact basalts—reported by Johnson and DeGraff (1988), in Schön (2015), illustrated in Fig. 5.25. However, SH measurements are considered insufficient for reliable *UCS* input values in the numerical model: the influence of blasting on rock integrity appears evident, and only the *Enni Formation* basalts unit was assessed, with no data collected from the *Malinstindur Formation*.

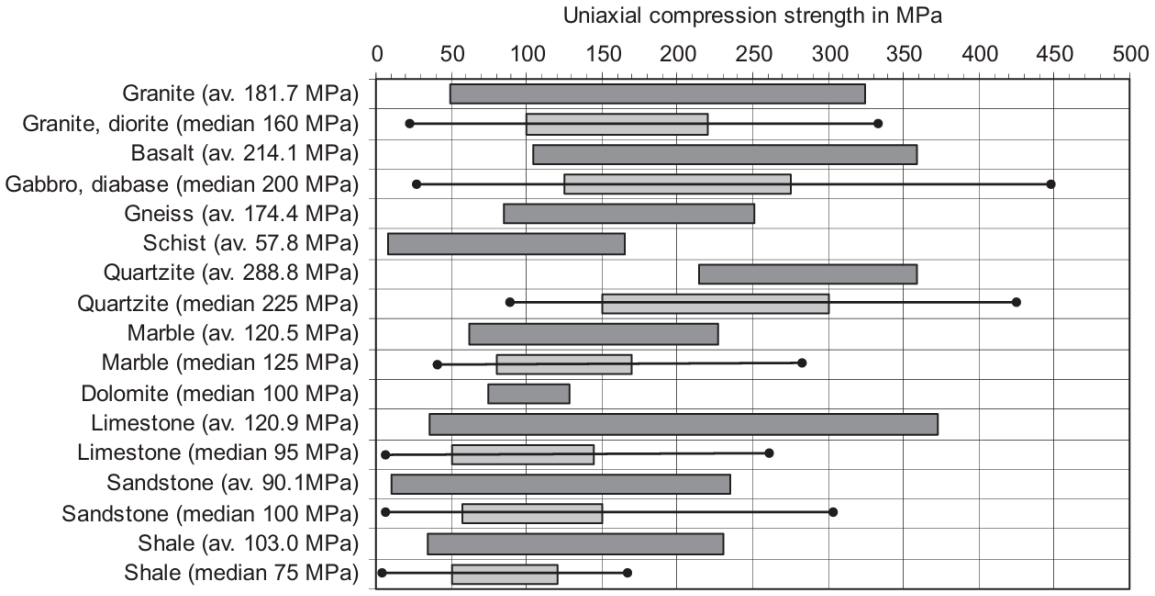


Figure 5.25: Typical average values and strength ranges in uniaxial compression for common rock types. The dark grey boxes illustrate the ranges as reported by Johnson and DeGraff (1988). Adapted from Schön (2015).

Due to the lack of other site-specific data, *UCS* estimates are obtained from prior lab test results contained in the SINTEF database from two previous Faroese projects (Tab. 5.11)—anonymised as Project 1 and 2. Project 1 samples are from the *Malinstindur Formation*, and Project 2 from the *Enni Formation*. Both sets of samples exhibit significantly higher *UCS* values compared to in-situ estimates, which is typical when testing under controlled laboratory conditions.

Table 5.11: UCS values from SINTEF laboratory tests of Faroe Islands basalt samples.

# Project	Basalt formation	UCS
SINTEF Project 1	*Malinstindur Fm.*	197.9 MPa
SINTEF Project 1	*Malinstindur Fm.*	188.0 MPa
SINTEF Project 2	*Enni Fm.*	139.7 MPa

Given the large disparity among in-situ and lab *UCS* estimates, a sensitivity analysis is finally proposed to assess model response over a broad value range. Three *UCS* levels—minimum, medium, and maximum—are defined for the Upper and Middle Formation lava cores.

For *Enni* basalts, the minimum *UCS* is from the SH correlation from Aufmuth (1973), the maximum from Project 2 (Tab. 5.11), and the medium is set as their average. This medium value also aligns with the lower bound of basalt *UCS* in literature (Fig. 5.25). For *Malinstindur*, only the maximum *UCS* can be evaluated from Project 1; minimum and medium values are based on expert judgment, supported by field observations at the *Suduroy 1* outcrop, which indicates a strong intact rock quality. According to this, the minimum *UCS* exceeds that of the *Enni Formation*, and the medium value is again the average. The selected *UCS* ranges for the two formations are grouped in Tab. 5.12.

Table 5.12: Selected UCS ranges defined by the 5^{th}, 50^{th} (mean), and 95^{th} percentiles for the numerical model inputs.

Basalt formation	**UCS range (average)**
Enni Fm.	80–130 (105)
Malinstindur Fm.	90–150 (120)

Rock mass strength – Conclusions

SH tests were conducted exclusively on the *Streymoy 1* outcrop within the *Enni Formation*, revealing substantial variability in the derived *UCS* values from the eight selected correlations. Among these, Aufmuth (1973) showed the best alignment with typical *UCS* ranges for intact basalt. However, due to limitations in data quality and coverage, as well as an R_N–R_L conversion falling outside the ideal value range, the *UCS* estimates based on SH tests were considered insufficient for direct use in numerical modelling. Instead, higher-strength values from previous SINTEF laboratory tests on geologically similar samples were used to supplement the site-specific data. To account for uncertainties in rock strength, a three-level *UCS* sensitivity scheme (minimum, medium, maximum) is adopted for both the *Enni* and *Malinstindur Formations*, with the latter ultimately proven to possess a higher *UCS* range.

5.3.6 Rock mass deformability

In addition to seismic log–derived estimates of Young's modulus (see Tab. 4.1, Chapter 4), empirical relationships linking rock mass properties to index parameters were used to approximate the deformation modulus. Besides *Q* and *GSI* values, some of these correlations also rely on the Rock Mass Rating (*RMR*), which can be directly derived from the *GSI*.

Several empirical approaches have been proposed to estimate the rock mass deformation modulus based on classification indices. Starting with the correlation to the *Q*-value, Barton (1995, 2006, in Vallejo and Ferrer, 2011) related the deformation modulus to the *Q* index, incorporating intact rock properties. Bieniawski (1978) established a correlation between the in situ modulus (E) and the *RMR*, applicable primarily to rock masses with $RMR > 50–55$. For lower-quality rock masses ($RMR < 50$), Serafim and Pereira (1983) proposed an alternative formula.

Hoek and Brown (1997) revised Serafim and Pereira's correlation by replacing the *RMR* with the *GSI* and incorporating the intact compressive strength. Further refinements by Hoek et al. (2002) and Hoek and Diederichs (2006) introduced the disturbance factor (D) to account for excavation-induced damage. Although these correlations are widely used, they have limited sensitivity and should be regarded as approximate average estimates of the deformation modulus (Vallejo and Ferrer, 2011).

The outcomes of these correlations are compared with those obtained from geophysical data interpretation (Tab. 5.13), the latter generally leading to significantly higher E moduli (see Tab. 4.1, Chapter 4). As a result, seismic log-derived values between the 5^{th} and 50^{th} percentiles are adopted for numerical modelling, as this range comprises most E_{min} values from empirical estimates for the basaltic lava core. In contrast, *GSI*- and *RMR*-based correlations for flow top and volcaniclastic sandstone tend to further underestimate E_{min}, even falling below the 5^{th} percentile of geophysical estimates, while the correlation provided by Barton (1995, 2006) fits much better within the aforementioned percentiles range.

Table 5.13: Rock mass deformability empirical relationships outcomes for Enni (a) and Malinstindur (b) geotechnical units.

	Correlation	***Lava core***		***Lava flow top***		***Sandstone***	
		E_{min}	E_{max}	E_{min}	E_{max}	E_{min}	E_{max}
Enni Fm.	Barton (1995, 2006)	20 GPa	39 GPa	13 GPa	20 GPa	15 GPa	16 GPa
	Hoek et al. (2002)	10 GPa	43 GPa	5 GPa	5 GPa	4 GPa	5 GPa
	Hoek & Diederichs (2006)	9 GPa	50 GPa	3 GPa	3 GPa	3 GPa	6 GPa
	Bienawski (1978)	10 GPa	60 GPa	–	–	–	–
	Serafim & Pereira (1983)	13 GPa	56 GPa	6 GPa	6 GPa	6 GPa	9 GPa
	Geophysics	11 GPa	38 GPa	12 GPa	39 GPa	14 GPa	20 GPa

(a)

	Correlation	***Lava core***		***Flow top***		***Sandstone***	
		E_{min}	E_{max}	E_{min}	E_{max}	E_{min}	E_{max}
Malinstindur Fm.	Barton (1995, 2006)	21 GPa	39 GPa	–	–	–	–
	Hoek et al. (2002)	26 GPa	82 GPa	–	–	–	–
	Hoek & Diederichs (2006)	29 GPa	71 GPa	–	–	–	–
	Bienawski (1978)	40 GPa	80 GPa	–	–	–	–
	Serafim & Pereira (1983)	13 GPa	56 GPa	–	–	–	–
	Geophysics	17 GPa	36 GPa	15 GPa	29 GPa	12 GPa	18 GPa

(b)

Rock mass deformability – Conclusions

Empirical correlations for estimating the deformation modulus generally yield lower value ranges than geophysical estimates derived from seismic log velocities. Although geophysical data tend to overestimate E, limiting these values to the 5^{th}–50^{th} percentile range brings them into closer alignment with most empirical results, particularly for basaltic lava cores. However, *GSI*- and *RMR*-based correlations often underestimate the minimum modulus (E_{min}) in lava flow tops and volcaniclastic sandstone, sometimes falling below the geophysical 5^{th} percentile. Nevertheless, using seismic log-derived E values within the 5^{th}–50^{th} percentile range for numerical modelling remains a sound approach to ensure a robust design framework.

6

Cavern design guidelines

Hann eigur reiðina, ið fyri ríður

Who rides first, controls the speed

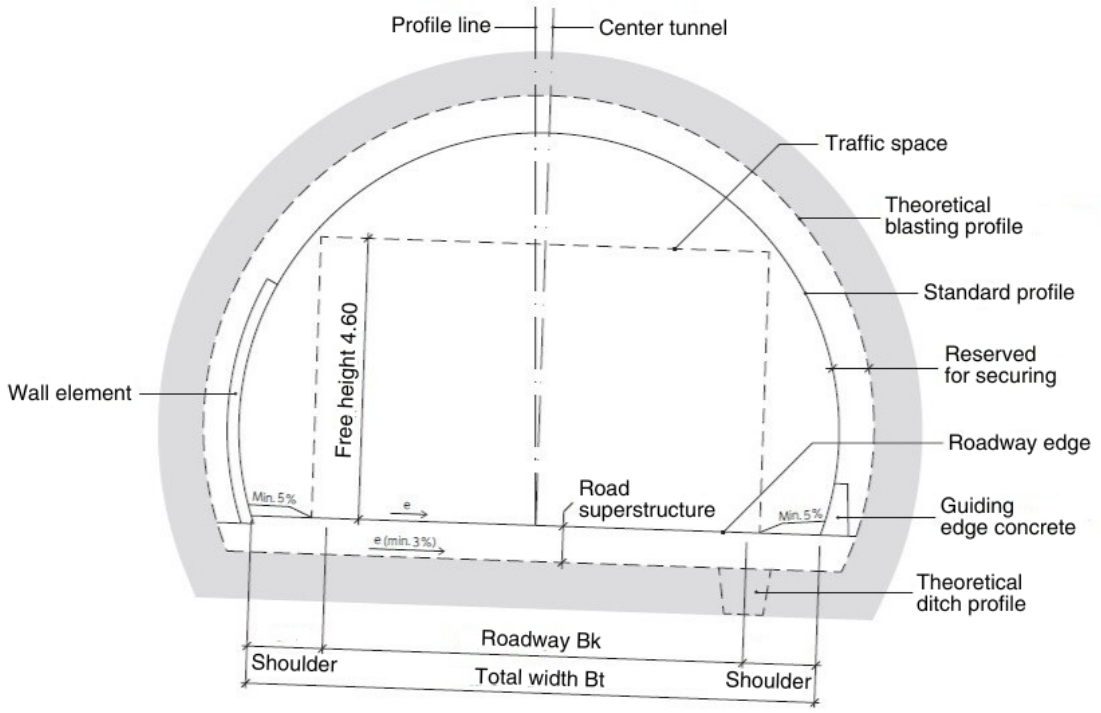
The Faroe Islands, while politically part of the Kingdom of Denmark, differ significantly in geography from the Danish flatlands. As a result, Norwegian guidelines are consistently used for tunnel projects in the archipelago. The particular nature of this project excavation—a combination of a tunnel, a roundabout, and a cavern—requires integrating design principles from multiple sources. The primary reference for tunnel design is Handbook N500–Vegtunneler ("Road Tunnels", Statens Vegvesen, 2024b). However, since the project includes a U-turn roundabout and lane widening, design criteria also rely on Handbook N100–Veg-og-Gateutforming ("Road and Urban Street Design", Statens Vegvesen, 2024a), specifically section 4.1.2 Rundkjøringer ("Roundabouts"). Both handbooks are published by the Norwegian Public Roads Administration. For structural integrity in underground widenings, the Norwegian Rock Caverns guidelines (Norwegian Tunnelling Society, 2016) are followed. Together, these three references define the design envelope for the underwater roundabout along the chapter.

6.1 Tunnel

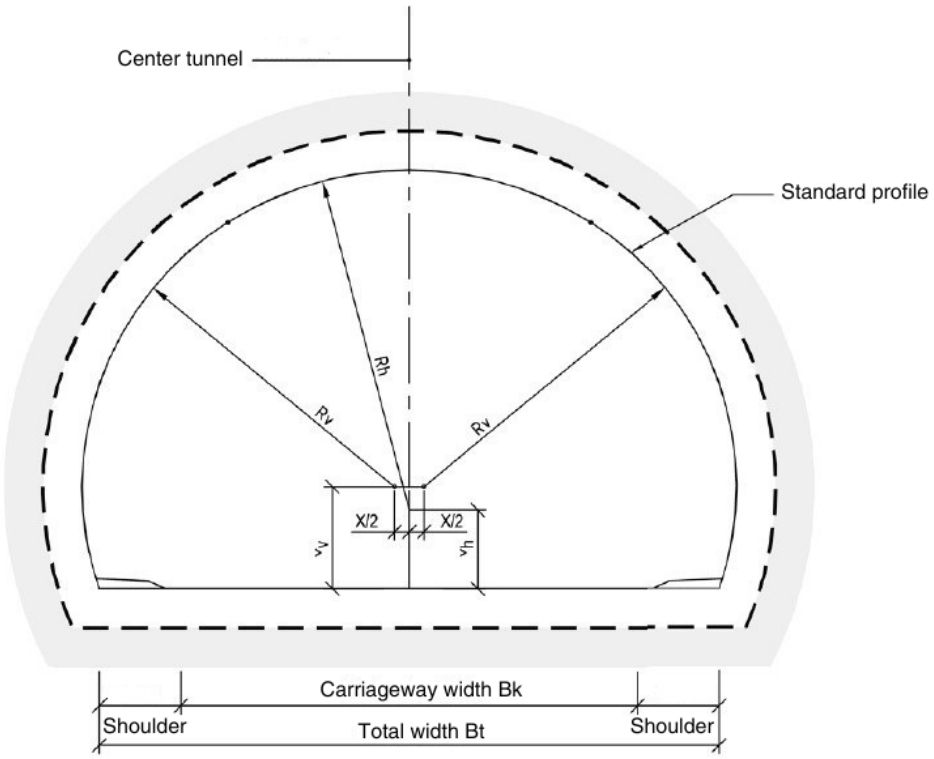
The geometry to be designed is well-suited for subdivision into three main blocks: (i) the approaching tunnel, (ii) the cavern, which primarily functions as a roundabout, and (iii) the intermediate connection that hosts the roundabout branch.

According to Norwegian standards, tunnels must be designed following a list of geometric specifications outlined in Handbook N500 (see Tab. D.1 and Fig. 6.1b). Additionally, cross-sectional details for tunnel profiles, based on specific conditions, are provided in Tab. D.2 and Fig. 6.1a. These tables apply regardless of the magnitude of the one-sided cross slope, the specification of which is beyond the scope of this project. Ultimate construction tunnels in the Faroe Islands have adopted T10.5 profiles (FAE, 2024); however, for this project, the client has explicitly specified the use of a T9.5 horseshoe tunnel profile.

It should be noted that Tab. D.2 specifies two different cross-sectional areas and contours for each profile. The second pair represents the standardised cross-section details (*Normalprofil*) used when the tunnel is operational. The first pair corresponds to the theoretical blasting profile (*Teoretisk sprengningsprofil*), applicable during the excavation phase and aligned with the scope of this project. Here, "theoretical" assumes a 1:1 vertical-to-horizontal proportionality when resizing the standardised cross-sectional area. No invert is planned in the provided cross section.



(a)

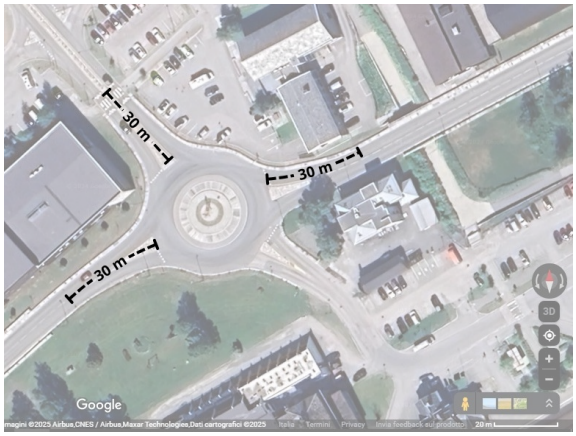


(b)

Figure 6.1: Schematic tunnel profile with its main elements (a), and geometric dimensions for T9.5–T14.0 tunnel profiles (b), with measurements varying for each individual profile. Adapted from Statens Vegvesen (2024b)

6.2 Connection

This section of the design process begins with an analysis of the typical dimensions of main roundabout branches along the E6 Norwegian high communication road (Oslo–Trondheim section). Since Handbook N100 does not provide comprehensive guidelines for these features, satellite images from Google Maps (see Fig. 6.2) are used as the primary reference for the design geometry.



(a)



(b)



(c)

Figure 6.2: Roundabout branch measurements in Oppdal (a), Dombås (b), and Otta (c) along the E6 high-communication road. Satellite images are modified from https://www.google.com/maps.

The extrapolated connection measurements are summarised in Fig. 6.3. Analysis of the images shows that, for an average branch length of approximately 30 m along the main roads, the first 10 m roughly match the width of a standard road lane. Therefore, this initial section can be incorporated into the tunnel block of the design, with only the remaining 20 m forming the connection building block.

Additionally, three significant constraints, informed by Norwegian guidelines and Faroese experience, should be incorporated into the design of this project:

(i) The external radius of entrance and exit lane, denoted as R_k in Handbook N100 (Fig. 6.5), must not exceed 80 m (Statens Vegvesen, 2024a).

(ii) Observations from prior Eysturoy Tunnel project indicate that (nearly) tangential connections have been established between the roundabout and the entry and exit lanes excavations. The purpose is to avoid stress concentrations in the corners that would eventually be created.

(iii) The rooftop connection should link the roundabout cavern using smooth or minimal curvature transitions to avoid stress concentrations. Accordingly, the upper vault is designed with a gentle curvature that merges as tangentially as possible with the cavern vault.

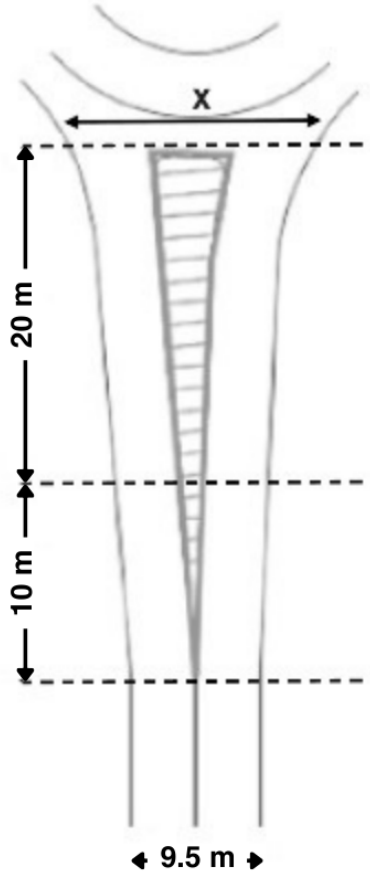


Figure 6.3: Sketch of the connection element and its dimensions. The first 10 m are integrated into the tunnel section, while the last 20 m represent the connection block itself. The upper width of the element varies slightly depending on the external radius of the roundabout. in order to ensure a joint that is as smooth and cornerless as possible.

Within the 20 m tunnel-cavern connection, the lateral wall will be constructed at a fixed height based on the Y_h tunnel geometry (Tab. D.1) to ensure continuity. This design accounts for a slight increase in Y_h when transitioning from the normal to the blasting profile. To meet geometric requirements, the wall will feature a hybrid curvature, transitioning from the T9.5

curved blasting profile to the curvature specified within the cavern cross section. No structural supports (e.g., pillars) are currently planned for the central median of the connection, as they have never been required in previous projects (see Section 1.3, Chapter 1). However, this may be reconsidered if simulations indicate significant displacements or stress concentrations in the connection rooftop.

6.3 Roundabout

The cavern is the project's key element, with numerical analysis focused primarily on its excavation. The client requires a roundabout large enough to allow even large-size vehicles to complete a U-turn in a single manoeuvre, facilitating faster evacuation during emergencies. The cavern is designed with a circular base, ensuring radial geometry throughout the entire excavation block. This approach has proven effective in maintaining excavation stability, even when the direction of the major stresses is uncertain (see Section 3.3, Chapter 3), while also fulfilling the facility's primary function as a roundabout.

6.3.1 Roundabout design guidelines

According to Requirement 4.1.2.1–3 (Fig. 6.4) of the roundabout design principles in Handbook N100, the circulation area width is determined by the outer diameter for three vehicle categories, listed here from least to most demanding: truck, bus, and road train (articulated vehicle). This

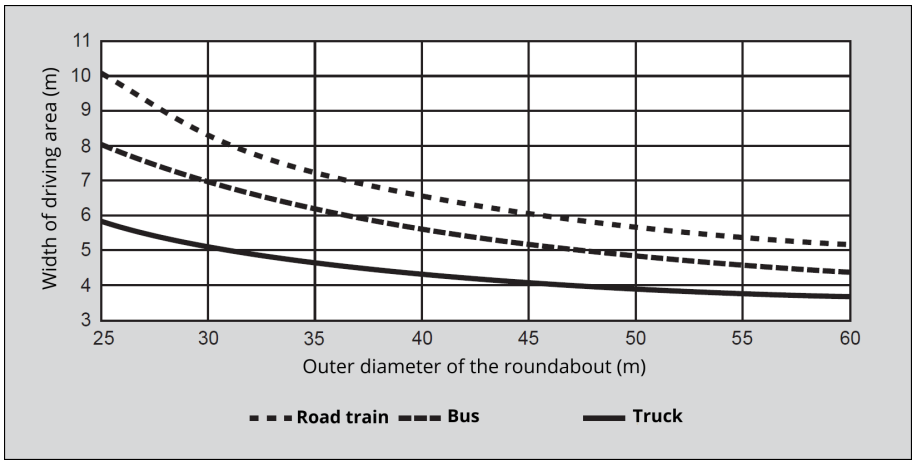


Figure 6.4: Outer diameter of roundabout versus driving area width for three vehicle categories. Adapted from Figure 4.1.2.1—1 in Statens Vegvesen (2024a).

study considers the road train category, the most conservative option, which demands the widest lanes for a given outer diameter.

Allowed roundabout diameters range from 25 to 60 m (Fig. 6.4). As shown in the plot, larger radii are associated with narrower circulation widths. This study presents a preliminary design and corresponding numerical analysis of stress and displacement evolution for varying outer radii, with a tolerance of 2 m, reduced to 1 m if significant geometric changes or large variations in numerical simulations occur.

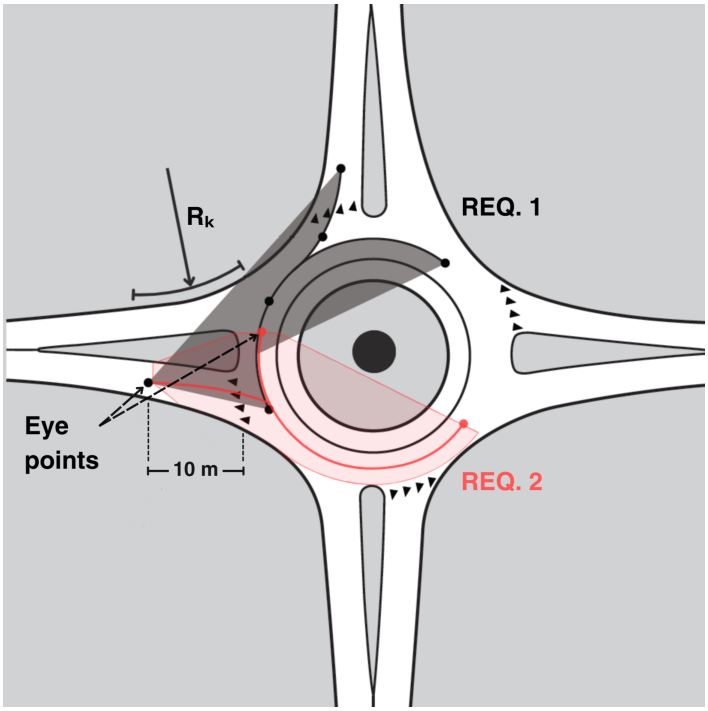


Figure 6.5: Visibility requirements in roundabout design in Norway: Requirement 1 ensures that drivers approaching the roundabout (black eye point) have a reasonable unobstructed view of vehicles already circulating within it. Requirement 2 addresses the need for clear forward visibility when already in the roundabout (red eye point) and approaching another entry arm. Adapted from Figures 4.1.2.5—1, 4.1.2.7—1, and 4.1.2.7—2 in Statens Vegvesen (2024a).

Visibility requirements (Fig. 6.5) check for possible incoming vehicles inside the roundabout (Requirement 1) and ensure sufficient sight distance along the circulation lane for vehicles both inside and approaching the roundabout (Requirement 2). Since the central island may include a rock pillar, these guidelines are critical in defining the maximum pillar radius based on the outer diameter and lane width. Calculations assume the driver's eye conventional height at 1.25 m ("Eye point", Fig. 6.5; Statens Vegvesen, 2024a), requiring an unobstructed view of an object situated on a specific position in the roadway ground. The driving path curvature, determined by the central island diameter and drivable width, defines the radius extending to the driver. The arc length L depends on the driving radius and estimated speed, varying with respect to the radius itself (Tab. 6.1).

Given the lane width, driving radius, and path length, the dimensions of triangle OAB (Fig. 6.6) are calculated trigonometrically. The length OB represents the radial distance from the roundabout center to the shaded visibility zone. If OB exceeds the pillar radius, visibility is

Table 6.1: Length of the driving curve L as a function of the driving curve radius $R_r - w/2$. Adapted from Table 4.1.2.7—1 in Statens Vegvesen (2024a).

Driving curve radius	Assumed speed level along the driving curve
$\leq$ 15 m	25 km/h
20 m	30 km/h
30 m	35 km/h

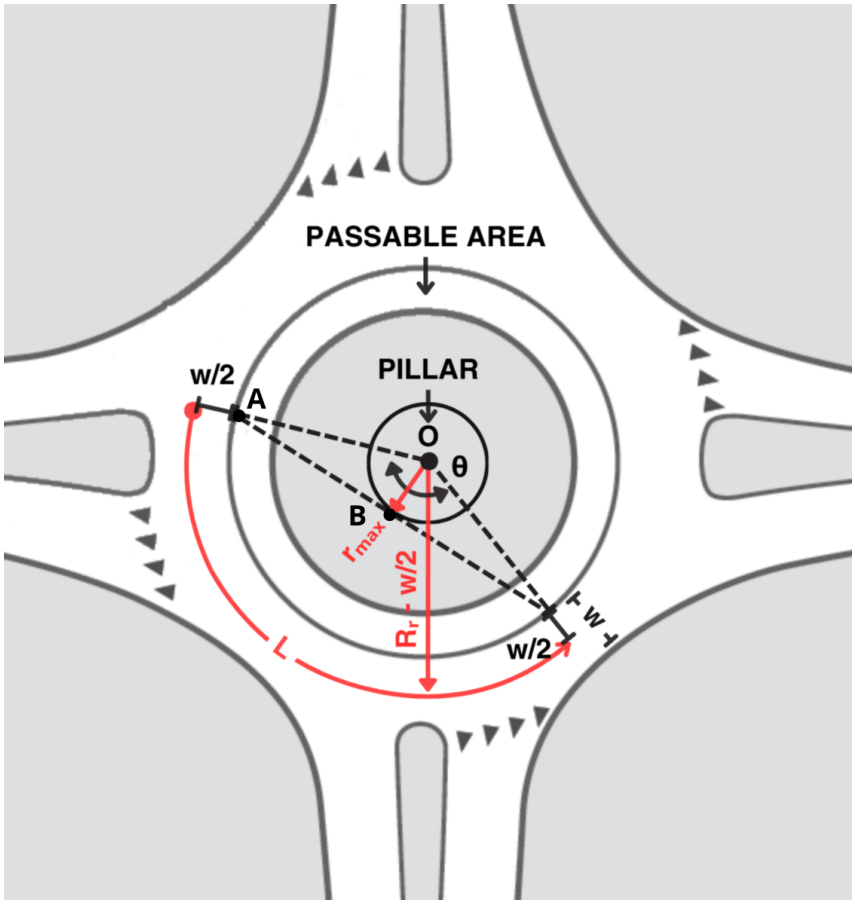


Figure 6.6: Trigonometric relationships to estimate the maximum allowable pillar radius (r_{max}), given the roundabout's external radius (R_r) and the corresponding lane width (w), for the "road train" vehicle category.

unobstructed. Additionally, no objects in the shaded zones in Fig. 6.5 must surpass 0.5 m in height. The maximum pillar radius is linked to the external roundabout radius, which equals half the lane width plus the driving radius, as expressed in Eq. 6.1.

$$r_{\max} = (R_r - w) \cdot \cos\left(\frac{1}{2} \cdot \frac{L}{R_r - w/2} \cdot \frac{180}{\pi}\right) \tag{6.1}$$

It is important to emphasise that the outer radius of the roundabout, R_r, does not coincide with the outer radius of the excavation, R. In practice, a gap of at least 1 m is intentionally left between the edge of the carriageway and the excavation wall. Consequently, for a given external widening radius R, the corresponding roundabout outer radius R_r will be $\leq R - 1$ m. This adjusted radius corresponds to the reference value for applying the design guidelines.

For R values between 13 and 30 m, the roundabout's external radius varies from ~12.5 to 29 m. Achieving the maximum allowable radius of $R_r = 30$ m (as shown in Fig. 6.4) would require further adjustments. However, designing for $R = 31$ m is considered excessive, as it would cause substantial widening unlikely to match the final project geometry.

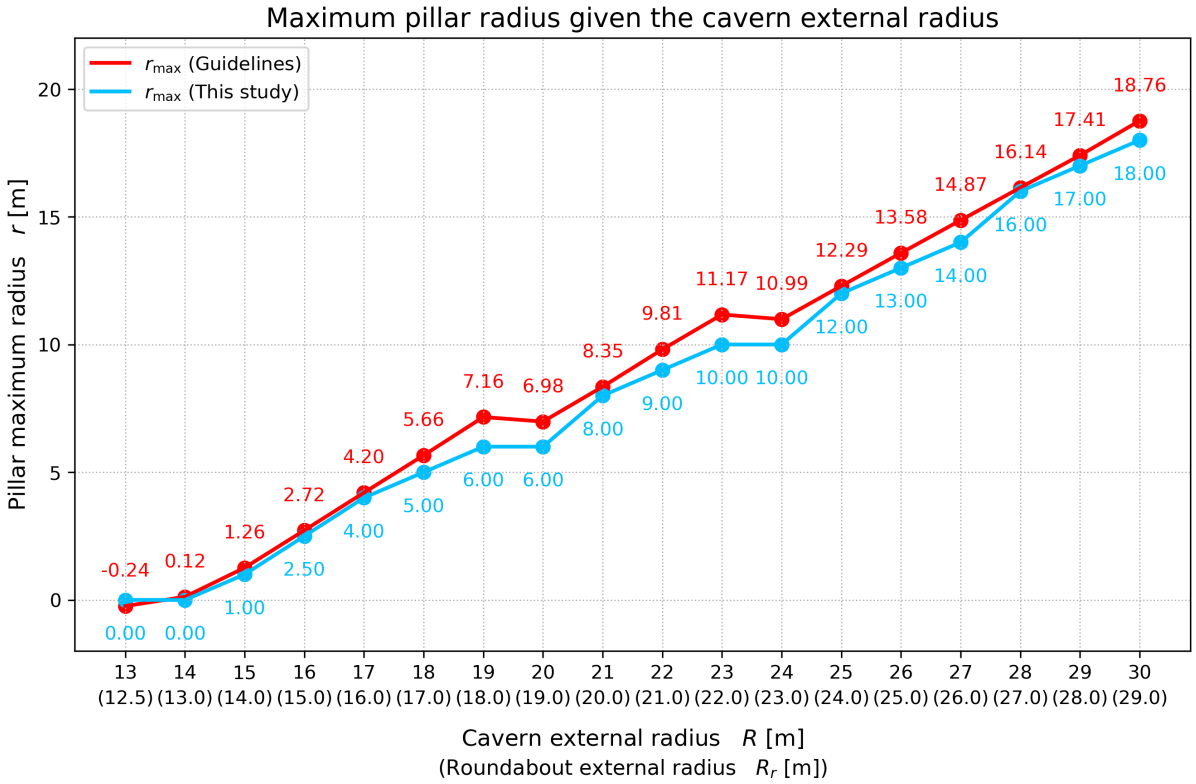


Figure 6.7: Maximum pillar radius corresponding to the cavern's external radius.

The maximum pillar radii, $r_{\max}$, corresponding to their outer diameters R_r, are rounded down to the nearest half-integer for intervals between 0 m and 3 m, and to the nearest integer otherwise. These rounded values define the reference limits for generating the input geometries. A

graphical summary of the results from Eq. 6.1 is shown in Fig. 6.7. Note that for roundabout radii of $R_r = 12.5\,\text{m}$ and $R_r = 13\,\text{m}$, the maximum pillar radius is negative or near zero, indicating no allowable visibility obstacles; thus, a fully open span widening is the only possible solution in these cases.

6.3.2 Cavern structural stability considerations

Structurally, the underwater roundabout resembles a cavern excavation and must comply with cavern design and stability guidelines. Selmer-Olsen and Broch (1978) provide Norwegian criteria for underground openings' cross-sections, categorised by stress level and principal stress direction (Fig. 6.8). Given the relatively low rock overburden of this underwater excavation—compared to that of many mountain tunnels—and the fairly good assessed rock mass quality and strength (see Section 5.3.1 and 5.3.5, Chapter 5), the in-situ stress levels are expected to be moderate.

A vertical wall extends from the excavation level up to height Y_v (Tab. D.1), where the T9.5 tunnel profile narrows (Fig. 6.1b). This height varies slightly with the blasted profile (Tab. D.2) but remains below 2 m, making principal stress orientation negligible in the wall curvature

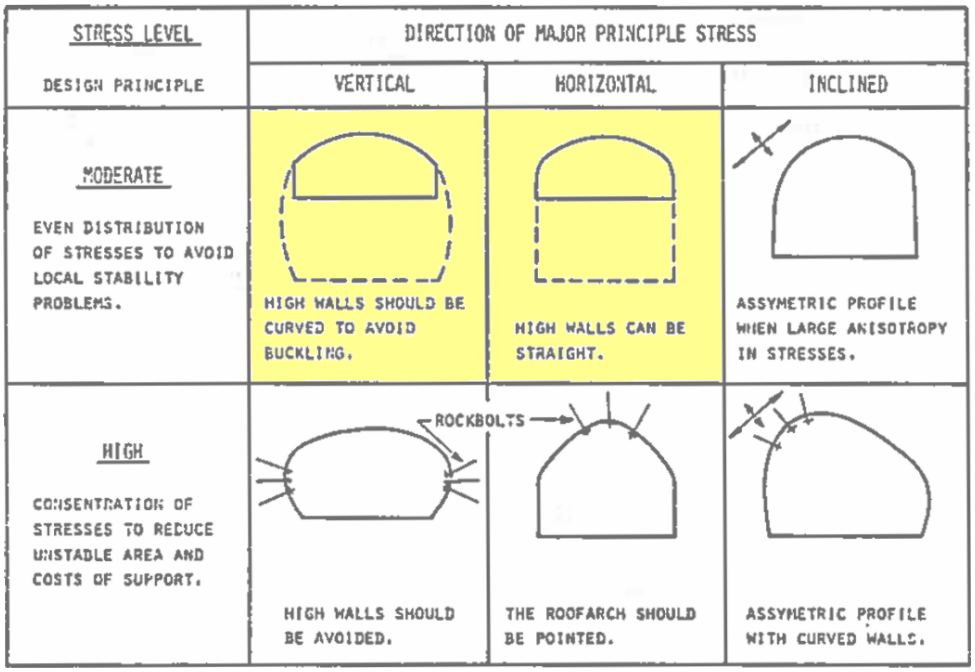


Figure 6.8: Design principles for underground openings in rocks at varying stress levels and stress directions, with the candidate cross sections for this project highlighted. Adapted from Selmer-Olsen and Broch (1978).

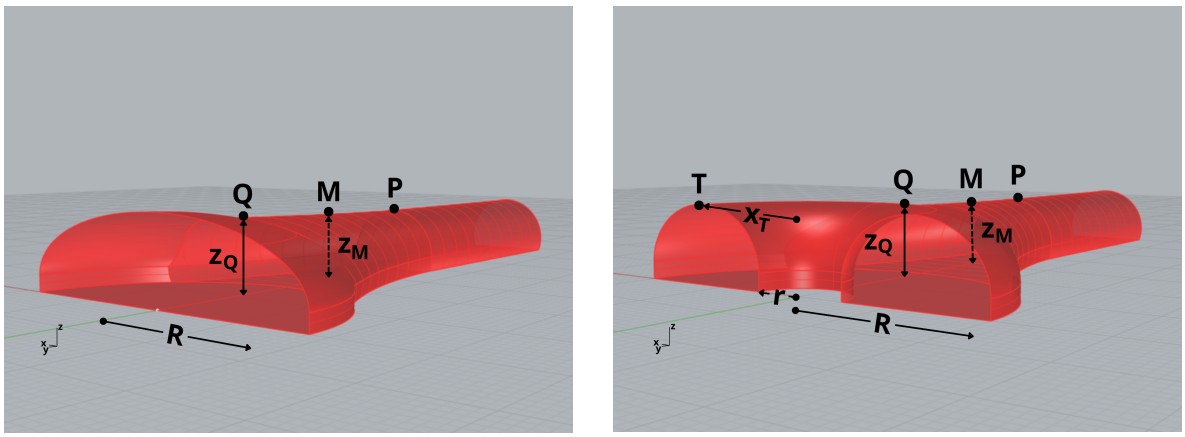
determination (Fig. 6.8).

The rooftop arch height is approximated as one-fifth of the cavern diameter (Norwegian Tunnelling Society, 2016), with distinctions depending on whether the excavation includes a pillar or not: in the latter case, the span corresponds to the outer diameter, while in the former it corresponds to a single roundabout cross-sectioned arm. In this second option, the estimated arch heights are relatively modest, sometimes even lower than the tunnel vault. When this occurs, the cavern height is designed to at least match the T9.5 profile blasting vault.

The pillar rises from the centre of the roundabout, with a base radius no greater than the corresponding r_{max} for the specified outer radius (Fig. 6.7). It gradually widens with height to connect horizontally to the cavern vault at the mid-width of the tube's cross-section, optimising light installation efficiency. As previously mentioned, the driver's eye height is set at 1.25 m per Handbook N100 (Statens Vegvesen, 2024a). However, road train drivers usually sit higher than this reference height. Thus, the pillar's lower section is designed to remain slender, with most widening concentrated at the top.

6.4 Parametric design

All guidelines and calculation results from this chapter are integrated into Rhino® CAD software to ensure design accuracy. To generate a wide range of geometries, Rhino® is used in couple with its visual programming interface, Grasshopper, enabling algorithmic creation of complex parametric models through a nodes- and connections-based workflow.



(a) (b)

Figure 6.9: Non-pillar (a) and pillar (b) output geometries in Rhino Grasshopper and their respective variables.

Grasshopper input boxes contain fixed or variable parameters representing essential inputs for geometry generation. Two network architectures are designed (refer to APPENDIX X), differentiating between geometries without a central pillar (Fig. 6.9a) or with it (Fig. 6.9b). In both cases, constant parameters relate to tunnel and connection sections: tunnel length, T9,5 profile specifics (Tab. 6.1b), and their area and perimeter scaling remain fixed. Connection length and lateral curvature radius R_k are invariant regardless of cavern diameter, while the rooftop central line forms a three-point arch in the vertical plane, defined by a fixed-height point at the tunnel-connection junction and two variable-height points M (z_M) and Q (z_Q) at the connection's midpoint and end. Variability in M and Q allows near-tangential connection with the cavern, mainly adapting to other variables rather than acting as primary design parameters. This ensures the height of the arch curve PMQ never decreases toward the widening.

The roundabout, as the primary study object, determines the key Grasshopper input variables (Tab. 6.2). For caverns without a pillar, the only effective design variable is the external radius

Table 6.2: Variables and parameters for pillar and non-pillar geometries in Rhino® Grasshopper.

		Description	Symbol
Non-pillar geometry	**Vars.**	Cavern radius	R
		Connection rooftop mid- and ending height	z_M, z_Q
	Params.	Tunnel profile specifics	–
		Tunnel length	–
		Connection lateral radius	R_k
		Connection length	–
		Cavern wall height	–
		Cavern span-height ratio	–
Pillar geometry	**Vars.**	Cavern radius	R
		Pillar base radius	r
		Connection rooftop mid- and ending height	z_M, z_Q
		Cavern rooftop radial coordinates	x_T
	Params.	Tunnel profile specifics	–
		Tunnel length	–
		Connection lateral radius	R_k
		Connection length	–
		Cavern wall height	–
		Pillar height	–

R (Fig. 6.9a), which represents the first variable for the pillar geometry as well. Although cavern height varies, the initial vertical wall height equals the modified parameter Y_h from the T9.5 tunnel blasting profile to maintain geometric continuity. The ellipsoid vault height adheres to a fixed 5:1 height-span ratio, producing an oblate spheroid dome. This ratio shifts to 4:1 for R_r between 12.5 and 14.0 m to prevent the blasted tunnel height from exceeding the cavern rooftop.

With a central pillar, the rooftop is formed by two merging elliptical quarters meeting at vault apex T, situated in proximity of the midpoint of the opening width (Fig. 6.9b). This is beneficial not only for light optimisation but also for structural stability, especially in case principal stresses orientation is found nearly vertical or horizontal in the excavation site (see Section 3.3, Chapter 3). In particular, the variable x_T introduced in Grasshopper defines the radial position of T with respect to the cavern central axis. The apex height is instead fixed at approximately 8 m, decoupled from cavern radius to avoid excessively low rooftops.

The pillar base radius r is the third variable, defined relative to the cavern radius R (see Fig. 6.7). It maintains a constant thickness up to 1.75 m above ground to allow for potential road elevation in later stages, such as asphalting and other operations, thereby still accommodating the 1.25 m driver's eye conventional height. Vertical walls extend from the cavern exterior to match connection wall height, ensuring cross-sectional continuity. Rooftop profile and pillar's conical widening are obtained by rotating 360° the two elliptical quarters around the cavern central axis. Corner avoidance guided the choice of a circular cavern over polygonal alternatives, which, despite still offering an acceptable stress distribution, would introduce post-excavation stress concentrations and greater sensitivity to varying in-situ stress orientations.

The number of output geometries both for the non-pillar and pillar options is determined by the selected input R values (blasted cavern span). Increments of the external radius has been finally confirmed at 2 m between geometries, except from $R = 12.5$ m to $R = 16$ m where 1 m steps are used due to the significant impact of small changes on the resulting geometries at these early stages. The operational space is reduced from R by excluding wall reinforcements and maintaining a $\geq$1 m clearance from the carriageway. Candidate geometries begin at $R = 13$ m, rounding the maximum pillar radius r_{max} down to its nearest integer, and then decreasing it in 1 m increments, except between 0 and 3 m, where 0.5 m steps are used to better capture changes as rock support thins. In total, the design includes 11 non-pillar and 105 pillar geometries for simulation.

As a supplementary material for the project, the two Grasshopper architectures (`.gh` files) are available at the following link.

Parametric design – Conclusions

The design centres on the underground cavern with the main functionality as a road roundabout that enables road trains to perform U-turns in a single manoeuvrer. Two main geometries, both exhibiting radial symmetry, are developed: non-pillar and pillar configurations, each governed by distinct parametric variables. Non-pillar designs vary as a function of the external radius R and the rooftop connection heights z_M, z_Q, while pillar configurations introduce additional variables: the pillar base radius r and the radial distance of the rooftop apex from the cavern centre x_T.

Algorithmic generation of these complex forms is achieved through CAD software, enabling the efficient creation of 11 non-pillar and 105 pillar geometries. Geometric and operational constraints, including fixed height-to-span ratios, wall reinforcements, and clearance requirements, ensure feasibility and compliance with design guidelines, with minor adaptations for low-radius cases and permissible vertical walls due to expected moderate stress conditions.

7

Numerical modelling approach

Har ein skriðan er lopin, er onnur væntandi

After a landslide one more can be expected

Having outlined the geotechnical properties and preliminary design features of the project, the key steps involved in building the numerical model—carried out at the client's request—can now be presented. Beginning with the definition of the domain, meshing strategy, materials, in-situ conditions, and boundary conditions, this chapter then proceeds to examine the simulation of the sequential excavation process and the characterisation of the rock mass response, as captured by failure criteria and constitutive laws. It is important to note that no data are available for model calibration; therefore, a theoretical approach is adopted.

In the second part, a comprehensive numerical simulation plan is presented, focusing both on the model's response to the various geometries identified during the preliminary design phase and on the uncertainty associated with specific parameters of the continuum medium and failure criteria, which remain unresolved.

7.1 Model domain

The output cavern geometries—comprising the three blocks of tunnel, connection, and cavern—are integrated within a simple parallelepiped domain. Fixed offsets from the roundabout base and external radius R define the domain size (Tab. 7.1): 40 m (x), 50 m (y), and 60 m (z), with 20 m below and 40 m above the cavern base.

Table 7.1: Model domain size in relation of the cavern external radius R. Note that the z-interval is kept constant regardless of the cavern excavation size

Direction	Domain [m]
x-axis	[-(R+40); +(R+40)]
y-axis	[-(R+50); 0]
z-axis	[-20; +40]

A key modelling choice concerns the domain's upper boundary: despite past projects employing detailed topography such as the work of Høien (2006), the current 50 m-spaced bathymetric data provide insufficient seabed resolution. In combination with the gentle seabed slopes in the Sandoy–Suðuroy strait (see Fig. 3.2, Chapter 3), this justifies using a flat top surface, simplifying the model and reducing computational demands by eliminating the need to account for the entire stratigraphic sequence up to the seabed.

Due to the plane symmetry with respect to the cavern centre, the analysis can be simplified by modelling only half of the overall geometry. A quarter model was also considered, but later discarded because of the increased complexity in defining the boundary conditions.

7.2 Meshing

Excavation geometry is segmented into 5 m blasting sections, a choice justified by favourable geotechnical conditions and the absence of sensitive zones (Trinh et al., 2021). Although this uniform length may cause some caverns to end with 1–5 m final segments due to varying outer radii—impacting equilibrium in simulations—it remains the most realistic approach. In fact, it avoids smaller or mixed-section divisions at transitions, maintaining uniform 5 m sections throughout. As a result, each model comprises 6 steps for tunnels, 4 for connections, and 3–6 for caverns, depending on the outer radius.

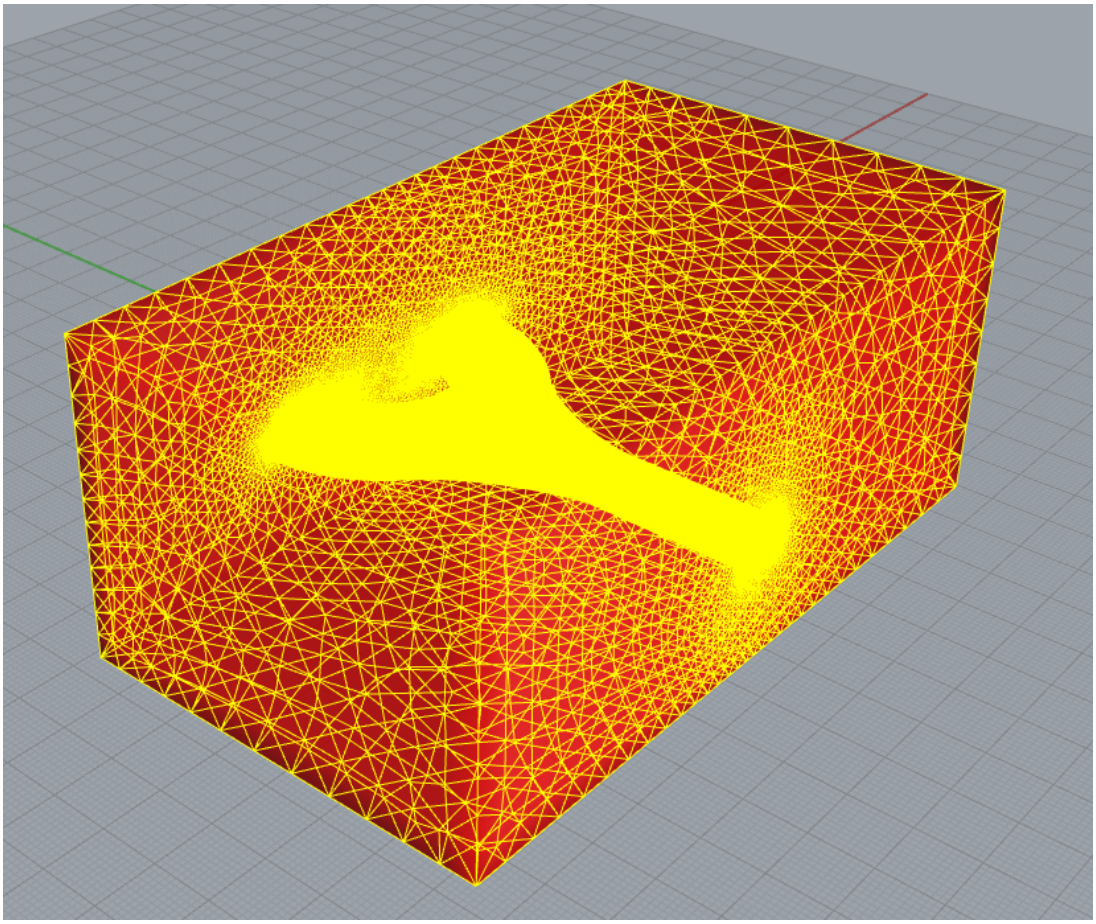


Figure 7.1: Pillar geometry model mesh, with the finest tetrahedra elements sized 0.1 m (100 mm) and the largest up to 10 m.

Tetrahedral meshing is adopted. Element sizes range 0.1–0.3 m (100 to 300 mm) in the cavern geometry per Griddle's tunnel excavation guidelines by Itasca Consulting Group (2023) and up to 10 m at the model boundaries (Fig. 7.1). Mesh sizes span from 2.4 to 7.1 million elements and 0.4 to 1.2 million nodes. Evolution of nodes and elements with respect to outer and pillar radii (R, r) is detailed in Appendix E.1.

To ensure consistent meshing for simulations with fixed R and varying pillar radii, a single input file comprising all excavation options would be ideal. However, modifying such a file for each scenario introduces minor sensitivity variations due to mesh changes—finer meshes may resolve features better, while coarser ones might miss them. The proximity of excavation steps also requires high precision to avoid mesh overlaps. Moreover, using a unified file limits meshing optimisation for individual cases, significantly increasing computational cost. Thus, distinct input geometries are finally employed for each excavation scenario.

7.3 Materials

The local stratigraphy and site investigations revealed three primary material groups, previously classified as lava core, lava breccia, and sediment (see Chapter 4, Section 4.1). Seawater above the excavation is modelled as a static load, while hydraulic aspects have been discussed separately in Chapter 4, Section 4.4.

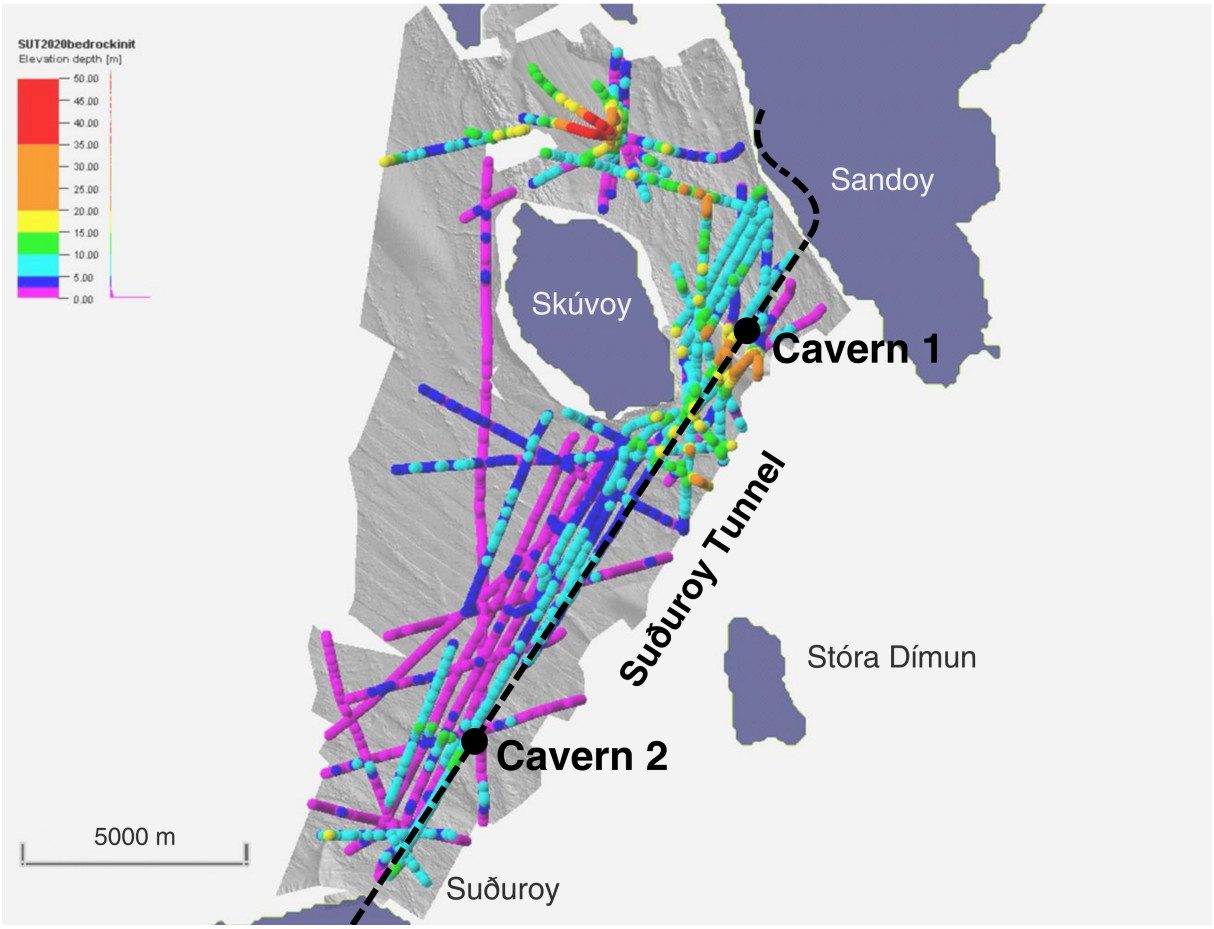


Figure 7.2: Sediment cover thickness in the seabed along the Sandoy-Suðuroy area. The majority of the deposits have been located between Sandoy and Skúvoy in an area bypassed by the proposed tunnel alignment. However, another relevant deposit is visible slightly southern of Cavern 1 proposed location. Adapted from Petersen (2023).

For simplicity, the model domain is characterised as a homogeneous continuum medium throughout the entire 60 m vertical extent. Since boreholes confirm frequent alternation of basalt and sedimentary sequences, especially along the *Enni Formation* (Petersen et al., 2022), assuming only lava core beneath the excavation is optimistic; therefore, a specific set of simulations is planned to incorporate sandstone and breccia media for Caverns 1 and 2, within

the *Enni* and *Malinstindur Formations*, respectively.

Overburden static distributed loads are based on lithostratigraphy and sea depth. While up to 40 m of sediment exists in Skúvoy Fjord (Petersen, 2020), according to the seismic surveys reported by Petersen (2023) the sequence overlying Cavern 1 (Fig. 7.3a) appears dominated by minor (10–20 m) sediment layers (Fig. 7.2). For clarity, Fig. 7.3 groups the lava core and lava breccia under the "basalt" unit, while both the multiple sandstone lithologies and any sediments present on the seafloor are included in the "sediment" layer.

Although further offshore, Cavern 2 (Fig. 7.3b) is also underlain by 10–15 m of sediments (Holter et al., 2021, Petersen, 2023). Due to limited drilling (see Fig. 3.4, Chapter 3), breccia and sedimentary layers thicknesses remain poorly identified along the second cavern stratigraphy.

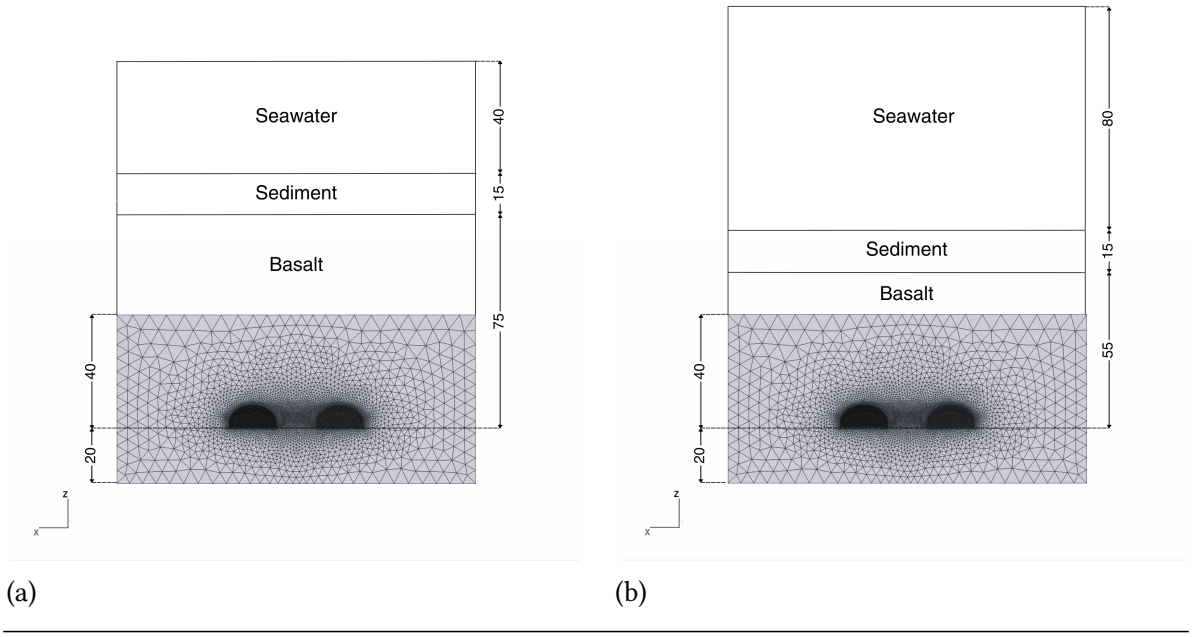


Figure 7.3: Overview of thickness distribution among basaltic units, sediment or sedimentary units and seawater at (a) Cavern 1 and (b) Cavern 2.

While sediment thicknesses are similar, Caverns 1 and 2 differ in overburden and sea depth. Cavern 1 lies beneath 90 m of rock and sediment in shallower water, while Cavern 2 is under 80 m of seawater and 75 m of stratigraphy, with only ~60 m being bedrock. In the largest proposed geometries, its overburden may drop to ~45 m, below Norway's 50 m guideline but still within acceptable limits as demonstrated in previous projects (Grøv and Trinh, 2022). As a result, Cavern 1, with greater overburden, is expected to face higher body forces—therefore vertical stresses—while Cavern 2 may be more susceptible to deformation due to its lower overburden.

7.4 In–situ and boundary conditions

The model adopts essential boundary conditions: the top surface is free to deform under loading, lateral boundaries allow shear deformation but prevent rigid motion via rollers ($u_n = 0$), and the base is fully fixed ($u_x = u_y = u_z = 0$), simulating rigid bedrock. Half-domain modelling is employed under symmetry assumptions, with no normal displacement and therefore no material flow across the central vertical plane.

Table 7.2: Displacement boundary conditions overview.

Boundary	Type	Description
Lateral sides	Roller	$u_x = 0$ or $u_y = 0$
Bottom boundary	Fixed	$u_x = u_y = u_z = 0$
Top surface	Free	–
Symmetry plane	Symmetry condition	$u_n = u_x = 0$

A uniform distributed load is applied to the top boundary, representing the weight of overburden and seawater. This is modelled using a mono-material equivalent load (basalt, sandstone, or breccia) with adjusted lithostratigraphic thickness, converting the true stratigraphy into an external load. Material density values are based on GEUS data (Waagstein and Andersen, 2004). Consequently, model depth varies by material, though the real excavation depth remains indeed constant.

Due to the lack of in-situ stress data, vertical stress is assumed to be purely gravitational. A parametric study is planned to investigate the impact of varying the horizontal-to-vertical stress ratio k from 0.5 to 2.5 on the model results, as discussed in Section 3.3, Chapter 3.

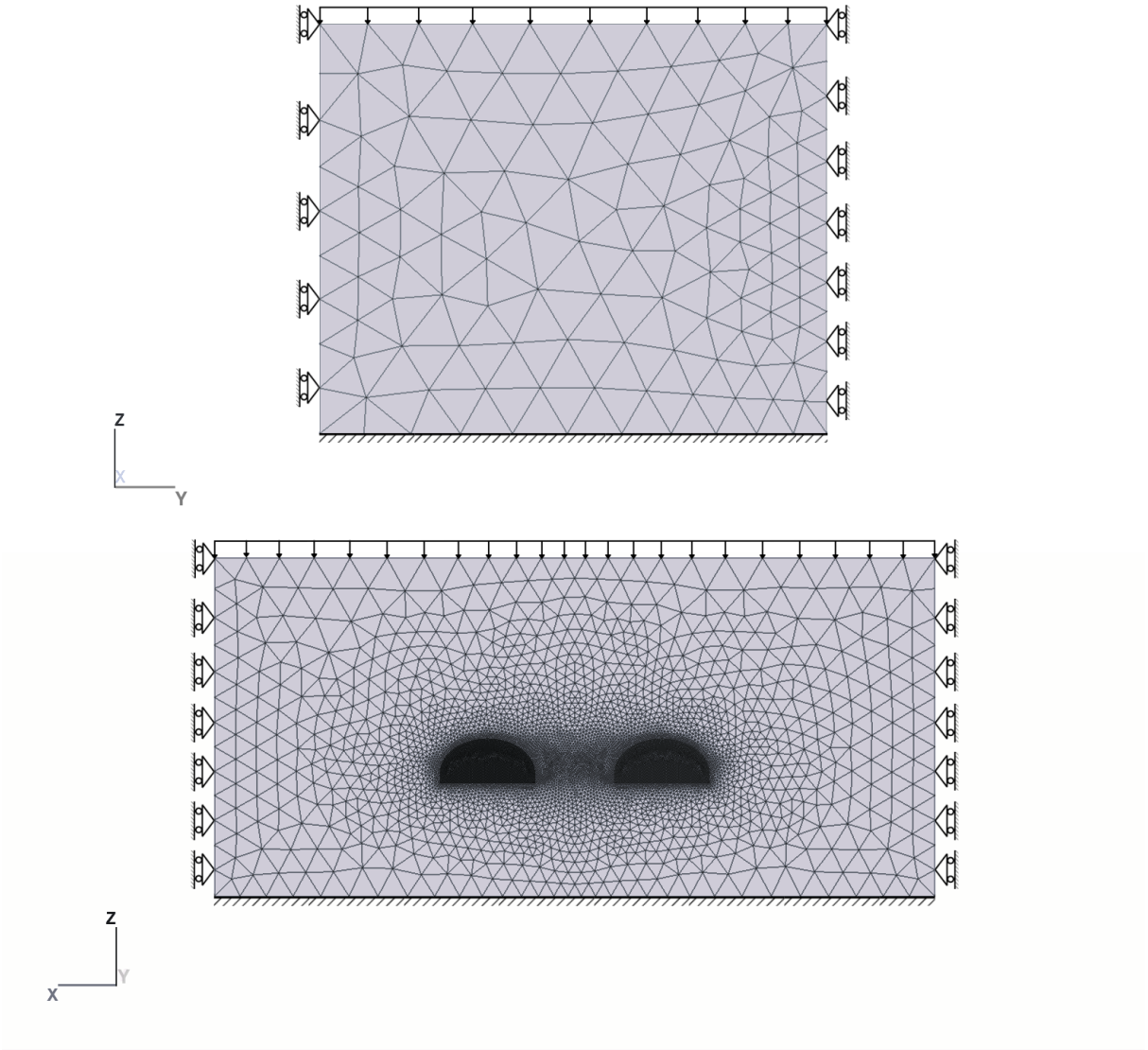


Figure 7.4: Representation of the model's boundary conditions in terms of imposed constraints.

7.5 Constitutive models

7.5.1 Mohr–Coulomb

The Mohr–Coulomb (MC) failure criterion, defined by cohesion (c) and internal friction angle (ϕ), expresses failure as a linear shear–normal stress relationship. While simple, it reliably represents key rock behaviour, especially in preliminary design stages, and is the basis of more advanced models. In this study, c and ϕ are not directly available but are estimated via correlations with the Hoek–Brown (HB) criterion and empirical relationships based on the rock mass estimated Q-parameters (Tab. 5.7, Chapter 5).

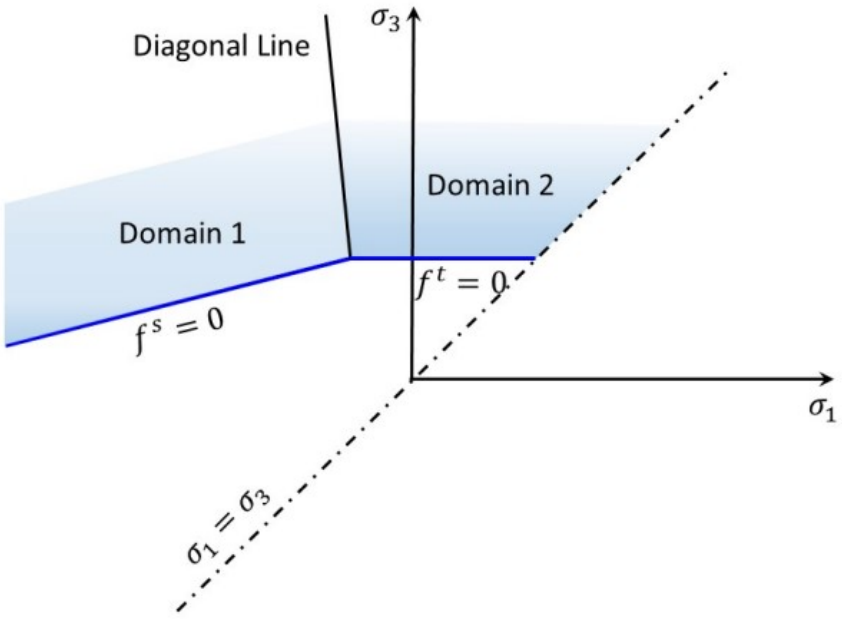


Figure 7.5: Mohr-Coulomb domain used to define the non-associated flow rule in FLAC. When an elastic guess violates the composite yield function it can fall either into Domain 1 or Domain 2. Adapted from Itasca Consulting Group (2017).

The MC model adopts a composite yield surface with a tensile cut-off, characterised by non-associated plastic flow defined through separate shear and tensile potential functions (Fig. 7.5). An initial elastic stress estimate is evaluated against the composite yield surface in the principal stress space; plastic corrections are applied based on domain-specific shear or tensile failure modes.

7.5.2 Hoek–Brown

The Hoek-Brown (HB) criterion is the most commonly used criterion to model rock mass failure in tunnelling (Jimenez et al., 2008), Its generalised form was first introduced by Brown and Hoek (1980), revised by Hoek and Brown (1997), and further refined by Hoek et al. (2002). Specifically, in the numerical modelling software the criterion is treated as a stress-dependent yield surface, with a flow rule adapted with the formulations proposed by Pan and Hudson (1988), Shah (1992), and Carter et al. (1993)—referred to as Hoek–Brown PAC—to ensure continuity across the entire stress space, particularly where the intermediate principal stress σ_2 is zero (Itasca Consulting Group, 2017). The implementation employs a composite flow rule combining associated, radial, and constant-volume behaviours, with plastic strain increments iteratively updated using a modified Newton–Raphson method. This approach ensures convergence across a wide range of stress paths, including those with low confining pressure or zero unconfined compressive strength.

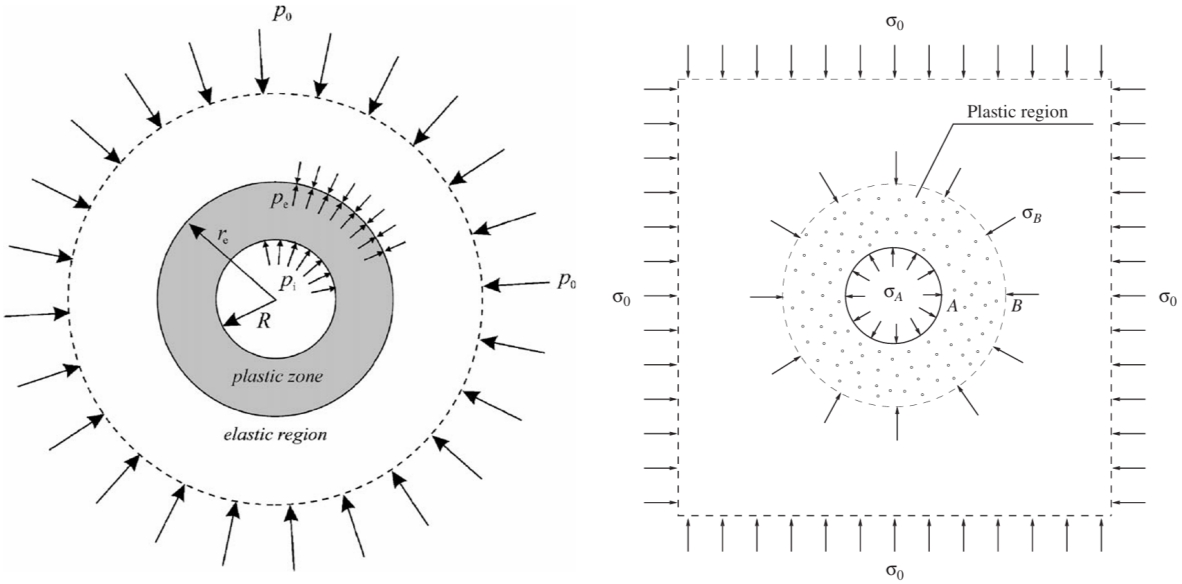
7.5.3 Hoek–Brown to Mohr–Coulomb fitting

Hoek et al. (2002) also referred to a method to align HB with the MC criterion for compatibility with certain software. This is done by equating the areas between HB and MC curves in a σ_1–σ_3 plane over a defined minor stress range ($\sigma_t < \sigma_3 < \sigma'_{3\max}$), enabling estimation of equivalent friction angle and cohesion. Despite its popularity, this fitting method has been debated, and alternative, project-specific approaches have since been proposed (Trinh et al., 2006). This section reviews four such formulations and select one of them to derive the MC parameters for this study. All of them assume a circular tunnel cross-section, different from the roundabout geometry, but still able to offer a valid initial approximation.

Sofianos and Nomikos (2006) introduced a linearisation approach in the mean–deviatoric (p–q) stress space, defining the stress range from tunnel support pressure (p_i) to in-situ hydrostatic pressure (p_0), with the intermediate pressure (p_e) marking the elastoplastic boundary (Fig. 7.6a). Equivalent cohesion and friction angle are then derived from this range using normalised stress components (p_N). The method separates rock mass plastic and brittle behaviour and computes the MC parameters accordingly.

Jimenez et al. (2008) debated the area-equivalence method proposed by Hoek et al. (2002) and suggested an alternative approach based on a normalised p^*–q^* plot under plane strain conditions. The stress path between tunnel points A (support pressure) and B (hydrostatic pressure) is analysed graphically to determine the MC parameters (Fig. 7.6b). The slope of the equivalent AB segment on the plot corresponds to the tangent of the friction angle. For

cohesion, the value is selected in the q^* axis using an empirical fitting parameter, ξ_C^*, with a proposed optimal value of 0.60 to ensure minimal approximation error.



(a) Sofianos & Nomikos (2006) (b) Jimenez et al. (2008)

Figure 7.6: Assumption of circular tunnel in an elastoplastic rock mass subject to hydrostatic initial stress field—p_0 (a), σ_0 (b)—and a tunnel support pressure—p_i (a), σ_A (b)—from (a) Sofianos and Nomikos (2006) and (b) Jimenez et al. (2008). Adapted from Sofianos and Nomikos (2006) and Jimenez et al. (2008).

Meng et al. (2016) proposed a robust linearisation method using best uniform approximation, minimising the maximum error between the HB and linear MC envelopes. By expressing the MC envelope in σ_1–σ_3 space, they derived analytical expressions for k (equivalent slope of the failure envelope) and C_0 (equivalent cohesion) based on the stress interval from p_i to p_e, offering a stable alternative to least squares fitting.

The mathematical formulations of the three HB–MC fitting methods are widely reported in Appendix E.2.

In conclusion, Barton (2002) proposed a formulation to estimate MC shear strength parameters for continuum analysis by using field-mapped *Q*-parameters (*RQD*, J_n, *SRF* for cohesion; J_r, J_a, J_w for friction angle).

Results from the HB-MC fitting methods

Equivalent friction and cohesion for the main basaltic medium (i.e., lava core) were estimated using average density, HB parameters, *Q*-parameters, and average *UCS* from the *Enni* (Cavern 1) and *Malinstindur* (Cavern 2) formations (Tab. 7.3). The empirical formulation by Barton (2002) produces relatively high friction–cohesion pairs, whereas HB-based approaches yield more conservative results that are consistent among themselves. These results demonstrate a balanced trade-off between friction and cohesion: overall, the friction angle is slightly lower and the cohesion slightly higher than reported by Hoek et al. (2002). Among the three alternative formulations by Sofianos and Nomikos (2006), Jimenez et al. (2008), and Meng et al. (2016), the results are very similar.

Table 7.3: Results from the HB-MC selected fitting methods given the average HB parameters and typical Q-parameters and average UCS values of Enni and Malinstindur lava cores.

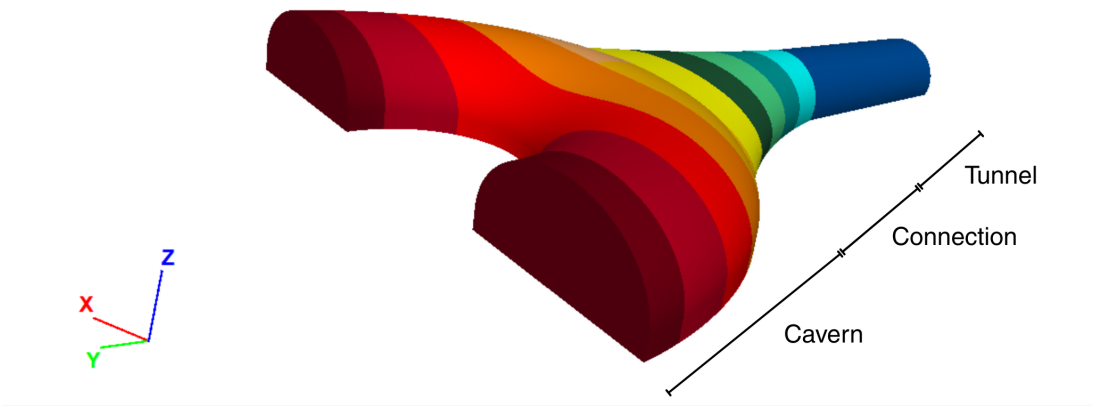
Correlation	**Cavern 1**		**Cavern 2**	
	ϕ [°]	c [MPa]	ϕ [°]	c [MPa]
Hoek et al. (2002)	60	1.78	63	2.62
Sofianos & Nomikos (2006)	51	3.71	58	3.31
Jimenez et al. (2008)	52	3.04	58	3.59
Meng et al. (2016)	52	2.85	58	3.67
Barton (2002)	56	7.00	76	2.33

However, Sofianos and Nomikos (2006) caution against applying their model to unsupported excavations such as the one to be analysed in the current numerical model, and Meng et al. (2016) emphasise relevant improvements from their formulation in case of poor-quality rock and high-stress conditions. While basalt may not be considered poor-quality rock, the method provided by Meng et al. (2016) is preferred for its purely mathematical formulation and its independence from arbitrary parameters like ξ_C^* used in Jimenez et al. (2008).

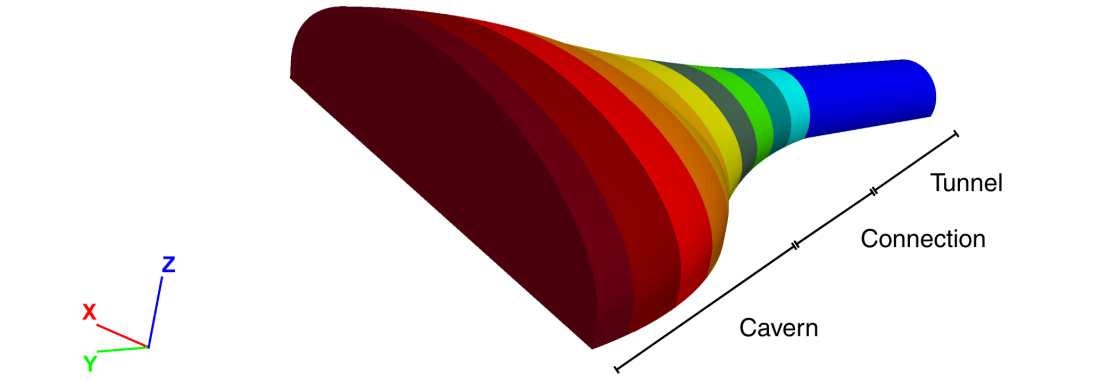
7.6 Drill and blast sequential excavation stages

The excavation process—including the 50 m approach tunnel, 20 m connection, and the roundabout—is modelled in accordance with the sequential excavation method. Each blasting block is set to 5 m thickness, yielding overall 13 to 16 blocks depending on the outer radius R (Fig. 7.7).

Excavation is simulated by assigning null material to a block, releasing stress around it, and allowing the model to stabilise. Simulations employ the Finite Volume Method (FVM).



(a)



(b)

Figure 7.7: Excavation blocks in a pillar (a) and non-pillar (b) input geometry. The stages of excavation are as follows: 6 blocks for the tunnel section (blue), 4 blocks for the connection (light blue to dark green), and between 3 to 6 blocks (or couple of blocks) for the roundabout (yellow to dark red).

Due to the high computational cost of each stability analysis, the excavation is initially simplified by removing the entire tunnel section (six blocks) in a single stage. Additionally, whether the central pillar is included within the cavern (Fig. 7.7a), both sides of the widening are blasted simultaneously. While the first assumption is acceptable for this study—where the tunnel is not the primary focus—the latter simplification may overestimate stresses and displacements

in the key excavation element compared to real sequential blasting practices, which impose excavation on only one side at a time (see Section 1.3, Chapter 1). If such overestimation proves excessive, the excavation will be revised to two stages on either side of the pillar.

Mechanical equilibrium at each stage is evaluated via the local mechanical ratio (stress-to-strain ratio per control volume). The maximum value across the model guides each iteration. Convergence is instead assessed through the average mechanical ratio, typically peaking after excavation initiates and then gradually declining (Fig. 7.8).

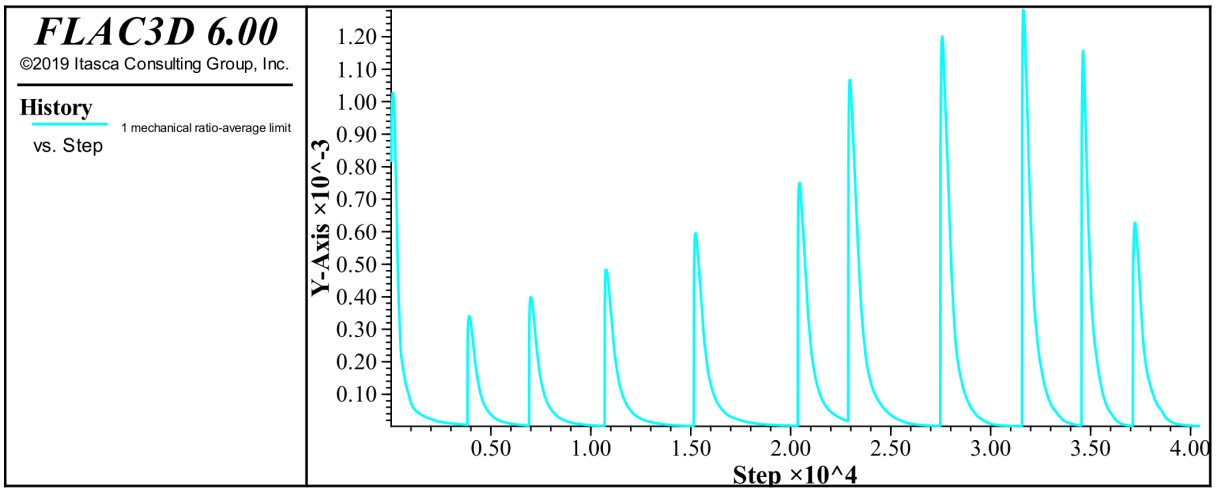


Figure 7.8: Average mechanical ratio evolution during the excavation stages of a cavern with arbitrary outer (R) and pillar (r) radius. Each subsequent excavation step is executed once the system's equilibrium drops below a predefined threshold. The first peak appears significantly higher than the subsequent ones, as all six tunnel blocks were excavated in a single step, causing increased instability.

Numerical model configuration – Conclusions

The numerical model is designed for scalability and computational efficiency. It employs a consistently scaled parallelepiped domain with fixed offsets, ensuring comparability across excavation scenarios. Simplifying the top boundary to a combination of flat surface and uniform distributed load—justified by low-resolution bathymetric data and a gentle seabed slope—strongly reduces computational load. Geometric symmetry is exploited through a half-domain configuration, still preserving the accuracy. In the absence of in-situ stress data, purely gravitational loading is assumed for the vertical component. The horizontal component is addressed through a planned parametric study exploring a range of horizontal-to-vertical stress ratios from 0.5 to 2.5. Furthermore, the use of the HB–MC fitting method from Meng et al. (2016) provides a robust approach for obtaining reliable material parameters for the MC criterion.

However, the model has several important limitations. It assumes lithological homogeneity, ignoring significant stratigraphic and structural heterogeneity—especially the thin interflow layers—limiting local stress prediction accuracy and likely the ability to capture some potential failure mechanisms. Hydro-mechanical coupling is excluded, reducing the model's realism in water-sensitive formations. Scenario-specific meshing introduces minor mutual variations that may affect comparability. The use of gravitational stress without field calibration can result in inaccurate boundary stresses, particularly in fractured zones. Assuming simultaneous mobilisation of cohesion and frictional strength may lead to unrealistic shear strength parameters and unrepresentative breakout and stress-failure predictions (Vallejo and Ferrer, 2011). Furthermore, staged excavation is modelled in large discrete steps rather than incremental sequences, potentially exaggerating stress redistribution.

In conclusion, the impossibility of performing a model calibration remains a huge limitation. Thereby, as already mentioned in the introduction, the current modelling approach is to be considered purely theoretical.

7.7 Numerical simulations plan

Following the model development, a two-stage simulation strategy is adopted. In the first stage, the numerical response is examined across varying geometries while keeping the continuum medium and failure properties fixed. The second stage investigates the effects of varying material typologies, properties, and failure criterion parameters on the model response

7.7.1 First round

The first simulation phase focuses on the effects of varying the roundabout size and central support thickness. Geometries follow design guidelines specifying external radius R and corresponding pillar radius r as discussed in Section 6.3, Chapter 6. R is set to increase in 1 m steps from 13 to 16 m, then in 2 m increments up to 30 m. Steps will be reduced to 1 m if results show significant changes. Likewise, r increases by 0.5 m up to 3 m, then by 1 m to the maximum radius $r_{\max}$ for each R (see Fig. 6.7, Chapter 6). This yields 116 geometry cases and simulations in total. Due to high computational cost required, the Mohr–Coulomb (MC) elastoplastic model is adopted in this first simulations round.

Caverns 1 and 2 are equally relevant, but modelling both would double the number of simula-

tions. Their load conditions are comparable: Cavern 2's higher seawater column balances its lower rock overburden, and stratigraphic differences are moderate (see Section 7.3). Therefore, modelling a single cavern may be considered sufficient. In-situ stress estimates indicate that the *Enni Formation* basalts have a higher horizontal-to-vertical stress ratio ($k \approx 1.5$) than the *Malinstindur* ($k \approx 0.5$–1.0), despite local variability. These regimes affect failure mechanisms differently (spalling/slabbing vs. roof stability), so no clear preference for k can be established.

Table 7.4: Mechanical properties characterising the rock mass for the first simulation round.

Rock mass	Modulus	Poisson's ratio	Cohesion	Friction	Tensile strength
Basalt (lava core)	37 GPa	0.284 [-]	2.85 MPa	52°	0.21 MPa

Cavern 1 is finally chosen due to its lower HB (and consequently MC) parameters (Tab. 5.7, Chapter 5), despite slightly better elastic properties (Tab. 4.1, Chapter 4). Mechanical properties for the first simulations round are listed in Tab. 7.4. Subsequent simulations will also prioritise *Enni Formation* basalt properties over *Malinstindur* when a choice is required.

7.7.2 Second round

The first simulation round provides an overview of principal stresses and displacements across all input geometries, assuming average lava core continuum properties and in-situ stresses. At the end of this phase, two final geometries—one with a central pillar and one without—are selected based on:

(1) Maximum induced compressional stress
(2) Depth and magnitude of tensional stress zone relative to excavation
(3) Maximum induced translational displacement
(4) Expected tunnel traffic flow
(5) Potential water inflow (analysed in Section 4.4, Chapter 4)

Following the selection of the two candidate geometries, the second simulation phase comprises three stages:

(i) **Sensitivity Analysis**: A local and global sensitivity analyses are performed on both pillar and non-pillar design to evaluate the impact of uncertain parameters, namely the horizontal-to-vertical stress ratio (k), uniaxial compressive strength (UCS), Young's

modulus (E), and Poisson's ratio (ν), while retaining the *Enni Formation* basaltic lava core as the reference continuum medium.

(ii) **Material Variation Study**: Both Cavern 1 and 2 are also tested in the volcaniclastic sandstone and brecciated flow top units, identified from boreholes and field mapping, to account for the potential involvement of these geologies in the excavation-induced arching effect despite the dominance of basaltic lava core and crust.

(iii) **Disturbance Factor Analysis**: A final analysis investigates the effect of the Hoek–Brown (HB) disturbance factor ($D \in [0, 1]$), extending prior simulations which all assumed $D = 0$ (ideally undisturbed blasting), to identify the threshold at which stress and displacement around the excavation significantly change.

All simulations use the Hoek–Brown PAC model, suitable for brittle materials like basalt and sandstone and more accurate than MC in terms of results, despite computationally more demanding.

Sensitivity analysis

The sensitivity analysis evaluates how uncertainty in key parameters—horizontal/vertical stress ratio (k), uniaxial compressive strength (UCS), Young's modulus (E), and Poisson's ratio (ν)—affects the model response. It consists of two parts:

- **Local one-at-a-time (OAT) analysis**, varying each parameter individually around a baseline (i.e. average values) using its 5th and 95th percentiles (Tab. 7.5), for a total of 9 simulations per geometry. The main goal is to identify which parameters have the most immediate impact near the baseline scenario.
- **Global analysis**, assessing full-range simultaneous variation with 4 levels for k, 3 for UCS, and 2 for both E and ν (Tab. 7.6).

Table 7.5: Low and high bound of the four parameters to perform the local sensitivity analysis, alongside with the baseline scenario inputs.

Parameter	Baseline scenario	Low bound	High bound
k	1.5 [-]	0.5 [-]	2.5 [-]
UCS	105 MPa	80 MPa	130 MPa
E	37 GPa	11 GPa	64 GPa
ν	0.284 [-]	0.228 [-]	0.340 [-]

In the global sensitivity analysis, only the 50th and 5th percentiles of Young's modulus and Poisson's ratio are considered. This range has been identified as well representative but also the most interesting to study based on comparisons between geophysical and empirical relationships used to estimate the deformation modulus (refer to Section 5.3.6, Chapter 5). Regarding Poisson's ratio, selecting its 50th percentile reflects more brittle-like material properties in the medium.

Table 7.6: Parameter levels used for the global sensitivity analysis. Note that the Young's modulus and Poisson's ratio do not have levels higher than the baseline scenario, since the focus is on studying the model response with weaker and brittle-like (i.e., lower percentiles) mechanical properties.

Parameter	Level 1	Level 2	Level 3	Level 4
k	0.5 [-]	1.0 [-]	1.5 [-]	2.5 [-]
UCS	80 MPa	105 MPa	130 MPa	—
E	11 GPa	37 GPa	—	—
ν	0.228 [-]	0.284 [-]	—	—

By considering both pillar and non-pillar geometries, the total number of simulations for the global sensitivity is set to 96. To reduce this amount and relative computational costs, the Taguchi method is employed. Introduced by Taguchi (1986), this method uses orthogonal arrays to efficiently sample the parameter space. The Taguchi method is still applicable even when parameters have mixed levels, as is the case in this study. Its first stage involves calculating the degrees of freedom (DoF) for each parameter. Assuming all factors are independent, the DoF are as follows:

Factor $k \rightarrow$ 4–1 = 3 DoF Factor $E \rightarrow$ 2–1 = 1 DoF

Factor $UCS \rightarrow$ 3–1 = 2 DoF Factor $\nu \rightarrow$ 2–1 = 1 DoF

for a total of 7 DoF.

In this case, an L16b array is suitable for the design, as it accommodates up to 15 degrees of freedom and allows for 4 levels across a maximum of 5 factors. Consequently, the number of simulations per geometry is significantly reduced from 48 to 16 (32 in total). Simulations within the L16b array must be organised in a way that preserves their statistical independence.

Model response to different materials

In addition to basalt, two other main geotechnical units—interlava volcaniclastic sandstone and brecciated basaltic units—are present within the Sandoy–Suðuroy stratigraphy. They fall, respectively, within the "sediment" and "lava breccia" material groups defined in Section 4.1, Chapter 4. Though thinner and more discontinuous than basalt flows, they may still be involved in the arching effect due to excavation widening. Moreover, because of their low dip angles, these weak units can remain exposed along the excavation surface for tens of meters whether intersected, justifying their inclusion in separate analyses.

Based on borehole data, the average continuous layer thicknesses in the *Enni Formation* are approximately 1.75 m for sandstone and 4.00 m for lava breccia (Petersen et al., 2022). Although reliable estimates are unavailable for the *Malinstindur Formation*, similar or slightly lower values are expected, along with a reduced frequency. Given the relatively thin sedimentary or breccia/conglomerate units compared to the 60 m vertical model domain, a simplified approach is used by assigning either sandstone or breccia properties to the entire domain. This simplification is justified by the following considerations:

(i) The sub-horizontal lithostratigraphy primarily affects roof stability and pillar integrity in zones of weaker material, while making shearing phenomena less likely. These failure mechanisms are expected to be amplified, not fundamentally altered, even when basalt is not the dominant lithology.

(ii) The mono-material assumption of the model and the resulting equivalent depth transformation introduced in Section 7.3, which would otherwise necessitate extensive model modifications and potentially lead to incompatible results.

Despite an accurate characterisation of HB properties for lava core basalts in both the Upper and Middle Formations based on desk study and field mapping, the m_i parameter remains unknown. Data on sandstone and breccia are even more incomplete (see Table 5.7, Chapter 5). Therefore, these missing values must be supplemented. This is accomplished using SINTEF laboratory test results from project samples across the Faroe Islands, along with theoretical reference values for the constant mi obtained from RocLab® (Rockscience®). All parameters and their sources are detailed in Tab. 7.7, with project names anonymised as “Project 3,” “Project 4,” and “Project 5.”

Table 7.7: Average properties of the three main material groups, corresponding to the (a) Enni and (b) Malinstindur Formations, representing the input for the simulations set related to material characterisation.

Enni Formation			
Lava core	$\rho = 2790$ kg/m^3[4]	$E = 37$ GPa[4]	$\nu = 0.284$ [-][4]
	$UCS = 105$ MPa[2][5]	$GSI = 60$ [-][5]	$mi = 25$ [-][6]
Lava breccia	$\rho = 2580$ kg/m^3[4]	$E = 30$ GPa[4]	$\nu = 0.306$ [-][4]
	$UCS = 94$ MPa[3]	$GSI = 37$ [-][5]	$mi = 19$ [-][6]
Sandstone	$\rho = 2330$ kg/m^3[4]	$E = 20$ GPa[4]	$\nu = 0.269$ [-][4]
	$UCS = 54$ MPa[3]	$GSI = 40$ [-][5]	$mi = 17$ [-][6]

(a)

Malinstindur Formation			
Lava core	$\rho = 2730$ kg/m^3[4]	$E = 36$ GPa[4]	$\nu = 0.277$ [-][4]
	$UCS = 120$ MPa[2]	$GSI = 70$ [-][5]	$mi = 25$ [-][6]
Lava breccia	$\rho = 2500$ kg/m^3[4]	$E = 29$ GPa[4]	$\nu = 0.294$ [-][4]
	$UCS = 94$ MPa[3]	$GSI = 37$ [-][5]	$mi = 19$ [-][6]
Sandstone	$\rho = 2390$ kg/m^3[4]	$E = 18$ GPa[4]	$\nu = 0.269$ [-][4]
	$UCS = 54$ MPa[3]	$GSI = 40$ [-][5]	$mi = 17$ [-][6]

(b)

[1] SINTEF Project 3.
[2] SINTEF Project 4.
[3] SINTEF Project 5.
[4] GEUS (Waagstein and Andersen, 2004).
[5] Field mapping (this project).
[6] RocLab® (Rocscience®).

Influence of the disturbance factor

In the HB failure criterion the disturbance factor (D) represents the degree of damage from excavation activities (e.g., blasting, stress relief, Hoek et al., 2002). Ranging from 0 (undisturbed rock mass) to 1 (highly disturbed rock mass), D accounts for strength and stiffness degradation (Hoek and Brown, 1997). While TBM or road-header methods cause minimal disturbance, selecting D is crucial to model drill-and-blast operations, as higher values can significantly affect rock mass strength parameters in the model.

Previous models for this project assumed a baseline value of $D = 0$, despite the uncertainty surrounding the blasting quality, which was not clarified by the client. Therefore, a final

analysis is conducted using D values of 0.2, 0.4, 0.6, 0.8, and 1.0 to assess percentage changes in stresses and displacements relative to the baseline scenario. The simulations use lava flow core material from the *Enni Formation* for both pillar and non-pillar excavation cases (10 simulations in total).

Although Hoek and Brown (2019) advise against assigning a uniform D across the entire model domain and instead recommend varying this parameter within a 2–3 meter zone around the excavation, localised remeshing of the current model would be in this case required and consequently hinder comparison with previous analyses. Therefore, a uniform D is applied, with the awareness that the resulting analyses will produce conservative outcomes.

8

Numerical modelling results

Mongum brestur ætlan

Things don't always go as planned

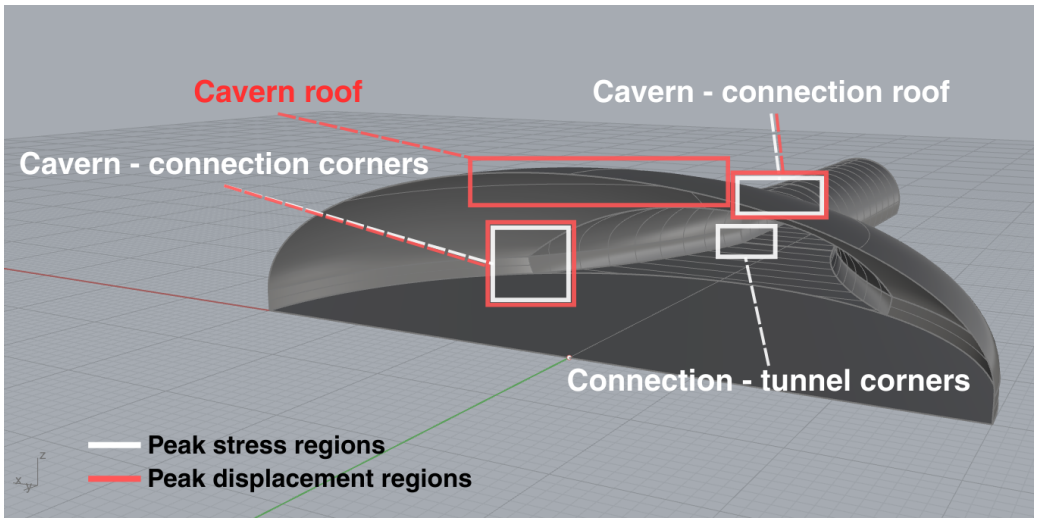
Results of the numerical simulations conducted using the previously detailed two-stage modelling strategy are presented in this chapter. Geometrical range testing of the excavation, combined with uncertainty characterisation of key parameters, enabled alignment between the project's macro areas of engineering geology, geotechnical and geophysical site characterisation on one hand and preliminary design development on the other. Graphical visualisations are extensively used to display simulation results, providing an immediate overview and understanding of the outcomes. Due to the lack of calibration of the numerical models, quantitative results are extensively complemented by a qualitative assessment, which, despite the limited pinpoint accuracy, offers valuable insights.

The chapter concludes with a brief section on the structural support characterisation for the two final selected geometries, based on estimated Q-values for lava core, lava breccia (flow top), and sediment (sandstone) from the field mapping campaign. Although these supports were not integrated into the model, the estimated bolt lengths, spacings, and shotcrete thicknesses can serve as a useful starting point for future research and modelling efforts.

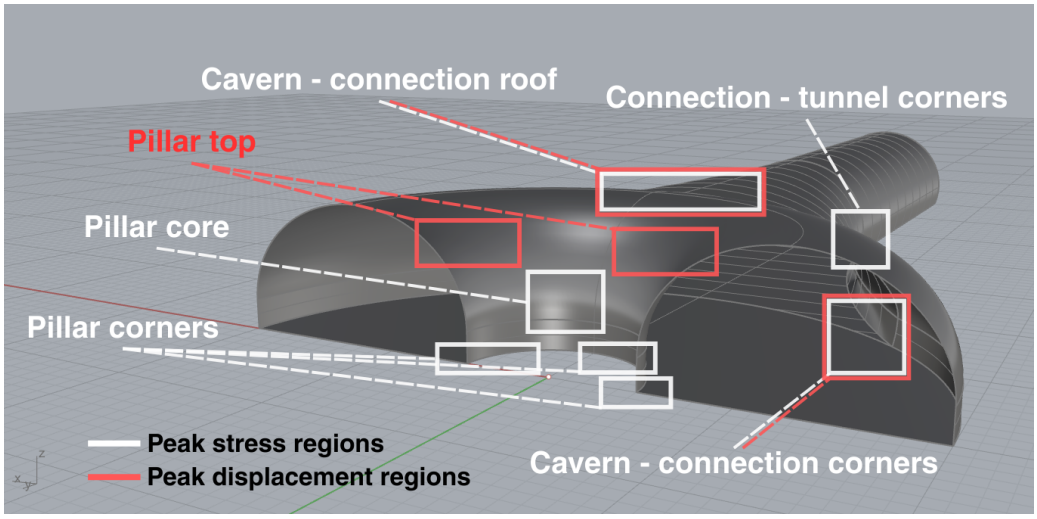
8.1 First simulations round

A total of 116 simulations are conducted to evaluate 11 external radii (R) configurations, with central pillar radii (r) ranging from 0 up to 18 m. The model assumes a basaltic lava core governed by the Mohr–Coulomb (MC) elastoplastic failure criterion, with parameters derived from the *Enni Basalt Formation* (Cavern 1; see Tab. 7.4, Chapter 7).

Three output variables are analysed: (i) major principal stress σ_1, (ii) minor principal stress σ_3, and (iii) translational displacement along the excavation. For each, the peak magnitude and their distribution within the excavation (Fig. 8.1) are recorded.



(a)



(b)

Figure 8.1: Characteristic regions of peak stress and displacement localisation along (a) non-pillar and (b) pillar geometries.

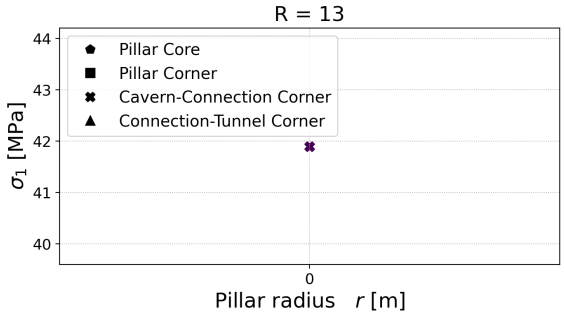
Peak stresses locations fall within five characteristic zones: (i) pillar core, (ii) pillar corners (pillar–cavern base), (iii) cavern–connection roof, (iv) cavern–connection corners, and (v) connection–tunnel corners.
Maximum displacements are also concentrated in four typical areas: (i) cavern roof (for $r = 0$), (ii) pillar top, (iii) cavern–connection roof, and (iv) cavern–connection corners.

Note: FLAC3D adopts a sign convention where compressive stresses are negative and tensile stresses are positive. Thus, σ_1 and σ_3 refer to minimum and maximum principal stresses, respectively. In plots external to FLAC3D, a geotechnical convention is used, treating compressive stresses as positive.

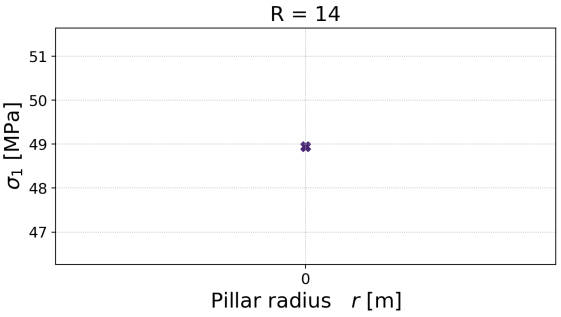
Stress

Outcomes in terms of peak maximum principal stress for each geometry are illustrated in Fig. 8.2. The lowest σ_1 peak values along the R-series occur in geometries without central pillars, confirming the effectiveness of the 1:5 diameter-to-roof arch ratio. In these cases, stress is redistributed to the outer walls, indicating structurally valid span arches. The highest σ_1 values among non-pillar cases are seen in $R = 13$ m (Fig. 8.2a) and $R = 14$ m (Fig. 8.2b), which apply a slightly lower ratio (1:4) due to design constraints (see Section 6.3, Chapter 6).

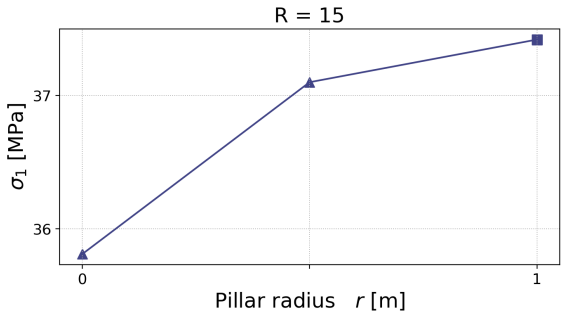
Across most R-series geometries, peak σ_1 consistently occurs at $r = 1$ m, except within the range $R = 20$–24 m, with peak values at $r = 0.5$ m positioned between those at $r = 0$ m and $r = 1$ m. As the outer radius increases, these intermediate values shift closer to the $r = 0$ m values. At $r = 1$ m, stress localisation varies by range: it occurs at cavern–connection or connection–tunnel corners for $R = 13$–20 m, and at pillar cores or corners for $R = 22$–30 m. Beyond the peak at $r = 1$ m, σ_1 drops sharply at $r = 1.5$ m and continues to decline, in some cases approaching the magnitudes observed at $r = 0$ m. Some irregularities arise, likely due to local stress concentrations or meshing artifacts inherent in the semi-automated process and therefore difficult to fully control (refer to Appendix E.1).


R = 13
Pillar Core
Pillar Corner
Cavern-Connection Corner
Connection-Tunnel Corner
σ_1 [MPa]
Pillar radius r [m]

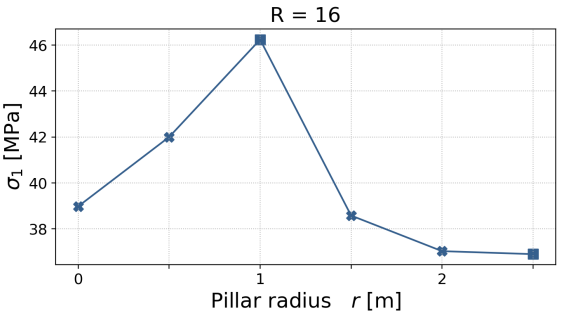
(a)


R = 14
σ_1 [MPa]
Pillar radius r [m]

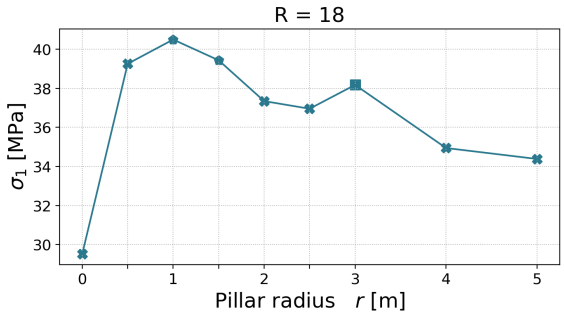
(b)


R = 15
σ_1 [MPa]
Pillar radius r [m]

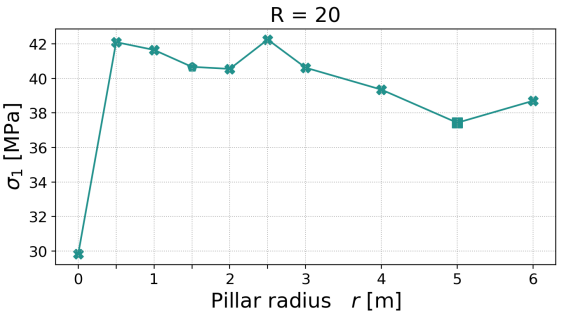
(c)


R = 16
σ_1 [MPa]
Pillar radius r [m]

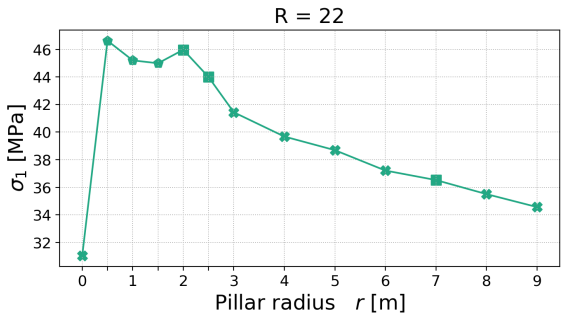
(d)


R = 18
σ_1 [MPa]
Pillar radius r [m]

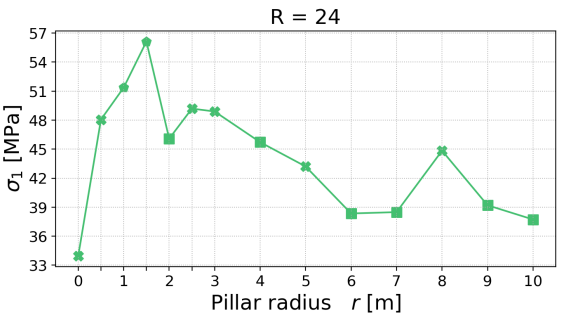
(e)


R = 20
σ_1 [MPa]
Pillar radius r [m]

(f)


R = 22
σ_1 [MPa]
Pillar radius r [m]

(g)


R = 24
σ_1 [MPa]
Pillar radius r [m]

(h)

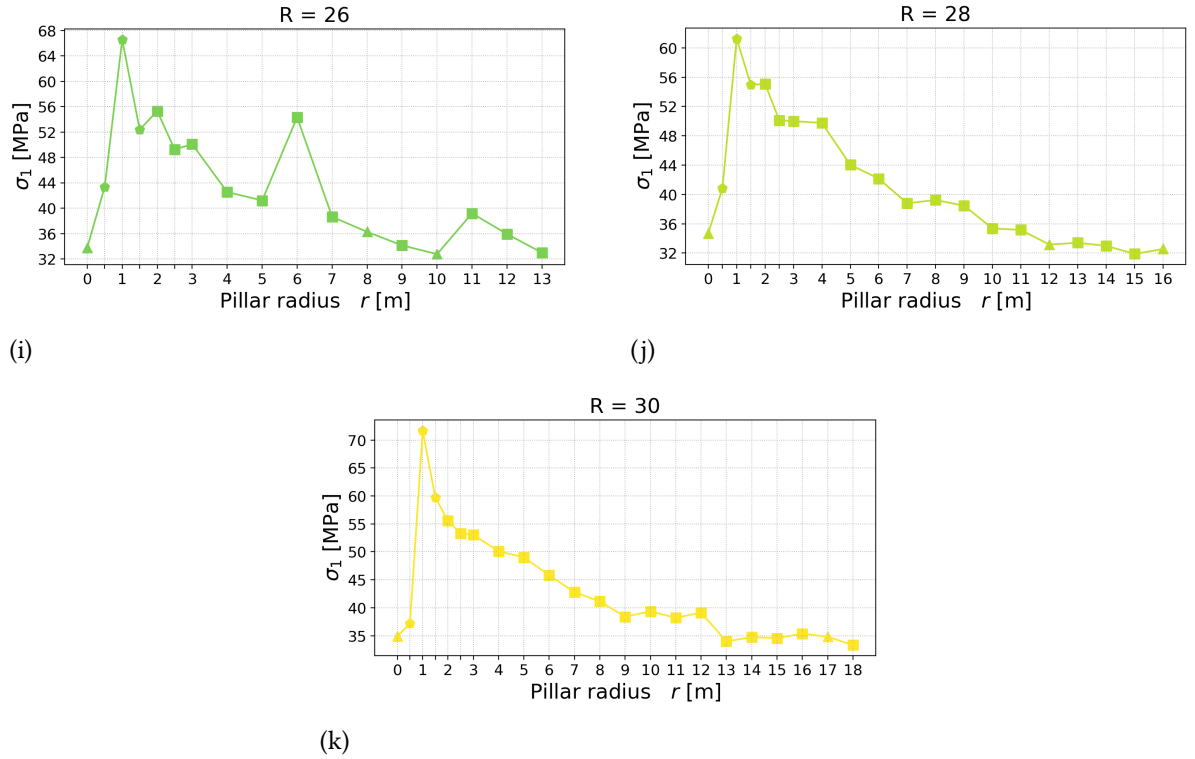


Figure 8.2: Evolution of major principal peak stress for different pillar radii along each R-series.

Among the identified stress peaks, values exceeding half of the defined *UCS* for the lava core continuum—and thus surpassing the moderate stress regime—begin to appear starting from the $R = 24$ m series onward (Fig. 8.2h–k).

By focussing on the pillar element (Fig. 8.3), the stress distribution evolves with increasing r, not only in magnitude but also in the localisation of stress concentrations. At $r = 0.5$ m it is uniform (Fig. 8.3a); at $r = 1$ m, a highly stressed core emerges (Fig. 8.3b); by $r = 1.5$ m, stress becomes more evenly distributed again along the cross section (Fig. 8.3c). For $r \geq 2$ m, stress concentrates at the pillar's outer edges and floor contact points (Fig. 8.3d–e). In some geometries (e.g., $R = 20$ and 22 m), peak stress occurs at $r = 0.5$ m, thereby resembling the distribution seen instead at $r = 1$ m in the previously discussed case.

However, the distinct stress peak generally observed at $r = 1$ m, and not at $r = 0.5$ m, indicates that a pillar with $r = 1$ m may in most of the R-series still be sufficient to bear the excavation-induced loads—although with extremely high energy stored in the core, potentially triggering failure initiation. In contrast, localised yielding commenced at $r = 0.5$ m. Generally speaking, the closer the peak stress at $r = 0.5$ m is to that at $r = 0$ m, the greater the likelihood of plastic failure initiation; the closer it is to the peak at $r = 1$ m, the more energy remains stored in the pillar.

Simulations reproduce the well-known formation of a pressure arch around underground cavities—often utilised for rock bolt installations (Li, 2017)—with tangential stress increases observed between 2 and 6 m from the surface within the surrounding rock mass.

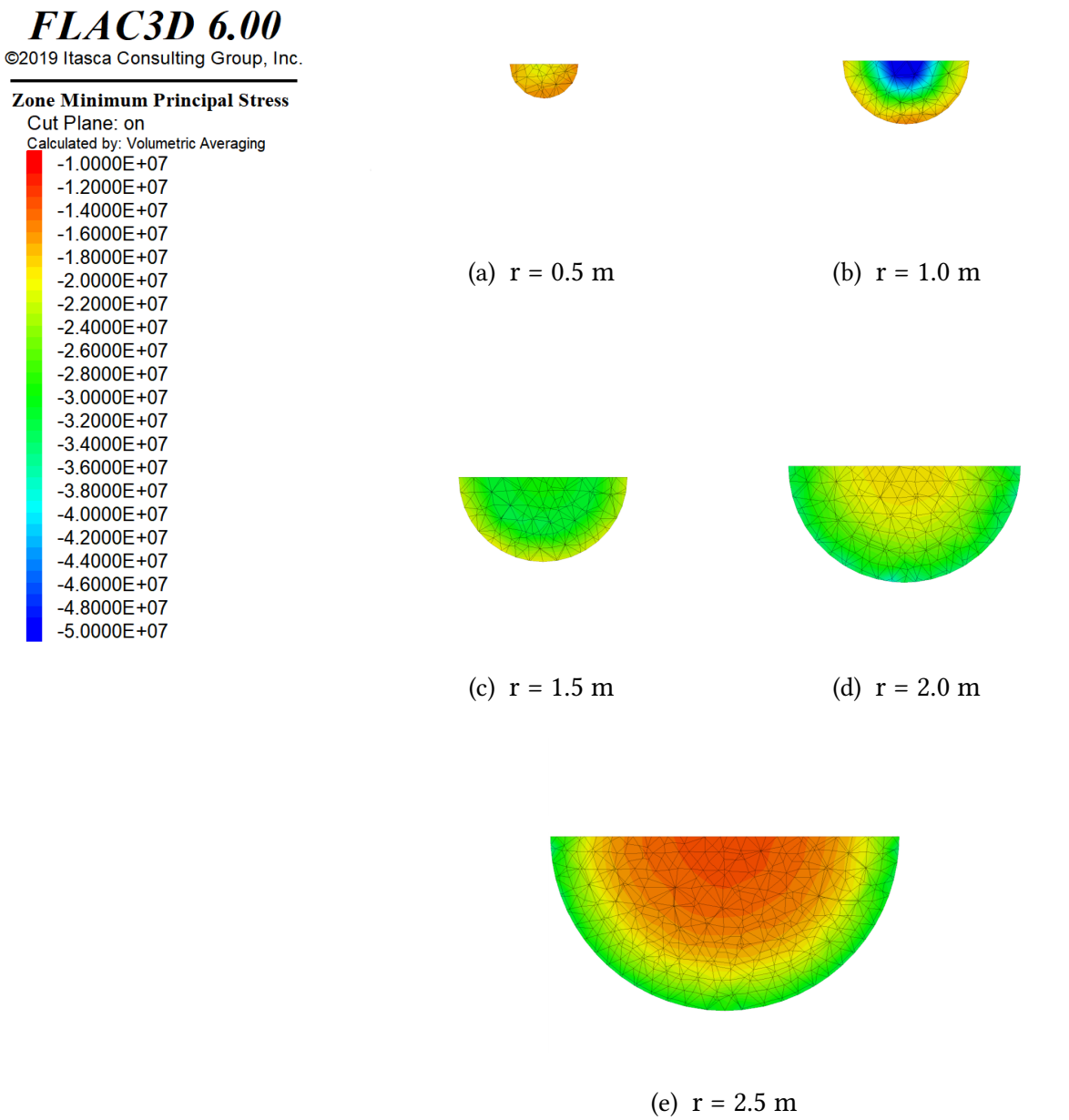
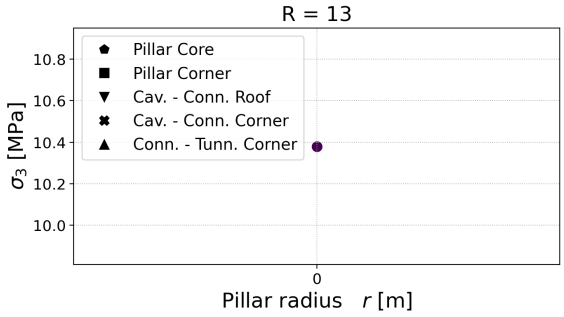
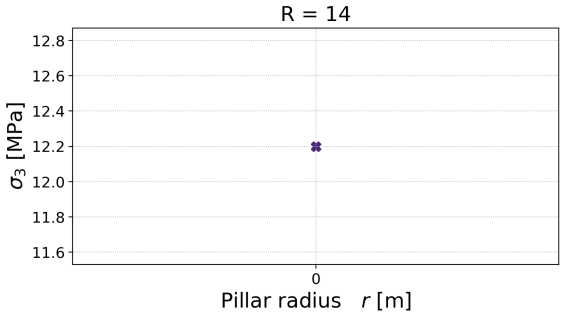


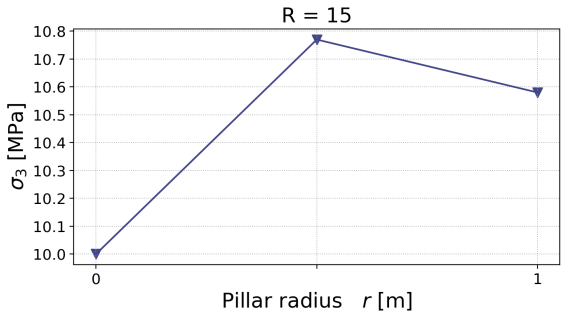
Figure 8.3: Stress distribution and magnitude evolution in the pillar element core and edges by varying its radius from 0.5 to 2.5 m. The reference geometry series is R = 26 m.


R = 13
Pillar Core
Pillar Corner
Cav. - Conn. Roof
Cav. - Conn. Corner
Conn. - Tunn. Corner
σ_3 [MPa]
Pillar radius r [m]

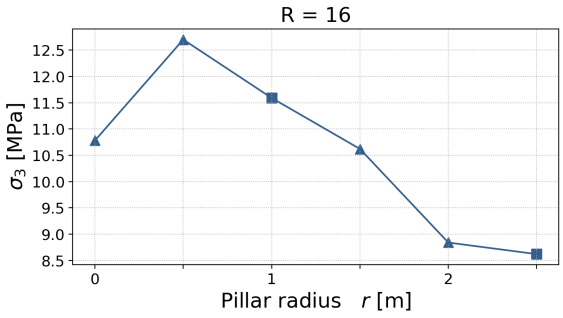
(a)


R = 14
σ_3 [MPa]
Pillar radius r [m]

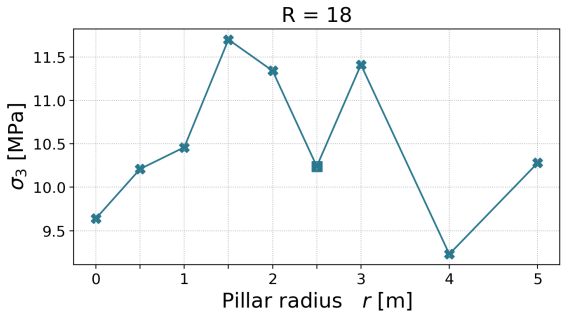
(b)


R = 15
σ_3 [MPa]
Pillar radius r [m]

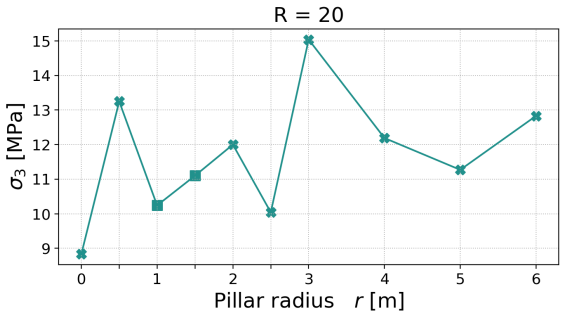
(c)


R = 16
σ_3 [MPa]
Pillar radius r [m]

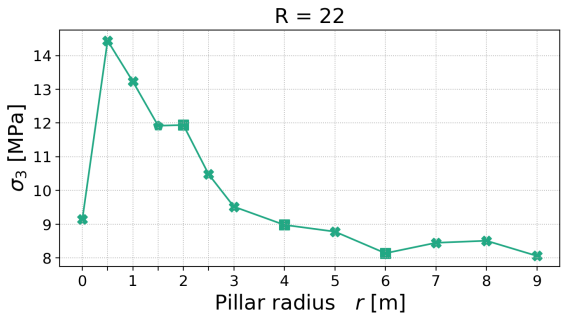
(d)


R = 18
σ_3 [MPa]
Pillar radius r [m]

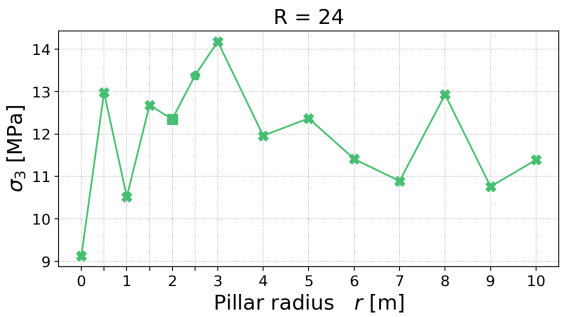
(e)


R = 20
σ_3 [MPa]
Pillar radius r [m]

(f)


R = 22
σ_3 [MPa]
Pillar radius r [m]

(g)


R = 24
σ_3 [MPa]
Pillar radius r [m]

(h)

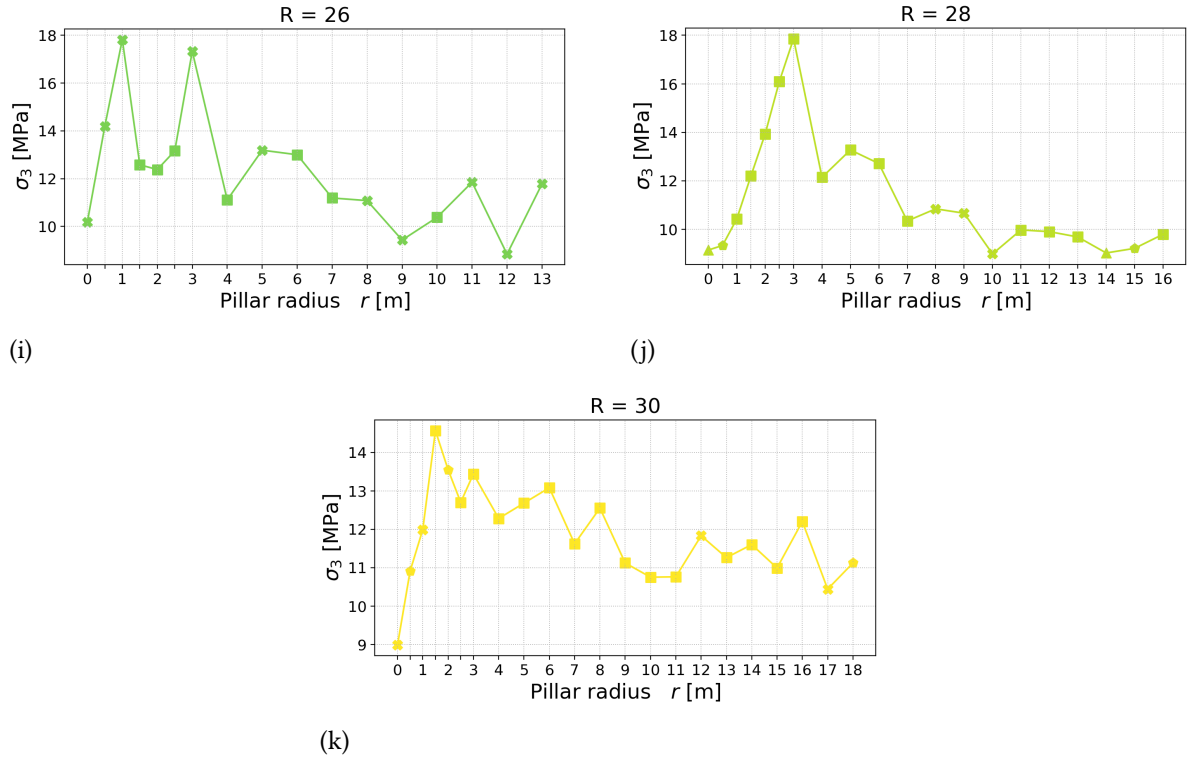
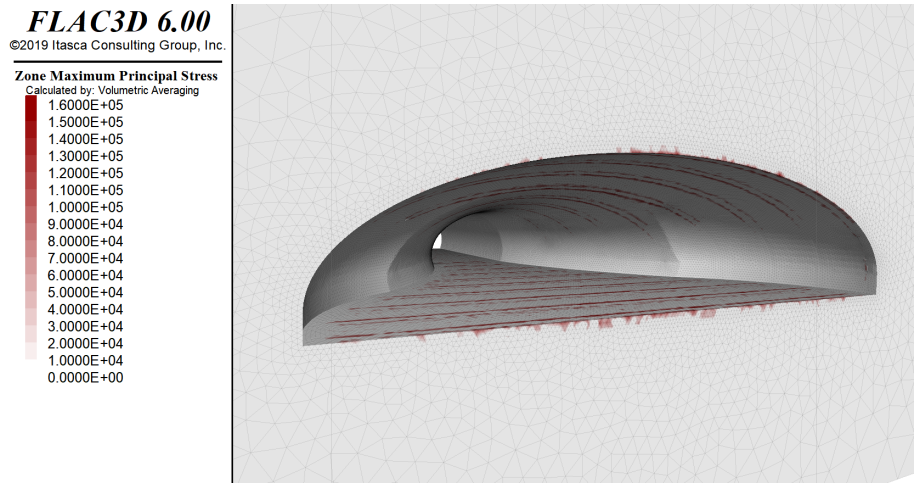


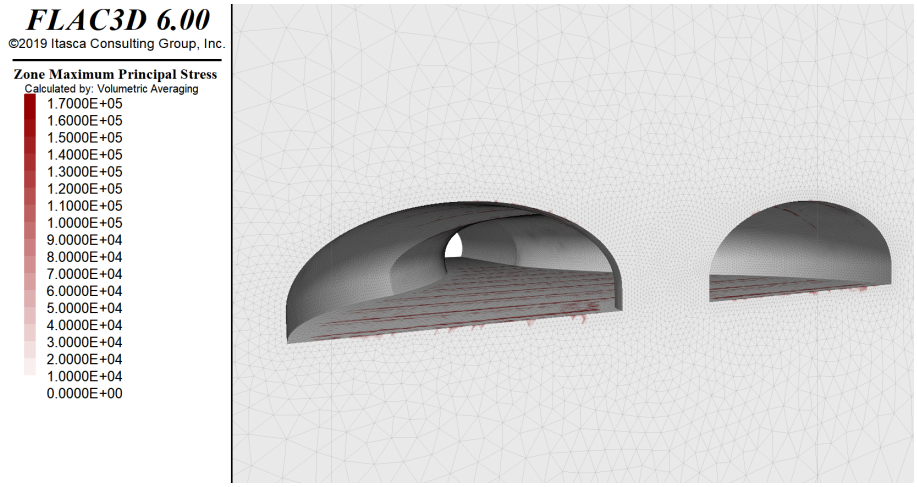
Figure 8.4: Evolution of minor principal peak stress for different pillar radii along each R-series.

Minor principal stress trends are less distinct (Fig. 8.4), with still minimum values at $r = 0$ in most R-series. The sharp σ_1 peak near $r = 1$ m is diminished in σ_3, whose maximum spans a broader range ($r = 1$–4 m), then gradually decreases with increasing r, with some exceptions for $r = 18$, 20 and 24 m. Peak σ_3 localisation within the excavation closely aligns with that of σ_1.

Tensile stress areas (Fig. 8.5) remain localised along the excavation, with concentrations primarily occurring at the excavation face and contour corners during blasting stages—particularly in the floor and roof, where low-pressure zones and stress drops develop. In some simulations of the $R = 26$ m series, their magnitudes approach the tensile strength assigned in the model (0.21 MPa; see Tab. 7.4, Chapter 7), with peak values reaching 80–85% of σ_t. This indicates a marginally stable stress regime with a high likelihood of tensile fracture initiation.



(a)



(b)

Figure 8.5: Extension and magnitude range of tensional areas in (a) pillar and (b) non-pillar excavations. The reference geometries are the R = 26 m, r = 0 m and r = 4 m, respectively.

Displacement

Displacement patterns across different R-series show high regularity (Fig. 8.6). A sharp increase occurs between $r = 0$ m and $r = 0.5$ m, followed by a gradual decline as r increases. For $r \geq$ 2–3 m, pillar geometries start showing lower displacements than $r = 0$ m along the different R-series. Concurrently, peak translational displacement shifts from the pillar roof to the cavern–connection roof, which is now the largest span. Notably, increasing the excavation radius up to $R = 30$ m does not substantially raise much larger displacement gaps between one series and the next, even when thin pillars are employed. Only at $R = 30$ m the peak magnitude

does shift from $r = 0.5$ m to $r = 0$ m (non-pillar case).

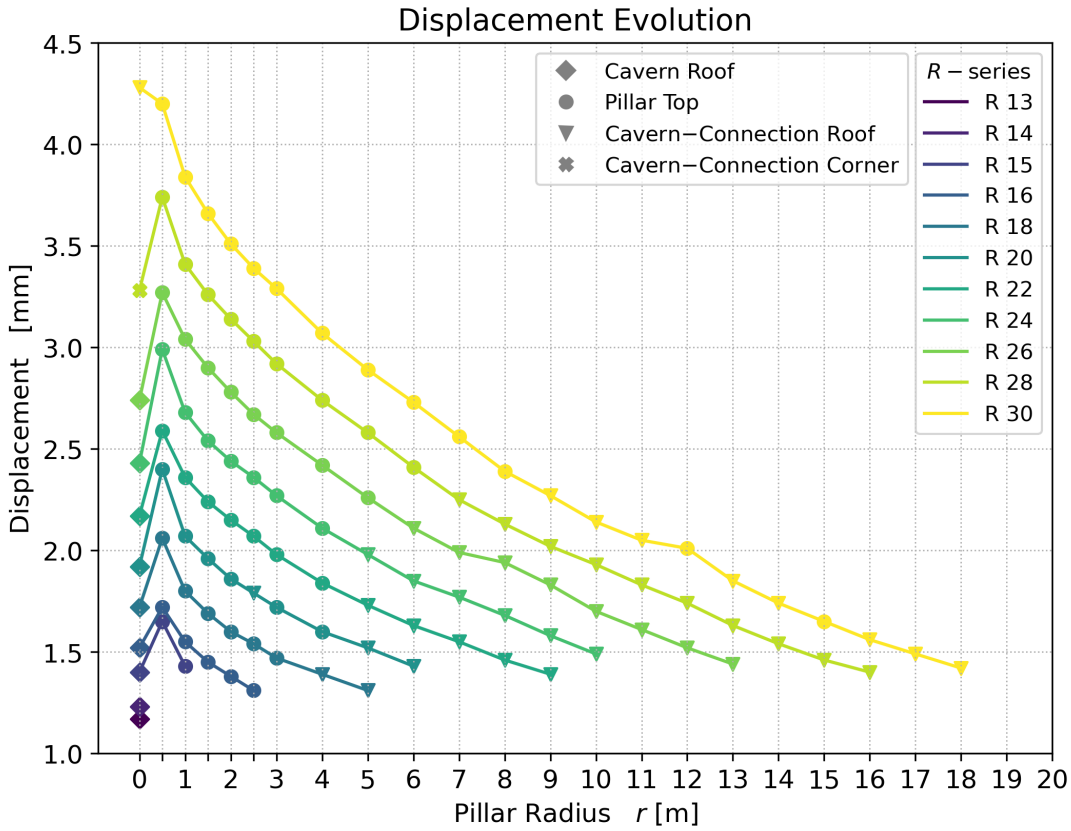


Figure 8.6: Evolution of translational displacements for different pillar radii along each R-series.

Discussion

Based on the model responses, some observations regarding the numerical model configuration and its consequent performances can be drawn:

(i) Modelling all six tunnel blocks as a single excavation phase is conservative but valid; peak stresses and displacements still consistently occur in the cavern and adjacent blocks, thereby without shifting the focus from the most important element of the model.

(ii) The continuum's favourable mechanical properties permit excavation of blocks on either side of the central pillar contemporary or the full cavern face when the pillar is absent, though real blasting will proceed in stages anyway.

(iii) The selected 2 m step size from $R = 16$ to $R = 30$ m is adequate; stress and displacement trends remain consistent, aside from minor outliers.

While focusing on the evolution of principal stresses and displacements with respect to their

contour paths and magnitudes within the model outcomes, the following key points emerge:

1. No shear failure or plastic collapse was observed in the roof, pillars, or other areas in any of the simulations, even during large-scale excavations. Localised failure initiation may be hypothesised at excavation corners or in the pillar core in simulations where peak stresses exceeded half the *UCS* value (105 MPa), identified in specific geometries among the $R = 24$–30 m series (see Fig. 8.2). This widespread stability may be attributed to: (i) adequate strength of the continuum material, and (ii) limitations of the continuum-based finite volume model using the MC criterion in capturing brittle failure along joints or fractures. To better represent the fracture-prone nature of the rock, future studies could benefit from adopting a discontinuum approach. The *Q*-values obtained from the field mapping campaign, when compared to the image reproduced from Barton (2022) further support the selection of DEM modelling as the most appropriate method for this problem (refer to Fig. 1.7, Chapter 1).

2. A preliminary identification of failure modes beyond the scope of an elastoplastic continuum framework, along with initial reinforcement considerations, can already be derived from stress and displacement contours. A more refined evaluation—incorporating the lava breccia and sediment geotechnical units within both final geometries (pillar and non-pillar)—will follow in the simulations' second phase.

   Non-pillar configurations: Principal stresses (major and minor) concentrate at outer corners, with the cavern–connection junction emerging as a critical area due to stress concentration, partly attributed to incomplete CAD corner rounding. Maximum displacements and low stress contours localise at the cavern roof, indicating that gravitational collapse via roof block failure is the dominant mechanism in the absence of supports, even under significant horizontal confinement. This failure mode becomes even more likely in regions where tensile stresses develop, as they facilitate the initiation and propagation of fractures leading to block detachment. Thus, support strategies should prioritise stabilising detached roof blocks, with strength being the primary design parameter for reinforcements (Li, 2017).

   Pillar configurations: slender pillars show stress concentration near the core of the narrow base, while peak displacements occur at the top, marking the pillar as the weakest structural component. Failure is most likely through cracking and rockburst, suggesting the use of energy-absorbing supports (Li, 2017). With increasing pillar thickness, stress distribution improves, concentrating instead at the pillar base corners while reducing displacements at the pillar top. Displacements shift to the roof–connection junction, and though rockburst risk at the base remains due to concentrated stresses, basalt's stiffness restricts deformation. The pillar body, less confined by high stress, may favour failure along discontinuities, making a hybrid of strength- and energy-absorbing support systems the most effective reinforcement

strategy (Li, 2017).

3. Face stability was consistently maintained throughout the simulations. Displacements at the final excavation stage exceeded those from earlier stages—even with the largest excavated blocks—indicating no evidence of face instability.

4. When pillar thickness increases relative to the external radius, maximum displacements shift to the cavern–connection interface, now representing the widest unsupported span. Nevertheless, these displacements remain limited, excluding the need to introduce an additional pillar element in that region, an option previously considered in Section 6.3, Chapter 6.

First simulations round – Conclusions

A total of 116 simulations were conducted to assess 11 external radii configurations (R), with central pillar radii (r) ranging from 0 up to 18 m, using a basaltic core model governed by the Mohr–Coulomb (MC) elastoplastic criterion and *Enni* lava core medium properties. The analysis focused on three primary outputs, major and minor principal stresses (σ_1, σ_3) and translational displacements, recording their peak values and spatial distributions. Results showed that non-pillar geometries generally produce the lowest peak σ_1, confirming the structural efficiency of the 1:5 span-to-roof-arch ratio. In pillar geometries, stress within the load-bearing element evolves with size: $r = 0.5$ m approaches plastic yielding, $r = 1$–1.5 m already demonstrates effective load-bearing performance though with high energy stored in the pillar core, and for $r \geq 2$ m, peak stresses gradually shift toward the corners. Tensile stress zones, though limited, appear near excavation contours and approach the tensile strength value (0.80 to 0.85 σ_t), indicating a high risk of tensile failure initiation. Displacement patterns experience sharp increases from $r = 0$ m to $r = 0.5$ m and gradual reduction thereafter. As pillar thickness increases, peak displacement shifts from the pillar roof to cavern–connection areas.

Examining the model's performance, the simplifications adopted do not compromise key outcomes. No failure was observed across the simulations, potential localised failure initiation was noted in some geometries starting from the R = 24 m series. These largely positive outcomes may reflect limitations of the continuum model in capturing the behaviour of brittle, jointed rock. Therefore, future studies should incorporate discontinuum methods (e.g., DEM) to achieve greater realism.

Among the failure typologies that the elastoplastic model is unable to capture, the following appear to be the most likely from a first evaluation for the specific geometry: roof block detachment predominates in non-pillar designs, whereas slender pillars are more susceptible to rockburst and stress-induced cracking.

8.2 Proposed final geometries

Following the initial simulation phase, two input geometries were selected for further analysis, based on criteria outlined in Chapter 7 and now augmented with a qualitative ranking (high, medium, low). Note that the selection, grounded in critical interpretation of the first phase results, does not constitute a formal optimisation process.

The following considerations were made with respect to each criterion:

- **Compressional Stress:** High compressive tangential stress peaks in the R-series must be avoided, even if due to numerical artifacts in some singularities. A moderate stress regime must be ensured, with a normalised major principal stress below 0.5 *UCS* ($\sigma_{1,\text{peak}} < 0.5\,\sigma_c$, Fig. 8.7), minimising crack initiation risks and aligning with the preliminary design intents (see Fig. 6.8, Chapter 6).
- **Tensional Stress:** Tensile stresses affect limited volumes but peak values approach the material tensile strength (σ_t), translated into moderate risk.
- **Displacement:** Millimetric displacements suggest that plastic deformation is not the dominant excavation response in such setting, consistent with previous findings by Xiao et al. (2024) in a similar geological context. Maximum stress and displacement occur at $r = 0.5$ m as expected.
- **Water Inflow:** While subsea tunnels carry inherent risks of significant water ingress, especially at the fjords deepest points (Samuelsen and Grøv, 2018), in the Faroese setting contact with freshwater is more likely than seawater (see Section 4.3, Chapter 4). Porous subsurface layers, such as sandstones and lava breccias, are expected to be nearly or fully saturated. Although current inflow estimates remain largely theoretical and with significant uncertainty still holding, they suggest ingress levels well below critical threshold.
- **Traffic Flow:** With projected daily traffic of 1 050–1 550 vehicles (Landsverk, 2022), smaller cavern sizes ($R = 15$–20 m) appear sufficient; large roundabouts instead may be unnecessary.

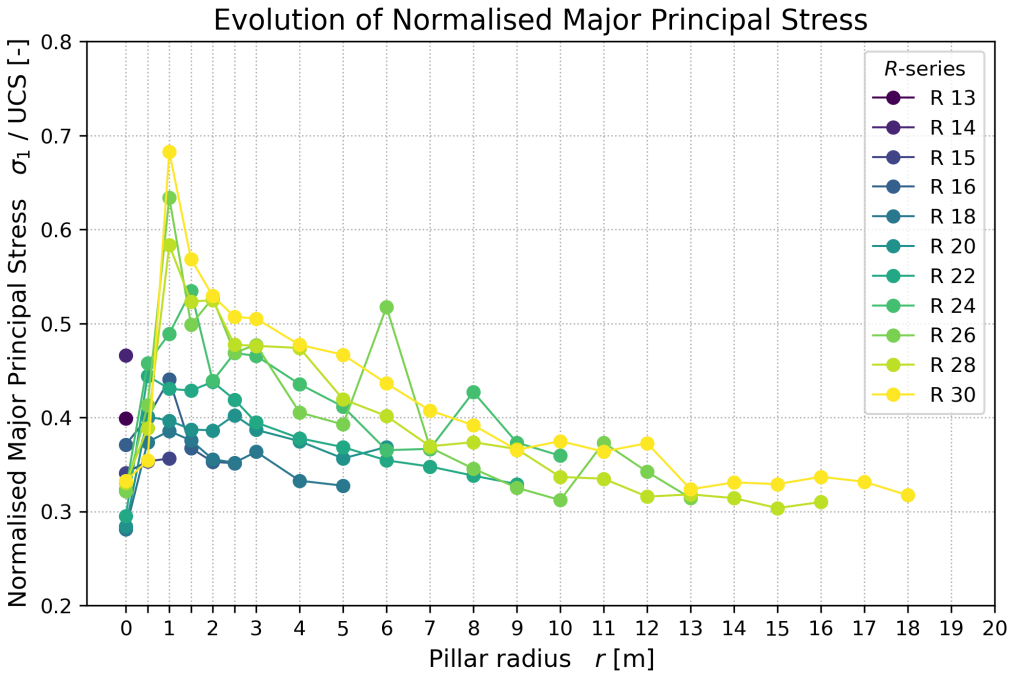


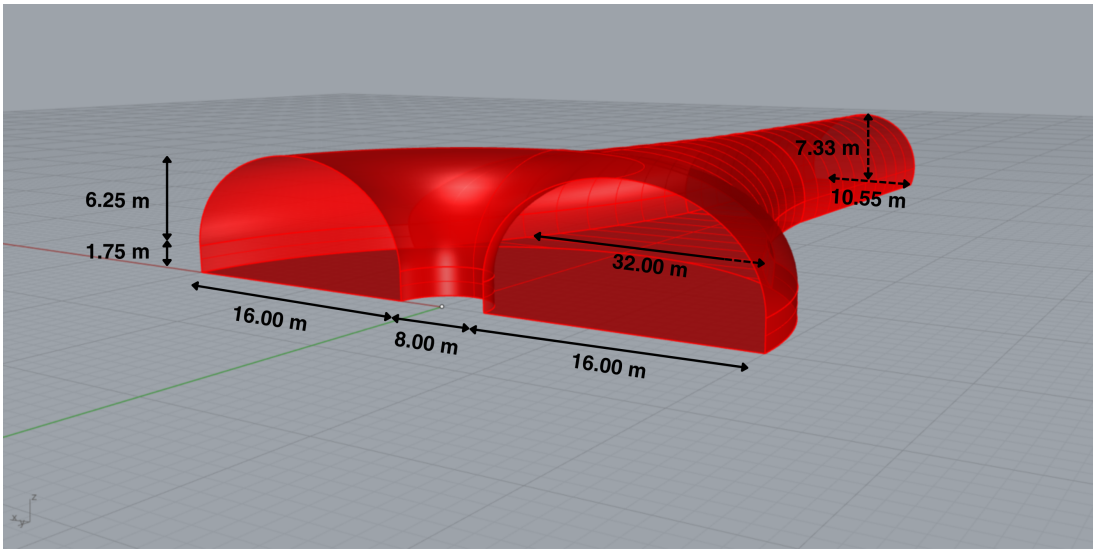
Figure 8.7: Normalised major principal stresses from the first simulations round w.r.t. to the uniaxial compressive strength characterising the Enni lava core continuum.

As a result of this discussion, the following ranks are assigned to each criterion:

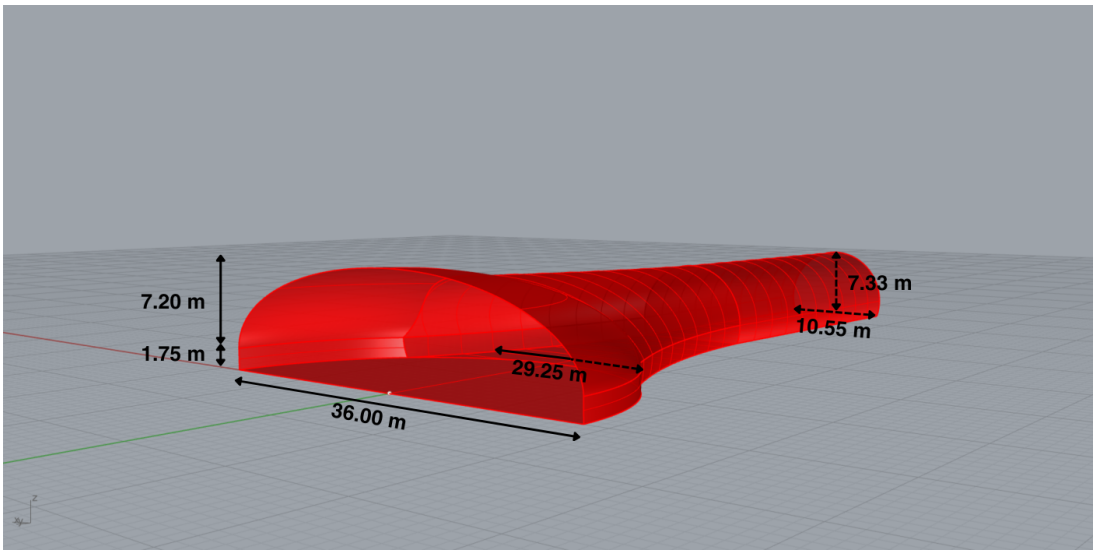
(1) Maximum stress induced by the excavation in the numerical model — **High**.
(2) Maximum displacement induced by the excavation in the numerical model — **High**.
(3) Expected traffic flow within the tunnel — **High**.
(4) Depth of the tensional stress zone within the rock mass relative to the excavation surface — **Medium**.
(5) Potential water inflow — **Medium to Low**.

Based on the above, the geometric parameters are refined as follows:

- **Cavern Radius** (R)**:** Simulations confirm structural stability across various diameters. Given low traffic demands, an optimal range of 18–20 m is identified.
- **Pillar Radius** (r)**:** The range 3.0–4.0 m is considered optimal for the selected R range, ensuring low displacement, and distributed stress. Larger values would yield diminishing returns and hinder visibility, while narrower pillars would increase usable space for operational needs but also increase instability. Existing underground roundabouts (see Section 1.3, Chapter 1) provide useful benchmarks, with due regard for contextual differences in geology and topography.



(a)



(b)

Figure 8.8: Final selected geometries related to the underwater roundabout: one configuration including (a) the central pillar and (b) one without.

In conclusion, the following geometries will represent the candidates for the final preliminary designs and further modelling analyses in the second round:

Final selected geometries

Pillar Geometry:

$R = 20$ m $\quad r = 4.0$ m (Fig. 8.8a)

Non-Pillar Geometry:

$R = 18$ m (Fig. 8.8b)

In particular, the absence of a central pillar frees central space while maintaining visibility requirements, allowing for a reduced external radius. Simulation results from the first round of the final selected geometries are shown in Appendix F.1.

8.3 Second simulations round

By having narrowed down the range of geometries to a single pillar and non-pillar candidate, it is therefore possible to proceed with the second round of simulations, structured into four stages. The first two involve conducting both local and global sensitivity analyses on parameters related to the *Enni* basalts, characterised by a high degree of uncertainty (k, *UCS*, E, ν). This is followed by an examination of the numerical model's response to the predominant geological units present in the stratigraphic sequence of both the *Enni* and *Malinstindur Formations*. The final stage focuses on the disturbance factor (D), aiming to determine the threshold at which variations in principal stresses and displacements become significant. All simulations are governed by Hoek–Brown (HB) PAC failure criterion.

8.3.1 Local sensitivity analysis

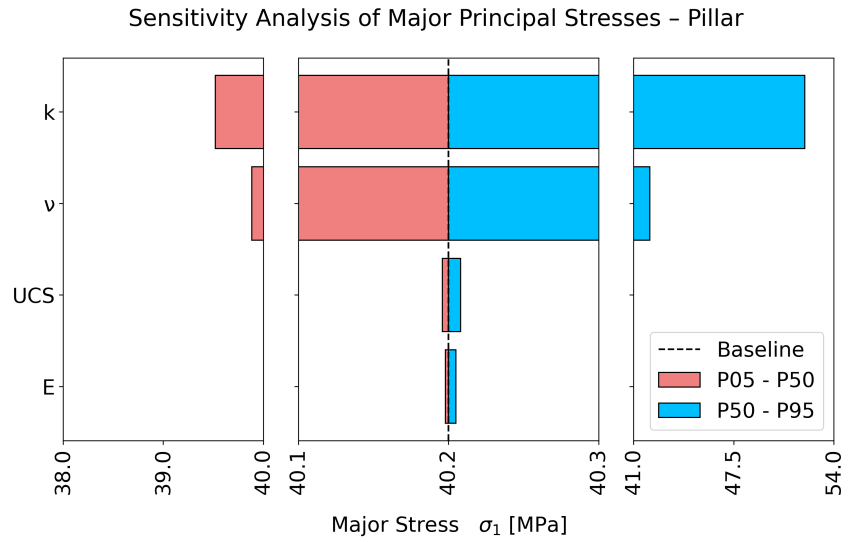
A local sensitivity analysis was conducted with 18 simulations—9 per geometry—including a baseline (mean input values) and cases where each parameter varied individually at the 5^{th} and 95^{th} percentiles under a normal distribution. Material properties were averaged from basalt lava cores of the *Enni Formation* (refer to Tab. 7.5, Chapter 7). Results are shown as tornado charts (three per geometry, one for each model output: σ_1, σ_3, displacement) to highlight the most influential parameters near the baseline.

Plots for both major (Fig. 8.9) and minor (Fig. 8.10) principal stresses consistently rank k as the most influential parameter, followed by ν, with E and *UCS* showing negligible effects regardless of the input geometry. This suggests stress development is primarily controlled by boundary/loading conditions rather than material properties.

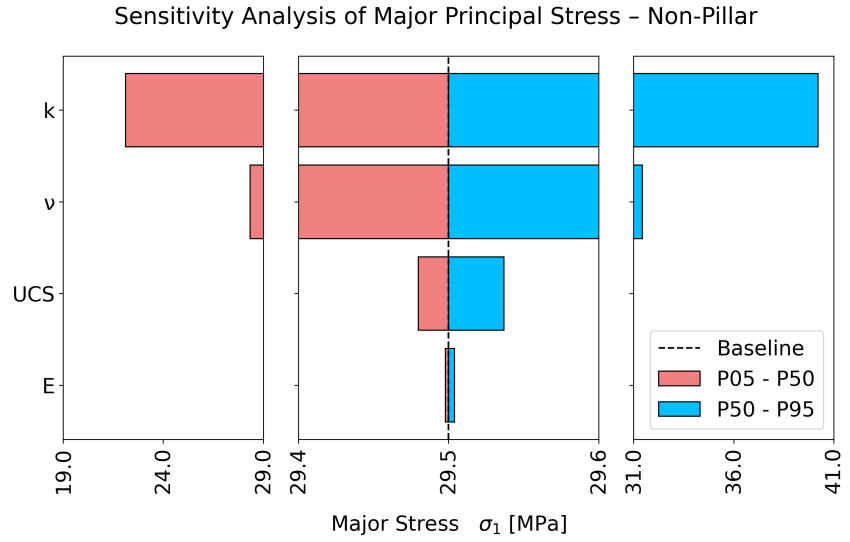
Conversely, displacement bar charts (Fig. 8.11) identify E as the dominant factor, with k still relevant although reduced. In particular, higher k appears to enhance lateral confinement, lowering the translational displacements. The influence of ν diminishes compared to the stress charts, while *UCS* remains largely ineffective, possibly indicating that the HB failure envelope is not reached and plasticity is minimal.

As expected, P05–P50 and P50–P95 bar dispositions are generally reversed between stress and

displacement plots, except for ν. Despite normally distributed input parameters, the tornado bars are rarely symmetric around the baseline.

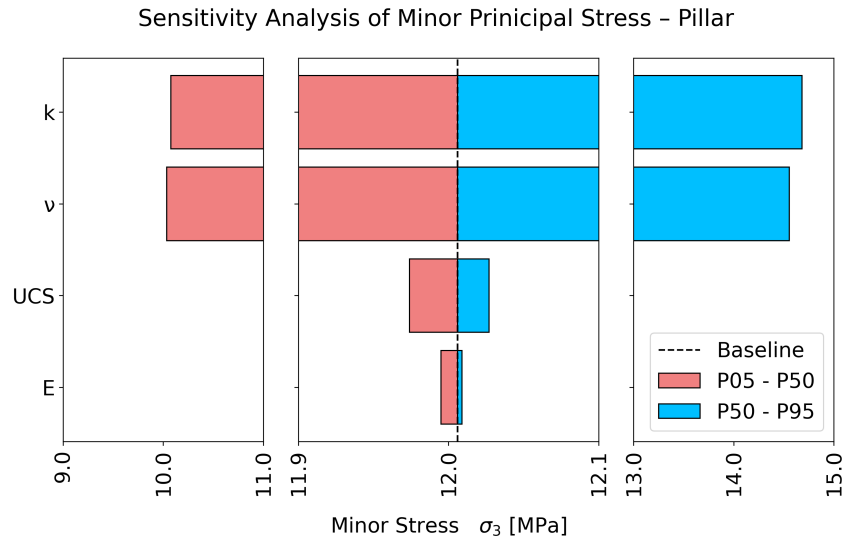


(a)

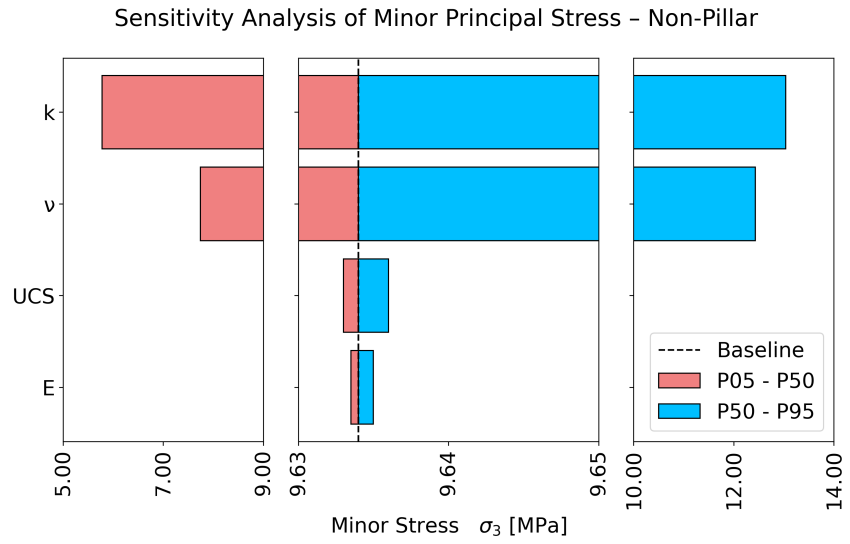


(b)

Figure 8.9: Local sensitivity results for major principal stress outcomes in (a) pillar and (b) non-pillar geometries.

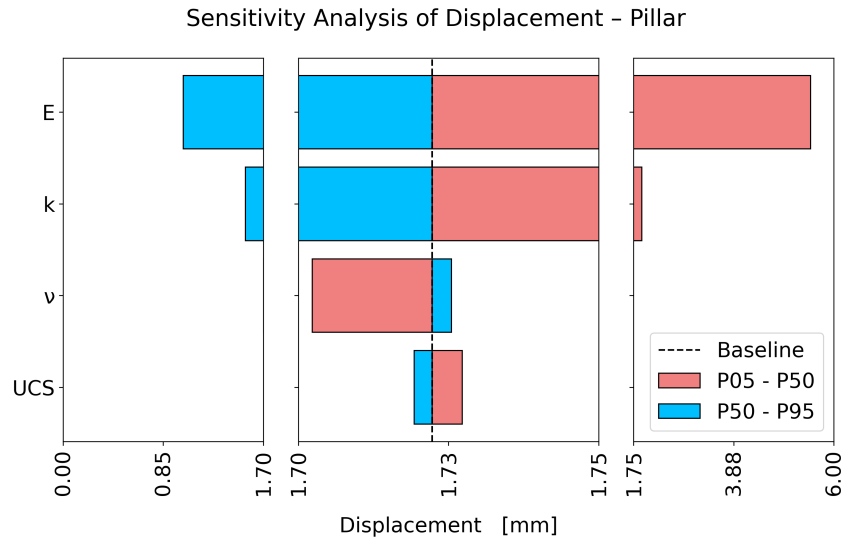


(a)

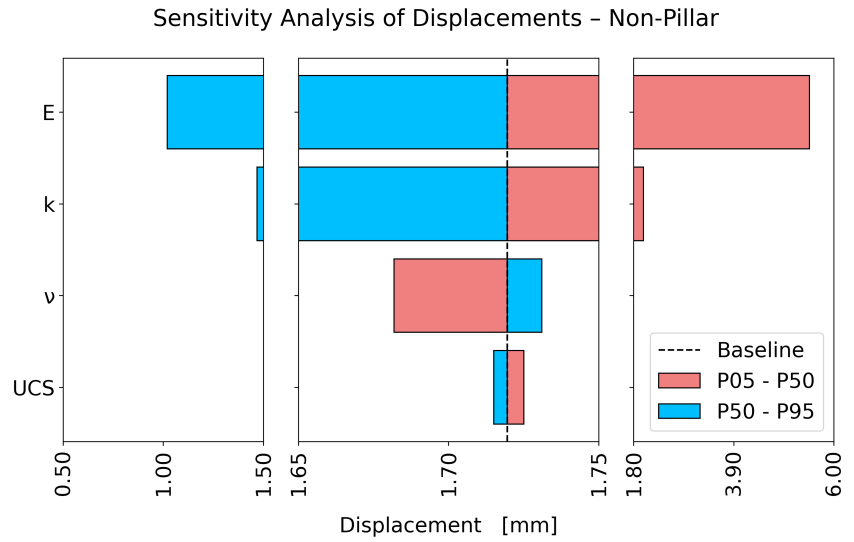


(b)

Figure 8.10: Local sensitivity results for minor principal stress outcomes in (a) pillar and (b) non-pillar geometries.



(a)



(b)

Figure 8.11: Local sensitivity results for displacement outcomes in (a) pillar and (b) non-pillar geometries.

8.3.2 Global sensitivity analysis

Global sensitivity analysis was performed with 16 simulations per geometry. The baseline case, defined by the average values of all four parameters, was also included as the 17th contribution, by considering again *Enni Formation* lava core properties.

Unlike the previous local analysis, the global method is able to capture complex parameter interactions. Results are presented as contour plots, which effectively highlight peaks, troughs,

and gradients. Given the limited dataset, interpolation through contour plots also helps estimate intermediate values.

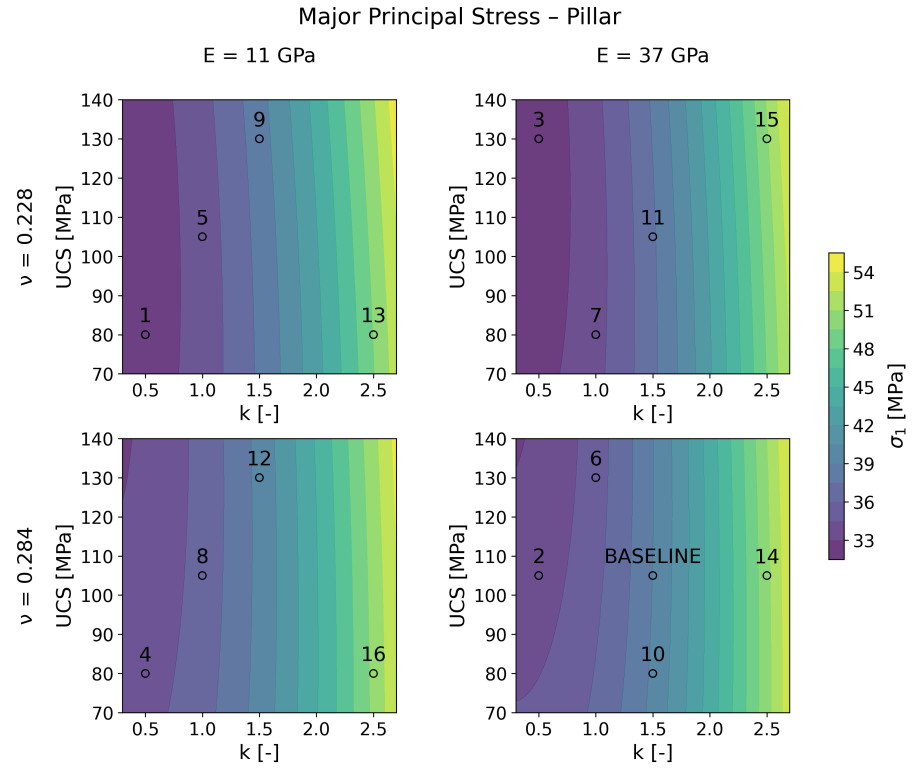
A second-order polynomial was fitted using the 17 data points per geometry, modelling a four-variable function:

$$Y(K, UCS, E, \nu), \quad \text{where} \quad Y \in \{\sigma_1, \sigma_3, u\}.$$

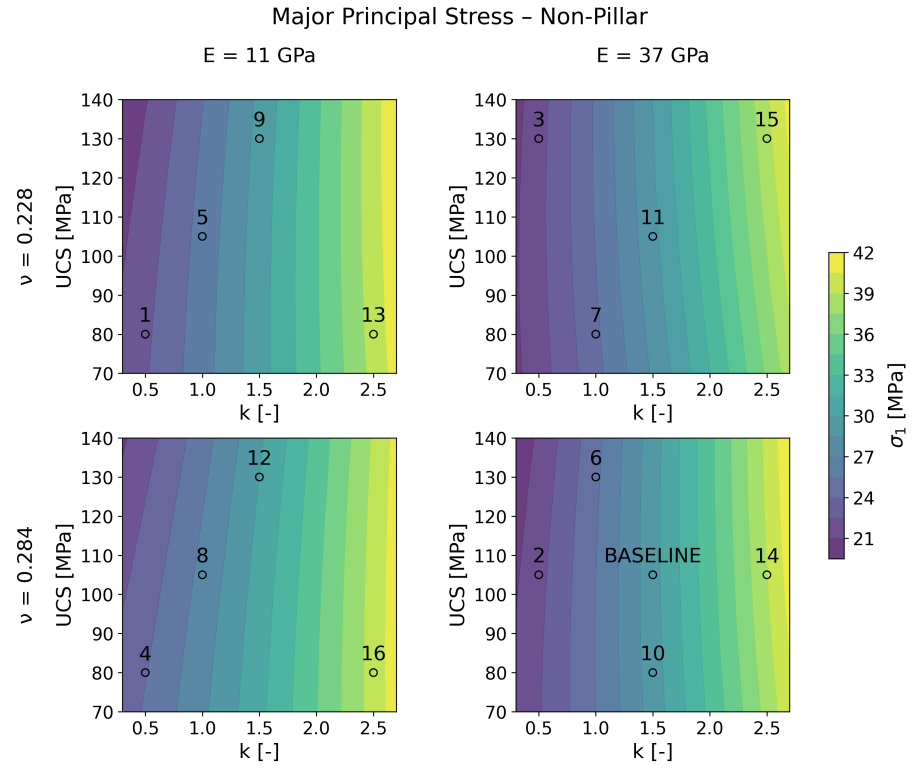
Contour plots of k vs. *UCS* were generated with E and ν fixed at level 1 or 2.

In both pillar and non-pillar geometries, major and minor principal stress-related functions exhibits a strong dependence on k. For the pillar configuration, σ_3 contour (Fig. 8.13a) behaves similarly to σ_1 (Fig. 8.12a), with function gradients consistently pointing from left to right across both plots. Conversely, in the non-pillar case, notable differences in contour lines distribution emerge: again a left to right pointing gradient for σ_1 (Fig. 8.12b) and instead a more pronounced influence of E in σ_3 (Fig. 8.13b), with the gradient pointing toward the upper right. This suggests the non-pillar setup is more deformation-sensitive, where E affects both rock deformation and stress redistribution. Greater excavated volumes due to the absence of a central pillar and the higher cavern arch may contribute to the different spatial variation of contour lines. Implementing benching or sequential excavation in the model could potentially make the non-pillar response more similar to the pillar case. Within the sensitivity domain, stress remains below 0.5 *UCS* (moderate range), indicating favourable excavation conditions in lava core units.

Displacement patterns differ significantly between the two contour plot sets. In the pillar geometry (Fig. 8.14a), displacements are highly constrained in magnitude, with a local minimum at high k and ν in the lower right plot of the set. In the non-pillar geometry (Fig. 8.14b), instead, peak values occur in the upper left ($E = 11$ GPa) and lower right ($E = 37$ GPa) corners of the domain. Thus, large displacements arise when the material is either very stiff but poorly laterally confined or very soft but strongly laterally confined, thereby suggesting that the function gradient is similarly affected by k and E, an aspect already identified in the local sensitivity (Fig. 8.11). Higher-order fitting functions suggest the presence of several local maxima and minima in a close space. These complex parameter interactions may therefore limit reliable interpolation through the utilised polynomial order along the k–*UCS* planes. Nevertheless, displacement magnitudes remain below 2 mm in the pillar contour plot domain and below 5 mm in the non-pillar one.

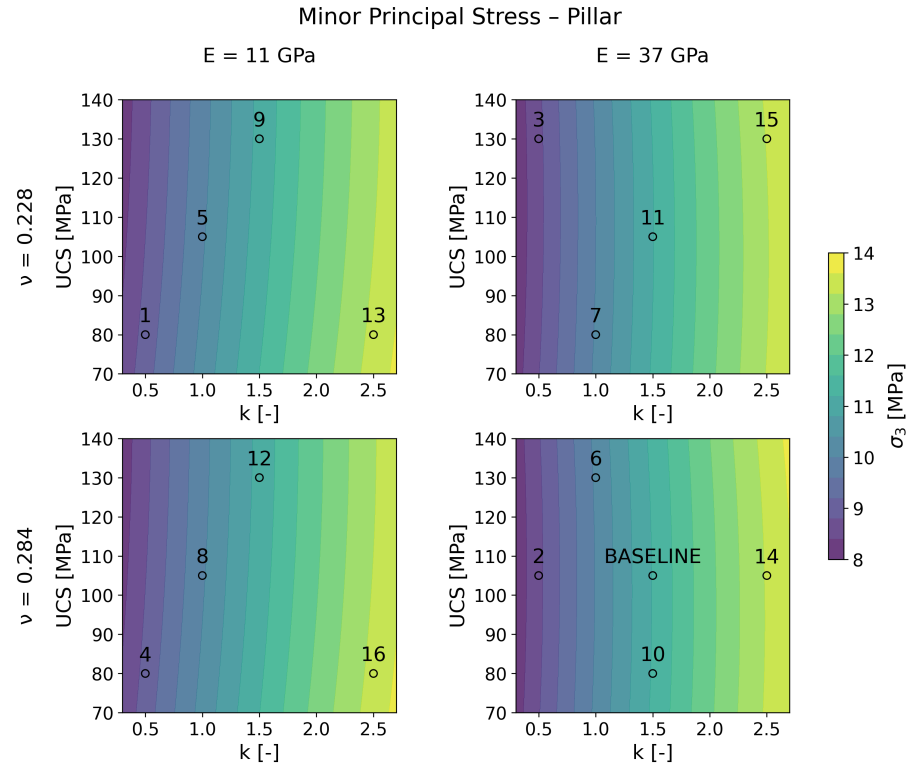


(a)

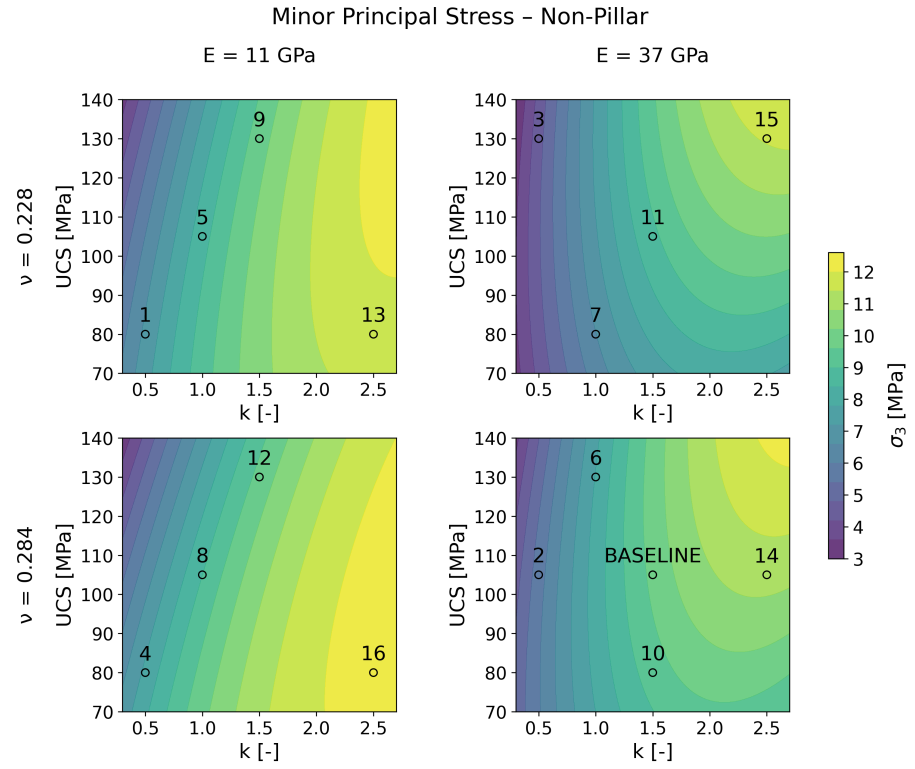


(b)

Figure 8.12: Major principal stress contour plots for global sensitivity analysis in (a) pillar and (b) non-pillar geometries.

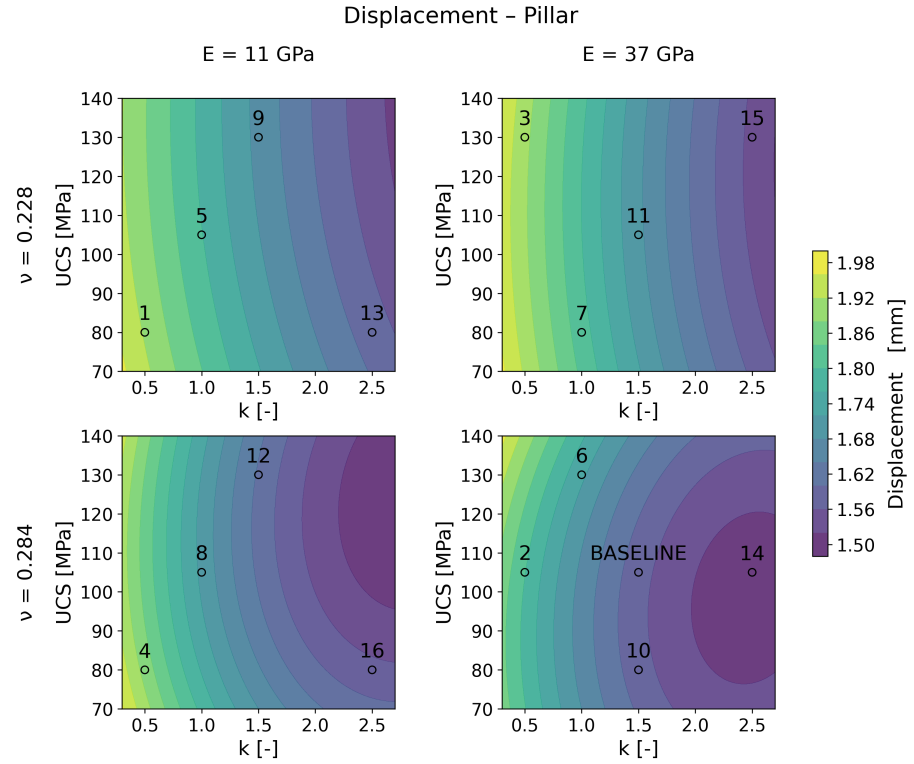


(a)

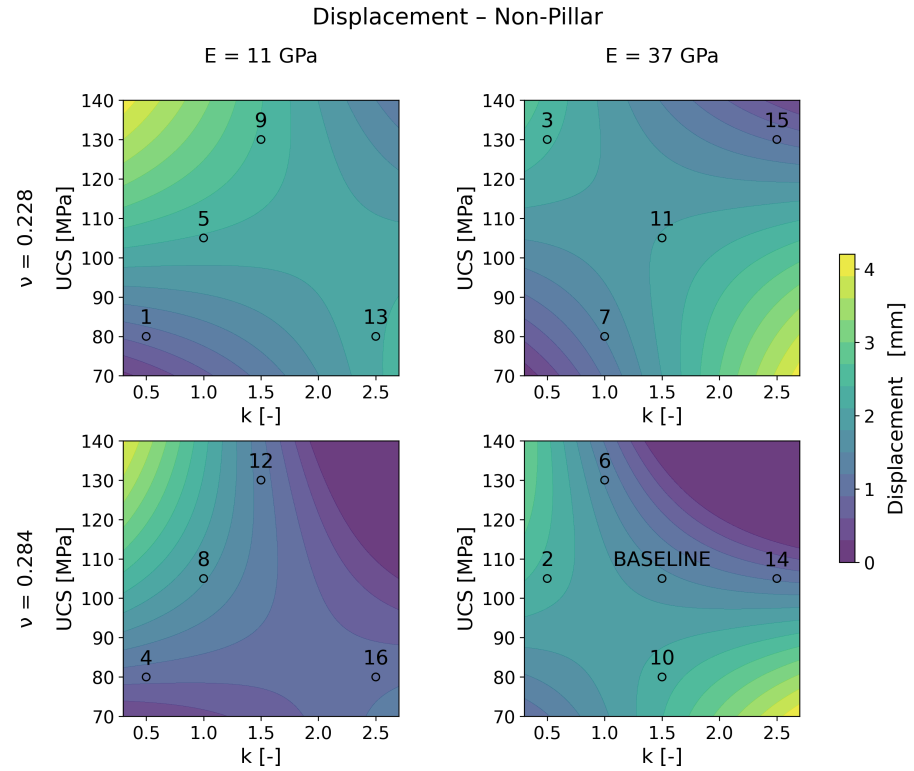


(b)

Figure 8.13: Minor principal stress contour plots for global sensitivity analysis in (a) pillar and (b) non-pillar geometries.



(a)



(b)

Figure 8.14: Displacement contour plots for global sensitivity analysis in (a) pillar and (b) non-pillar geometries.

Sensitivity analysis – Conclusions

Both local and global sensitivity analyses indicate that the lateral stress ratio (k) is the dominant factor influencing both major and minor principal stresses, underscoring the primary influence of in-situ conditions over material properties (ν, E, and *UCS*). In contrast, displacement is most sensitive to E, particularly in the non-pillar geometry, although k also contributes via lateral confinement effects. *UCS* remains largely ineffective throughout, confirming predominantly elastic behaviour among the simulations. The global sensitivity analysis reveals non-linear parameter interactions that are perhaps suggested but not clearly captured in the local analysis—most notably, the interplay between E and k in driving displacement within the non-pillar domain. Furthermore, in the global analysis, the pillar geometry yields more uniform responses for σ_1 and σ_3, whereas non-pillar configurations exhibit greater variability, especially in the response of σ_3 to E. Overall, stress magnitudes remain in a favourable range ($<$0.5 *UCS*) within the sensitivity domain, supporting stable excavation conditions in the *Enni* lava core units.

8.3.3 Numerical model response with different geotechnical units

A total of 12 simulations were conducted integrating lava core material with other key geotechnical units—namely, the lava flow top and sandstone units—mapped during the field campaign. These belong to the lava breccia and sediment material groups, respectively (refer to Section 4.1, Chapter 4). Average continuum and Hoek–Brown (HB) parameters were used for Cavern 1 (*Enni Formation*) and Cavern 2 (*Malinstindur Formation*). Cavern-specific stress regimes were adopted: $k = 1.5$ for Cavern 1 and $k = 1.0$ for Cavern 2, reflecting differing in-situ stress conditions as identified in Section 3.3, Chapter 3. The responses of the three different materials are compared using histograms grouping Cavern 1 and Cavern 2 results when the same widening geometry is implemented. In addition to the σ_1 histograms, the position of the material point with the highest major stress value along the HB failure plane—σ_3–σ_1 and σ_n–τ spaces—is shown for each material group.

Among the three materials and both Cavern 1 and Cavern 2, peak major principal stress (σ_1) ranges from 32 to 39 MPa for pillar geometries (Fig. 8.15a) and from 24 to 30 MPa for non-pillar ones (Fig. 8.16a)—well below mean *UCS* values of the lava core (105 MPa for Cavern 1, 120 MPa for Cavern 2) and (brecciated) flow top (94 MPa). In contrast, sandstone shows more critical conditions, with σ_1 exceeding 50% of its *UCS* (54 MPa) in 3 out of 4 simulations using this material, suggesting the potential initiation of rock damaging and stable cracks propagation.

Minor principal stress (σ_3) decreases progressively in its peak magnitude from lava core to sandstone, confirming superior confinement in the mechanically stronger units (Fig. 8.17). For both σ_1 and σ_3, Cavern 1 consistently shows higher magnitudes than Cavern 2 under the same material properties. Notably, simulations using the HB criterion yielded significantly lower minor peak stresses compared to their correspondent ones that were performed with the MC criterion in the first round.

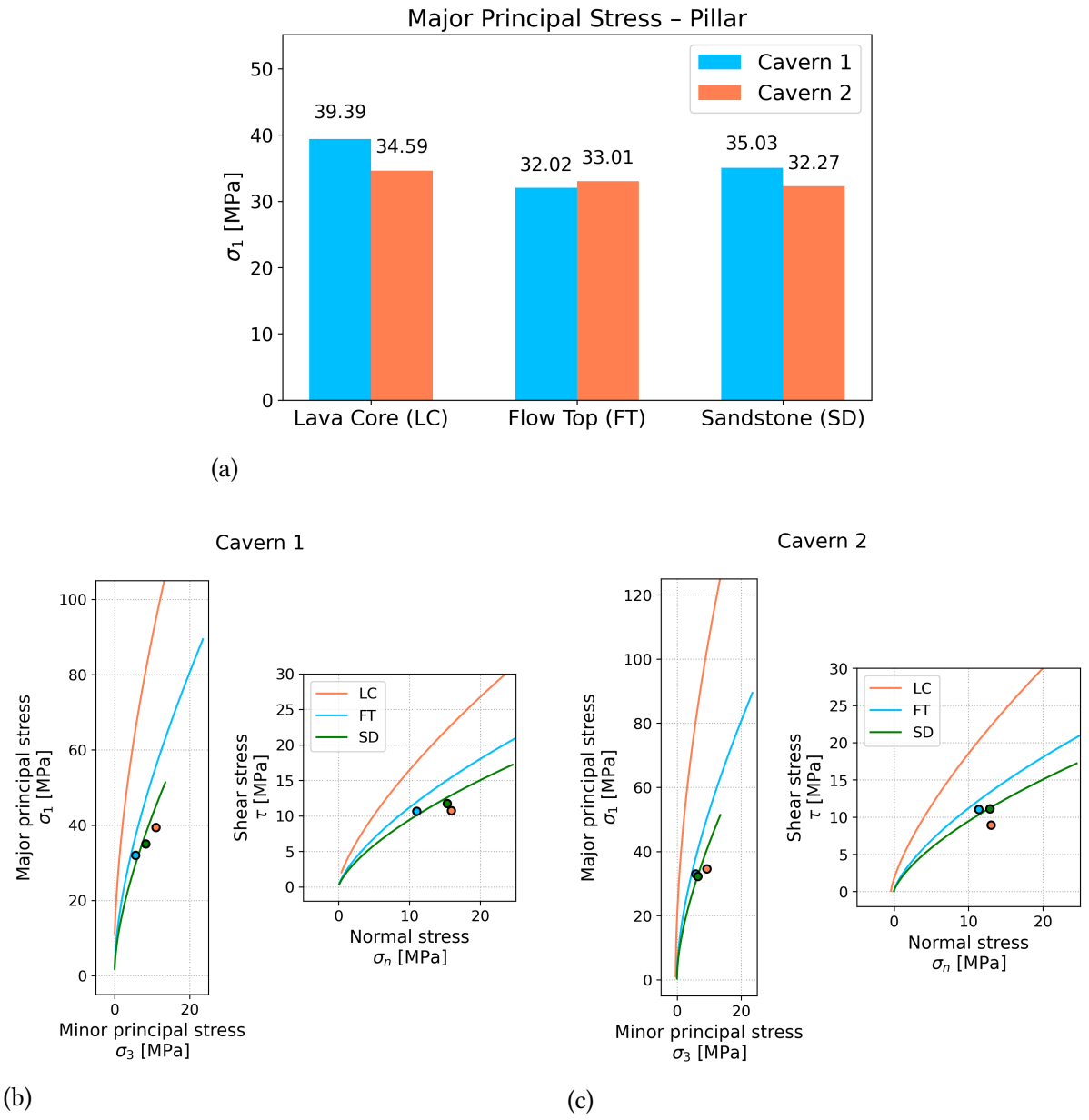


Figure 8.15: (a) Comparison of peak major principal stress (σ_1) responses for the three materials for Cavern 1 and Cavern 2 (pillar geometry). For each material group, the stress coordinates of the material point with the highest σ_1 in (b) Cavern 1 and (c) Cavern 2 models are shown in the σ_3–σ_1 and σ_n–τ spaces relative to the HB failure envelopes for the three materials.

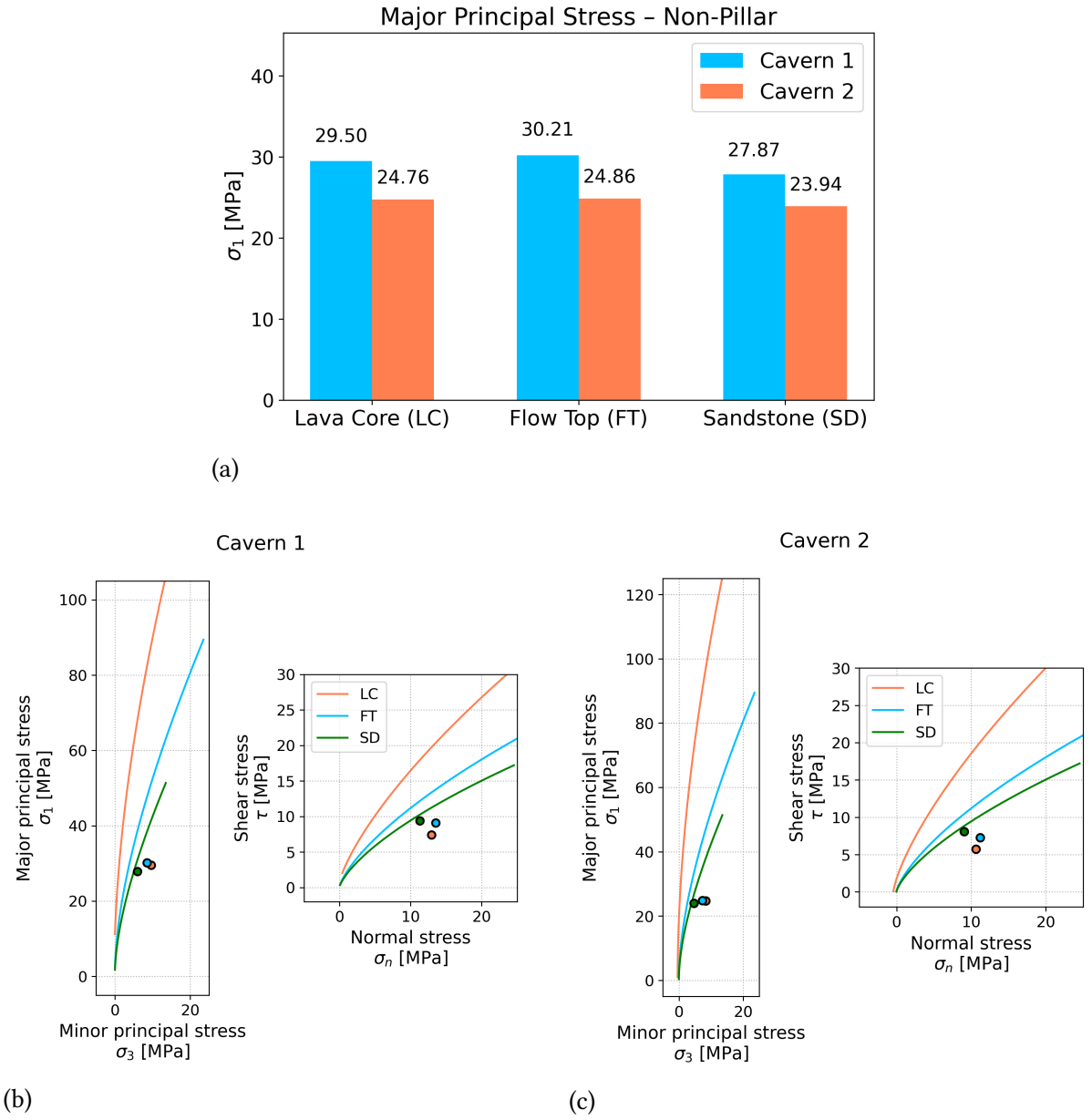


Figure 8.16: (a) Comparison of peak major principal stress (σ_1) responses for the three materials for Cavern 1 and Cavern 2 (non-pillar geometry). For each material group, the stress coordinates of the material point with the highest σ_1 in (b) Cavern 1 and (c) Cavern 2 models are shown in the σ_3–σ_1 and σ_n–τ spaces relative to the HB failure envelopes for the three materials.

Analyses on peak stress states along the HB envelope (Fig. 8.15b–c; Fig. 8.16b–c) reveal that lava core simulations remain far from failure conditions. In flow top cases, stress states approach the HB envelope, indicating possible spalling (pillar geometry) or damage accumulation (non-pillar geometry) in accordance with Diederichs and Kaiser (1999). Sandstone simulations show material points near or on the failure envelope, implying the possible initiation of plastic yielding.

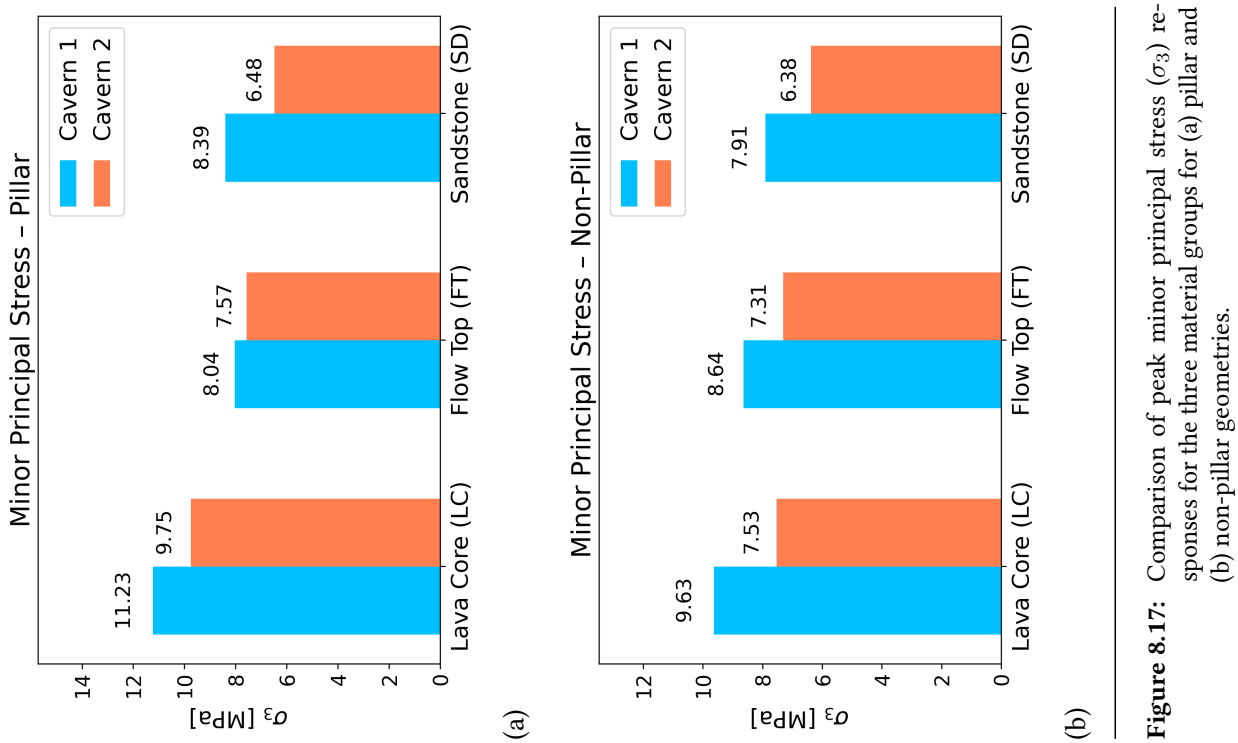


Figure 8.17: Comparison of peak minor principal stress (σ_3) responses for the three material groups for (a) pillar and (b) non-pillar geometries.

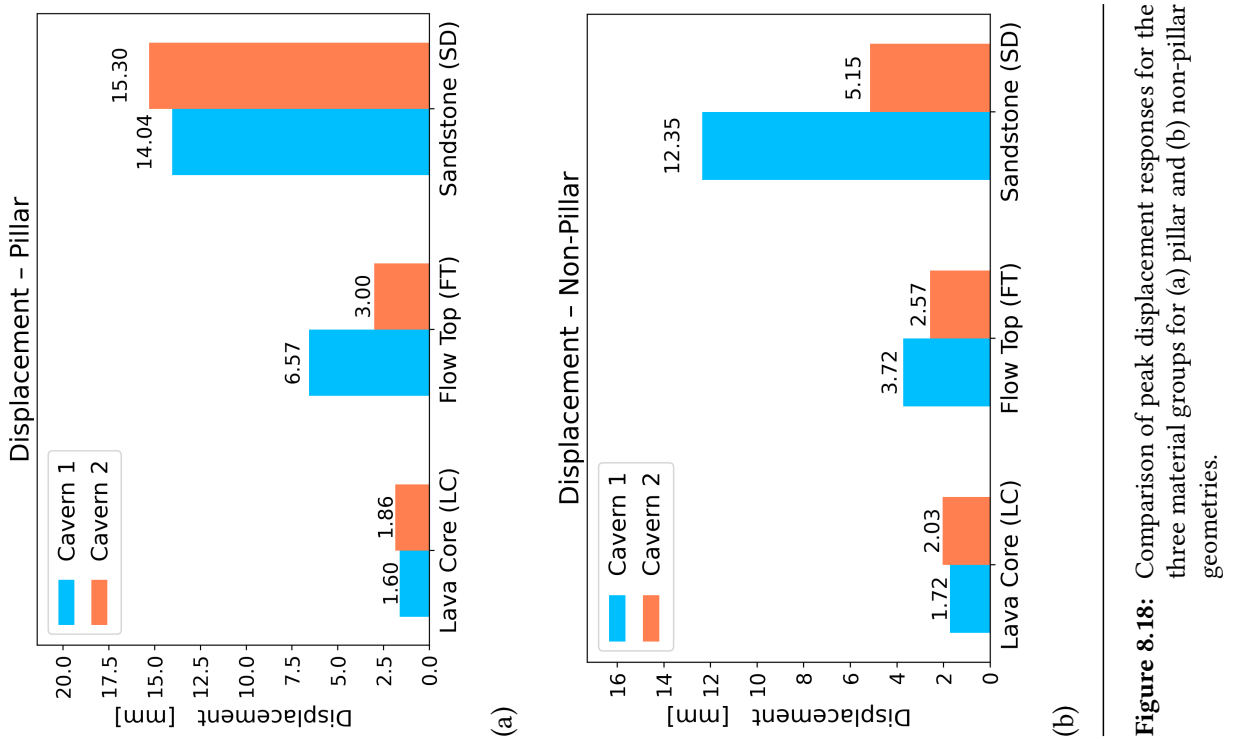


Figure 8.18: Comparison of peak displacement responses for the three material groups for (a) pillar and (b) non-pillar geometries.

Displacement histograms (Fig. 8.18) support these findings: lava core simulations show minimal displacements (1.60–2.03 mm), while flow top induces moderate displacements (3.72–6.57 mm in Cavern 1, 2.57–3.00 mm in Cavern 2). The model responses from the latter unit suggest an

amplification of effects compared to the lava core units, rather than a fundamental change in the distribution of stress and displacements. Sandstone cases depict the highest displacements by far—more than 10 mm, with the exception of Cavern 2 (non-pillar)—peaking at 15.30 mm in Cavern 2 (pillar). Displacement contours also differ significantly along the excavation faces in sandstone compared to those in the lava core. Large displacement areas now extend also along the pillar body (pillar configuration) and the connection rooftop (non-pillar configuration).

Despite a lower confinement stress in Cavern 2 initial stress regime, no consistent displacement trend emerges between Caverns 1 and 2, as peak translational magnitudes vary significantly from one cavern to the other with different material properties and geometry. This suggests that the overburden in Cavern 2 is still thick enough to avoid excessive deformation, supporting the feasibility of excavating under a slightly reduced overburden compared to the 50 m recommended by Norwegian guidelines.

It is important to remind that the breccia units exhibit significant morphological variability (refer to Section 4.1, Chapter 4) compared to the volcaniclastic sandstone. Stratigraphic variations in flow tops and bases significantly impact the heterogeneity of material properties. Samples from across the archipelago reveal considerable discrepancies in rock mass quality within different flow-base and flow-top units (National Museum of the Faroe Islands, n.d.). Thus, detailed examination of the conglomerate/breccia in the drilled stratigraphy is essential, as formation-wide averages may obscure critical variability.

Model response with different geotechnical units – Conclusions

Analyses of the three main geotechnical units within the project site—namely, lava core, flow top, and sandstone—indicate that the first provides the greatest mechanical stability, characterised by low stress levels relative to its uniaxial compressive strength (*UCS*) and minimal displacements (1.60–2.03 mm). In contrast, the sandstone (sediment) unit approaches critical stress conditions, with σ_1 magnitudes nearing or exceeding 50% of *UCS* (54 MPa) and large displacements (up to 15.30 mm) indicating potential yielding. Lava breccia exhibits intermediate behaviour, with peak stresses nearing the HB failure envelope in pillar configurations, thereby potentially amplifying failure mechanisms experienced in lava core units. Additionally, the morphological heterogeneity of lava breccias (flow tops and bases) underscores the need for site-specific characterisation, as the findings of this study may be overly specific to the single mapped flow top unit. Cavern 1 consistently experiences higher stress magnitudes than Cavern 2 for the same material and geometry, primarily due to the higher lateral stress ratio ($k = 1.5$ vs. $k = 1.0$).

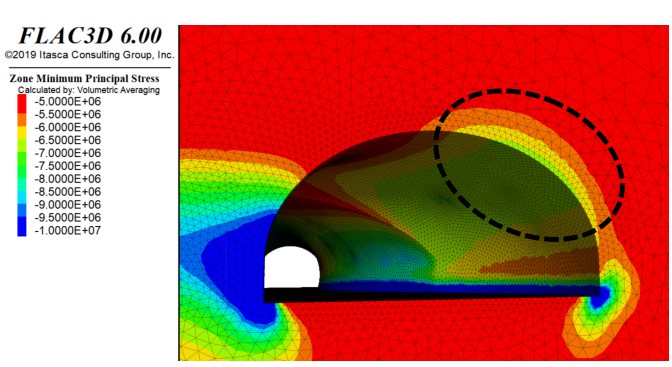
Cavern 2 on the other hand is proven to be overlain by sufficient overburden in practice, although this may be slightly below the national guidelines for underwater excavations.

8.3.4 Discussion on potential failure mechanisms

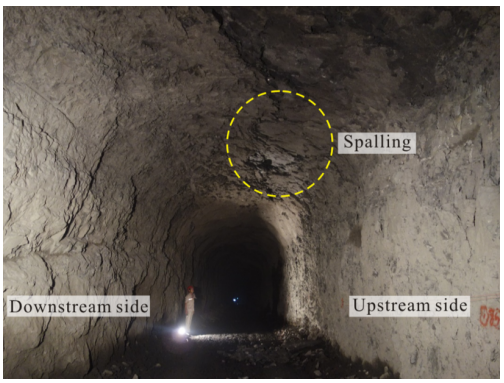
By taking advantage on the model responses for all the three main geotechnical units in the excavation lithostratigraphy, a comprehensive assessment of the likely failure modes in the most sensitive excavation zones is established, integrating insights from this simulation set and relevant case studies, and extending the discussion from the simulations first round (refer to Section 8.1).

Large span

In large spans, excavation activities largely induce stress redistribution in the surrounding rock mass, characterised by radial stress relief and an increase in tangential stresses near free surfaces (Fig. 8.19a), potentially leading to spalling. Unfavourable principal stress orientations, such as large angles relative to the excavation axis and steep inclinations, further exacerbate this failure mechanism. A prominent case of spalling in such a geological context was reported by Wang et al. (2023) during the excavation of a hydropower cavern in lithologies including aphanitic basalt, oblique tholeiite, amygdaloidal basalt, breccia lava, and tuff (Fig. 8.19b).

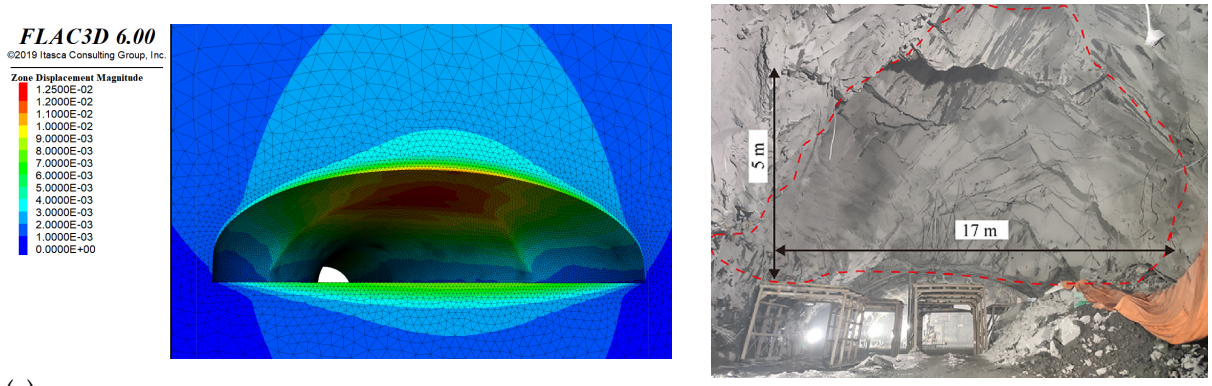


(a)



(b)

Figure 8.19: Tangential stress accumulation at the excavation boundary in the numerical model, potentially triggering failure by spalling (a), and a documented case of spalling at the Baihetan Hydropower Station in China (b). Image (b) reproduced from Wang et al. (2023).



(a) (b)

Figure 8.20: Large-magnitude displacements mobilised in the non-pillar cavern and connection rooftops characterised by sandstone material (a), and the extent of collapse damage caused by block failure in the top arch of a main powerhouse excavation (b). Image (b) adapted from Xiao et al. (2024).

The detachment of rock blocks poses a significant hazard when nearly horizontal fractures and stress relaxation occur, potentially leading to the collapse of the roof arch in large-span openings (Fig. 8.20a). These collapse zones can extend several metres. Xiao et al. (2024) documented such a failure mode in interbedded metamorphic fine sandstone and carbonaceous phyllite, with gently inclined primary discontinuity sets and additional random cracks (Fig. 8.20b).

Pillar element

As previously discussed, the pillar—whether present—is the most critically stressed element in the modelled geometry. In the field of mining, two primary failure mechanisms are recognised in pillar elements, depending on the prevailing in-situ stress conditions: (i) **stress-controlled failure** (Fig. 8.21a), induced by high in situ stress and characterised by progressive degradation of the pillar, and (ii) **structurally controlled failure** (Fig. 8.21b), dictated by rock mass discontinuities that create preferential failure paths (Monsalve et al., 2020). From the model responses, stress-controlled failure is likely to initiate at the corners of the pillar base, whereas structurally controlled failure tends to occur along the less stressed body of the pillar or in zones with weak jointing between distinct basalt flows or different geotechnical units.

Furthermore, in hard rock pillars with a width-to-height ratio below 1.0 (exactly 1.0 in the present study), increased confinement may result in pillar bursts, which manifest in two failure modes: surface spalling and core failure (Askaripour et al., 2022).



(a) (b)

Figure 8.21: Comparison between (a) stress-controlled and (b) displacement-controlled failure modes in rock pillars. Reproduced from Esterhuizen et al. (2011).

Interlava shear zones

Shear zones can develop when lava flows are interbedded with thin sandstone layers (Fig. 8.22). These phenomena cannot be captured by the current model due to its mono-material nature, although at the specific project site they may be mitigated by the generally sub-horizontal bedding of the stratigraphic units.

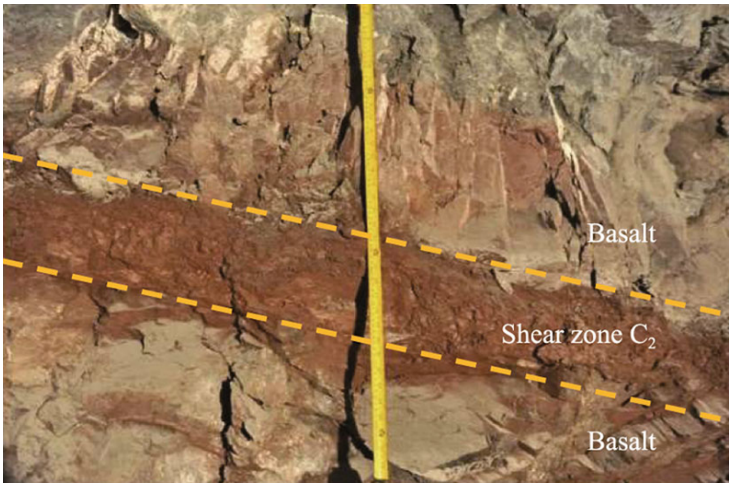


Figure 8.22: Shear zone represented by a thin sedimentary unit sandwiched by massive basalt flows. Reproduced from Zou et al. (2024).

As long as the surrounding rock mass remains largely undisturbed, shear displacement can occur along the hanging wall and footwall interfaces without compromising the overall structural stability. To manage relaxation effects induced by such shear during excavation, Zou et al. (2024) proposed a replacement-tunnel strategy in a Chinese hydropower project.

Potential failure mechanisms – Conclusions

Failure mechanisms are driven by the interplay between mechanical stress and geological structures. Large excavation spans are prone to spalling and roof collapse due to stress redistribution: brittle rocks, such as basalt, experience tangential spalling under unfavourable stress orientations, while stratified units (e.g., sandstone interbeds) promote roof block detachment through stress relaxation. Pillars are subject to high stress concentrations and may fail via stress- or structure-controlled mechanisms; slender pillars (width-to-height ratio < 1.0) are particularly vulnerable to bursts from confinement-induced spalling and core failure. Shear zones along weak interlayers pose localised risks, especially where bedding deviates from the regional sub-horizontal orientation.

8.3.5 Disturbance factor

The final simulations set aims to determine the disturbance factor threshold (D) at which excavation-induced stress and displacement patterns deviate from the baseline ($D = 0.0$, i.e., excellent quality-controlled blasting). This analysis provides insight into the level of blasting variability that can be tolerated before significant impacts occur. It focuses exclusively on the averaged lava core properties of the *Enni Formation*; for weaker units (sandstone or breccia) controlled blasting with $D = 0.0$ is assumed to be the standard practice. A total of 10 simulations were performed in addition to the baseline cases, with results presented as percentage changes in major and minor principal stresses (σ_1, σ_3) and displacements. As already noted in Section 7.7, Chapter 7, applying a uniform D across the domain may lead to an overestimation of damage, thus representing a highly conservative scenario.

Fig. 8.23 highlights that while response trends are quite similar between pillar (Fig. 8.23a) and non-pillar (Fig. 8.23b) geometries, magnitudes differ—displacements and to some extent minor stresses being most affected, major stresses less so.

Notable changes begin at $D = 0.8$ during the pillar excavation, where displacement variations reach 5%. At $D = 1.0$, these variations exceed 25% in the pillar and 12% in the non-pillar excavation. Minor stresses also start varying significantly only at $D = 1.0$—11% in the pillar

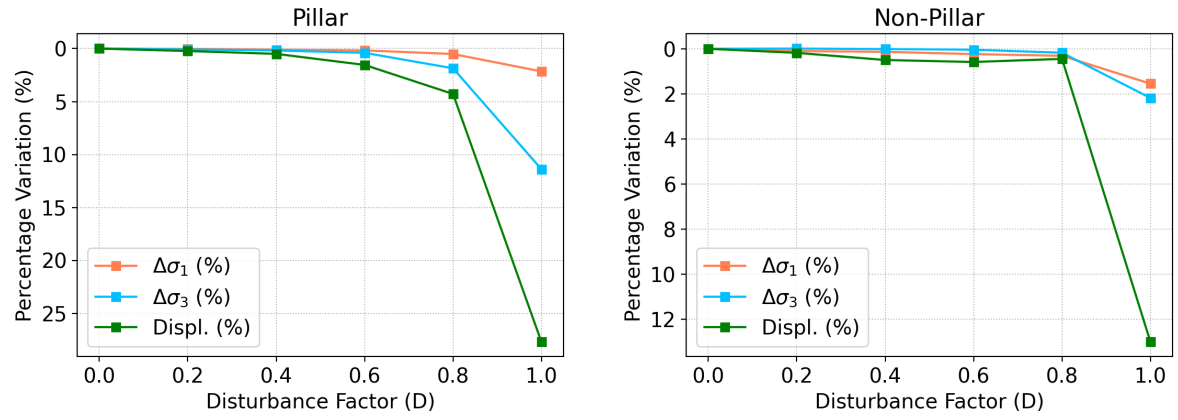


Figure 8.23: Percentage changes in major and minor stresses and displacement with varying disturbance factor (D) in both (a) pillar and (b) non-pillar geometries, assuming lava core properties from the Enni Formation.

and 2% in the non-pillar—while major stresses remain almost unchanged. Therefore, the study shows that substantial variations in model responses occur only at the upper levels of D, where, under nearly constant tangential stress conditions within the excavation contour, a significant rise in displacements is experienced. In actual excavation practice, this implies that even with moderately controlled blasting, the response of the most widespread geotechnical unit in Cavern 1 (assuming lava core properties) is expected to remain largely unaffected compared to the baseline case.

8.4 Suggested structural reinforcements

In conclusion, this chapter provides a recommendation for structural reinforcements for the two finally selected excavation geometries, based on field-mapped rock mass quality and numerical simulation results.

The initial support design is based on the Rock Support Chart (RSC, Norwegian Geotechnical Institute, 2015), which is derived from the *Q-system* (see Appendix F.2). The chart relates the rock mass Q-value to the equivalent wall or span—defined as the excavation wall or span divided by the Excavation Support Ratio (ESR)—and categorises support needs into eight classes (8 = poorest, 1 = best), along with a "Special Evaluation" category for exceptional cases. The chart offers guidance on bolt length and spacing, sprayed concrete thickness, and energy absorption class (EFNARC/NCA No. 7–2011).

Although widely used, the application of the *Q-system* in the Faroese context has been debated

as overly conservative for jointed basalts (Rodrigues et al., 2002), particularly when apparent weaknesses are due to large feldspar grains rather than true jointing. As a result, local adaptations have been developed. Prof. Grøv and colleagues are currently working on a support chart specialised for Faroese lithologies (see Appendix F.2). The chart comprises six quality classes (A–F), each with qualitative descriptors, typical Q-values, and corresponding support guidelines. In particular, Class C is intended for specific non-basaltic units such as volcaniclastic sandstones.

RSC and Revised Support Chart application

Starting from the RSC, an ESR value of 1 is assigned (i.e., for "major road and railway tunnels"). Equivalent spans for both pillar and non-pillar geometries are identified on the chart. The equivalent wall heights is equal for both geometries. The supports specifications are grouped in Tab. 8.1. Based on the input Q-values, the RSC assigns Support Class 3–2 for the lava core, and Class 4–3 for lava breccia and sandstone in the pillar geometry span. For the non-pillar geometry span, it assigns Support Class 4–3 for the lava core and Class 5–4 for lava breccia and sandstone. Class 1 is applied to all walls. Comparing the designs for Cavern 1 (Fig. F.13) and Cavern 2 (Fig. F.14), reinforcements in the Upper Formation lava core allow slightly wider bolt spacing on walls. However, the overall support system remains largely similar across the basalt formations, with only minor practical differences. A slightly thicker shotcrete layer is recommended for breccia units, and in some cases a denser bolt spacing as well.

Specifications from the revised rock mass support system for the Faroese context are grouped in Tab. 8.2. The chart establishes relatively uniform design guidelines for the three geotechnical units (see Fig. F.15). The exception is that in high-Q lava core units, bolts can be scattered (spot bolting), whereas in breccia and sandstone units, a minimum bolt density of 0.2 bolts/m^2 must be maintained. Compared to the SRF-based approach, bolt lengths are generally reduced—especially for the non-pillar geometry—while shotcrete thickness is increased and its energy class generally upgraded for lower-quality rock. However, this revised system does not permit the specification of span or wall dimensions to refine the support estimation. As a result, no distinction is made between pillar and non-pillar geometries, despite their significant differences in span. This is a major limitation, as the chart is primarily developed for standard tunnel excavations. Its applicability to larger spans, such as those in caverns, must therefore be carefully evaluated.

Thus, in conclusion, despite its limitations, the RSC is considered to remain the most suitable approach currently available for this project.

Table 8.1: Support specifications for pillar and non-pillar geometries across the various geotechnical units, as per NGI handbook (Norwegian Geotechnical Institute, 2015).

Material			**Lava core (Upper Fm.)**	**Lava core (Middle Fm.)**	**Lava breccia**	**Sandstone**
Q-range			8–56	7.5–48	2.33–8	6.25–6.85
Pillar	Span	Support class	3–2	3–2	4–3	3
		Shotcrete	SFR (6–5 cm)	SFR (6–5 cm)	SFR E500 (9–6 cm)	SFR (6 cm)
		Bolts spacing	2.2 m –spot bolting	2.2 m –spot bolting	1.9–2.2 m	2.2 m
		Bolts length	4 m	4 m	4 m	4 m
	Wall	Support class	1	1	1	1
		Shotcrete	—	—	—	—
		Bolts spacing	1.9–3.4 m	1.9–3.2 m	1.5–1.9 m	1.7–1.8 m
		Bolts length	1.5 m	1.5 m	1.5 m	1.5 m
Non-Pillar	Span	Support class	4–3	4–3	5–4	4
		Shotcrete	SRF E500 (9–5.5 cm)	SRF E500 (9–5.5 cm)	SRF E700 (12–9 cm)	SRF E500 (10–9 cm)
		Bolts spacing	2.2–2.5 m	2.2–2.5 m	1.9–2.2 m	2.2 m
		Bolts length	8 m	8 m	8 m	8 m
	Wall	Support class	1	1	1	1
		Shotcrete	—	—	—	—
		Bolts spacing	1.9–3.4 m	1.9–3.2 m	1.5–1.9 m	1.7–1.8 m
		Bolts length	1.5 m	1.5 m	1.5 m	1.5 m

Table 8.2: Support specifications for pillar and non-pillar geometries across the various geotechnical units, as per revised rock support classification for the Faroese context.

Material		**Lava core (Upper Fm.)**	**Lava core (Middle Fm.)**	**Lava breccia**	**Sandstone**
Q-range		8–56	7.5–48	2.33–8	6.25–6.85
Span	Support class	B–A	B–A	B	C
	Shotcrete	SFR E700–SFR (8 cm)	SFR E700–SFR (8 cm)	SFR E700 (8 cm)	SFR E700 (8 cm)
	Bolts spacing	0.2 bolts/m^2 –Scattered	0.2 bolts/m^2 –Scattered	0.2 bolts/m^2	0.2 bolts/m^2
	Bolts length	4–3 m	4–3 m	4–3 m	4–3 m
Wall	Support class	B–A	B–A	B	C
	Shotcrete thick.	Scattered (8 cm)	Scattered (8 cm)	Scattered (8 cm)	SFR E700 (8 cm)
	Bolts spacing	—	—	—	0.2 bolts/m^2
	Bolts length	—	—	—	4–3 m

9

Conclusions and recommendations

Tá ið ølið fer inn, fer vitið út

When ale goes in, the wit goes out

The final chapter is structured into four main sections. First, the main findings and developments are summarised, highlighting the geological, geotechnical, design, and numerical insights gained through the study. Second, the chapter revisits the research questions, demonstrating how the results address the previously identified gaps. Third, it outlines both the limitations and constraints of the current work, as well as opportunities for further improvements in all the main aspects covered by this project. Finally, the chapter concludes with a reflection on the social impact of the Suðuroy Tunnel project, linking technical outcomes to their broader relevance for connectivity and community development in a unique archipelago such as the Faroe Islands.

9.1 Main findings and developments

Two twin widenings are planned along the Suðuroy Underwater Tunnel alignment, located at one-third and two-thirds of its length and at depths of approximately -130 and -150 m a.s.l., respectively. These caverns will mainly function as U-turn roundabouts to allow even large size vehicles to turn around safely in case of emergencies. A numerical analysis was required to assess the feasibility of excavating these widenings. To address this research objective, the project involved a review and integration of the geological and geotechnical characteristics of the excavation site, a preliminary design of the cavern excavation, and a series of numerical analyses. The main uncovered findings and relevant developments during the project are presented here.

Geotechnical Profiling: The two caverns lie within two distinct basalt formations—*Enni* and *Malinstindur*—within a lithostratigraphy comprising three principal geotechnical units: massive *lava core*, fractured and weathered *lava breccia*, and *volcaniclastic sediments*. Each unit has distinct strength and deformability characteristics that directly affect excavation stability.

Anticipated Geotechnical Hazards: In the identified sub-horizontal lava flow setting (maximum mapped dip of 16°), prolonged tunnel intersections with weaker or more permeable layers may locally reduce stability and increase the risk of water ingress.

Fracturing and in-situ stress: Fracture orientations mapped and plotted during the field campaign closely match known regional geological patterns, though core logs reveal significant local variability. Applying theoretical methods to estimate the horizontal-to-vertical stress ratio (k) produced divergent results, highlighting the need for sensitivity testing across a range of k values in numerical modelling.

Hydrogeological Conditions: Near-complete freshwater saturation is expected underground. Most permeable zones stay well within acceptable inflow limits for excavation, but even below optimal rates for efficient water pumping.

Rock Mass Quality: Field assessments indicate fair to good rock mass quality, with *Malinstindur* generally superior to *Enni* in massive outcrops. Lava cores show the highest quality, while lava breccia and sediments are considerably weaker both in terms of *Q*- and *GSI* values.

Proposed Designs: Given their proven ability to handle uncertain main stress orientations underground and their suitability for a roundabout cavern, the main design proposals have been developed around a circular-base cavern. Among these proposals, two alternatives have been put forward, differing in whether a central pillar is included or not in the excavation.

Deviations from Design Guidelines: Minor adjustments to Norwegian design guidelines—specifically reduced overburden in some Cavern 2 layouts and increased height-to-span ratios in smaller non-pillar caverns—had negligible adverse effects, indicating limited potential for safely relaxing these thresholds.

Wide Geometry Range Testing: Across various geometries modelled in lava core medium, stresses and displacements remained within acceptable limits. Larger spans showed higher local stresses and displacements but always stayed below critical failure thresholds.

Failures Assessment: No global or local failure was observed across the full range of cavern geometries modelled with a lava core medium. However, localised yielding occurred in pillars with a 0.5 m radius, within the pillar element itself. In geometries with a 1 m pillar radius, especially those with larger spans, high strain energy concentrations were observed in the pillar core.

Sensitivity to Parameters: The stress k ratio is proven to exert the strongest control on stress magnitudes, while both k and elastic modulus significantly influence displacement in the numerical model. Non-linear parameter interactions mean that these complexities are not always well captured by the polynomial approximation methods used.

Optimal Cavern Dimensions: Considering mechanical performance, water ingress risk, and operational requirements, the most favourable configurations identified in this study are:

- Non-pillar configuration: 18 m external radius
- Pillar configuration: 20 m external radius with a 4 m pillar radius

Performance in Volcaniclastic Sediment: Modelling sedimentary rock properties along the two selected cavern geometries revealed stress states nearing the failure envelope, peak principal stresses exceeding half the uniaxial compressive strength, and displacements up to 15 mm. This indicates a higher risk of yielding, stable crack propagation, and reduced stability compared to basalt units, highlighting the need for appropriate reinforcement strategies.

9.2 Tackling research gaps

The contribution of the previous findings returns the focus to the research question and the gaps identified in the outline of this project, which can now be more thoroughly addressed in this section.

Geological setting

(Q 1.1) What rock mass fracture orientation and quality are expected at the depth where the caverns will be excavated?

Fracture orientations vary significantly but generally follow regional trends: E–W in the *Enni Formation* and NW–SE in the *Malinstindur Formation*, partially supported by (limited) field data. Fracture density is expected to be higher at the fjord bottoms, which are however far enough from the cavern locations.

Three geotechnical units were identified: lava flow core, lava breccia (brecciated/conglomerate flow base and top), and sediment (volcaniclastic sandstone). *Q*- and *GSI* parameters and scores for each unit were determined during field mapping for use in the numerical model.

(Q 1.2) Beyond rock mass parameters, what other factors—such as in-situ stresses, water seepage, and rock-environment interactions—affect tunnel cavern construction and long-term performance in this area?

Numerical sensitivity analyses highlight in-situ stresses—particularly the horizontal-to-vertical stress ratio—as the most critical factor influencing stress distribution, and to a slightly lesser extent, displacements during excavation. Although the rock mass is expected to be nearly fully saturated with freshwater, water inflow remains below critical thresholds, though artesian conditions and pore pressure development along joints are possible in the area. No significant chemical reactivity or rock-environment interaction concerns have been identified for the Suðuroy Tunnel units.

(Q 1.2) Which vertical and horizontal variability in the rock mass is expected at the cavern locations?

The nearly horizontal bedding suggests geological continuity along the horizontal direction and also implies prolonged contact with specific lithostratigraphic units during tunnel excavation.

Vertically, the same elastic and geomechanical properties can be assigned to all the flows within

the same basalt formation, paying attention though to still distinguish between their massive lava core, brecciated bases and tops and sedimentary interbeds.

A distinction in geomechanical properties and elastic parameters must be made instead when transitioning from the *Enni* (Upper) to the *Malinstindur* (Middle) flows, reminding that Cavern 1 will be situated within the Upper Fm. while Cavern 2 in the Middle Fm.

Underground widenings preliminary design

(Q 2.1) How do the geometrical parameters of cavern excavation affect tunnel stability and design functionality?

In non-pillar designs, stability is ensured by maintaining a height-to-span ratio of 1:5, in accordance with Norwegian guidelines. For pillar configurations, stability primarily depends on the relative dimensions of the external radius R and the pillar radius r.

A central pillar allows lower roof heights than non-pillar designs but may obstruct driver visibility, making the choice of r crucial for the facility correct functionality. Without a pillar, proper signage is needed to compensate for the lack of visual cues alerting drivers to the roundabout presence.

(Q 2.2) How will the different purposes of the Suðuroy caverns influence their design compared to the Eysturoy roundabout and other existing ones?

The Suðuroy Tunnel caverns follow current roundabout and cavern design guidelines to ensure functionality across most tested geometries. Minor adjustments are made for low-radius ($R <$ 15 m) non-pillar designs, particularly in the height-to-span ratio.
Vertical walls are here suitable due to expected moderate stress conditions for most of the candidate geometries, optimising space in comparison with previous projects.
Although some configurations at Cavern 2 have overburden less than 50 m (the minimum stated by Norwegian guidelines), numerical simulations confirm adequate stability.

Numerical modelling

To what extent can an underwater road tunnel widening be excavated given the specific in-situ stresses field, rock layer typology and orientation of the Suðuroy Tunnel, both including and excluding a central rock pillar?

Assuming a uniform continuum and typical lava core properties at the site, and within current Norwegian design boundaries, all tested tunnel geometries achieved stability globally. Thin central pillars ($r = 0.5$–1.0 m) showed localised yielding or high energy accumulation, the latter especially in combination with large external radii R.

Other geometries exhibited relatively moderate stress concentrations at corners and displacements in wide spans, at pillar tops, or in the roof between the cavern and its connection to the tunnel element. Observations indicate the potential onset of localised failure only in geometries with exaggerated R-to-r discrepancies.
This overall global stability achieved in all the tested geometries may stem from:

(i) Model limitations in capturing mechanisms like sliding, block detachment, rockburst, or interlava shearing.

(ii) The good mechanical properties of the main rock mass typology (lava core), overall considered favourable for blasting.

(Q 3.1) How do stresses and displacements vary with changes in cavern geometry, and where are the most critical stress conditions located within the excavation?

Following the general trend, the maximum principal stresses increase sharply when transitioning from the non-pillar geometry to thinner pillar configurations, peaking between $r = 0.5$ m and $r = 2.0$ m for σ_1, and between $r = 0.5$ m and $r = 4.0$ m for σ_3, depending on the specific external radius R. Beyond these ranges, the stresses drop suddenly then gradually decrease as r increases. Outliers in simulations likely stem from local stress concentrations or meshing artifacts.

Displacements reach their maximum uniformly at $r = 0.5$ m—except for $R = 30$ m—due to yielding, then progressively decrease, approaching or falling below non-pillar levels. Variations in pillar radius affect both the magnitude and spatial distribution of principal stresses and displacements.

The typical evolution of peak locations with increasing r is as follows:
Stresses: connection corners → pillar core → pillar corners.
Displacements: cavern rooftop (at $r = 0$) → pillar top → connection–cavern rooftop area.

(Q 3.2) How do rock mass quality, lithostratigraphic variability, and blasting methodology (disturbance factor) affect the model response and the design of cavern size?

Among the two final candidate geometries—one with a central pillar and one without—measuring $R = 20$ m, $r = 4.0$ m and $R = 18$ m, $r = 0.0$ m, respectively, characterising the corresponding numerical models using lava breccia properties instead of the lava core (the most widespread geotechnical unit in the stratigraphy) primarily amplifies potential failure mechanisms without fundamentally altering them. This may initiate failures in critical excavation zones.

When the models are instead characterised with the properties of the sedimentary unit (volcaniclastic sandstone), two key effects are observed: (i) the peak major principal stresses exceed half the uniaxial compressive strength (*UCS*), indicating stable crack growth in sensitive areas, and (ii) translational displacements increase significantly, both in magnitude and extent within the excavation contour, leading to yielding in critical sections.

To address weaker materials potentially encountered at excavation sites within either of the proposed cavern locations, it would be necessary to (i) adjust cavern design parameters—such as the ratio between cavern radius R and pillar radius r, the excavation cross-section, and eventually the span-to-height ratio in non-pillar designs—and (ii) plan structural reinforcements accordingly, guided by appropriate design charts.

Significant changes in model response only emerge at a disturbance factor of $D = 1.0$ (very poor blasting control), suggesting that only extremely large deviations from high-quality blasting practices would significantly compromise cavern stability.

9.3 Limitations and possibilities

9.3.1 Limitations

The geological characterisation of the project area is constrained by several factors. Firstly, **a substantial lithostratigraphic section (approximately 400 m) remains undrilled**, necessitating reliance on indirect methods such as stereonets and seismic surveys, which introduce higher uncertainty in interpreting geological structures and bedding orientations. Secondly, **key input parameters for modelling in-situ stresses and uniaxial compressive strength were primarily inferred from theoretical models, literature, and analogous basalt formations**, reducing the reliability of site-specific assessments. Additionally, **rock mass quality evaluation for the lava breccia unit relied exclusively on observations at**

the *Streymoy 2* outcrop, which is inadequate for capturing the unit's heterogeneity across the project area. This limitation also applies, albeit to a lesser extent, to the sedimentary (sandstone) unit, whose quality was assessed only at the *Sandoy 2* outcrop.

During the preliminary design phase, further constraints emerged. For instance, **CAD limitations hindered the full rounding of certain corners**, particularly at junctions between the cavern and the connection elements. These geometric imperfections resulted in **localised stress concentrations in numerical simulations**, at times **obscuring more critical zones requiring attention**. Moreover, **the absence of structural support elements in the initial design meant that the numerical models could not incorporate or test reinforcement strategies**, limiting the evaluation of structural performance under realistic loading conditions along the excavation contour for long-term response assessments.

The current numerical model also exhibits several important shortcomings. To begin with, **the lack of calibration necessitated a qualitative focus**, prioritising stress and displacement patterns over precise numerical values. Furthermore, **the assumption of a homogeneous material limits the representation of the site's stratigraphy**, preventing accurate simulation of interlava sedimentary layers and their interactions with the basaltic flows. Compounding this, **the exclusion of hydro-mechanical coupling precludes the modelling of pore pressure development**, a factor relevant to fluid–rock interactions. In addition, **the continuum approach overlooks discontinuity-driven phenomena**, such as crack propagation, spalling, and block detachment—key aspects of jointed rock behaviour. Finally, **using the Mohr–Coulomb failure criterion to address the project's main research question introduces a simplification**, which may prove overconservative compared to other failure criteria. That said, the excavation depth of the caverns is sufficiently great that only minor differences were observed between simulations using the Mohr–Coulomb and Hoek–Brown criteria.

9.3.2 Possibilities

The current project offers several opportunities to deepen geological understanding in the Sandoy–Suðuroy area. In terms of site investigation, the implementation of inclined boreholes could provide access to the currently undrilled stratigraphy, contributing to a more comprehensive geological profile. In addition, future core logging and field mapping should prioritise detailed descriptions of lava breccia units to better characterise their heterogeneity. Furthermore, in-situ stress measurements would provide essential data for refining the geomechanical model.

Promising results from numerical models, even under conditions involving large spans, indicate

significant potential for design evolution. Possible enhancements include expanding the cavern excavation to accommodate additional facilities, such as a groundwater reservoir, a pumping station, or lateral resting bays for vehicles beyond the outer roundabout lane. While the current design adequately addresses moderate stress conditions, its structural performance could be further improved by modifying the cavern geometry—for example, by incorporating curved walls—to better withstand higher stress levels.

Following the analysis of two final reference geometries, the project now presents an opportunity to advance numerical modelling using a discontinuum approach, offering a valuable complement to the method employed in this study. Moreover, while modelling through the Finite Volume Method on pure rock masses provided a solid qualitative foundation, transitioning to a more detailed framework that incorporates structural supports would enable further design refinement. Such developments could support the evaluation of reducing the pillar radius while maintaining structural stability, ultimately enabling an even more efficient configuration.

9.4 Social impact

In a world where "connectivity" and "globalisation" are often taken for granted, there are still parts of the globe that cannot fully benefit from these concepts. Life on the remote, sparsely populated islands of an archipelago like the Faroe Islands shows how things considered easily available for many—such as attending high school next door or quickly accessing hospital facilities—are not always so.

Until recently, for many residents of the Faroes, the only way to access essential services was by taking a ferry journey that could last tens of minutes or even hours. These inconvenient and uncomfortable living conditions have inevitably led many families, especially younger people, to leave the more isolated islands in recent decades. This small-scale but locally significant depopulation phenomenon has profoundly affected the country.

With the establishment of fixed links between islands, many people—particularly from the younger generations—have begun to see new opportunities even on the most peripheral islands. The opening of the Suðuroy Tunnel marks the final stage in completing the underwater fixed link network in the Faroe Islands and brings new possibilities to the southernmost island of the archipelago. This development will connect 99% of the Faroese population to the same road network (Steinhólm and Heinesen, 2017), freeing people from concerns about ferry cancellations due to rough seas or the long travel times previously required to reach Tórshavn.

References

Archie, G. E. (1942). The electrical resistivity log as an aid in determining some reservoir characteristics. *Transactions of the AIME*, *146*(1), 54–62. https://doi.org/10.2118/942054-G

Askaripour, M., Saeidi, A., Rouleau, A., & Mercier-Langevin, P. (2022). Rockburst in underground excavations: A review of mechanism, classification, and prediction methods. *Underground Space*, *7*. https://doi.org/10.1016/j.undsp.2021.11.008

Aufmuth, R. (1973). A systematic determination of engineering criteria for rocks. *Bulletin of the Association of Engineering Geologists*, *11*, 235–245.

Aydin, A., & Basu, A. (2005). The schmidt hammer in rock material characterization. *International Journal of Rock Mechanics and Mining Sciences*, *42*(6), 1013–1019. https://doi.org/https://doi.org/10.1016/j.enggeo.2005.06.006

Bardon, C., & Pied, B. (1969). Formation water saturation in shaly sands. *SPWLA Annual Logging Symposium*, SPWLA–1969.

Barton, N., By, T. L., Chryssanthakis, P., Tunbridge, L., Kristiansen, J., Løset, F., Bhasin, R. K., Westerdahl, H., & Vik, G. (1994). Predicted and measured performance of the 62 m span norwegian olympic ice hockey cavern at gjøvik. *International Journal of Rock Mechanics and Mining Sciences & Geomechanics Abstracts*, *31*(6), 617–641. https://doi.org/https://doi.org/10.1016/0148-9062(94)90004-3

Barton, N., Lien, R., & Lunde, J. (1974). Engineering classification of rock masses for the design of tunnel support. *Rock Mechanics*, *6*(4), 189–236. https://doi.org/https://doi.org/10.1007/BF01239496

Barton, N. (2002). Some new q-value correlations to assist in site characterization and tunnel design. *International Journal of Rock Mechanics and Mining Sciences*, *39*(2), 185–216. https://doi.org/10.1016/S1365-1609(02)00011-4

Barton, N., & Choubey, V. (1977). The shear strength of rock joints in theory and practice. *Rock mechanics*, *10*, 1–54.

Barton, N. (2022). Keynote lecture: Continuum or discontinuum–that is the question. *ISRM Latin American Rock Mechanics Symposium*, ISRM–LARMS.

Bennett, M. (2018). Underwater tunnels revolutionize the faroes. *The Maritime Executive*. https://www.maritime-executive.com/features/underwater-tunnels-revolutionize-the-faroes

Bieniawski, Z. (1978). Determining rock mass deformability: Experience from case histories. *International Journal of Rock Mechanics and Mining Sciences*, *15*, 237–248. https://doi.org/10.1016/0148-9062(78)90986-8

Blindheim, O. (2003). Learning from the lærdal tunnel. *Tunnels & Tunnelling International*, *35*(10).

Brooks, R. H. (1965). *Hydraulic properties of porous media*. Colorado State University.

Brown, E. T., & Hoek, E. (1978). Trends in relationships between measured in-situ stresses and depth. *International Journal of Rock Mechanics and Mining Sciences & Geomechanics Abstracts*, *15*(4), 211–215. https://doi.org/10.1016/0148-9062(78)91227-5

Brown, E., & Hoek, E. (1980). *Underground excavations in rock*. CRC Press. https://doi.org/10.1201/9781482288926

Cai, M., Kaiser, P., Tasaka, Y., & Minami, M. (2007). Determination of residual strength parameters of jointed rock masses using the gsi system. *International Journal of Rock Mechanics and Mining Sciences*, *44*(2), 247–265. https://doi.org/10.1016/j.ijrmms.2006.07.005

Carranza-Torres, C. (2021). Computational tools for the analysis of circular failure of rock slopes. *IOP Conference Series: Earth and Environmental Science*, *833*(1), 012003.

Carter, J. P., Manzari, M. T., & Dafalias, Y. F. (1993). A non-associated flow rule for cohesive-frictional soils. *Geotechnique*, *43*(1), 55–68.

Caudal, P. (2021, December). *Apport de la photogrammétrie et de l'intelligence artificielle à la détection des zones amiantées sur les fronts rocheux* [Doctoral dissertation].

Connect 3 Million. (2024, March). We're better connected: Tunnel presentation.

Cressler, A. (2007, April). Aa lava flow, december 27, 2005, kīlauea volcano, hawai'i volcanoes national park, hawai'i county, hawai'i [Photograph uploaded on April 8,2007; taken on December 27,2005; All rights reserved].

Cressler, A. (2011, February). Active pahoehoe lava flow, january 28, 2011, kalapana area, hawaii county, hawaii [Taken January 28,2011]. https://www.flickr.com/photos/alan_cressler/5446927690

Culshaw, M. G. (2015). Ulusay, r (ed.), 2015. the isrm suggested methods for rock characterization, testing and monitoring: 2007–2014: Cham, switzerland: Springer. *Bulletin of Engineering Geology and the Environment*, *74*(4), 1499–1500. https://doi.org/10.1007/978-3-319-07712-3

Cundall, P. A., & Hart, R. D. (1993). Numerical modeling of discontinua. In *Analysis and design methods* (pp. 231–243). Elsevier.

Darcy, H. (1856). *Les fontaines publiques de la ville de dijon*. Dalmont.

Deere, D., & Miller, R. (1966). *Engineering classification and index properties for intact rock* (tech. rep. No. AFNL-TR-65-116). Air Force Weapons Laboratory. Kirtland Air Force Base, New Mexico.

Diederichs, M., & Kaiser, P. (1999). Tensile strength and abutment relaxation as failure control mechanisms in underground excavations. *International Journal of Rock Mechanics and Mining Sciences*, *36*(1), 69–96.

Doré, A., Lundin, E., Kusznir, N., & Pascal, C. (2008). Potential mechanisms for the genesis of cenozoic domal structures on the ne atlantic margin: Pros, cons and some new ideas [Edited by H. Johnson, A.G. Doré, R.W. Gatliff, R. Holdsworth, E.R. Lundin, J.D. Ritchie]. *The Nature and Origin of Compression in Passive Margins, Geological Society, London, Special Publications*, *306*, 1–26.

Duncan, J. M., & Chang, C.-Y. (1970). Nonlinear analysis of stress and strain in soils. *Journal of the soil mechanics and foundations division*, *96*(5), 1629–1653.

Ellis, D., Passey, S. R., Jolley, D. W., & Bell, B. R. (2009). Transfer zones: The application of new geological information from the faroe islands applied to the offshore exploration of intra and sub-basalt strata. *Faroe Islands exploration conference: Proceedings of the 2nd Conference*, 205–226.

Esterhuizen, G., Dolinar, D., Ellenberger, J., & Prosser, L. (2011). Pillar and roof span design guidelines for underground stone mines. *9526*.

FAE. (2024). *Vága floghavn*. https://www.fae.fo/

Fookes, P. G., Baynes, F. J., & Hutchinson, J. N. (2000). Total geological history: A model approach to the anticipation, observation and understanding of site conditions. *ISRM International Symposium*, ISRM–IS.

Fraldi, M., & Guarracino, F. (2009). Limit analysis of collapse mechanisms in cavities and tunnels according to the hoek–brown failure criterion. *International Journal of Rock Mechanics and Mining Sciences*, *46*(4), 665–673.

Fraldi, M., & Guarracino, F. (2010). Analytical solutions for collapse mechanisms in tunnels with arbitrary cross sections. *International Journal of Solids and Structures*, *47*(2), 216–223. https://doi.org/10.1016/j.ijsolstr.2009.09.028

Freeze, R. A., & Cherry, J. A. (1979). *Hydraulic conductivity values for earth materials*. https://books.gw-project.org/hydrogeologic-properties-of-earth-materials-and-principles-of-groundwater-flow/chapter/hydraulic-conductivity-values-for-earth-materials/

Geoffroy, L., Bergerat, F., & Angelier, J. (1994). Tectonic evolution of the greenland-scotland ridge during the paleogene: New constraints. *Geology*, *22*(7), 653–656.

Gharsallaoui, H., Jafari, M., & Holeyman, A. (2020). Cavity expansion in rock masses obeying the "hoek–brown" failure criterion. *Rock Mechanics and Rock Engineering*, *53*(2), 927–941. https://doi.org/10.1007/s00603-019-01920-7

Gratchev, I. (2019). *Rock mechanics through project-based learning*. CRC Press. https://doi.org/10.1201/9780429278839

Grøv, E., & Trinh, N. Q. (2022). Sub sea tunneling in hard rock environment in scandinavia. *CIGOS 2021, Emerging Technologies and Applications for Green Infrastructure: Proceedings of the 6th International Conference on Geotechnics, Civil Engineering and Structures*, 1281–1289. https://doi.org/10.1007/978-981-16-7160-9_130

Herget, G. (1988). *Stresses in rock*. A.A. Balkema.

Hoek, E., & Brown, E. T. (1997). Practical estimates of rock mass strength. *International Journal of Rock Mechanics and Mining Sciences*, *34*(8), 1165–1186. https://doi.org/10.1016/S1365-1609(97)00335-X

Hoek, E., & Diederichs, M. S. (2006). Empirical estimation of rock mass modulus. *International Journal of Rock Mechanics and Mining Sciences*, *43*, 203–215. https://doi.org/10.1016/j.ijrmms.2005.06.005

Hoek, E., & Brown, E. (2019). The hoek–brown failure criterion and gsi–2018 edition. *Journal of Rock Mechanics and Geotechnical Engineering*, *11*(3), 445–463. https://doi.org/10.1016/j.jrmge.2018.08.001

Hoek, E., Carranza-Torres, C., Corkum, B., et al. (2002). Hoek-brown failure criterion-2002 edition. *Proceedings of NARMS-Tac*, *1*(1), 267–273.

Høien, A. H. (2006). Numerical modelling of subsurface roundabout in steinberget tunnel. *Fjellsprengningskonferansen 2006*.

Holter, K. G., Aagaard, B., Garshol, K., & Holmøy, K. H. (2021). *Sudurøy subsea road tunnel: Executive study for the early planning phase* (tech. rep. No. 20210198-01-R) (Executive study for the early planning phase). Norwegian Geotechnical Institute.

Itasca Consulting Group. (2017). Flac3d 6.0: Flac3d modeling (excerpt from flac3d help). https://itasca-software.s3.amazonaws.com/resources/flac3d_600_modeling.pdf

Itasca Consulting Group. (2023). Griddle 2.0 user manual (version 2.00.14, rev112423). https://itasca-int.objects.frb.io/assets/docs/about/Griddle_Manual_2-14.pdf

Japsen, P., & Waagstein, R. (2005). *Preliminary analysis of ultrasonic and geochemical properties of core samples from glyvursnes-1 and vestmanna-1, faroe islands: Contribution to the seifaba project funded by the sindri group* (tech. rep.). Geological Survey of Denmark and Greenland (GEUS). https://doi.org/10.22008/gpub/25963

Jimenez, R., Serrano, A., & Olalla, C. (2008). Linearization of the hoek and brown rock failure criterion for tunnelling in elasto-plastic rock masses. *International Journal of Rock Mechanics and Mining Sciences*, *45*(7), 1153–1163.

Johnson, R. B., & DeGraff, J. V. (1988). *Principles of engineering geology*. John Wiley & Sons.

Kender, S., Bogus, K., Pedersen, G., Dybkjaer, K., Mather, T., Mariani, E., Ridgwell, A., Riding, J., Wagner, T., Hesselbo, S., & Leng, M. (2021). Paleocene/eocene carbon feedbacks triggered

by volcanic activity. *Nature Communications*, *12*. https://doi.org/10.1038/s41467-021-25536-0

Landsverk. (2019). Infrastructure on the faroe islands, 2018–2030 [Original title: *Samferðsluætlan 2018–2030* (in Faroese)]. https://www.landsverk.fo/fo-fo/samfer%C3%B0sluaetlanin-2018-2030

Landsverk. (2022). Removing the island barrier: Suduroyartunnilin [Faroese Public Works Authority].

Larsen, L. M., Waagstein, R., Pedersen, A. K., & Storey, M. (1999). Trans-atlantic correlation of the palaeogene volcanic successions in the faeroe islands and east greenland. *Journal of the Geological Society*, *156*(6), 1081–1095.

Li, C. (2017). Principles of rockbolting design. *Journal of Rock Mechanics and Geotechnical Engineering*, *9*. https://doi.org/10.1016/j.jrmge.2017.04.002

Marinos, P., & Hoek, E. (2000). GSI: A Geologically Friendly Tool for Rock Mass Strength Estimation. *Proceedings of the GeoEng2000 Conference*.

Mavko, G., Japsen, P., & Boldreel, L. O. (2004). *Preliminary rock physics analysis of basalts in the lopra-1 well: Contribution to the seifaba project founded by the sindri group* (Report No. 2004/96). Geological Survey of Denmark and Greenland. https://doi.org/10.22008/gpub/25680

Meng, Q.-X., Wang, H.-L., Xu, W.-Y., Xie, W.-C., Wang, R.-B., & Zhang, J.-C. (2016). Robust equivalent tunnelling mohr–coulomb strength parameters for generalised hoek brown media. *European Journal of Environmental and Civil Engineering*, *20*(8), 841–860. https://doi.org/https://doi.org/10.1080/19648189.2015.1084380

Mihalis, I., Konstantis, S., Anagnostopoulos, A., Vlavianos, G., & Doulis, G. (2009). Tunnel stability factor–a new controlling parameter for the face stability conditions of shallow tunnels in weak rock environment. *Proc. 17th International Conference on Soil Mechanics and Geotechnical Engineering, Alexandria*, 5–9.

Millington, R., & Quirk, J. (1961). Permeability of porous solids. *Transactions of the Faraday Society*, *57*, 1200–1207. https://doi.org/10.1039/TF9615701200

Monsalve, J. J., Soni, A., Ripepi, N., & Rodriguez-Marek, A. (2020). A preliminary investigation on stochastic discrete element modeling for pillar strength determination in underground limestone mines from a probabilistic risk analysis approach.

Mualem, Y. (1976). A new model for predicting the hydraulic conductivity of unsaturated porous media. *Water Resources Research*, *12*(3), 513–522. https://doi.org/10.1029/WR012i003p00513

National Museum of the Faroe Islands. (n.d.). Geology [permanent exhibition] [Visited on May 26, 2024].

Niclasen, B., & Simonsen, K. (2012). High resolution wave climate of the faroe islands. *University of the Faroe Islands: Tórshavn, Faroe Islands*.

Noe-Nygaard, A., & Rasmussen, J. (1968). Petrology of a 3,000 metre sequence of basaltic lavas in the faeroe islands. *Lithos*, *1*(3), 286–304.

Norwegian Geotechnical Institute. (2015). *Using the q-system: Handbook – rock mass classification and support design* (Revised and new edition, June 2022). NGI.

Norwegian Tunnelling Society. (2016). *Norwegian rock caverns* (1st ed.) [Publication No. 25]. Norsk Forening for Fjellsprengningsteknikk NFF.

Norwegian Tunnelling Society. (2022, June). Norwegian tunnelling [Publication No. 14].

Olavsdottir, J., Stoker, M., Riishuus, M., & Eidesgaard, Ó. (2021). Discovery of two sub-volcanic basins below the north atlantic igneous province (naip), faroe platform, ne atlantic ocean. *Tectonics*, *40*. https://doi.org/10.1029/2020TC006589

Ólavsdóttir, J., & Eidesgaard, Ó. R. (2023). The management of freshwater on islands: Unique challenges or common opportunities? introductory session presenting the 1st iwra islands water congress on freshwater and islands [Presented at the 1st IWRA Islands Water Congress on Freshwater and Islands]. *XVIII World Water Congress*.

Pan, E., & Hudson, J. A. (1988). A three-dimensional strength criterion for jointed rock masses. *International Journal of Rock Mechanics and Mining Sciences & Geomechanics Abstracts*, *25*(6), 439–448.

Passey, S., & Jolley, D. (2009). A revised lithostratigraphic nomenclature for the palaeogene faroe islands basalt group, ne atlantic ocean. *Earth and Environmental Science Transactions of the Royal Society of Edinburgh*, *99*, 127–158. https://doi.org/10.1017/S1755691009008044

Passey, S. R., & Bell, B. R. (2007). Morphologies and emplacement mechanisms of the lava flows of the faroe islands basalt group, faroe islands, ne atlantic ocean. *Bulletin of Volcanology*, *70*, 139–156.

Passey, S. R. (2004). *The volcanic and sedimentary evolution of the faeroe plateau lava group, faeroe islands and faeroe-shetland basin, ne atlantic* [Doctoral dissertation, University of Glasgow].

Passey, S. (2009). Recognition of a faulted basalt lava flow sequence through the correlation of stratigraphic marker units, skopunarfjørður, faroe islands. *Faroe Islands exploration conference: Proceedings of the 2nd conference*, *50*, 174–204.

Patton, F. D. (1966). Multiple modes of shear failure in rock. *ISRM Congress*, ISRM–1CONGRESS.

Petersen, U. K. (2023). *Sediment cover between sandoy and suðuroy: A report on the sediment cover on bedrock between sandoy and suðuroy in connection with the planning of the suðuroyartunnil. based on marine seismic data* (tech. rep. No. JF-2023-08). Jarðfeingi.

Petersen, U. K., Madsen, T. H., Árting, U., & Højgaard, B. (2022). *A revised geological description of the suðuroy tunnel area. a work in progress. status report ultimo 2021* (tech. rep. No. 03) (Report to Landsverk). Jarðfeingi.

Petersen, U. K. (2020). *The suðuroyar subsea tunnel: Seismic processing report* (Report) (Report to Landsverk). Jarðfeingi.

Qarmout, M., König, D., & Wichtmann, T. (2022). A review of seven tunnel face stability models. *CivilEng*, *3*(1), 116–134. https://doi.org/10.3390/civileng3010008

Rambøll Norge AS. (2007). *Engineering geological report – steinbergtunnelen søndre part* (Technical Report). Rambøll Norge AS. Trondheim.

Rasmussen, J., Noe-Nygaard, A., & Troelsen, J. (1956). Faeröe islands (føroyar, færøerne, ıles faeröe). *Congres Géologique International & Commission De Stratigraphie (eds) Lexique Stratigraphique International: Europe*, *1*, 13–17.

Rasmussen, J., & Noe-Nygaard, A. (1970). Geology of the faeroe islands (pre-quaternary). *Danmarks Geologiske Undersøgelse I. Række*, *25*, 1–142.

Reynolds, J. M. (2011). *An introduction to applied and environmental geophysics* (2nd ed.). Wiley-Blackwell.

Rodrigues, C., Grøv, E., & Prada, S. (2002). Tunnelling in volcanic environment – experiences from projects in madeira island, iceland and faroe islands [Edited by C. Dinis da Gama and L. Ribeiro e Sousa, Sociedade Portuguesa de Geotecnia]. *ISRM International Symposium on Rock Engineering for Mountainous Regions: EUROCK 2002*, 643–655.

Samuelsen, T., & Grøv, E. (2018). Subsea road tunnels in the faroe islands. *Proceedings of the Institution of Civil Engineers-Civil Engineering*, *171*(5), 25–30. https://doi.org/10.1680/jcien.17.00032

Schön, J. H. (2015). Physical properties of rocks: Fundamentals and principles of petrophysics. In K. Helbig & S. Treitel (Eds.), *Developments in petroleum science* (2nd, Vol. 65). Elsevier. https://doi.org/10.1016/B978-0-08-100404-3.00007-X

Screening Eagle. (n.d.). Paper schmidt ps8000.

Selmer-Olsen, R., & Broch, E. (1978). General design procedure for underground openings in norway. In *Storage in excavated rock caverns: Rockstore 77* (pp. 219–226). Elsevier.

Serafim, J., & Pereira, J. (1983). Considerations of the geomechanical classification of bieniawski. *Proceedings of the International Symposium on Engineering Geology and Underground Construction*.

Shah, S. (1992). Aspects of flow of power-law fluids in porous media. *AIChE Journal*, *38*(5), 711–718.

Sheorey, P. (1994). A theory for in situ stresses in isotropic and transverseley isotropic rock. *International journal of rock mechanics and mining sciences & geomechanics abstracts*, *31*(1), 23–34.

Smith, G. A. (1991). Facies sequences and geometries in continental volcaniclastic sediments. *Sedimentation in Volcanic Settings*.

Sofianos, A., & Nomikos, P. (2006). Equivalent mohr–coulomb and generalized hoek–brown strength parameters for supported axisymmetric tunnels in plastic or brittle rock. *International Journal of Rock Mechanics and Mining Sciences*, *43*(5), 683–704. https://doi.org/10.1016/j.ijrmms.2005.11.006

Statens Vegvesen. (2000). Laerdalstunnelen: The laerdal tunnel.

Statens Vegvesen. (2024a). N100 veg-og gateutforming: Norm for prosjektering av veger.

Statens Vegvesen. (2024b). N500 vegtunneler: Norm for tunnelutforming.

Steinhólm, S., & Heinesen, E. (2017). Turning the faroes into one city: Demographic and spatial impacts of 60 years of transport infrastructure expansion. *Island Studies Journal*, *19*(2), 6–28. https://doi.org/10.24043/001c.123786

Stumo, R. V. (2016). Construction of an undersea tunnel on the t-connection. *Proceedings of the Norwegian Tunnelling Conference 2016*, [insert page numbers].

Su, S., & Stephansson, O. (1999). Effect of a fault on in situ stresses studied by the distinct element method. *International Journal of Rock Mechanics and Mining Sciences*, *36*(8), 1051–1056. https://doi.org/10.1016/S1365-1609(99)00119-7

Szöőr, G., Rozsa, P., Vekemans, B., Vincze, L., Adams, F., Uzonyi, I., Kiss, Á., & Beszeda, I. (2005). Characterization of cosmic micro-objects by sem-eds, dige, micro-pixe and srxrf techniques. *Acta Geologica Hungarica*, *48*, 419–434. https://doi.org/10.1556/AGeol.48.2005.4.4

Taguchi, G. (1986). *Introduction to quality engineering: Designing quality into products and processes*. Asian Productivity Organization.

Terzaghi, K., & Richart, F. E. (1952). Stresses in rock about cavities. *(No Title)*.

The Guardian. (2024). *The faroes' amazing underwater drive*. https://www.theguardian.com/artanddesign/2024/feb/20/faroes-amazing-underwater-drive-tunnel-viking-atlantic

Trinh, N., & Jonsson, K. (2013). Design considerations for an underground room in a hard rock subjected to a high horizontal stress field at rana gruber, norway. *Tunnelling and underground space technology*, *38*, 205–212.

Trinh, N. Q., Holmøy, K. H., & Wiig, H. E. (2021). Challenging infrastructure project assisted by monitoring and numerical modelling as the following tunnels were excavated below existing tunnels. *Rock Mechanics and Rock Engineering*, *54*(4), 1671–1685. https://doi.org/10.1007/s00603-021-02371-9

Trinh, Q. N., Broch, E., & Lu, M. (2006). Three dimensional modelling of a tunnel cave-in and spiling bolt support. In C. F. Leung & Y. X. Zhou (Eds.), *Rock mechanics in underground construction: Isrm international symposium 2006, 4th asian rock mechanics symposium, 8–10 november 2006, singapore* (pp. 15–22). World Scientific Publishing Co.

Troms County Municipality. (2025, January). Opening of breivika tunnel postponed.

Umhvørvisstovan. (2024). *Dátur á sjónum*. Retrieved April 6, 2024, from https://www.foroyakort.fo/tak-datur-nidur/datur-a-sjonum

U.S. Environmental Protection Agency. (2025). Single-point resistance borehole logging. https://www.epa.gov/environmental-geophysics/single-point-resistance-borehole-logging

Vallejo, L. I. G. d., & Ferrer, M. (2011). *Geological engineering*. CRC Press/Balkema. http://www.crcnetbase.com/isbn/9781439881996

Van Genuchten, M. T. (1980). A closed-form equation for predicting the hydraulic conductivity of unsaturated soils. *Soil Science Society of America Journal*, *44*(5), 892–898. https://doi.org/10.2136/sssaj1980.03615995004400050002x

Van Genuchten, M. T., & Nielsen, D. (1985). On describing and predicting the hydraulic properties. *Annales Geophysicae*, *3*(5), 615–628.

Visit Faroe Islands. (n.d.). Maps of the faroe islands. https://visitfaroeislands.com/en/plan-your-stay/get-ready-for-your-trip/maps-of-the-faroe-islands

Waagstein, R. (1988). Structure, composition and age of the faeroe basalt plateau. *Geological Society, London, Special Publications*, *39*(1), 225–238.

Waagstein, R., & Andersen, C. (2004). *Well completion report: Glyvursnes-1 and vestmanna-1, faroe islands* (tech. rep.) (Contribution to the SeiFaBa project funded by the Sindri Group (1 DVD included)). Geological Survey of Denmark and Greenland (GEUS). https://doi.org/10.22008/gpub/25378

Waagstein, R., Guise, P., & Rex, D. (2002). K/ar and 39ar/40ar whole-rock dating of zeolite facies metamorphosed flood basalts: The upper paleocene basalts of the faroe islands, ne atlantic. *The North Atlantic Igneous Province: Stratigraphy, Tectonic, Volcanic and Magmatic Processes*, *197*, 219–252.

Waagstein, R., Hald, N., Jørgensen, O., Nygaard, A. N., Schönharting, G., Nielsen, P., & Rasmussen, J. (1984). Deep drilling on the faeroe islands. *Bulletin of the Geological Society of Denmark*, *32*, 133–138.

Walker, G. (1971). Compound and simple lava flows and flood basalts. *Bulletin Volcanologique*, *35*, 579–590.

Walker, R. J., Holdsworth, R. E., Imber, J., & Ellis, D. (2011a). The development of cavities and clastic infills along fault-related fractures in tertiary basalts on the ne atlantic margin. *Journal of Structural Geology*, *33*(2), 92–106.

Walker, R. J., et al. (2010). *The structural evolution of the faroe islands, ne atlantic margin* [Doctoral dissertation, Durham University] [Available at Durham E-Theses Online: http://etheses.dur.ac.uk/134/].

Walker, R. J., Holdsworth, R., Imber, J., & Ellis, D. (2011b). Onshore evidence for progressive changes in rifting directions during continental break-up in the ne atlantic. *Journal of the Geological Society*, *168*(1), 27–48.

Wang, M., Shi, A.-C., Li, H.-B., Yan, H.-C., Fan, G., & Zhou, J.-W. (2023). Mechanism analysis of surrounding rock mass failure induced by the multi-cavern effect in a large-scale underground powerhouse. *Applied Sciences*, *13*(7), 4376. https://doi.org/10.3390/app13074376

Waxman, M. H., & Smits, L. (1968). Electrical conductivities in oil-bearing shaly sands. *Society of Petroleum Engineers Journal*, *8*(02), 107–122. https://doi.org/10.2118/1863-A

Xiao, P., Yang, X., Li, B., et al. (2024). Roof arch collapse of underground cavern in fractured rock mass: In situ monitoring and numerical modeling. *Journal of Rock Mechanics and Geotechnical Engineering*. https://doi.org/10.1016/j.jrmge.2024.05.018

Xu, S. (1990). Use of schmidt hammer for estimating mechanical properties of weak rock. *6ˆ< th> Int. IAEG Congress. Balkema, Rotterdam, 1990*.

Yarmolin, D. (2020, October). Scandinavia map: Norway, sweden, finland, denmark, iceland and faroe islands [stock illustration] [iStock].

Yaşar, E., & Erdoğan, Y. (2004). Estimation of rock physicomechanical properties using hardness methods. *Engineering Geology*, *71*(3-4), 281–288.

Yılmaz, I., & Sendır, H. (2002). Correlation of schmidt hardness with unconfined compressive strength and young's modulus in gypsum from sivas (turkey). *Engineering Geology*, *66*(3-4), 211–219.

Zhang, Z., Chen, F., He, M., & Wang, H. (2022). An analytical calculation method for displacement criterion on tunnel surrounding rock mass stability. *Advances in Civil Engineering*, *2022*(1), 2493968.

Ziska, H. (2012). Fracture orientations onshore faroe islands (north atlantic); evidence for dual rifting episodes in the palaeogene. *Proceedings of the 3rd Faroe Islands Exploration Conference. Annales Societatis Scientarum Færoensis Supplementum*, *56*, 40–58.

Zou, L., Meng, G., Jiayao, W., Fu, W., Chu, W., & Xu, W. (2024). A case study on the stability of a big underground powerhouse cavern cut by an interlayer shear zone in the china baihetan hydropower plant. *Deep Underground Science and Engineering*, *4*, 305–315. https://doi.org/10.1002/dug2.12094

A

Appendix A: Engineering geology for particular site

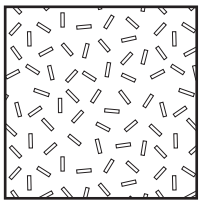
A.1 Jarðfeingi boreholes: Skúvoy-1

As a reference for the boreholes provided by Jarðfeingi (Petersen et al., 2022) covering the Sandoy–Suðuroy area, the *Skúvoy*-1 core log is presented here, along with lithology and fracture log keys. The significance of this borehole lies in the fact that it provides the clearest evidence for distinguishing the *Malinstindur–Enni* transition within the stratigraphy. The lithostratigraphic description is accompanied by core images, fracture illustrations, and single-point resistance (*SPR*) measurements. Rock quality designation (*RQD*) is not provided along the drilled core.

KEY FOR JARÐFEINGI LITHOLOGY LOGS

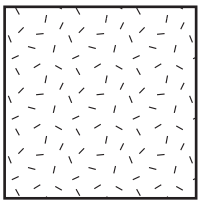
USGS Standard Pattern Chart (FGDCgeostdTM11A2_PattCh_poster.pdf)

Types of basaltic lithologies



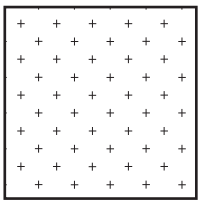
730

Coarse-grained Feldspar porphyric basalt



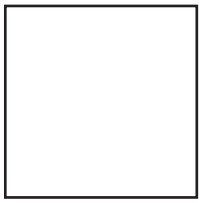
302-K

Fine-grained Feldspar porphyric basalt



327-K

Olivin porphyric basalt



Aphyric basalt



Pantone 485 CVU

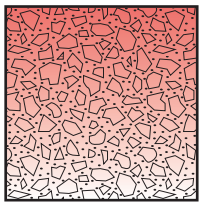
Volcaniclastic sand- and claystone (red)

Types of descriptive features



715

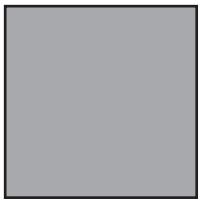
Volcanic breccia or agglomerate



606 + (0/70/50/2)

Core stone / saprolithic bole

Other features

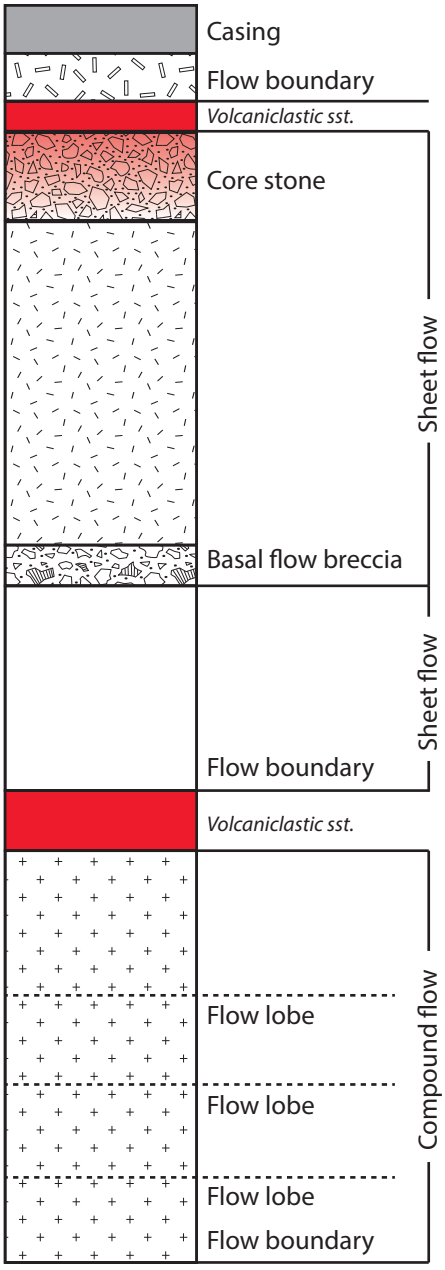


K40

Casing - No log

Log-Example

Lithology



KEY FOR JARÐFEINGI FRACTURE LOGS

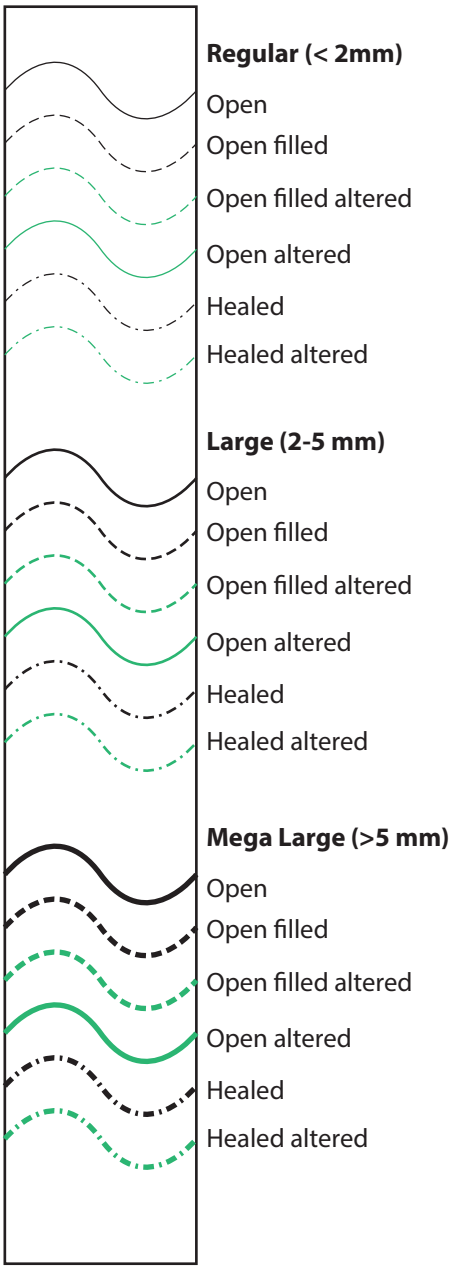
The fracture data are divided into classes defined by visual inspection of the televiewlog. The fractures were divided into following classes:

SIZE OF FRACTURE
Regular (< 2 mm)
Large (2 – 5 mm)
Mega Large (> 5 mm)

FRACTURE TYPE
Open
Filled
Healed
Altered

Log-Example

Fractures



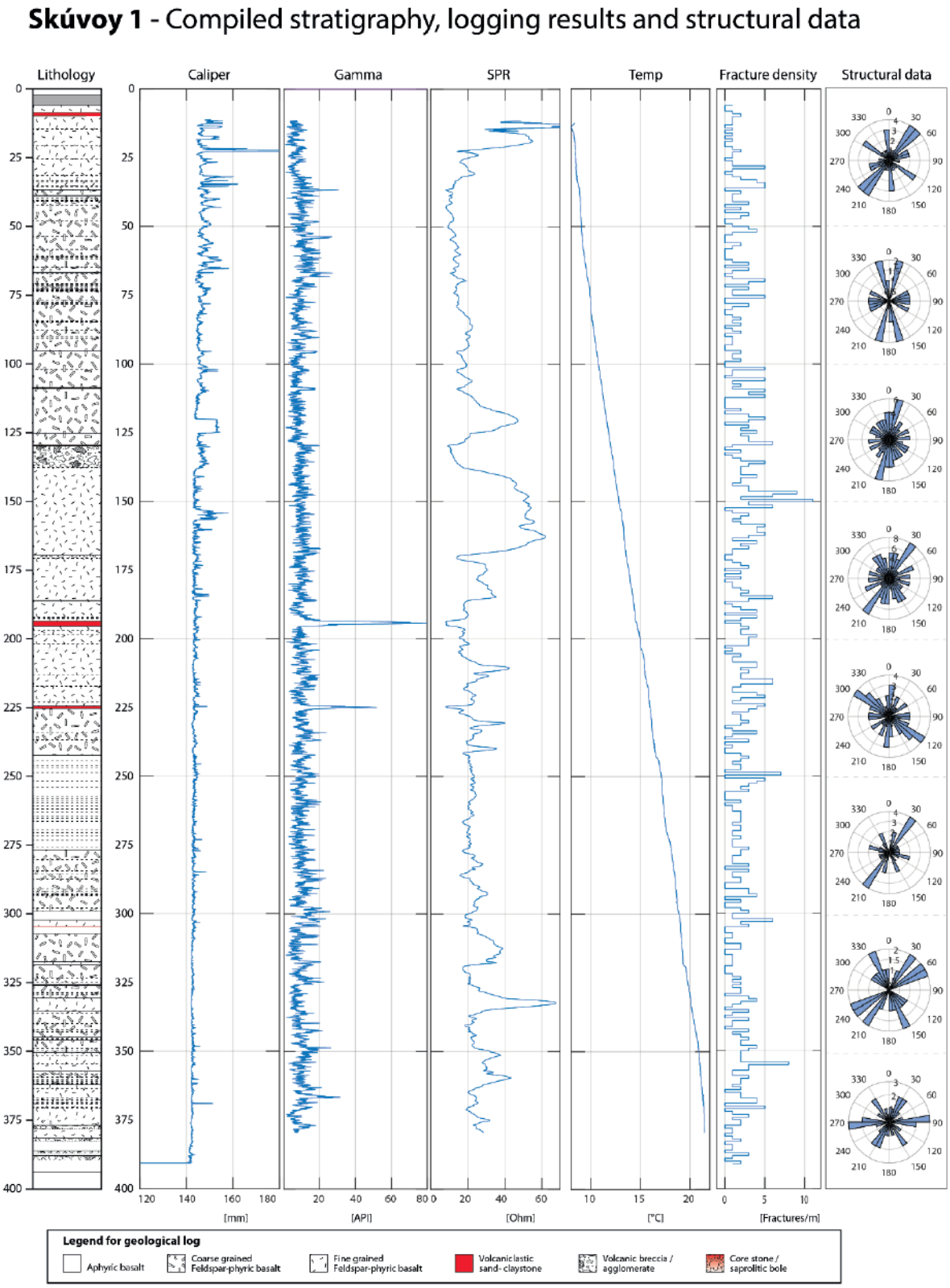
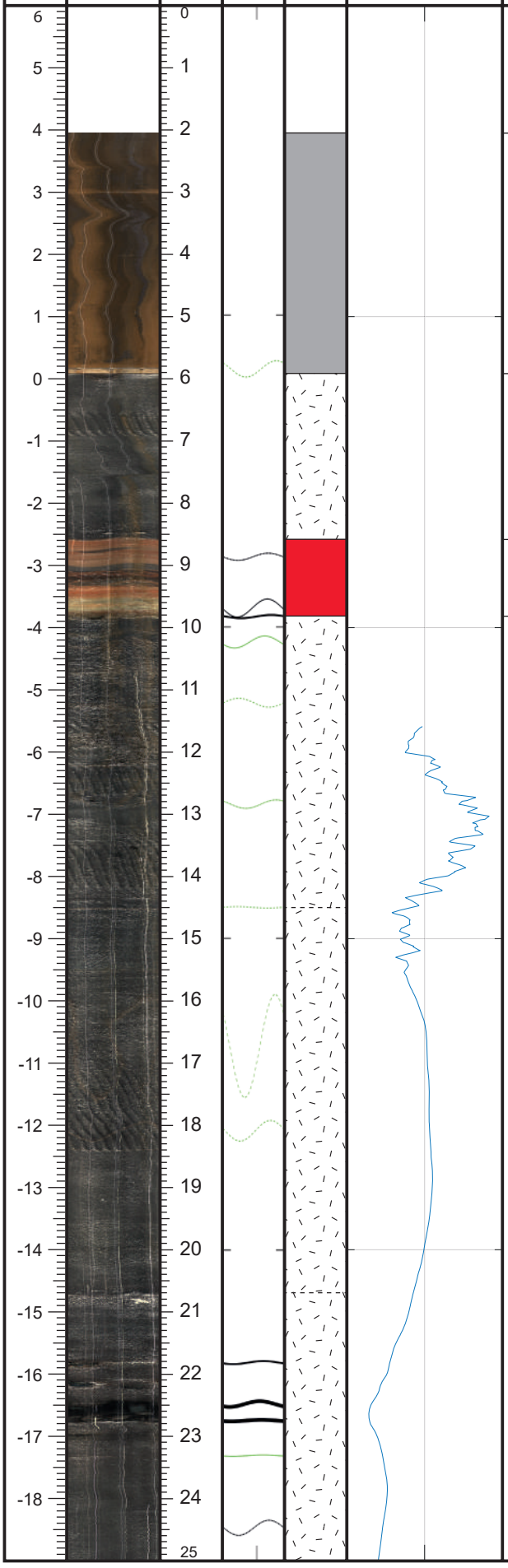


Figure 7. The composite logs for Skúvoy-1 comprise a series of columns. The first column shows the lithology, the next four columns show data from caliper, natural gamma (NGAM), point resistivity (SPR), and temperature logs. The last two columns present fracture density pr. meter and structural data in 50-m intervals.

1	Project: Suðuroyartunnilin	Year: 2021	Location: Skúvoy	Borehole 01
	Position: Y= ca 851471 X=ca 210345 Z= ca 6 m			Datum: FOTM



Remarks

Borehole starts at the lower boundary of a ca 3 m thick volcaniclastic sandstone.

0-5,9 m: Casing.

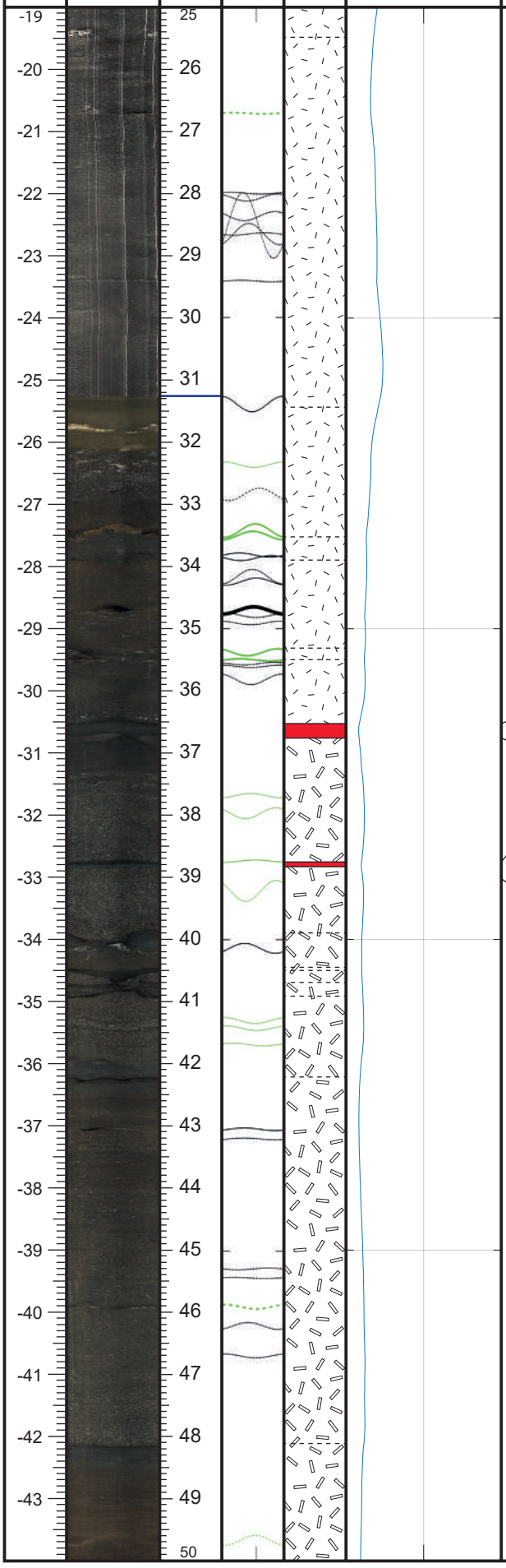
Fine feldspar phyric basalt. Probably 8-9 m thick.

Volcaniclastic sandstone. 8,6-9,8 m. 1,2 m thick. Banded. Light brown and grayish yellow to grayish green bands.

Fine feldspar phyric basalt. 27 m thick compound flow. 0,2-6 m thick flow units.

30 cm high cavity marked as two large fractures on the log. Above are megavesicles.

2	Project: Suðuroyartunnilin	Year: 2021	Location: Skúvoy	Borehole 01
	Position: Y= ca 851471 X=ca 210345 Z= ca 6 m			Datum: FOTM



Remarks

Fine feldspar phyric basalt. 27 m thick compound flow. 0,2-6 m thick flow units.

31,26 m drilled depth: water level in well.

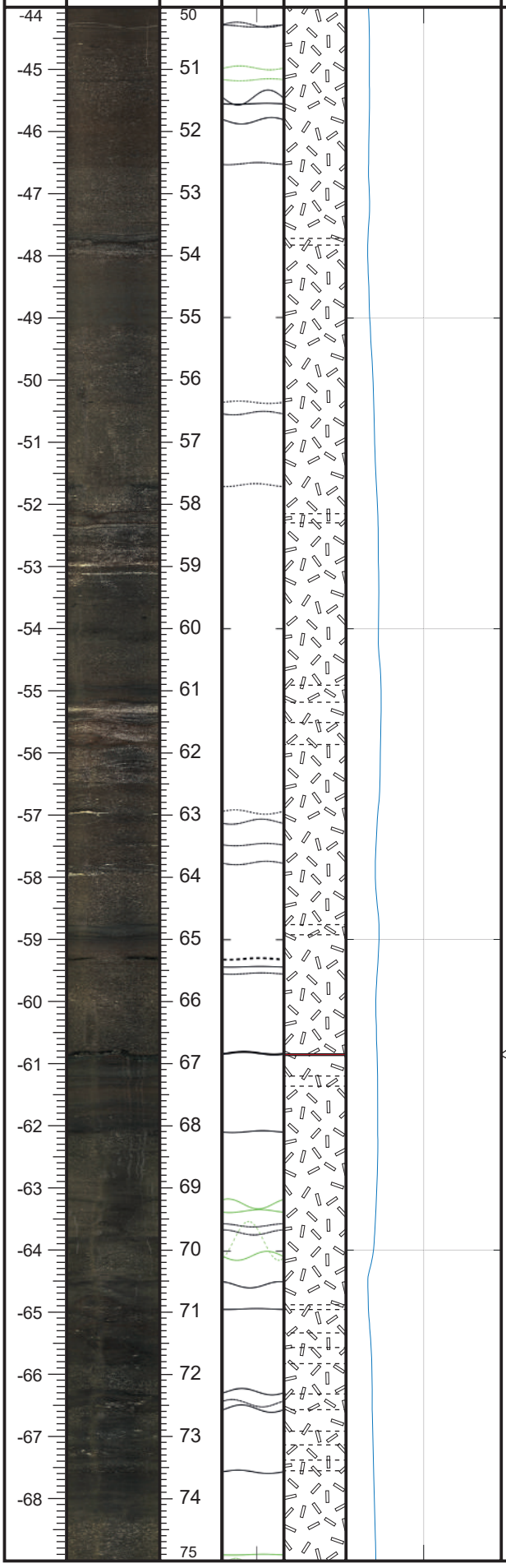
Volcaniclastic bed. 36,52-36,72 m. 20 cm thick. Grayish green.

Coarse feldspar phyric basalt. 2m thick.

Volcaniclastic sediment. 38,75-38,83 cm. 6 cm thick. Grayish green to blue green.

Coarse feldspar phyric basalt. 28 m thick compound flow with 0,1-6 m thick flow units.

3	Project: Suðuroyartunnilin	Year: 2021	Location: Skúvoy	Borehole 01
	Position: Y= ca 851471 X=ca 210345 Z= ca 6 m			Datum: FOTM



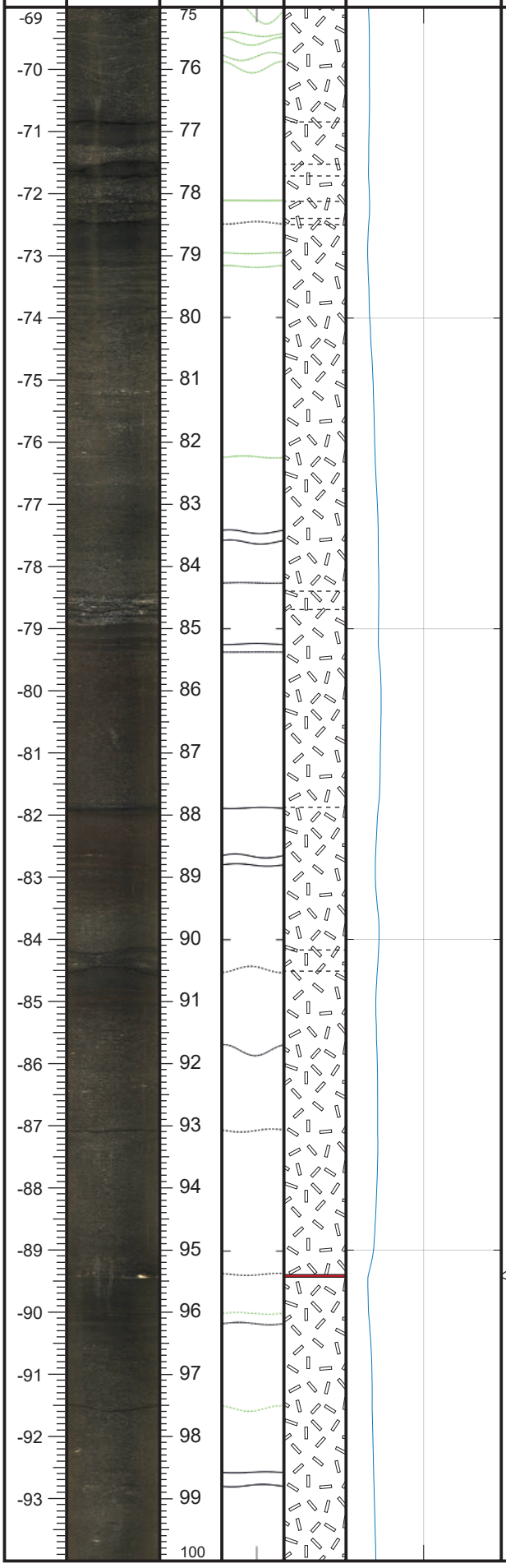
Remarks

Coarse feldspar phyric basalt. 28 m thick compound flow. 0,1-6 m thick flow units.

Thin (<2 cm) volcaniclastic. Dark green. 66,85 m.

Coarse feldspar phyric basalt. 29 m thick compound flow. 0,1-6 m thick flow units.

4	Project: Suðuroyartunnilin	Year: 2021	Location: Skúvoy	Borehole 01
	Position: Y= ca 851471 X=ca 210345 Z= ca 6 m			Datum: FOTM



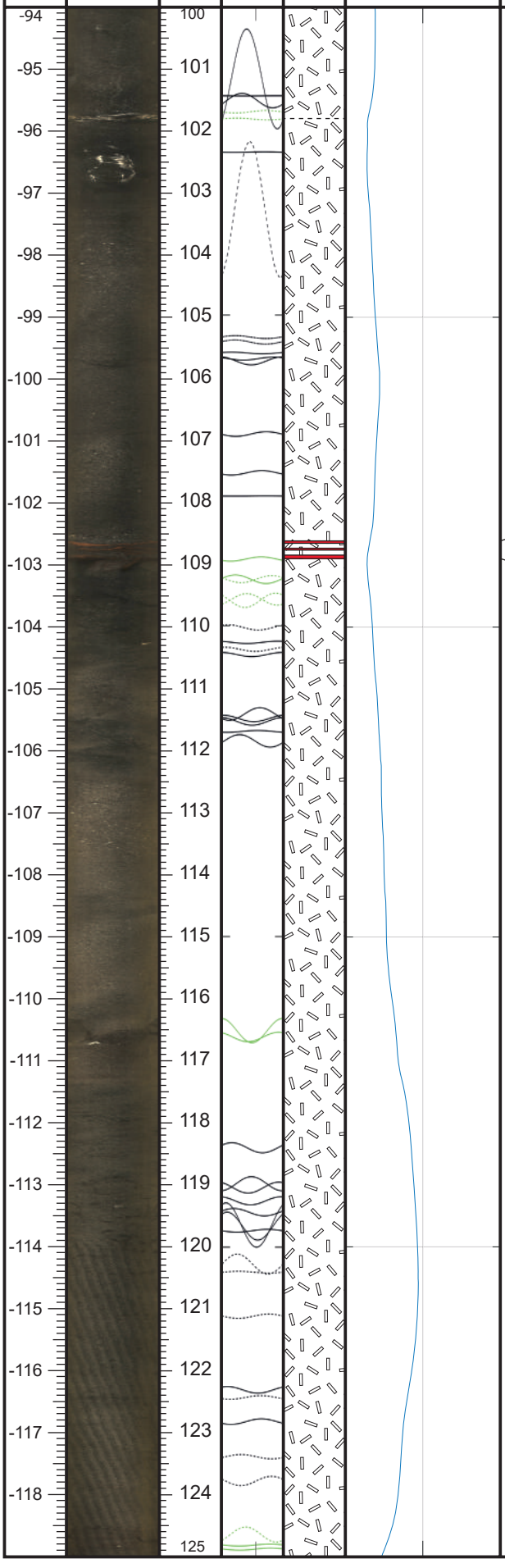
Remarks

Coarse feldspar phyric basalt. 29 m thick compound flow with 0,1-6 m thick flow units.

Thin volcaniclastic (<2 cm). Dark green.

Coarse feldspar phyric basalt. 13 m thick compound flow consisting of two 6 an 8 m thick flow units.

5	Project: Suðuroyartunnilin	Year: 2021	Location: Skúvoy	Borehole 01
	Position: Y= ca 851471 X=ca 210345 Z= ca 6 m			Datum: FOTM



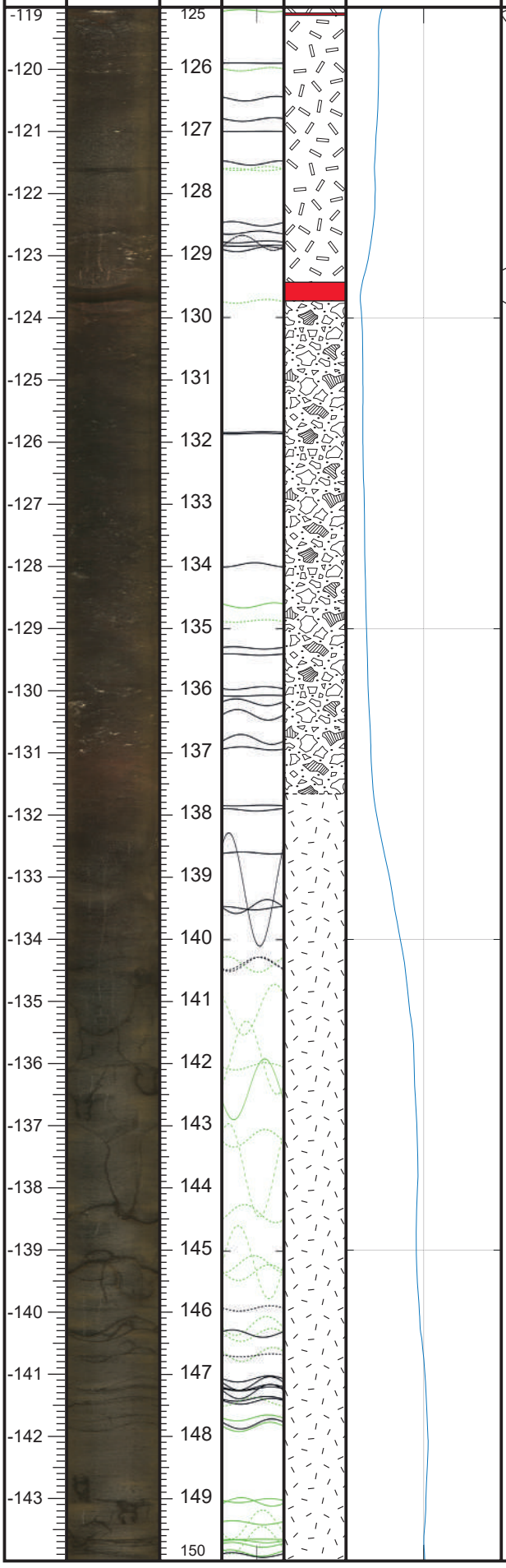
Remarks

Coarse feldspar phyric basalt. 13 m thick compound flow consisting of two 6 an 8 m thick flow units.

108,6-109,0: three 2-6 cm thick light brown volcaniclastic layers

Coarse feldspar phyric basalt. Sheet lobe. 16 m thick.

6	Project: Suðuroyartunnilin	Year: 2021	Location: Skúvoy	Borehole 01
	Position: Y= ca 851471 X=ca 210345 Z= ca 6 m			Datum: FOTM



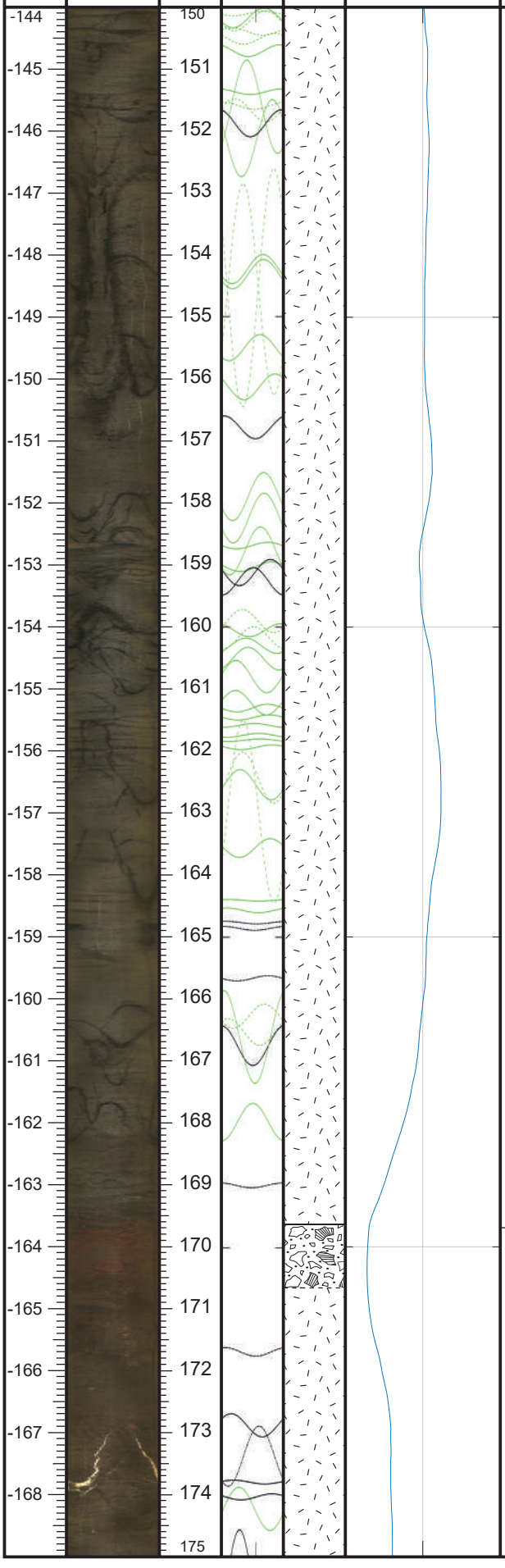
Remarks

Thin volcaniclastic sediment.
Coarse feldspar phyric basalt. ca 4 m thick.

Volcaniclastic sediment. 129,37-129,73 m. 36 cm thick.
Moderate brown to grayish brown.

Fine feldspar phyric basalt. 40 m thick sheet lobe with a brecciated flow top (8 m) and a massive lower part (32 m).

7	Project: Suðuroyartunnilin	Year: 2021	Location: Skúvoy	Borehole 01
	Position: Y= ca 851471 X=ca 210345 Z= ca 6 m			Datum: FOTM

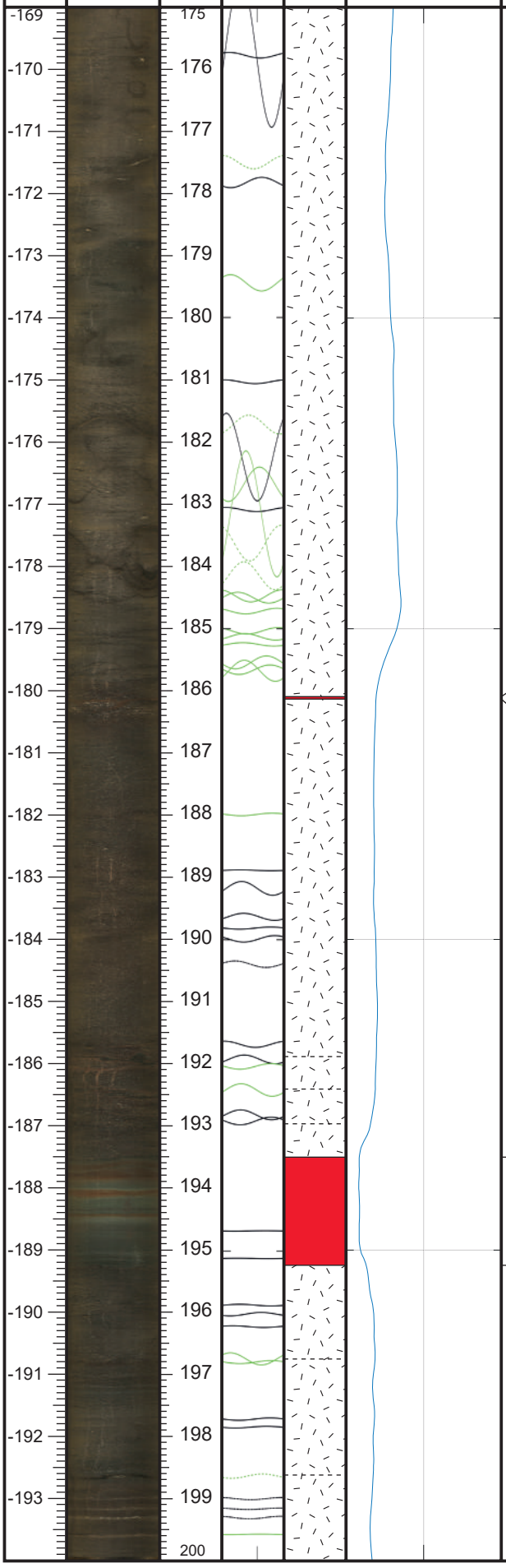


Remarks

Fine feldspar phyric basalt. 40 m thick sheet lobe with a brecciated flow top (8 m) and a massive lower part (32 m).

Fine feldspar phyric basalt. 16 m thick sheet lobe with a brecciated flow top (1 m) and a massive lower part.

8	Project: Suðuroyartunnilin	Year: 2021	Location: Skúvoy	Borehole 01
	Position: Y= ca 851471 X=ca 210345 Z= ca 6 m			Datum: FOTM



Remarks

Fine feldspar phyric basalt. 16 m thick sheet lobe with a brecciated flow top (1 m) and a massive lower part.

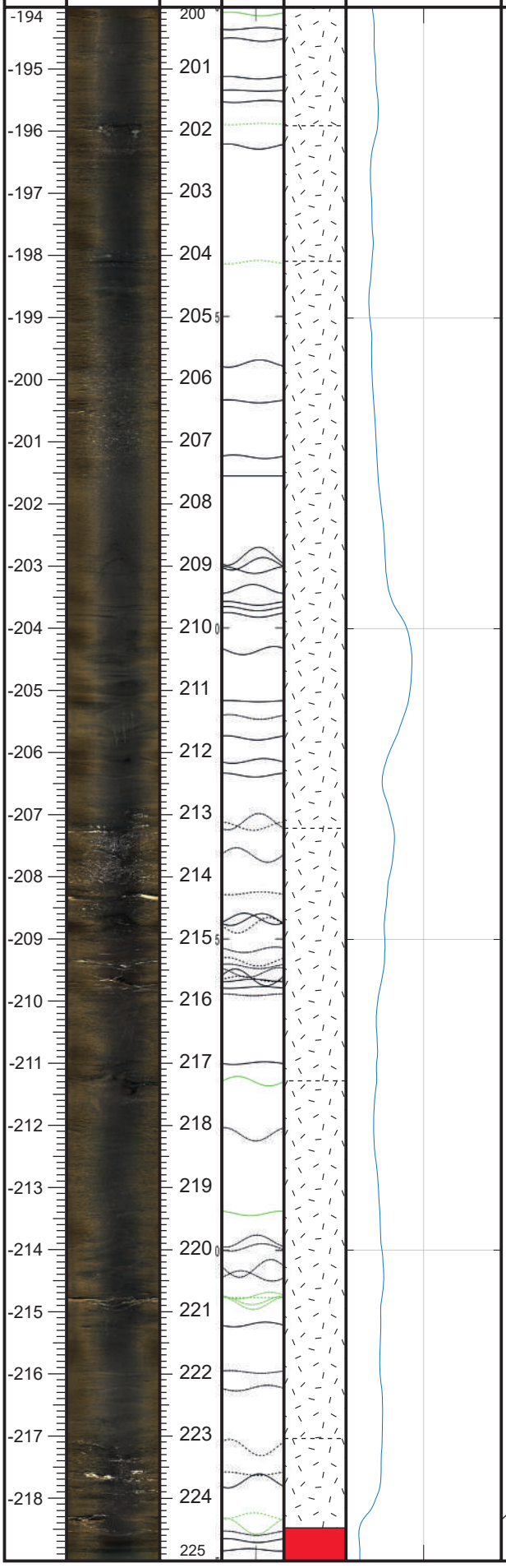
Thin volcaniclastic sediment. 186,1 m. Light brown.

Fine feldspar phyric basalt. 7 m thick compound flow with 0,5 to 6 m thick flow units.

Volcaniclastic sediment. Striped dominantly green and minor red. 193,45-195,28 m. 1,83 m thick. Three units, where the upper part is light brown and the lower part is moderat yellowish green to grayish green.

Fine feldspar phyric basalt. 29 m thick compound flow with 1-9 m thick flow units.

9	Project: Suðuroyartunnilin	Year: 2021	Location: Skúvoy	Borehole 01
	Position: Y= ca 851471 X=ca 210345 Z= ca 6 m			Datum: FOTM

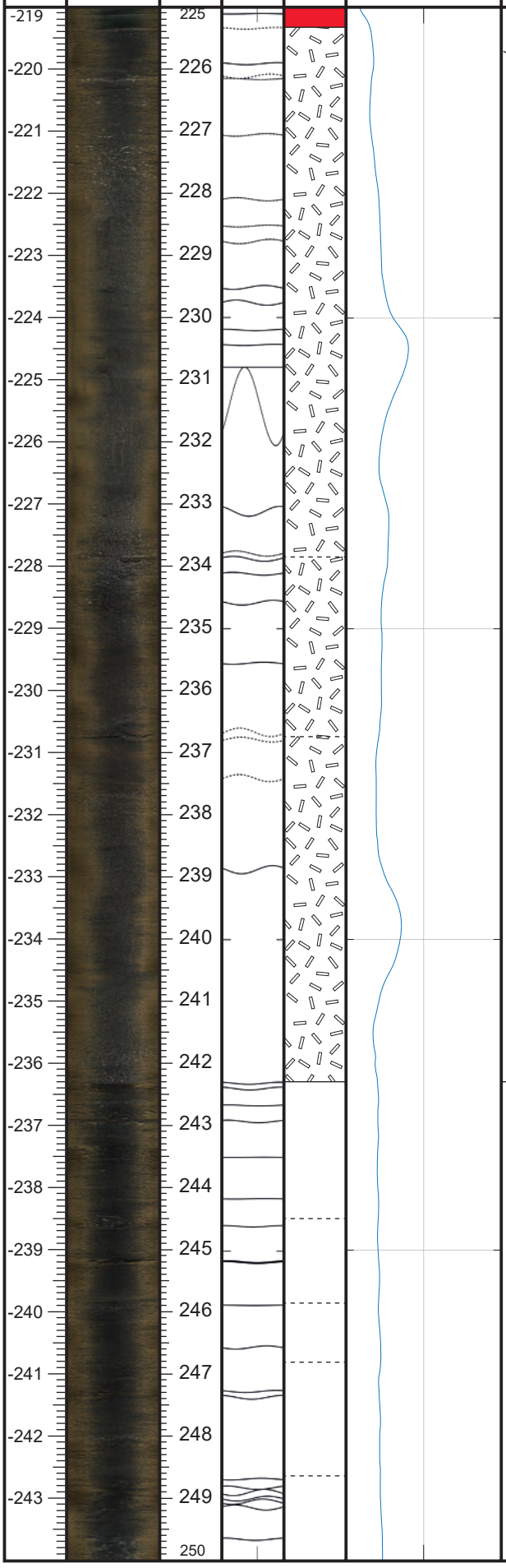


Remarks

Fine feldspar phyric basalt. 29 m thick compound flow with 1-9 m thick flow units.

Volcaniclastic sediment. 224,50-225,33 m. 83 cm thick. Banded. grayish brown and pale green bands.

10	Project: Suðuroyartunnilin	Year: 2021	Location: Skúvoy	Borehole 01
	Position: Y= ca 851471 X=ca 210345 Z= ca 6 m			Datum: FOTM



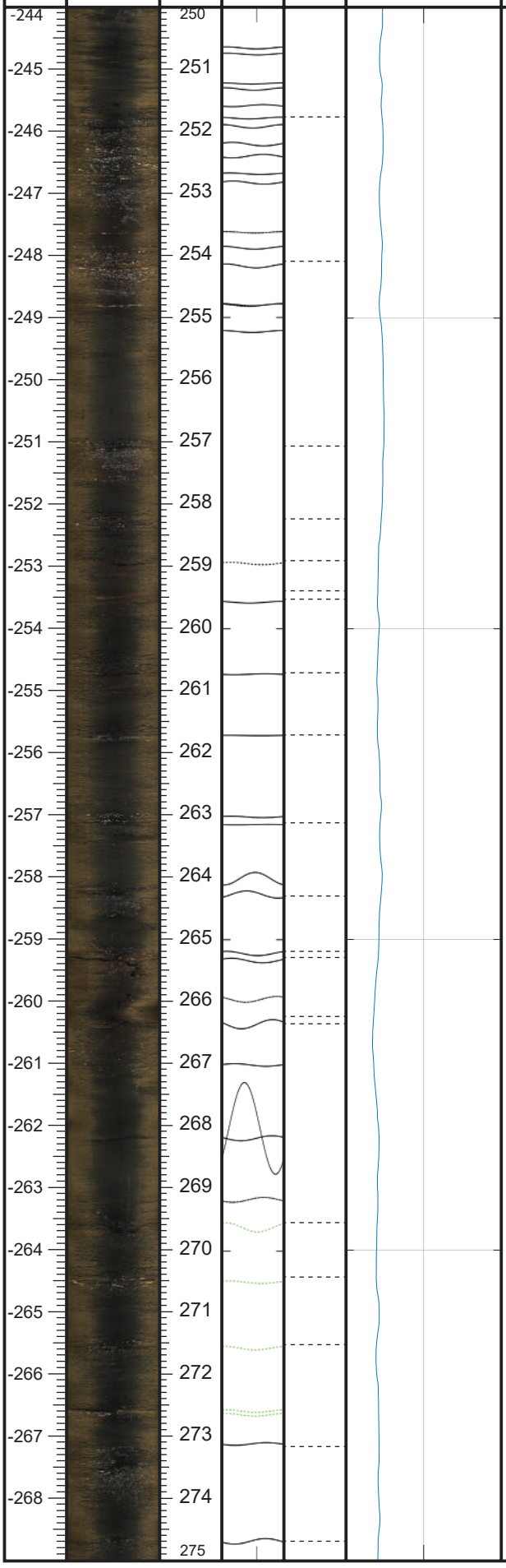
Remarks

Volcaniclastic sediment. 224,50-225,33 m. 83 cm thick. Banded. grayish brown and pale green bands.

Coarse feldspar phyric basalt. 17 m thick compound flow with 3-9 m thick flow units.

Dominantly aphyric basalt. 35 m thick compound flow with 0,1- 3 m flow units.
Pipe vesicles and thin lava tongues are observed.

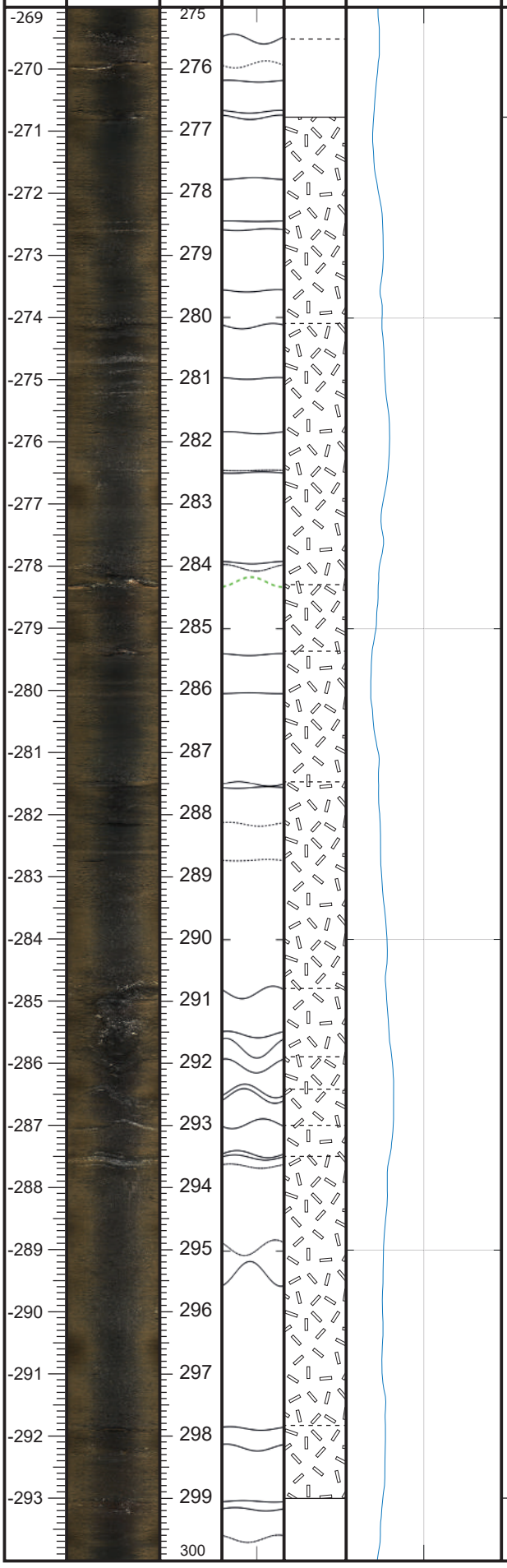
11	Project: Suðuroyartunnilin	Year: 2021	Location: Skúvoy	Borehole 01
	Position: Y= ca 851471 X=ca 210345 Z= ca 6 m			Datum: FOTM



Remarks

Dominantly aphyric basalt. 35 m thick compound flow with 0,1- 3 m flow units.
Pipe vesicles and thin lava tongues are observed.

12	Project: Suðuroyartunnilin	Year: 2021	Location: Skúvoy	Borehole 01
	Position: Y= ca 851471 X=ca 210345 Z= ca 6 m			Datum: FOTM



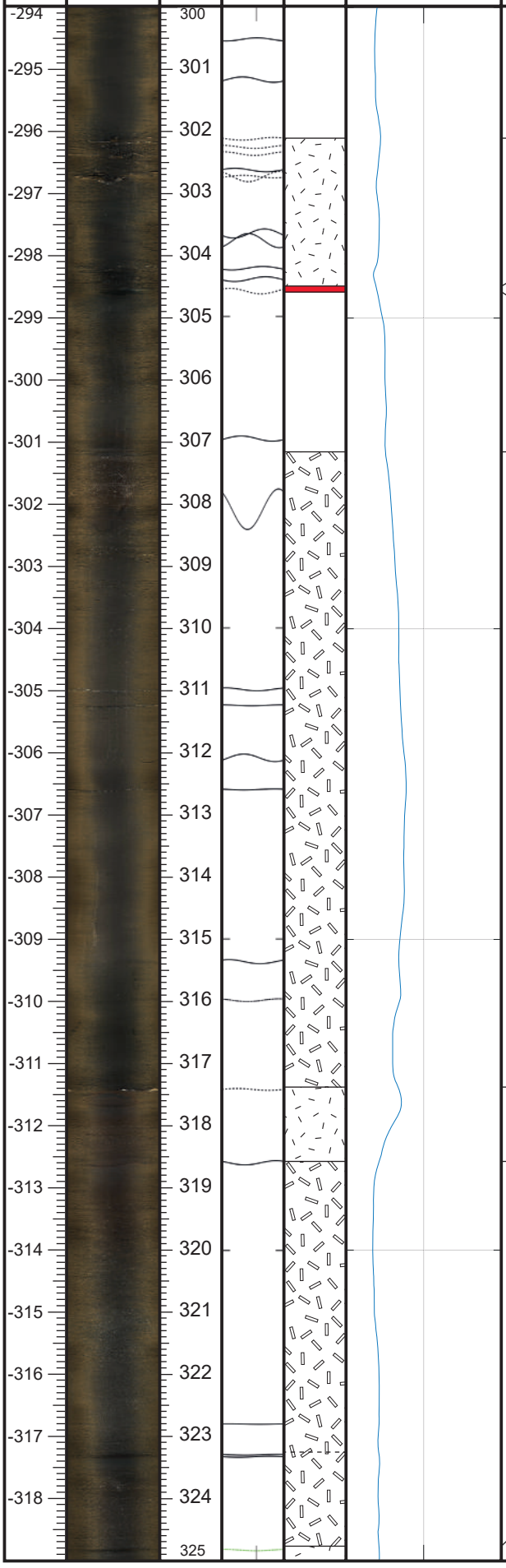
Remarks

Aphyric basalt. 35 m thick compound flow with 0,1- 3 m flow units.

Coarse feldspar phyric basalt. 22 m thick compound flow with 0,5 m to 4 m flow units.

Aphyric basalt. 3 m thick.

13	Project: Suðuroyartunnilin	Year: 2021	Location: Skúvoy	Borehole 01
	Position: Y= ca 851471 X=ca 210345 Z= ca 6 m			Datum: FOTM



Remarks

Aphyric basalt.3 m thick.

Fine feldspar porphyritic basalt. 2,3 m thick.

Pale green volcaniclastic sediment. 304,5-304,6 m. ca 10 cm

Aphyric basalt. 2,5 m thick.

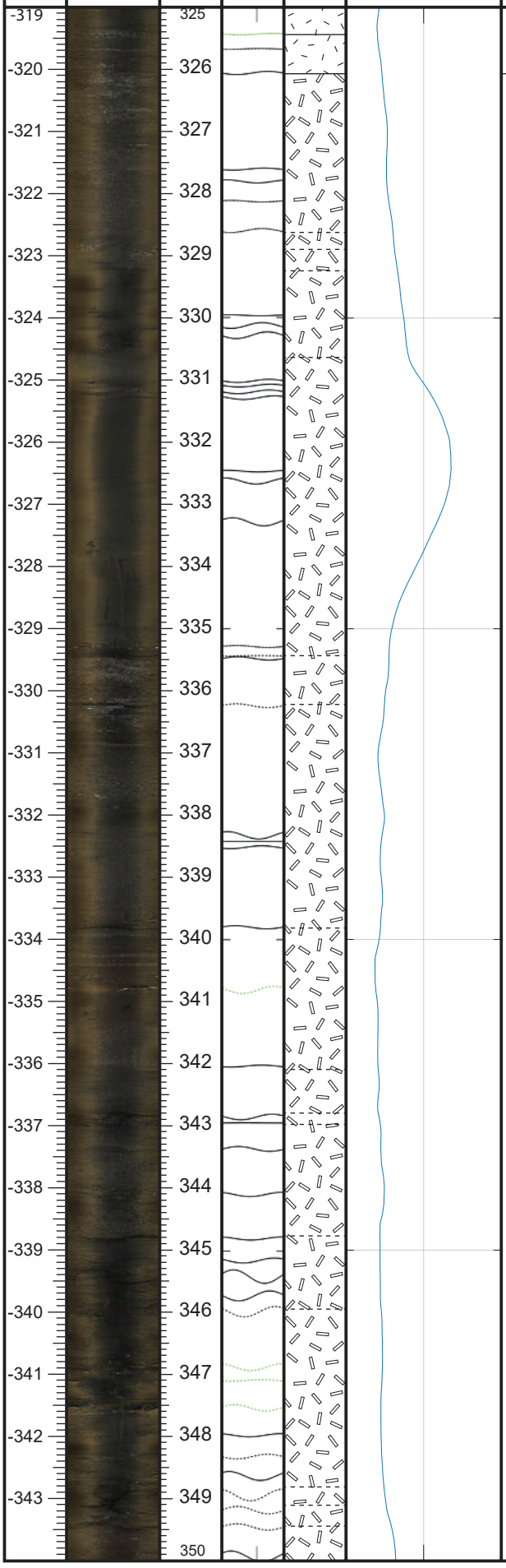
Sparse coarse and fine feldspar porphyritic basalt. 10 m thick.

Fine feldspar porphyritic basalt. 1, 2 m thick.

Coarse feldspar porphyritic basalt. 6 m thick. Two flow units, that are 4,7 and 1,5 m thick.

Fine feldspar porphyritic basalt. 1, 2 m thick.

14	Project: Suðuroyartunnilin	Year: 2021	Location: Skúvoy	Borehole 01
	Position: Y= ca 851471 X=ca 210345 Z= ca 6 m			Datum: FOTM



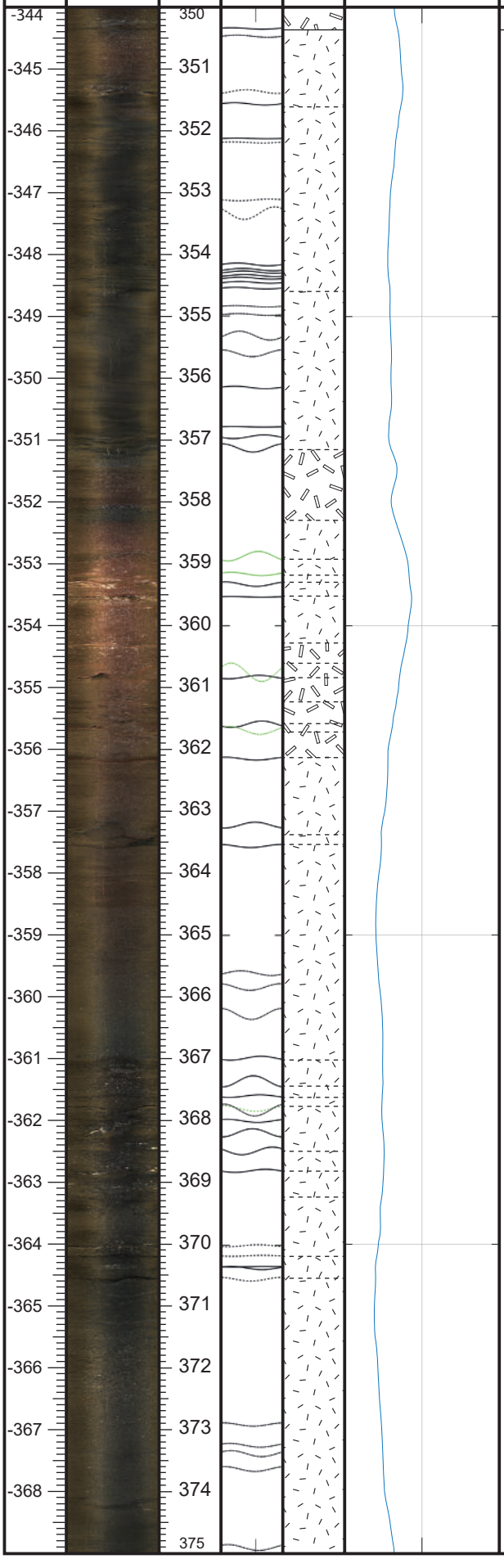
Remarks

Fine feldspar phyric basalt. 1,2 m thick. Two flow units.

Coarse grained feldspar-phyric basalt. 25 m thick compound flow with 0,2 m to 5 m thick flow units. Varying size and content of feldspar.

Zone with magma mixing signatures

15	Project: Suðuroyartunnilin	Year: 2021	Location: Skúvoy	Borehole 01
	Position: Y= ca 851471 X=ca 210345 Z= ca 6 m			Datum: FOTM



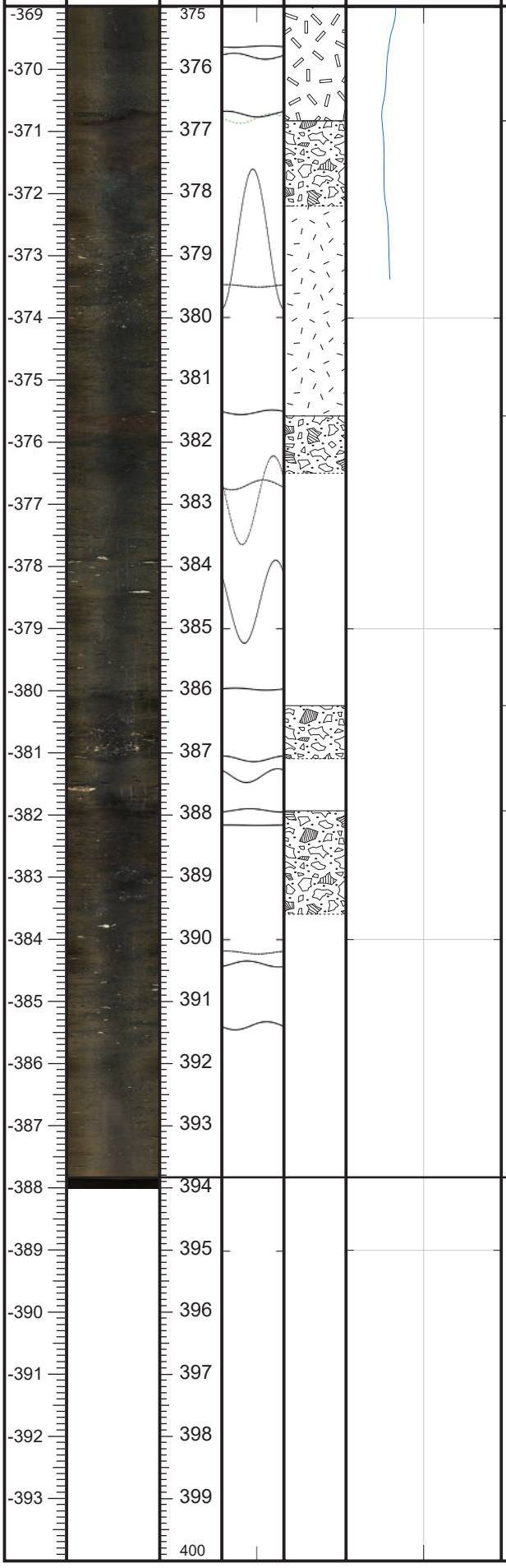
Remarks

Dominantly fine feldspar phyric basalt with some coarse feldspar. 27 m thick compound flow with 0,5 m to 7 m thick flow units.

Zone with magma mixing signatures

357-362 m: Reddish and altered basalt. Alteration probably fracture related.

16	Project: Suðuroyartunnilin	Year: 2021	Location: Skúvoy	Borehole 01
	Position: Y= ca 851471 X=ca 210345 Z= ca 6 m			Datum: FOTM



Remarks

Dominantly fine feldspar phyric basalt with some coarse feldspar. 27 m thick compound flow with 0,5 m to 7 m thick flow units.

Fine feldspar phyric to aphyric basalt. 5 m thick sheet lobe with brecciated crust (1,4 m).

Aphyric basalt. 5 m thick sheet lobe with brecciated crust (0,9 m).

Aphyric basalt. 1,7 m thick sheet lobe with brecciated crust (0,9 m).

Aphyric basalt. >6 m thick sheet lobe with brecciated crust (1,7 m).

A.2 Seismic surveys data processing: Line O1

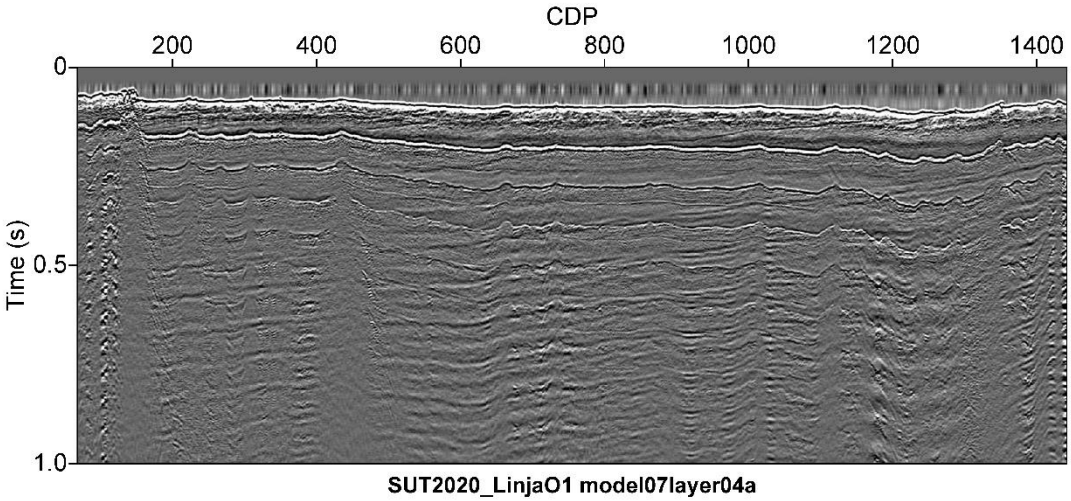
In the marine seismic surveys performed by Jarðfeingi in the Sandoy–Suðuroy area (Petersen, 2020), because the seismic signals were highly scattered, the usual method of analysing reflection travel times could not be used to determine underground velocities. Instead, the process relied on refraction seismic analysis, which focuses on the travel times of refracted waves that travel along interfaces underground. Only a wide bandpass filter was applied to keep most of the data clear. Noise from multiple reflections and the airgun source had to be identified and dealt with later during interpretation. In this appendix, the outcome results for Line O1 are illustrated, coupled with a brief procedure describing the data gaining process.

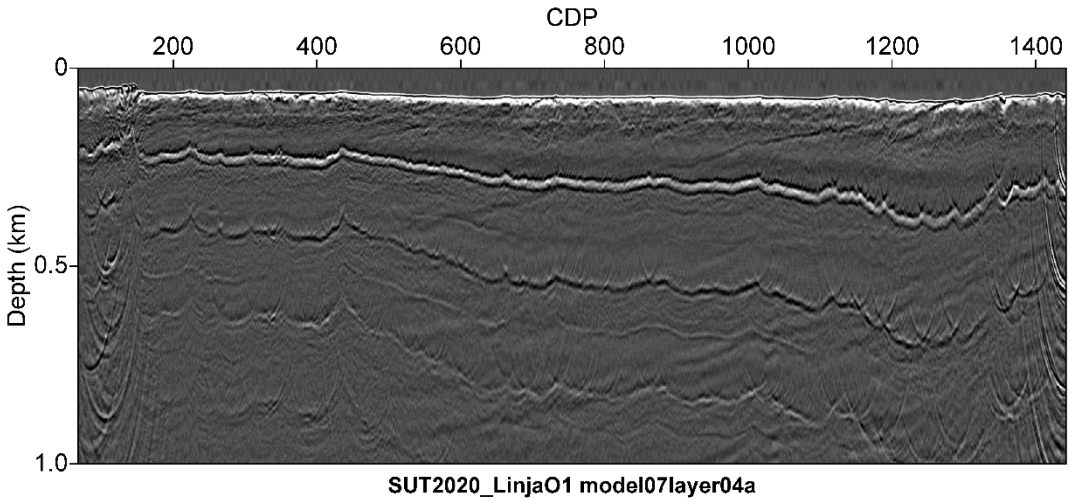
The **velocity models**, which describe how fast seismic waves travel through different layers underground, were created through an iterative approach. The process began by stacking raw data and picking the seabed reflection to define the first interface. The simplest model had two layers: the water above and basalt rock below. The water velocity was fixed, while the basalt velocity varied with depth based on previous studies. Using special inversion software, the model was adjusted to match the measured **travel times** (Fig. 5 in the document) of the first seismic arrivals, improving its accuracy. The models were built to depths of either 500 or 1000 m depending on location, and used a grid to organise velocity values horizontally and vertically. Unrealistically high velocities were limited to a maximum value to avoid errors during processing.

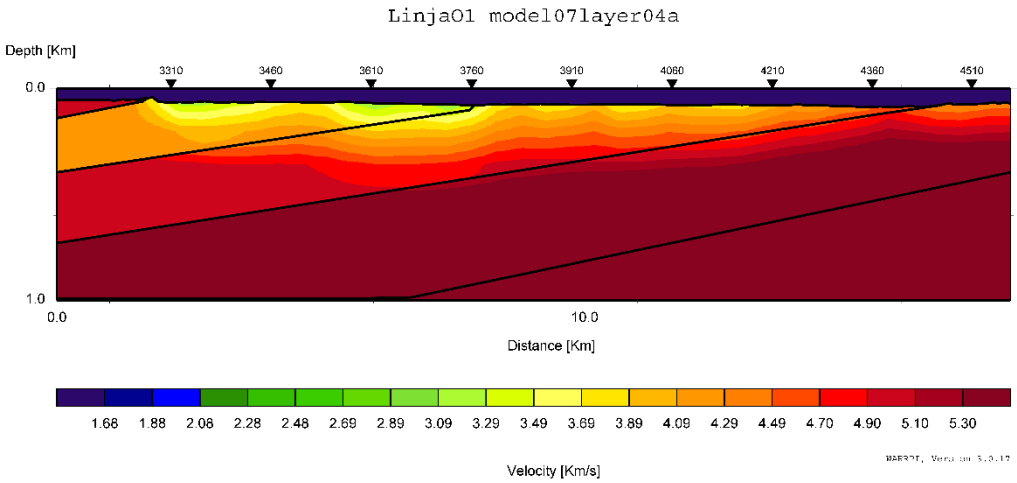
Once a reliable velocity model (Fig. 3) was obtained, the seismic data was processed through a series of steps. The data geometry was arranged along a 2D profile, then sorted by common reflection points. A gain correction compensated for signal weakening with distance. A bandpass filter helped keep the desired frequency range. Normal Move Out correction adjusted for the differences in travel time caused by the offset between source and receiver. The data was then stacked (Fig. 1) to enhance the true reflections and reduce noise. Finally, a median filter smoothed the results before applying **depth migration** (Fig. 2), which transforms travel times into true depth images.

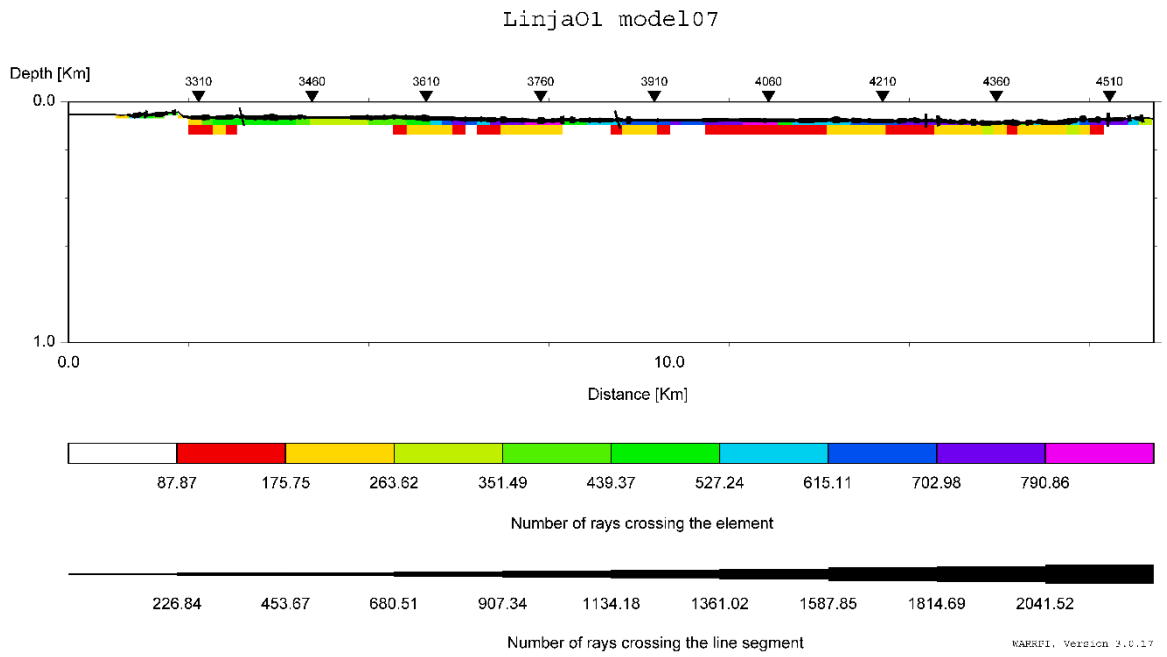
After the initial processing, a more detailed model was created including a third layer to represent the sedimentary basin beneath the seabed. The velocity of the sediments was estimated from the data. Depth migration was refined through repeated iterations to better define the basin's base. For some profiles, forward modelling was attempted. This means testing deeper and more complex layered models by predicting travel times and comparing them to the actual data. The model was not fully completed due to limited time.

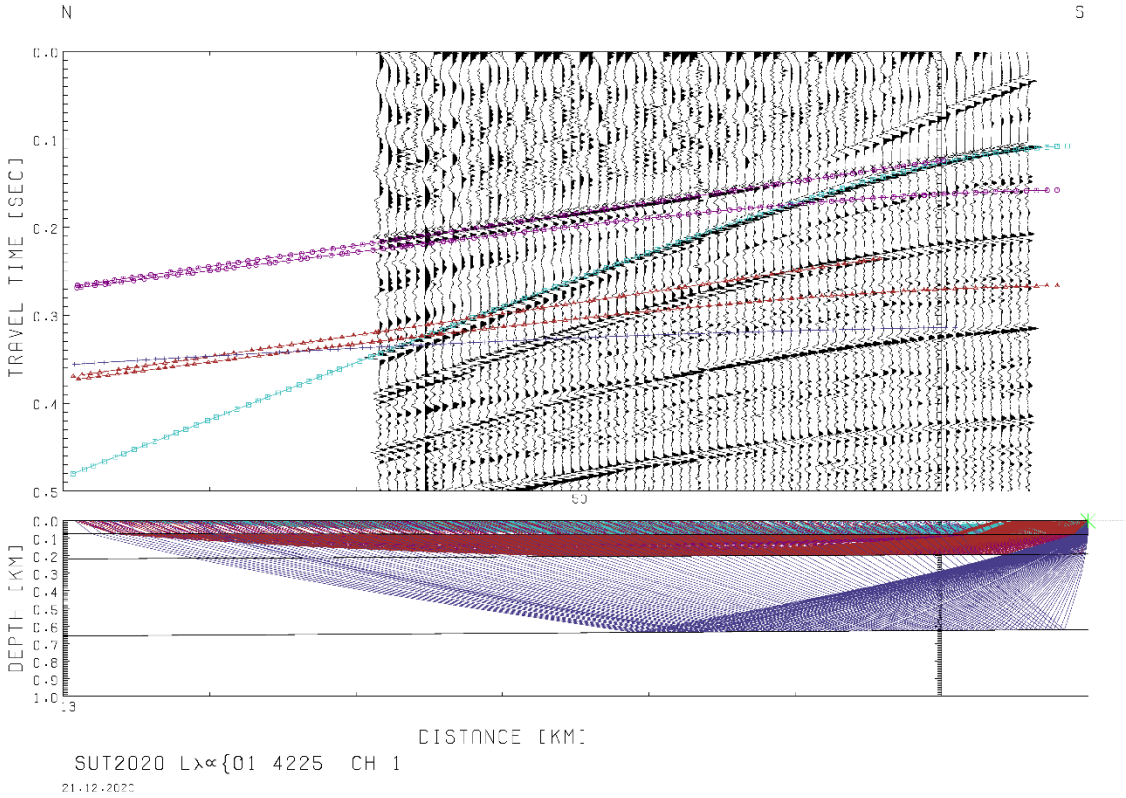
LinjaO1


CDP
200
400
600
800
1000
1200
1400
0
0.5
1.0
Time (s)
SUT2020_LinjaO1 model07layer04a


CDP
200
400
600
800
1000
1200
1400
0
0.5
1.0
Depth (km)
SUT2020_LinjaO1 model07layer04a


LinjaO1 model07layer04a
Depth [Km]
3310
3460
3610
3760
3910
4060
4210
4360
4510
0.0
1.0
0.0
10.0
Distance [Km]
1.68
1.88
2.08
2.28
2.48
2.69
2.89
3.09
3.29
3.49
3.69
3.89
4.09
4.29
4.49
4.70
4.90
5.10
5.30
Velocity [Km/s]


Linja01 model07
Depth [Km]
3310
3460
3610
3760
3910
4060
4210
4360
4510
0.0
1.0
0.0
10.0
Distance [Km]
87.87
175.75
263.62
351.49
439.37
527.24
615.11
702.98
790.86
Number of rays crossing the element
226.84
453.67
680.51
907.34
1134.18
1361.02
1587.85
1814.69
2041.52
Number of rays crossing the line segment
WAKRPI, Version 3.0.17


N
S
TRAVEL TIME [SEC]
0.0
0.1
0.2
0.3
0.4
0.5
50
DEPTH [KM]
0.0
0.1
0.2
0.3
0.4
0.5
0.6
0.7
0.8
0.9
1.0
DISTANCE [KM]
SUT2020 Línja01 4225 CH 1
21.12.2020

A.3 Faroe Islands seabed bathymetry

In addition to the depth contour lines plotted for the Sandoy–Suðuroy sea strait, this appendix provides an overview of the bathymetry of the entire archipelago. Around the Faroe Islands, ocean depths range from 0 m a.s.l. to roughly -150 m a.s.l. (the range shown in the plot) and extend significantly deeper further from the archipelago. Such shallow depths in the middle of the Atlantic Ocean are quite surprising and clearly reflect the sub-continental nature of the Faroe Islands and the oceanic plateau on which they are located. Bathymetric data are also extremely valuable for identifying submarine depressions or elevations, as first indicators of possible faults, rifts, or sedimentary deposits.

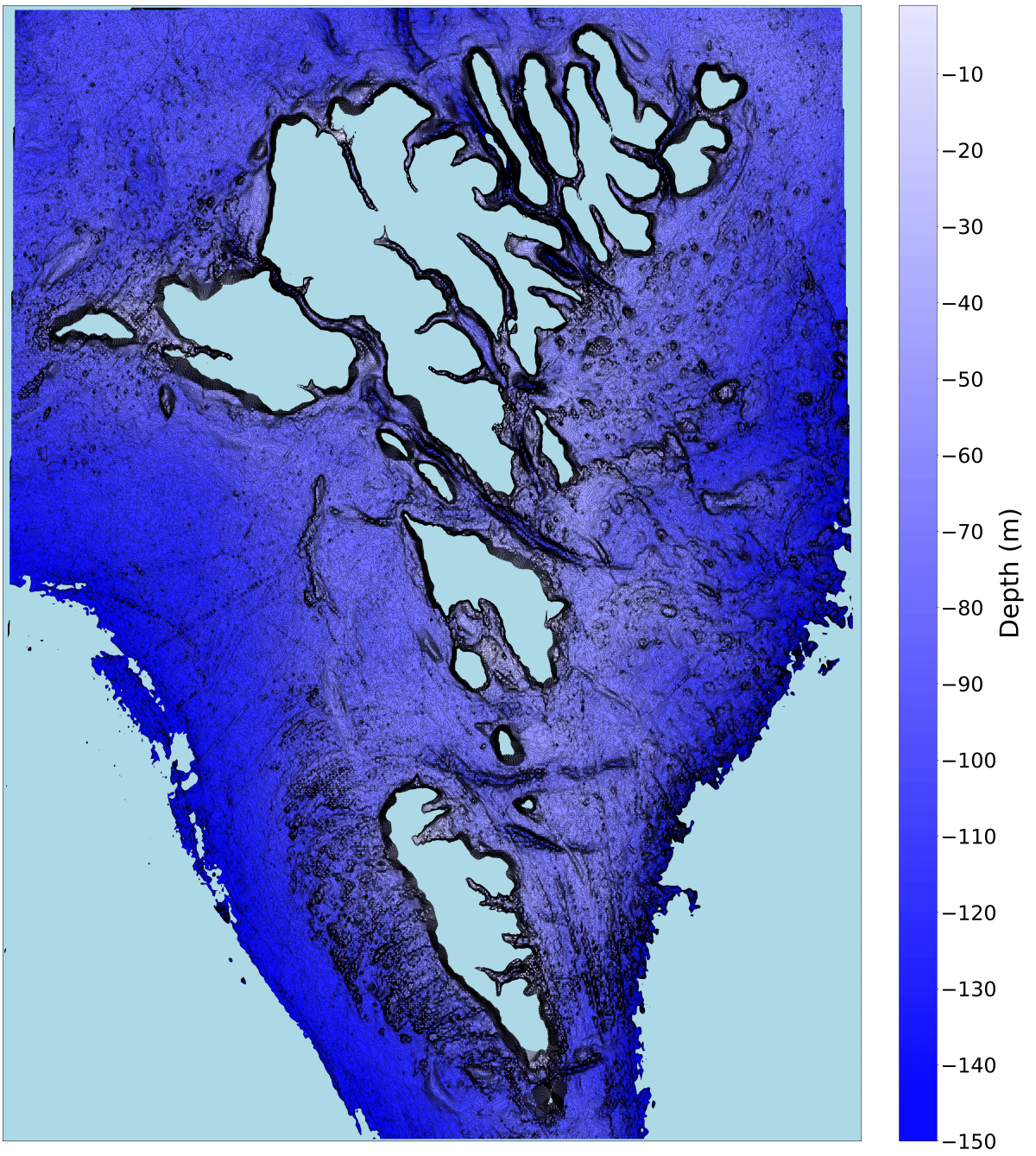


Figure A.1: Bathymetric profile of the Faroe Islands, with the depth range limited to 0 to -150 m a.s.l. to better highlight the trenches and underwater dunes on the oceanic plateau where the archipelago is located. Data retrieved from Umhvørvisstovan (2024)

A.4 Main lithostratigraphic units

In this section, the estimation of bedding planes used to characterise the main sedimentary and brecciated lithologies and horizons, as discussed in Chapter 3, is illustrated. The process involved core log descriptions (Petersen et al., 2022), data processed from seismic surveys (Petersen, 2020), and information from field mapping and literature sources. The background map for all the figures was retrieved from https://mapy.com.

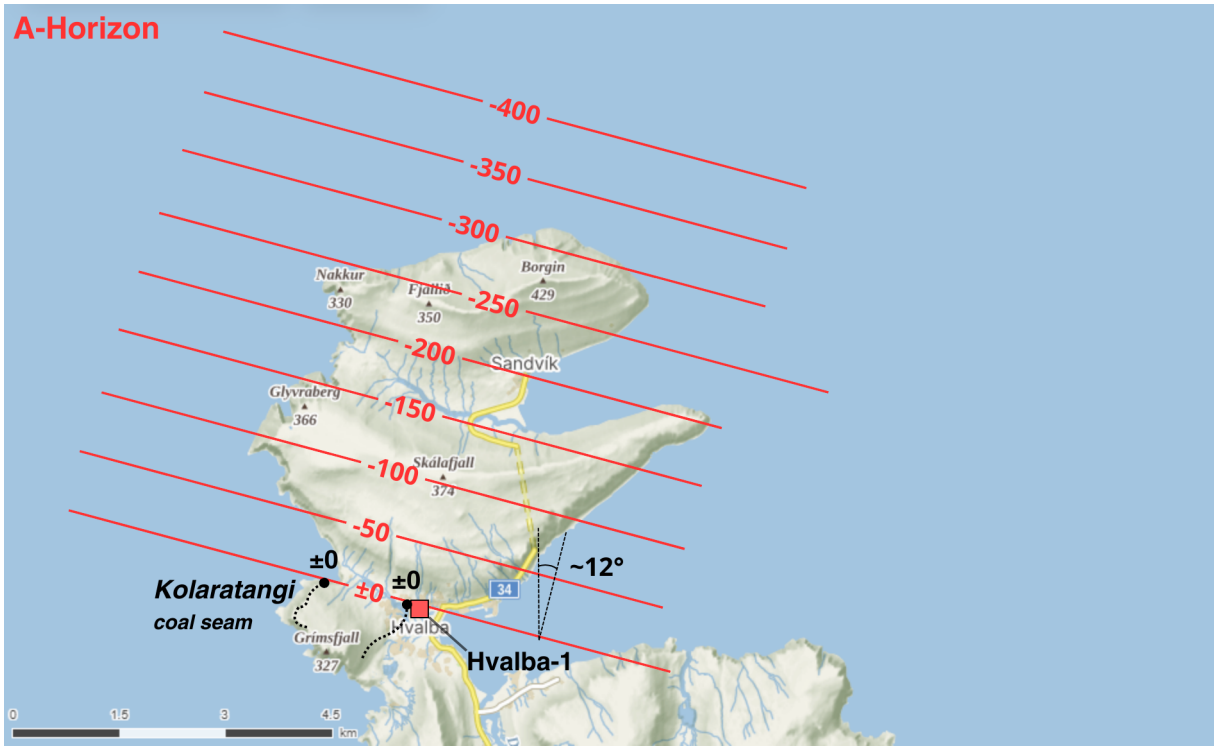


Figure A.2: A-Horizon layer bedding.

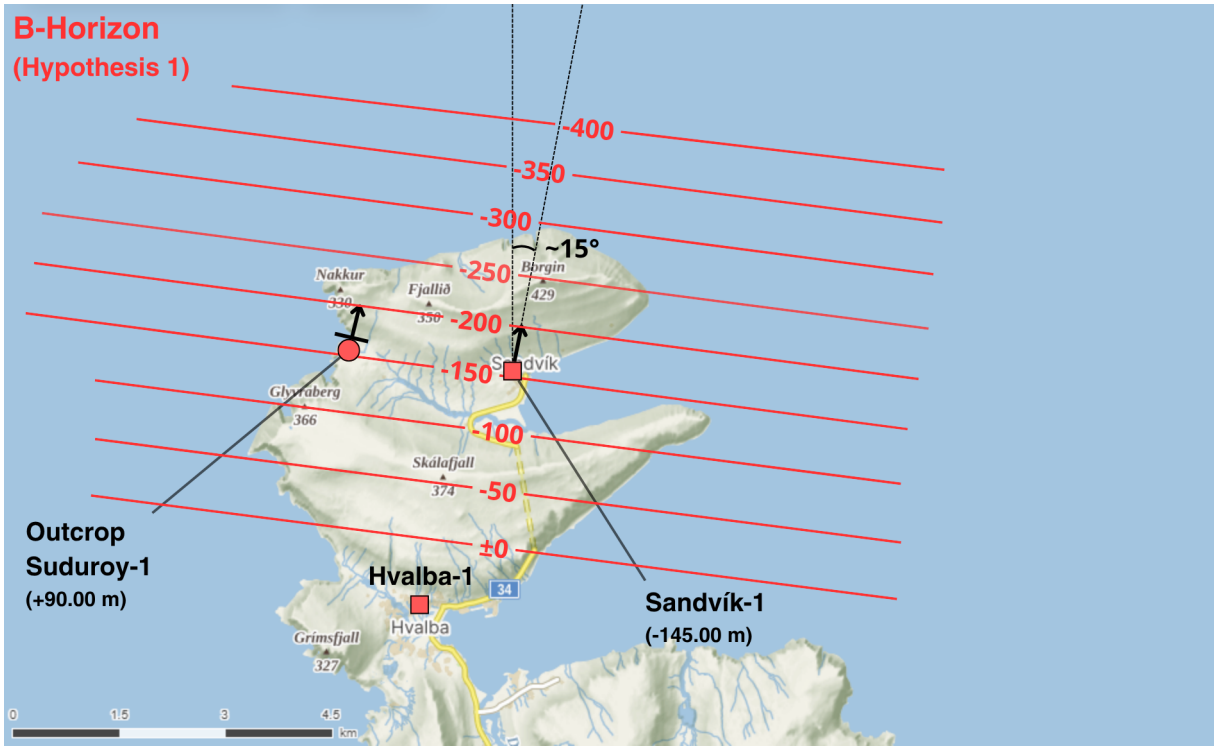


Figure A.3: B-Horizon layer bedding (Hypothesis 1).

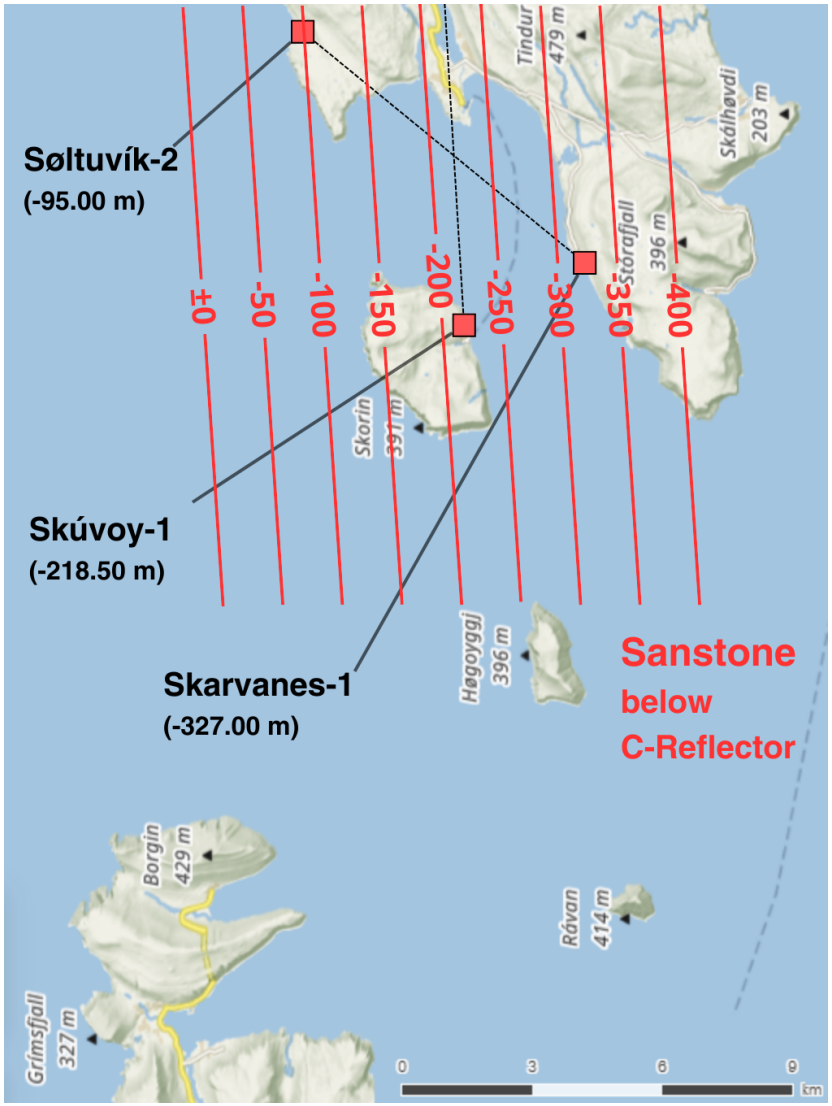


Figure A.5: Sandstone below C-Reflector layer bedding.

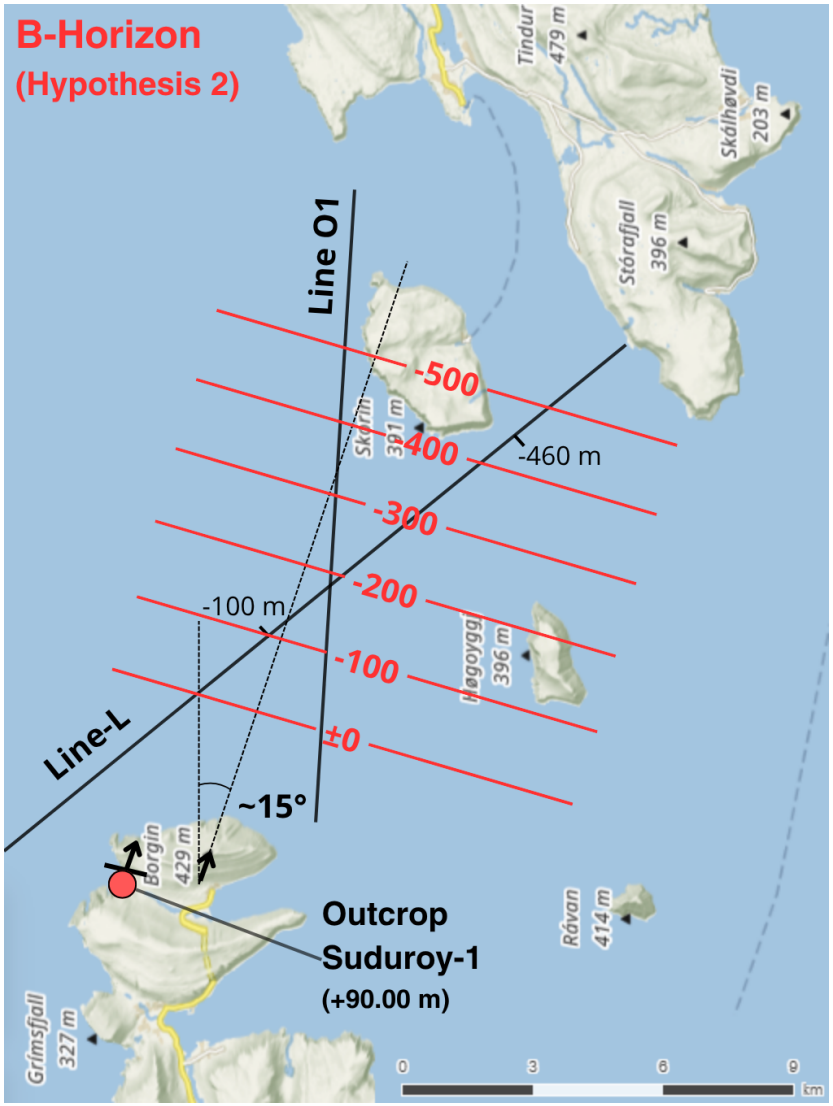


Figure A.4: B-Horizon layer bedding (Hypothesis 2).

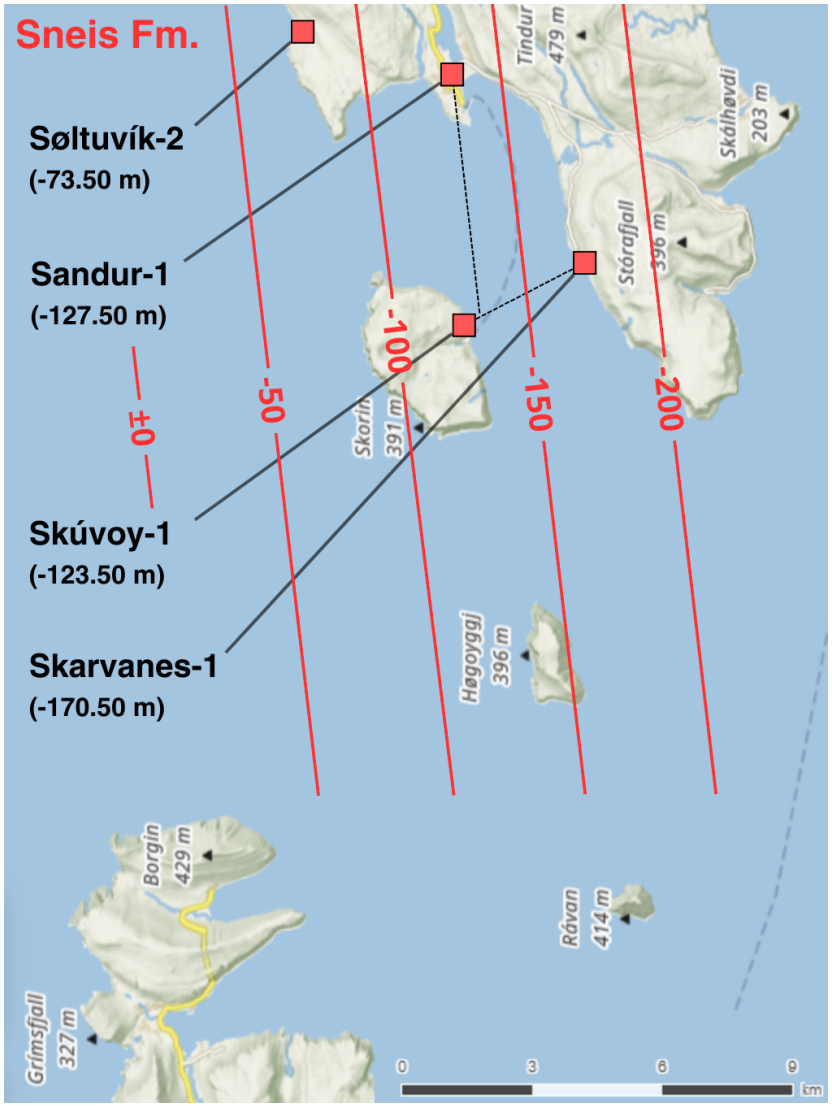


Figure A.7: Sneis Formation layer bedding.

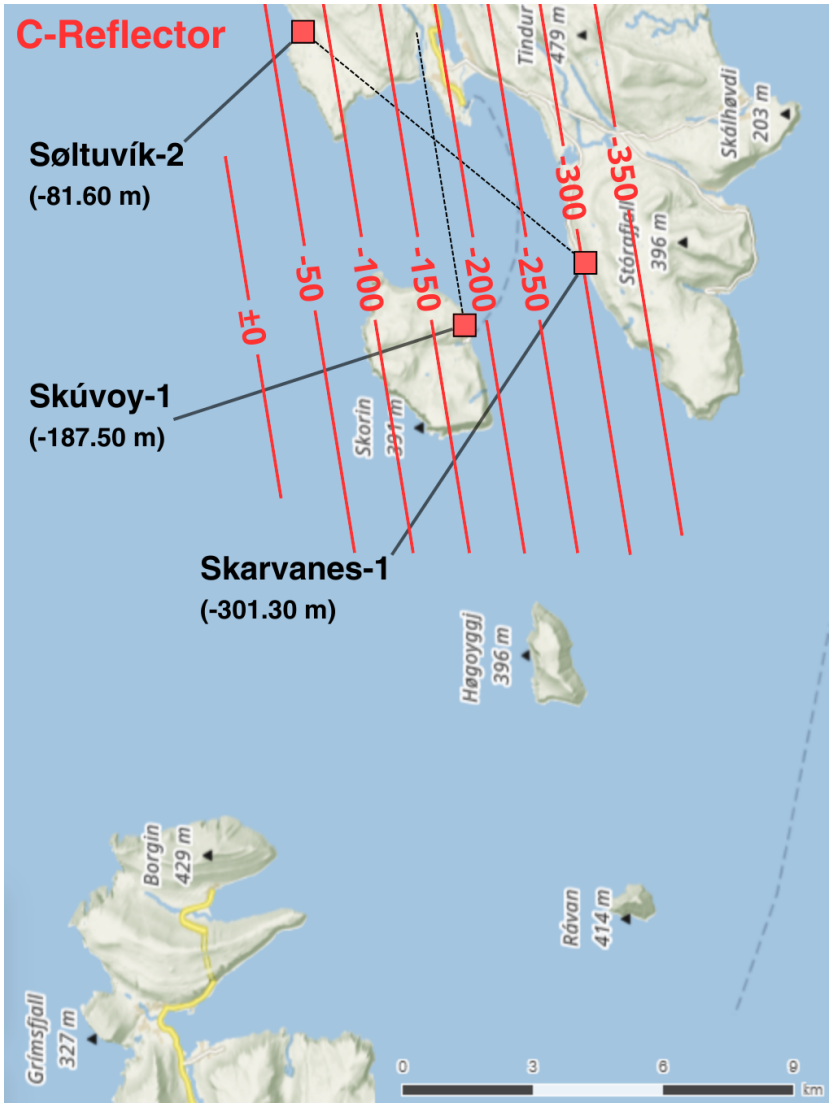


Figure A.6: C-Reflector layer bedding..

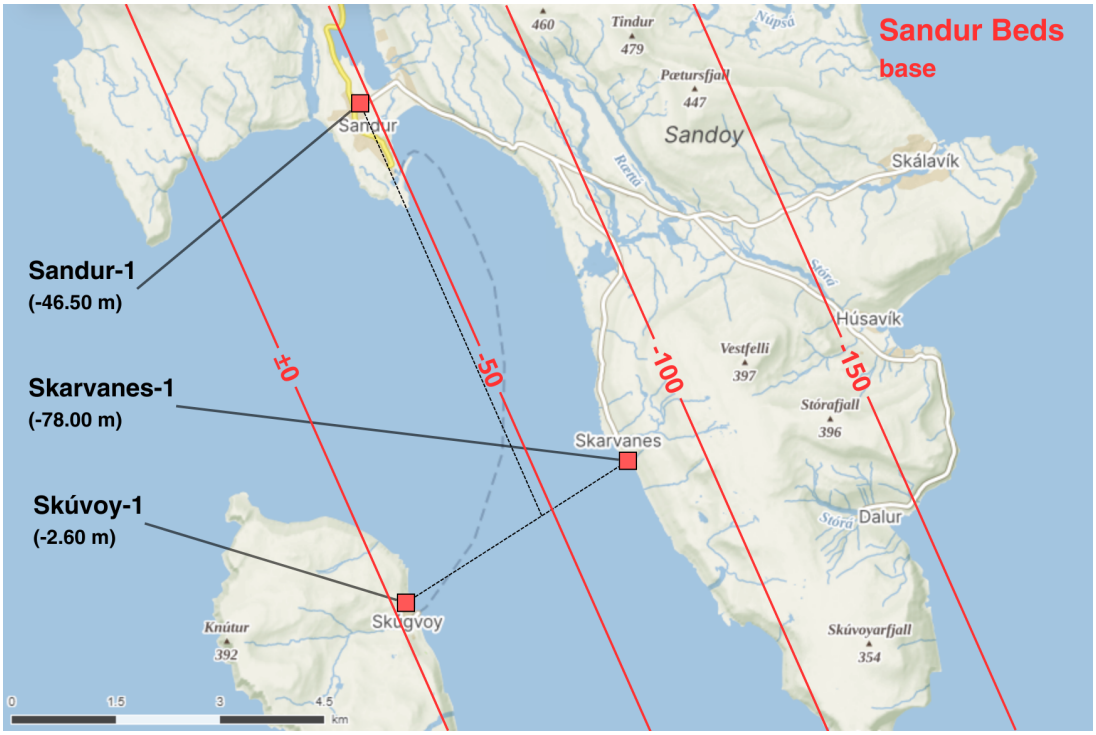


Figure A.8: Sandur Beds Base layer bedding.

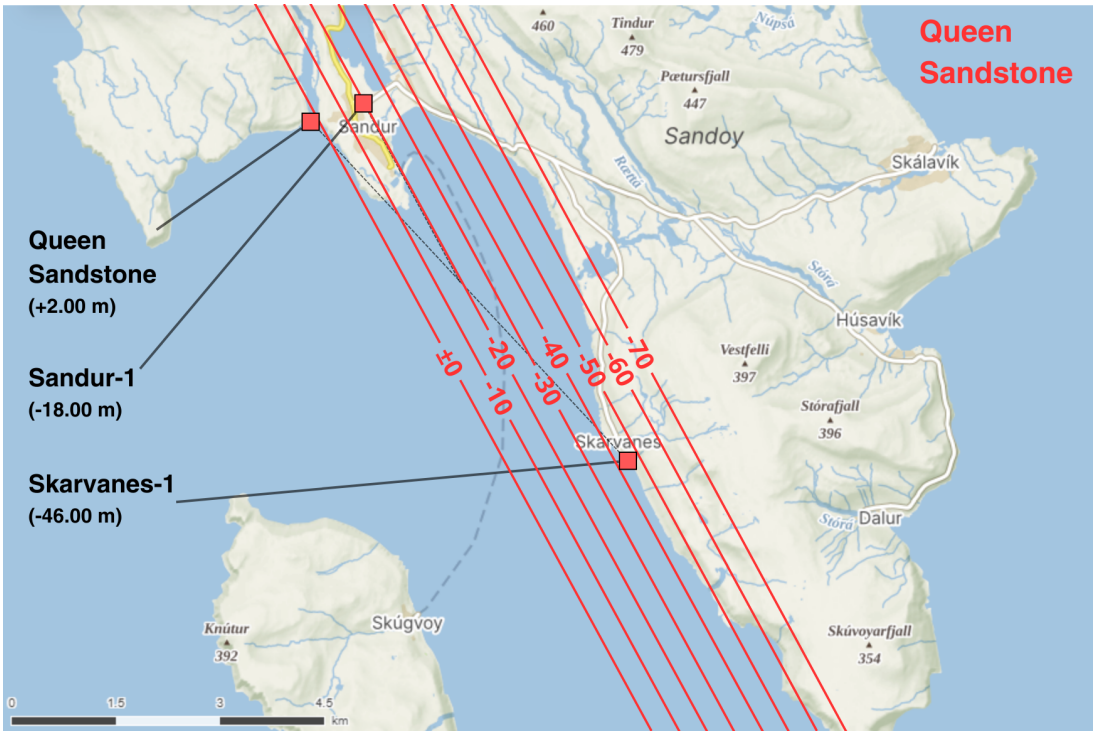


Figure A.9: Queen Sandstone layer bedding.

B

Appendix B: Geophysical properties for particular site

B.1 Glyvursnes-1 log parameters

The log parameters derived from the *Glyvursnes*-1 core are reported. Six major material groups were identified along the cored interval. For this project, the reference materials used for estimating elastic properties were “Lava Core”, “Top Lava Breccia,” and “Sediment.” The extracted data from the document included density, V_p (GEUS), V_p/V_s (GEUS), and NPHI porosity for saturation assessments. The dataset is reported from Waagstein and Andersen (2004).

Table 11. *Variation of log parameters with lithology and stratigraphic depth in Glyvursnes-1 and Vestmanna-1.*

Well	FM	Lithology	No. of standard log samples		Caliper inch		Gamma ray API units		NPHI porosity LPU		log10 Resistivity Ohm-m		Density g/ccm		Vp LogTek (1) km/s		Vp LogTek (2) km/s	
			min.	max.	mean	std.dev.	mean	std.dev.	mean	std.dev.	mean	std.dev.	mean	std.dev.	mean	std.dev.	mean	std.dev.
GL-1	UBF	Lava core	1669	1722	3.12	0.02	9.4	3.3	12.1	5.1	3.23	2.66	2.79	0.06	4.10	0.71	4.11	0.71
GL-1	MBF	Lava core	1394	1403	3.11	0.02	9.5	3.4	17.9	4.4	3.14	2.64	2.73	0.07	4.02	0.58	4.01	0.53
VM-1	MBF	Lava core	1514	1538	3.09	0.02	6.3	2.4	14.2	4.0	3.55	2.72	2.81	0.05	5.64	0.46	5.63	0.44
VM-1	LBF	Lava core	49	50	3.10	0.07	6.9	2.4	14.5	1.4	3.23	2.73	2.82	0.02	5.33	0.26	5.32	0.23
GL-1	UBF	Lava crust	420	422	3.14	0.04	9.8	2.9	23.5	4.2	2.93	2.59	2.65	0.06	3.73	0.49	3.70	0.50
GL-1	MBF	Lava crust	573	574	3.12	0.01	10.9	4.0	25.6	3.9	2.99	2.56	2.63	0.07	3.92	0.50	3.91	0.47
VM-1	MBF	Lava crust	1277	1289	3.10	0.03	7.3	2.7	24.6	4.2	3.41	2.54	2.69	0.06	5.07	0.32	5.07	0.31
VM-1	LBF	Lava crust	60	65	3.10	0.02	6.4	2.2	19.0	3.5	2.97	2.52	2.78	0.03	4.78	0.27	4.77	0.27
GL-1	UBF	Top lava breccia	285	286	3.22	0.15	11.6	3.1	25.9	5.9	3.08	2.71	2.58	0.09	3.41	0.65	3.37	0.66
GL-1	MBF	Top lava breccia	11	11	3.13	0.03	15.1	6.2	30.3	2.1	3.15	3.05	2.50	0.07	3.70	0.56	3.65	0.62
VM-1	MBF	Top lava breccia	245	247	3.10	0.01	7.7	2.8	27.7	4.4	3.20	2.59	2.64	0.06	4.74	0.31	4.76	0.30
VM-1	LBF	Top lava breccia	7	7	3.10	0.00	9.7	2.4	35.1	2.4	2.50	2.43	2.67	0.02	3.37	0.02	3.40	0.04
GL-1	UBF	Sediment	50	55	3.26	0.08	23.6	8.5	45.7	10.6	2.66	2.37	2.33	0.07	2.52	0.19	2.54	0.25
GL-1	MBF	Sediment	18	18	3.12	0.02	47.7	13.8	41.3	8.7	2.67	2.51	2.39	0.05	2.60	0.53	2.64	0.56
VM-1	MBF	Sediment	10	10	3.09	0.00	10.2	1.8	33.2	4.0	2.72	2.60	2.57	0.04	3.68	0.14	3.75	0.26
VM-1	LBF	Sediment	1	16	3.27	0.14	12.0	0.0	63.2	15.4	2.69	2.15	2.40	0.10	2.82	0.07	2.73	0.07
GL-1	UBF	Basal lava breccia	4	4	3.18	0.02	12.4	1.9	28.5	1.7	3.07	3.06	2.60	0.04	3.17	0.25	3.57	0.38
VM-1	MBF	Basal lava breccia	21	21	3.16	0.14	6.3	1.8	32.7	4.7	3.11	2.72	2.68	0.05	4.92	0.33	4.94	0.30
VM-1	LBF	Basal lava breccia	2	2	3.10	0.00	11.6	3.2	29.0	1.9	2.47	2.46	2.66	0.02	3.83	0.00	3.86	0.00
GL-1	UBF	Basal lava zone	15	18	3.18	0.09	12.8	4.4	25.3	2.8	2.89	2.74	2.81	0.05	3.56	0.69	3.67	0.50
GL-1	MBF	Basal lava zone	25	26	3.11	0.01	10.6	3.6	25.5	5.7	3.10	2.61	2.65	0.09	4.29	0.60	4.31	0.58
VM-1	MBF	Basal lava zone	115	116	3.10	0.02	6.7	2.6	25.5	4.4	3.32	2.73	2.70	0.05	5.06	0.30	5.08	0.29
VM-1	LBF	Basal lava zone	3	3	3.10	0.00	5.4	1.6	16.5	1.6	2.76	2.73	2.79	0.01	4.99	0.00	5.02	0.00

Well	FM	Lithology	Number of sonic log samples (1)	Vp GEUS (3) km/s		Vs LogTek (1) km/s		Vs LogTek (2) km/s		Vs GEUS (3) km/s		Vp/Vs LogTek (1)		Vp/Vs LogTek (2)		Vp/Vs GEUS (3)	
				mean	std.dev.	mean	std.dev.	mean	std.dev.	mean	std.dev.	mean	std.dev.	mean	std.dev.	mean	std.dev.
GL-1	UBF	Lava core	844	4.17	0.75	2.27	0.48	2.27	0.49	2.29	0.42	1.80	0.10	1.81	0.12	1.82	0.10
GL-1	MBF	Lava core	700	4.08	0.59	2.24	0.37	2.24	0.37	2.27	0.31	1.79	0.06	1.79	0.08	1.80	0.07
VM-1	MBF	Lava core	766	5.79	0.54	3.16	0.28	3.17	0.26	3.18	0.29	1.79	0.09	1.78	0.05	1.82	0.08
VM-1	LBF	Lava core	24	5.36	0.23	2.92	0.14	2.92	0.12	2.88	0.12	1.83	0.05	1.83	0.04	1.86	0.05
GL-1	UBF	Lava crust	215	3.76	0.52	2.03	0.31	2.02	0.31	2.05	0.31	1.85	0.09	1.84	0.11	1.84	0.15
GL-1	MBF	Lava crust	278	3.97	0.50	2.17	0.31	2.17	0.31	2.20	0.30	1.81	0.05	1.81	0.07	1.81	0.09
VM-1	MBF	Lava crust	645	5.12	0.40	2.81	0.21	2.80	0.21	2.82	0.19	1.81	0.08	1.81	0.07	1.82	0.06
VM-1	LBF	Lava crust	31	4.78	0.31	2.67	0.22	2.64	0.22	2.68	0.19	1.79	0.09	1.81	0.09	1.79	0.06
GL-1	UBF	Top lava breccia	141	3.99	0.70	1.97	0.35	1.96	0.35	2.11	0.33	1.82	0.12	1.82	0.14	1.89	0.14
GL-1	MBF	Top lava breccia	6	3.91	0.56	1.99	0.40	1.93	0.52	2.12	0.31	1.97	0.09	1.94	0.21	1.95	0.11
VM-1	MBF	Top lava breccia	124	4.76	0.37	2.62	0.24	2.63	0.21	2.64	0.24	1.82	0.12	1.82	0.09	1.81	0.10
VM-1	LBF	Top lava breccia	4	3.20	0.24	1.81	0.12	1.82	0.11	1.83	0.08	1.87	0.12	1.88	0.10	1.75	0.07
GL-1	UBF	Sediment	29	3.26	0.44	1.37	0.09	1.38	0.10	1.84	0.19	1.84	0.09	1.84	0.10	1.78	0.21
GL-1	MBF	Sediment	9	3.09	0.33	1.43	0.26	1.48	0.32	1.74	0.17	1.81	0.08	1.78	0.06	1.78	0.15
VM-1	MBF	Sediment	5	3.61	0.15	1.90	0.13	1.95	0.10	2.01	0.13	1.94	0.06	1.92	0.10	1.81	0.18
VM-1	LBF	Sediment	4	2.82	0.15	1.76	0.07	1.70	0.11	1.49	0.12	1.60	0.02	1.60	0.10	1.90	0.11
GL-1	UBF	Basal lava breccia	2	4.18	0.14	1.78	0.17	1.78	0.22	2.19	0.15	1.78	0.03	2.01	0.03	1.91	0.20
VM-1	MBF	Basal lava breccia	11	4.89	0.28	2.77	0.18	2.73	0.22	2.69	0.14	1.78	0.10	1.82	0.07	1.82	0.05
VM-1	LBF	Basal lava breccia	1	3.84	0.00	1.87	0.00	1.88	0.00	2.21	0.00	2.05	0.00	2.05	0.00	1.74	0.00
GL-1	UBF	Basal lava zone	9	3.97	0.81	1.98	0.45	2.03	0.36	2.08	0.26	1.81	0.13	1.82	0.11	1.91	0.26
GL-1	MBF	Basal lava zone	13	4.32	0.60	2.39	0.40	2.39	0.37	2.38	0.37	1.80	0.05	1.81	0.07	1.83	0.09
VM-1	MBF	Basal lava zone	57	5.05	0.34	2.81	0.15	2.81	0.15	2.78	0.16	1.80	0.06	1.81	0.04	1.82	0.05
VM-1	LBF	Basal lava zone	1	4.91	0.12	2.76	0.00	2.78	0.00	2.74	0.04	1.81	0.00	1.81	0.00	1.79	0.02

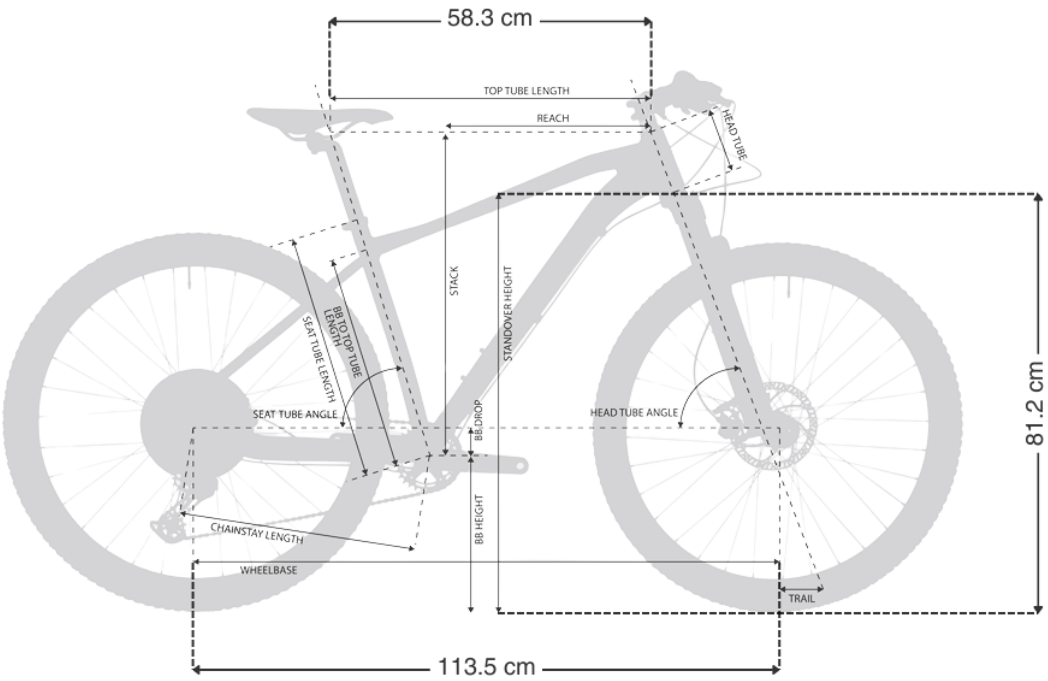
Specifications:
Sampling rate is 10 cm for standard logs and 20 cm for sonic logs.
In order to minimize boundary effects samples of log data acquired within a distance of +/- 0.2 m of lithological boundaries (cutoff distance) are excluded.
This means that a bed should be between 0.4 to 0.5 m thick to provide a single depth point.
Thin flow-units consisting of lava crust throughout have been merged with adjoining lava crusts of other units (but not with overlying basal zones).
Samples from a few intervals with a borehole diameter >20% larger than the nominal diameter of 3" are excluded (very few samples).
Log data <0 are excluded (to avoid missing values of '-999.25').
Number of standard log samples used is shown as a range. The variations mainly reflect that the logs do not have exactly the same start and end depths.
Different depth coverage of the logs is mainly a problem near TD in Vestmanna-1.
The number of sonic log samples (from LogTek receiver-array data set) is half the values of the standard logs due to the lower sampling rate of 0.2 m.
Three sets of sonic data are shown based on different processings of the same full wave sonic logs:
(1) Receiver-array type data based on results of LogTek using a guided peak finding method.
(2) Pseudo borehole compensated type data based on results of LogTek using a guided peak finding method.
(3) Receiver-array type data based on the results of GEUS using a WellCad semblance process.

C

Appendix C: Field mapping

C.1 Field Mapping reference objects

When taking photographs to document outcrop features or support parameter estimates, it is good practice to include a scale reference in the images. Due to delays in the delivery of instrumentation, proper metric measurement tools were unavailable throughout the field mapping campaign. As a workaround, three alternative objects were used to provide a sense of scale: (i) a bicycle for large-scale overviews, (ii) a bag for medium-sized features such as rock mass blocks, and (iii) a highlighter for detailed features like joints or water drips. The relative dimensions of these reference objects are provided in Fig. C.1.



(a)



(b)



(c)

Figure C.1: Reference objects used during the site investigation: (a) the bicycle for large size objects, (b) the bag for intermediate objects, (c) the highlighter for detailed pictures.

C.2 Outcrop mapping: Streymoy 1 (Section 2)

As a reference for the mapping methodology used during the field mapping campaign, the complete mapping sheet for Outcrop *Streymoy 1* (Section 2) is attached. The sheet includes: (i) rock mass quality assessment using the *Q-system* and *GSI*, (ii) images (with a reference object when possible) to support the estimated *Q*- and *GSI* parameters, (iii) a stereonet with projections related to the specific section, and (iv) Schmidt Hammer measurements presented in a histogram, along with the corresponding probability density function (assuming a normal distribution) that best fits the dataset, as well as the mean, median, and mode for the specific section.

The other mapping sheets compiled during the field mapping campaign can be consulted at the following link.

Outcrop Mapping Sheet - Q-System

Project Name: MSc Thesis - Suduroy Tunnel project

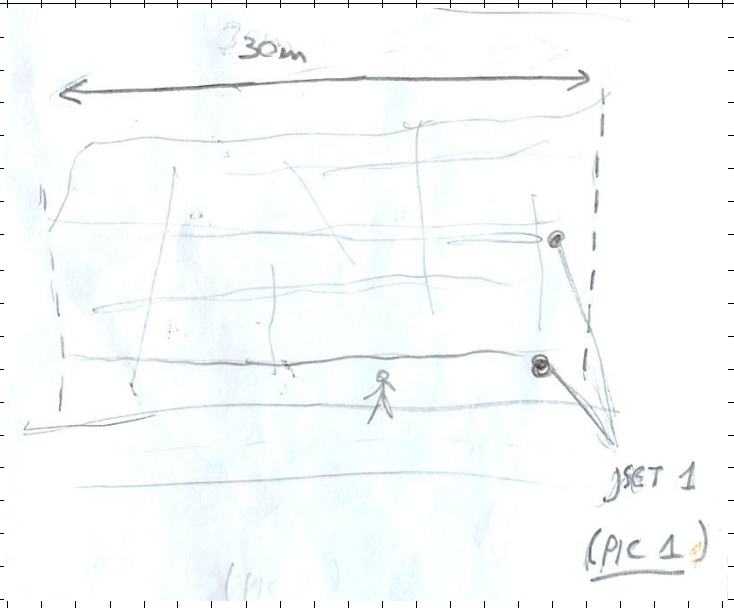
Outcrop coordinates:	Name	Location	Width (B)	Thickness (D)	Height (H)
61°57'49.5"N 6°49'10.0"W	Section 1-2 (LEFT to RIGHT)	Gamlarætt Harbour (Streymoy)	20 m	[-]	15-17 m

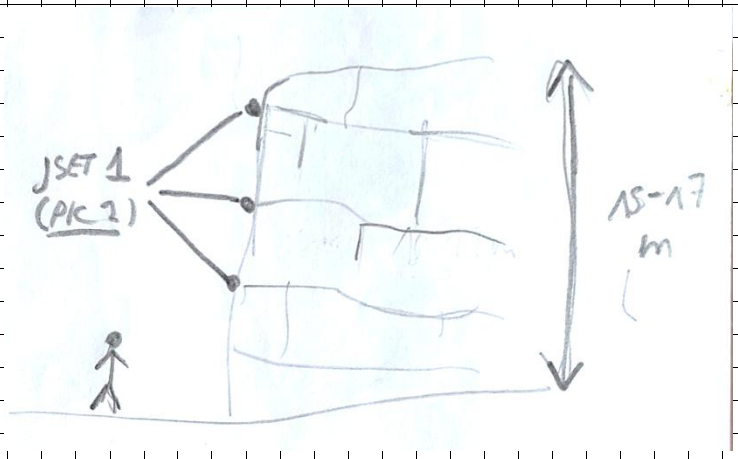
Nature of the outcrop: Man-made (controlled blasting, with evidence given from blast holes drilled into the rock)
Estimated age: tens of years

Mapped by: Cristian Tebaldi | Date of Mapping: 22/05/2024

RQD (%)	Jn	Jr (or JRC)	Ja	Jw	SRF	Q-Value = (RQD/Jn).(Jr/Ja).(Jw/SRF)	**26** (RQD = 65) **28** (RQD = 70)
65 - 70	3	3	1	1	2.5		

Sketch:





Notes:

RQD:
Fair to good RQD, regular jointing of roughly 1m of space along the whole section except to some particular areas at the top of the outcrop, probably due to blasting operations (Pic. 1)

Jn:
One clear main joint set and random joints along the section (Pic. 1) (Pic. 2)

Jr:
Rough and undulating joints as for Section 1-1

Ja:
Unaltered joint walls with exceptional presence of mineral fillings (quartz, calcite, …) along the section (Pic. 3)
Presence of grass in the joints as well as for Section 1-1 and also of debris still due to blasting operations

Jw:
The section is mostly humid with some minor inflows present (few drips) (Pic. 4)
The rock mass appears dry in the upper part (Pic. 5)

SRF:
Mainly closed joints with some openings especially at the top of the section, quite superficial stress conditions

Outcrop Mapping Sheet - GSI

Project Name: MSc Thesis – Suduroy Tunnel project

Outcrop coordinates:	Name	Location	Width (B)	Thickness (D)	Height (H)
61°57'49.5"N 6°49'10.0"W	Section 1-2 (LEFT to RIGHT)	Gamlarætt Harbour (Streymoy)	20 m	[-]	15-17 m

Nature of the outcrop: Man-made (controlled blasting, with evidence given from blast holes drilled into the rock)
Estimated age: tens of years

Mapped by: Cristian Tebaldi

Date of Mapping: 22/05/2024

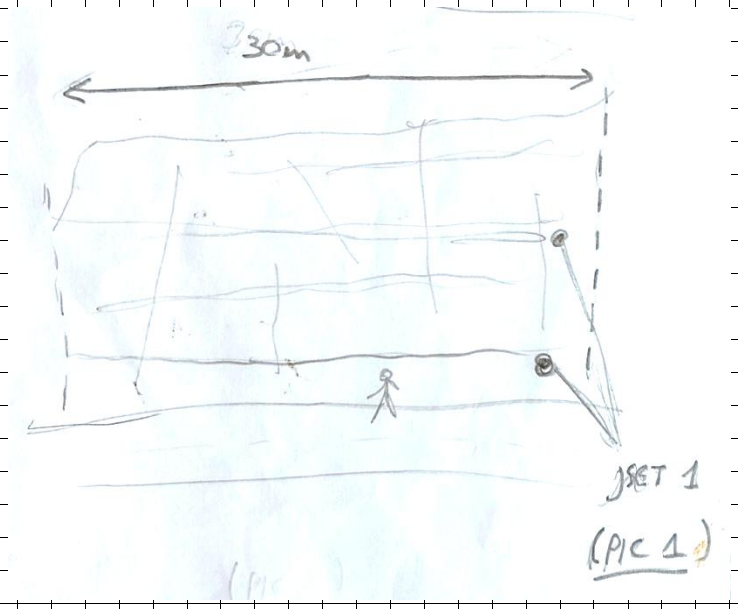
GSI from	GSI to	Preferred GSI = (the value that best fits as an average for the numerical model)	63
60	65		

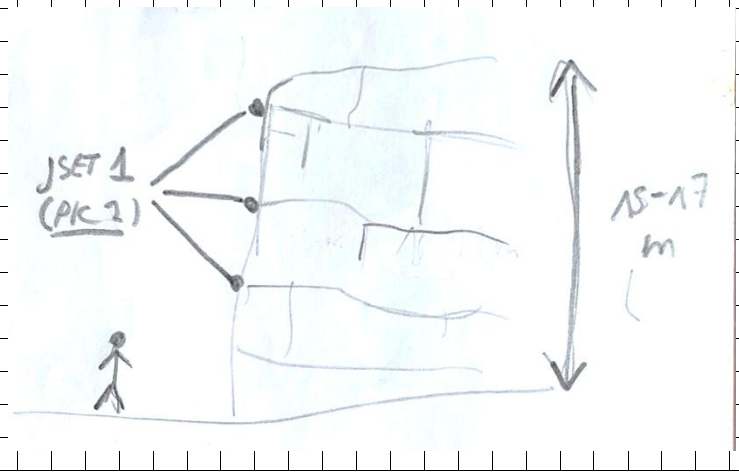
Notes:

Structure:
Very blocky to blocky with GSI value more likely 65-70 in the left-hand side of the section and 69-65 in the right-hand side

Surface conditions:
Rough and slightly weathered surface conditions

Sketch:



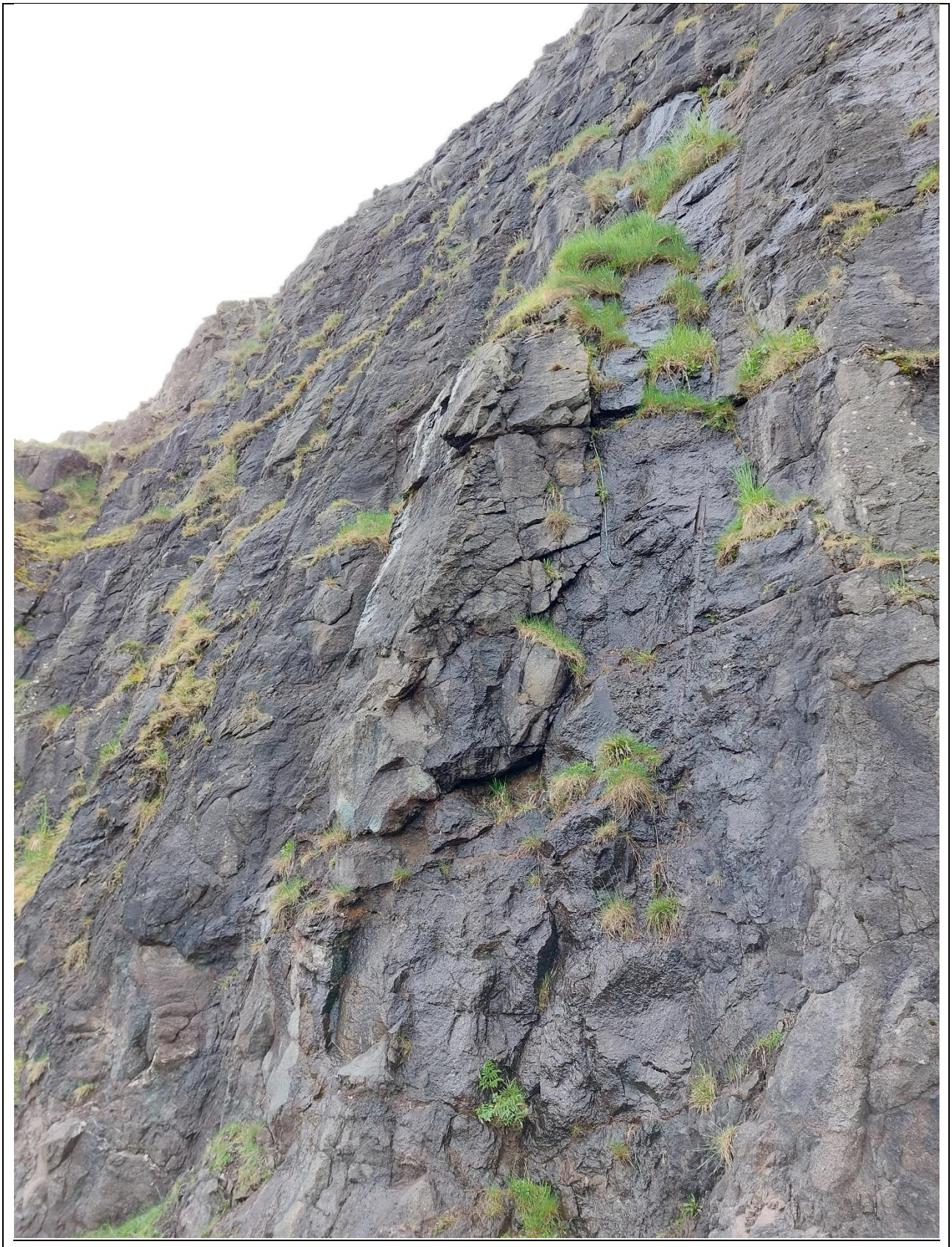


Pic. 1





Pic. 2





Pic. 3


STAEDTLER



Pic. 4



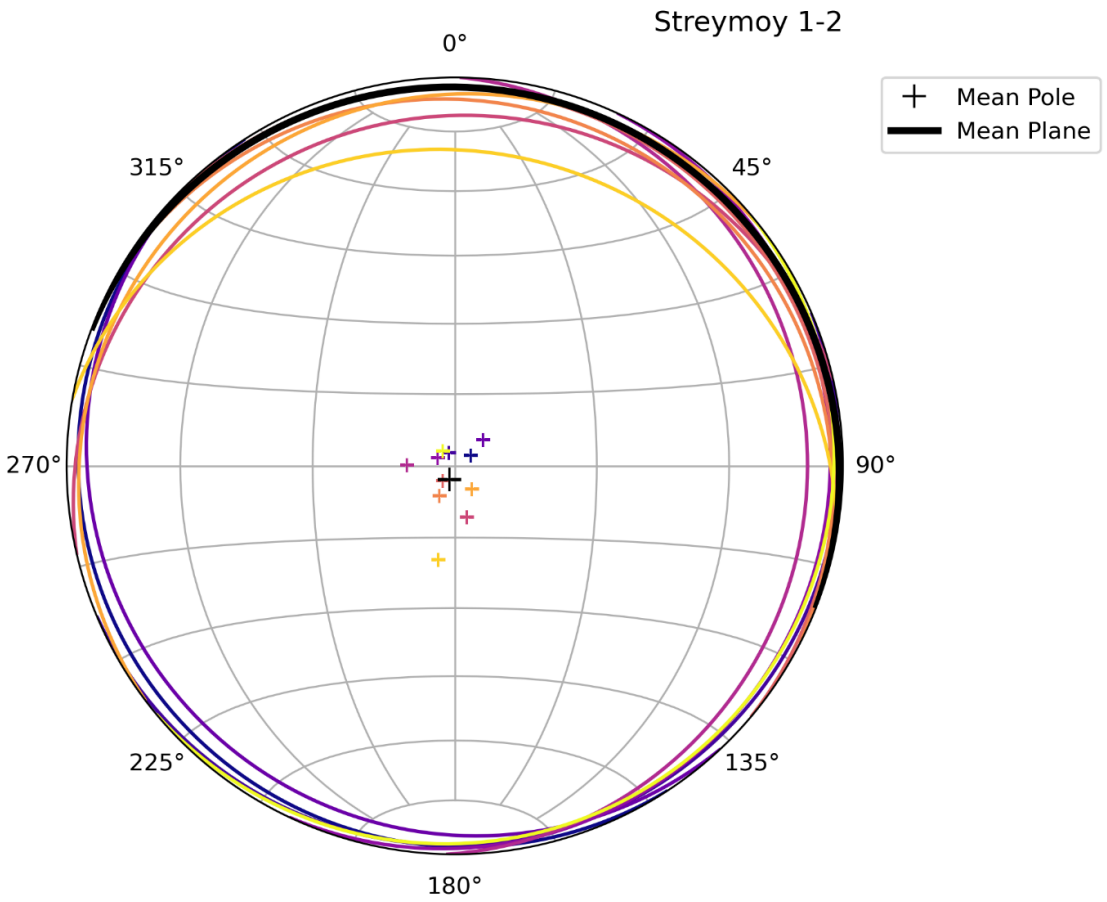




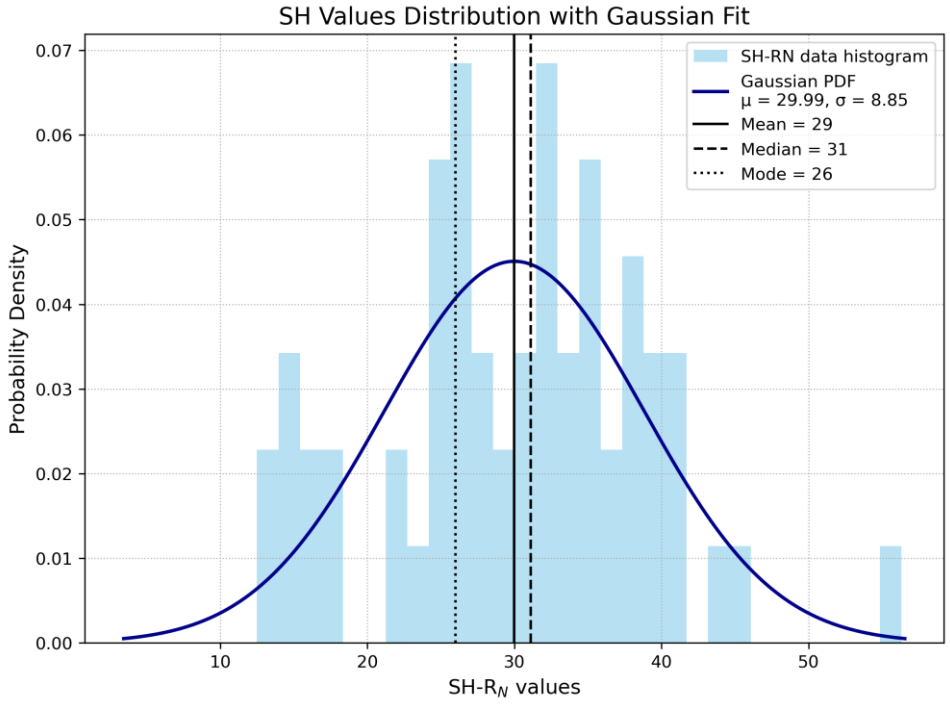
Pic. 5



Stereonet (Schmidt Projection)



Schmidt Hammer measurements



C.3 Q and GSI estimates per outcrop sections

In addition to the mapping sheets for each outcrop section, the resulting *Q*- and *GSI* values are summarised in this section. The tables group stratigraphic units that fall under the same geotechnical classification. Listed in order of appearance are: *Enni* lava cores (Tab. C.1), *Malinstindur* lava cores (Tab. C.2), volcaniclastic sandstone (sediment, Tab. C.3), and flow top (lava breccia, Tab. C.4).

Table C.1: (a) Q- and (b) GSI estimated values for Enni basalt cores along outcrop sections.

Location	$Sec.$	RQD	J_n	J_r	J_a	J_w	SRF	Q
Streymoy 1	1	60	6	3	1	1	2.5	12
	2	65–70	3	3	1	1	2.5	26–28
	3	60–65	6	3	1	0.66	2.5	7.92–8.58
	4	50	6	3	2	0.66	1	8.25
	5	55–60	3	3	2	1	1	27.5–30.0
Streymoy 2	1	65–70	3	3	1	1	2.5	26–28
	2	60	3	3	2	1	2.5	12
	3	45–50	3	3	2–3	1	2.5	6–6.67–9–10
Sandoy 1	1	50	3	3	2–3	1	2.5	10–6.67
Sandoy 2	1	80	3	4	1	1	1	106.70
	2	80–85	6	4	1	1	1	53.3–56.7
Sandoy 3	1	75–80	3	3	2	0.66	2.5	9.9–10.6
	2	50	6	3	2	0.66	1	8.25
	3	50–60	3	3	2	1	2.5	10–12
	4	50	3	3	2	0.66	2.5	6.6
	5	60	3	3	1	1	2.5	12

(a)

Location	$Sec.$	GSI **(from)**	GSI **(to)**	GSI **(proposed)**
Streymoy 1	1	55	60	58
	2	60	65	63
	3	55	60	58
	4	50	55	54
	5	55	60	58
Streymoy 2	1	65	70	69
	2	60	65	62
	3	35	40	39
Sandoy 1	1	45	50	53
Sandoy 2	1	70	75	74
	2	75	80	76
Sandoy 3	1	68	73	72
	2	75	80	78
	3	57	62	60
	4	48	53	50
	5	55	60	58

(b)

Table C.2: (a) Q- and (b) GSI estimated values for Malinstindur basalt cores along outcrop sections.

Location	$Sec.$	RQD	J_n	J_r	J_a	J_w	SRF	Q
Suduroy 1	1	85 - 90	3	4	1	1	2.5	45.3 - 48.0
	2	75 - 80	6	3	1	1	2.5	15 - 16
Suduroy 2	1	50 - 60	9	3	1 - 2	1	2.5	3.33 - 4 / 6.67 - 8
	2	65 - 75	6	3	2	1	2.5	6.5 - 7.5

(a)

Location	$Sec.$	GSI **(from)**	GSI **(to)**	GSI **(proposed)**
Suduroy 1	1	82	87	85
	2	70	75	74
Suduroy 2	1	62	67	65
	2	65	70	67

(b)

Table C.3: (a) Q- and (b) GSI estimated values for the volcaniclastic sandstone unit along outcrop sections.

Location	$Sec.$	RQD	J_n	J_r	J_a	J_w	SRF	Q
Sandoy 2	1	25	6	3	2	1	1	6.25
	2	35	6	3	2	1	1	8.75

(a)

Location	$Sec.$	GSI **(from)**	GSI **(to)**	GSI **(proposed)**
Sandoy 2	1	35	40	37
	2	40	45	44

(b)

Table C.4: (a) Q- and (b) GSI estimated values for flow top unit along outcrop sections.

Location	$Sec.$	RQD	J_n	J_r	J_a	J_w	SRF	Q
Streymoy 2	1	40	3	3	2 - 3	0.66	2.5	3.52 - 5.28
	2	40	3	3	2 - 3	1	2.5	5.33 - 8
	3	35	6	3	2 - 3	1	2.5	2.33 - 3.5

(a)

Location	$Sec.$	GSI **(from)**	GSI **(to)**	GSI **(proposed)**
Streymoy 2	1	35	40	37
	2	35	40	37
	3	35	40	37

(b)

D

Appendix D: Cavern design guidelines

D.1 Tunnel design specifics

The geometric measurements for standard tunnel profiles are presented (Tab. D.1) in accordance with the guidelines provided in Handbook N500 (Statens Vegvesen, 2024b). The details of this project-specific tunnel profile (T9,5) are highlighted. Note that the guidelines define specifics for both a normal (operational) profile and a theoretical blasted profile (Tab. D.2); for this project, the latter serves as the reference.

Table D.1: Geometric measurements (in metres) for the different tunnel profiles. Adapted from Statens Vegvesen (2024b)

Profile	Bt	Bk	Yv	Rv	X	Yh	Rh
T7,5	7.5	5.00	1.570	4.790	1.550	2.481	3.594
T9,5	9.5	7.00	1.570	4.790	0.450	1.213	5.212
T10,5	10.5	8.00	1.570	4.790	1.450	0.664	5.956
T12,5	12.5	10.00	1.570	4.790	3.050	-0.646	7.825
T13	13.0	10.50	1.570	4.790	3.450	-0.735	8.325
T13,5	13.5	11.00	1.570	4.790	4.450	-0.950	8.575
T14,0	14.0	11.50	1.570	4.790	4.950	-1.294	8.575

Table D.2: Tunnel cross-sectional data for the different tunnel profiles, including both theoretical blasted profile and normal profile. Adapted from Statens Vegvesen (2024b)

Tunnel profile	Teoretical blasted profile		Normal profile	
	Area A_S [m^2]	Arc length B_S [m]	Area A_N [m^2]	Arc length B_N [m]
T7,5	51.56	18.88	40.46	16.30
T9,5	66.62	21.04	53.61	18.46
T10,5	74.59	22.13	60.64	19.55
T12,5	91.32	24.32	75.49	21.73
T13	95.69	24.86	79.39	22.28
T13,5	100.52	25.46	82.88	22.88
T14	104.58	25.96	87.35	23.88

D.2 Grasshopper architectures

To generate a wide range of geometries, Rhino® is used in conjunction with its visual programming interface, Grasshopper, which enables the algorithmic creation of complex parametric models through a node- and connection-based workflow. Grasshopper input boxes contain fixed or variable parameters that serve as essential inputs for geometry generation.

Two network architectures were designed for this project, distinguishing between geometries with and without a central pillar. Their `.gh` files are available at the following link.

The network flows from left to right, with input numbers and parameters (fixed values or sliders) on the left to initiate the geometry generation. The remainder of the network consists of macro groups of nodes and connections that create the main blocks of the preliminary design geometry, ending with the boxes for baking the output design on the far right of the architecture.

Please note that a Rhino® license is required to open the files, along with the installation of the Grasshopper plugin and specific Grasshopper component libraries.

E

Appendix E: Numerical modelling approach

E.1 Mesh nodes and tetrahedra

The appendix presents the number of nodes (Fig. E.1) and tetrahedral elements (Fig. E.2) for different (R, r) output geometries. A general decrease in regularity in the number of nodes and elements is observed as r increases, up to the $R = 20\,\text{m}$ series. Beyond this point, the series exhibit a sharp increase at a specific R value, after which the numbers stabilise at a higher magnitude. This behaviour is linked to the semi-automated meshing process used by the CAD software in conjunction with its built-in meshing tool, making it difficult to adjust.

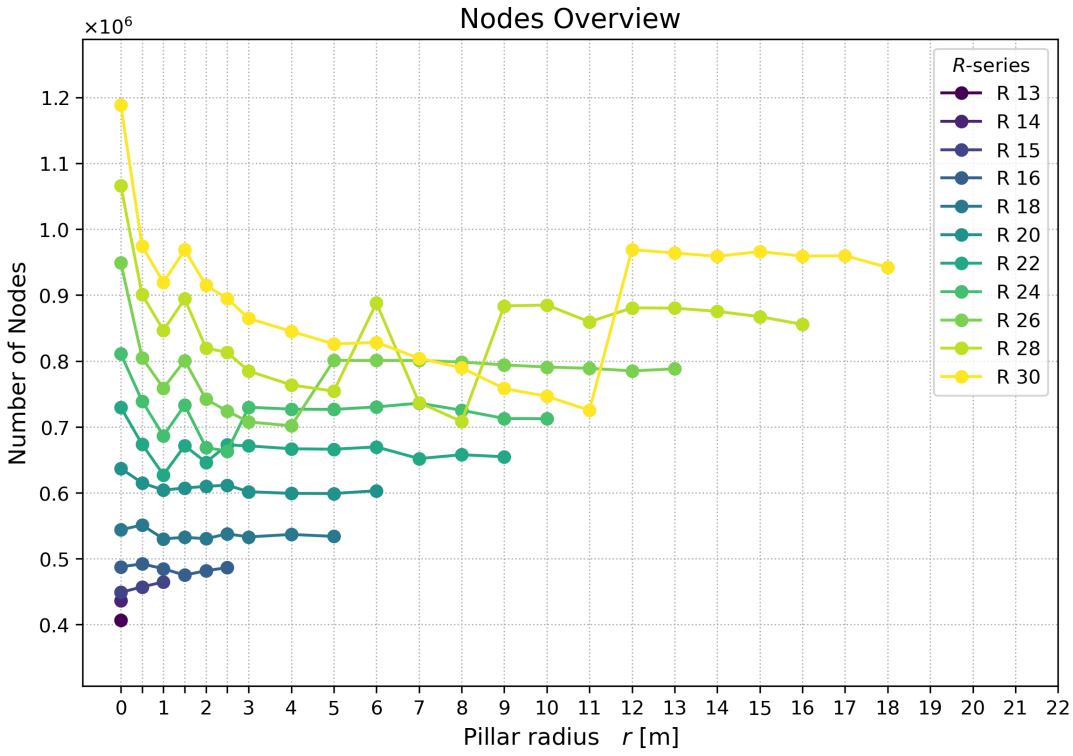


Figure E.1: Number of nodes in the domain meshes from the first simulations round geometries.

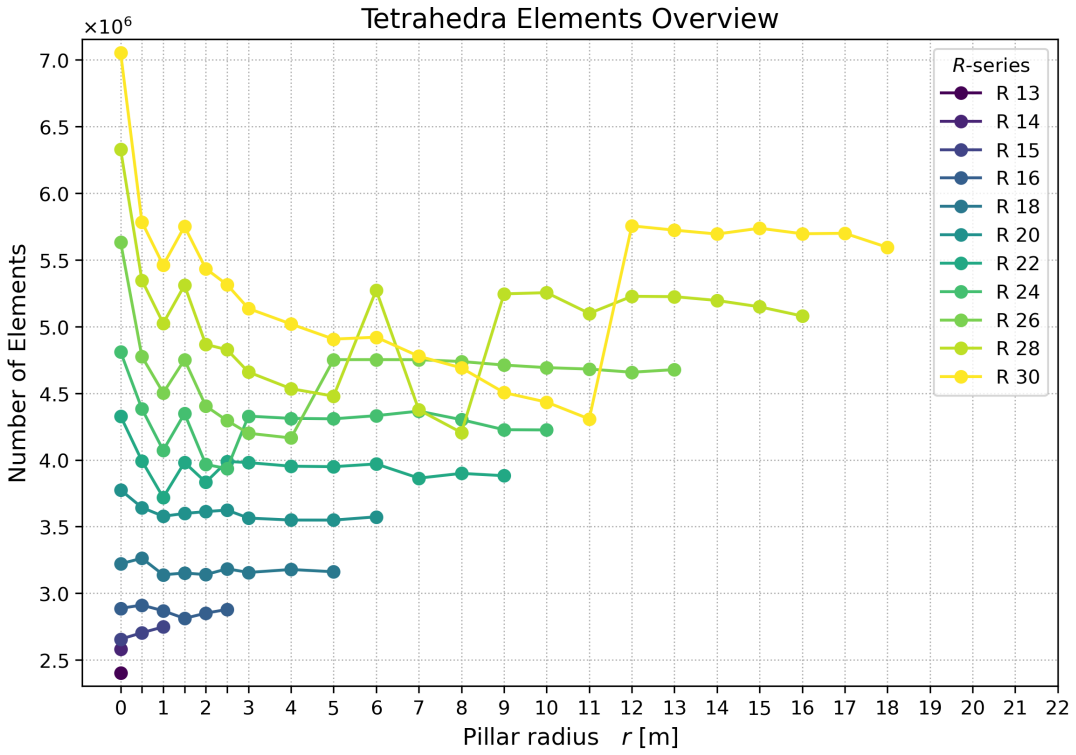


Figure E.2: Number of tetrahedra elements in the domain meshes from the first simulations round geometries.

E.2 HB-MC fitting methods

This appendix presents the key steps and equations used in three Hoek–Brown (HB) to Mohr–Coulomb (MC) fitting methods (Sofianos and Nomikos, 2006, Jimenez et al., 2008, Meng et al., 2016), developed as alternatives to the original approach by Hoek et al. (2002). The methods were introduced to overcome limitations of the original HB–MC fitting procedure, which has shown reduced effectiveness in characterising rock mechanical properties in certain projects.

Sofianos and Nomikos (2006)

The first step in determining equivalent MC parameters involves a linearisation procedure within a specified stress range. The HB criterion is initially expressed in terms of mean stress (p) and deviatoric stress (q). The linearisation process begins by defining the desired stress range in terms of p, with the lower bound given by the tunnel support pressure (p_i) and the upper bound by the natural field stress (p_0). The model accounts for an inner plastic region and an outer elastic region around the excavation, with the stress at their boundary denoted as p_e (refer to Fig. 7.6a, Chapter 7). In this project, the tunnel support pressure is assumed to be zero, as the excavation initially lacks structural support. Meanwhile, p_0 is determined by the maximum rock mass body forces affecting the tunnel, hence at its base.

$$\begin{gathered} 2(p_{0N} - p_{\mathrm{eN}}) - (m_{\mathrm{b}} p_{\mathrm{eN}} + s)^a = 0 \\ \text{with} \quad p_{\mathrm{e}N} = \frac{p_{\mathrm{e}}}{\sigma_{\mathrm{ci}}}, \quad p_{0N} = \frac{p_0}{\sigma_{\mathrm{ci}}} \end{gathered} \tag{E.1}$$

p_e depends only on the peak strength parameters of the rock mass and the stress field, p_0 represents the hydrostatic pressure and N denotes the normal component for the circular surface.

With these parameters defined, the equivalent cohesion (C_{0N}) and inclination (k) of the linear MC failure envelope can be determined. This is done using the $\sigma_{3N} - \sigma_{1N}$ graphical representation. The evaluation of C_{0N} and k differs depending on whether the rock material is perfectly plastic or brittle. In the case of brittle material, both peak and residual values must be evaluated.

$$C_{0N} = \frac{4m_b\left(p_{eN}^3 - p_{iN}^3\right) + 6s\left(p_{eN}^2 - p_{iN}^2\right)}{\left(p_{eN} - p_{iN}\right)^4} \cdot \frac{\left(m_b p_{eN} + s\right)^{a+1} - \left(m_b p_{iN} + s\right)^{a+1}}{m_b^2(a+1)} - \frac{6\left(p_{eN}^2 - p_{iN}^2\right)}{\left(p_{eN} - p_{iN}\right)^4} \cdot \frac{\left(m_b p_{eN} + s\right)^{a+2} - \left(m_b p_{iN} + s\right)^{a+2}}{m_b^2(a+2)} \tag{E.2a}$$

$$k = 1 - \frac{12s + 6m_b(p_{eN} + p_{iN})}{(p_{eN} - p_{iN})^3} \cdot \frac{\left(m_b p_{eN} + s\right)^{a+1} - \left(m_b p_{iN} + s\right)^{a+1}}{m_b^2(a+1)} + \frac{12}{(p_{eN} - p_{iN})} \cdot \frac{\left(m_b p_{eN} + s\right)^{a+2} - \left(m_b p_{iN} + s\right)^{a+2}}{m_b^2(a+2)} \tag{E.2b}$$

Note that the only requirements for Eq. E.2a and Eq. E.2b are p_{eN} and p_{iN}, along with the HB parameters.

Jimenez et al. (2008)

Hoek et al. (2002) proposed linearising the $\sigma_1 - \sigma_3$ stress space by equating the areas covered by the HB and MC criteria within the stress interval ($\sigma_t < \sigma_3 < \sigma_{3max}$). However, Jimenez et al. (2008) highlighted that this results in an artificial stress interval that does not match the actual stress state around a tunnel. As a result, the linearisation only partially accounts for the stress state in the rock mass. In contrast, the non-linear failure criterion can be approximated by a linear one with an acceptable error, but only if a suitable and realistic stress range is considered. To achieve this, the HB failure criterion is once again expressed in terms of mean and deviatoric stress for plain strain. p and q are afterward normalised (p^*, q^*) to obtain the following general adimensional equation:

$$p_0^* = \left(1 + (1-a)q^{*k}\right) q^* \tag{E.3}$$

With $q^* = \frac{q}{\beta}$ and $p_0^* = \frac{p}{\beta} + \zeta$ and k, β, ζ as HB parameters dependent.

Again, circular plastic and elastic regions are depicted around the excavation and the hypothesis of a circular tunnel stands (refer to Fig. 7.6b, Chapter 7), with an in situ stress field considered as hydrostatic. It is additionally assumed that the tunnel support pressure at point A (σ_A) is the minor principal stress at that point, as that is the most common case in practice.

A graphical solution is proposed by Jimenez et al. (2008) using the $p^* - q^*$ plot (Fig. E.3). In this approach, the mean stress p remains constant within the elastic region, as per elasticity

theory. This assumption is sufficient to determine the stress state at point B along the $p^* - q^*$ plot. At point A, the support pressure at the tunnel lining is equal to the minor principal stress ($\sigma_3 = \sigma_A$). Thus, the deviatoric stress at failure, q_A, can be calculated by following the 45° arrow from $p^* = \sigma_A^*$ (which equals 0 for the current project) until it intersects with the HB failure envelope. Once the stress range is defined along the HB envelope, the equivalent MC friction angle can be easily extrapolated from the slope of the AB segment. To calculate the equivalent cohesion, some graphical adjustments are needed. The value is taken along the deviatoric axis within a range defined by the tangent line at the midpoint M and the extension of the AB segment, with the "optimal" value determined by setting a fitting parameter ξ_C^* to 0.60, as recommended by Jimenez et al. (2008).

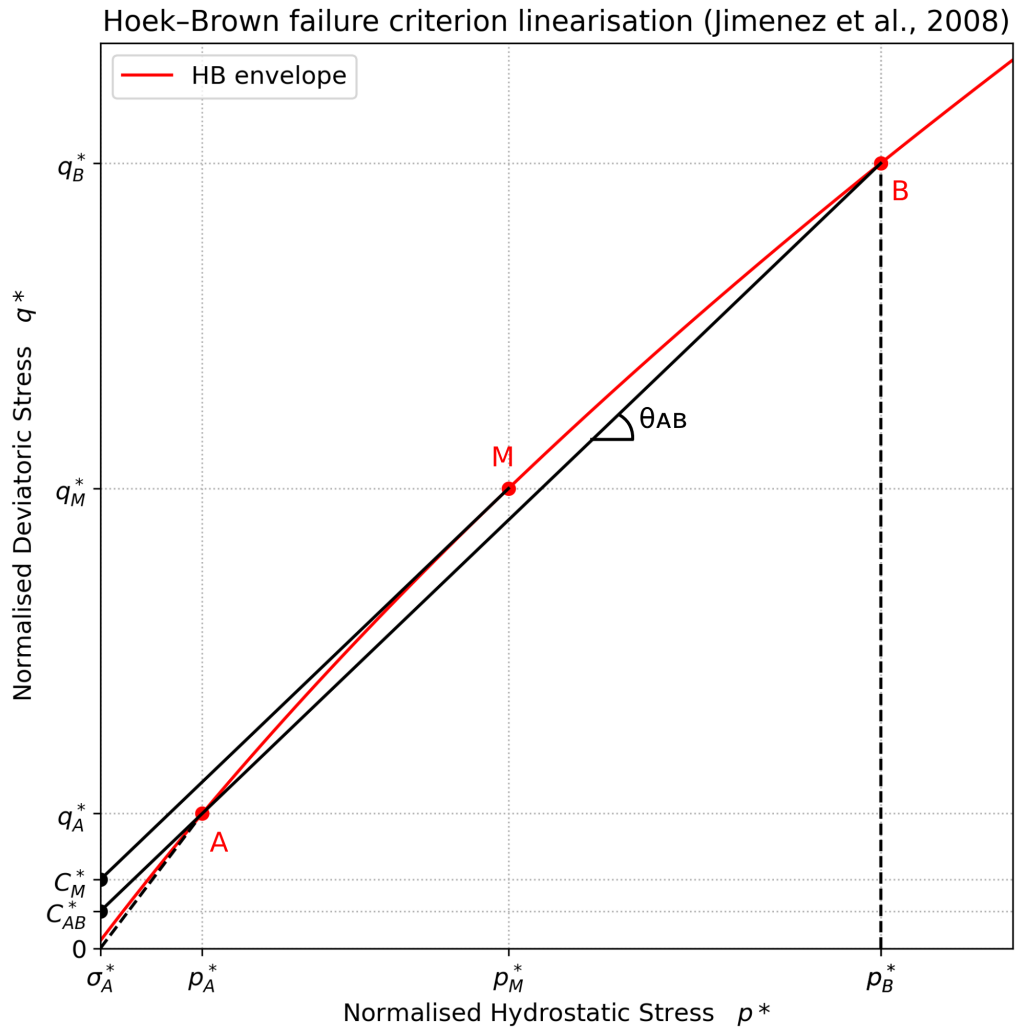


Figure E.3: Hoek–Brow linearisation graphical procedure in order to obtain the equivalent Mohr–Coulomb parameters described by Jimenez et al. (2008).

Friction angle and cohesion can be finally calculated with the following relationships:

$$k = \sin\phi = \tan\theta_{AB} \tag{E.4a}$$

$$c = \frac{\beta C^*}{\cos\phi} \tag{E.4b}$$

With C^* obtained by a combination of ${C^*}_{AB}$, C^*_M and the aforementioned parameter ξ^*_C (Fig. E.3):

$$C^* = C^*_{AB} + \xi^*_C \left(C^*_M - C^*_{AB}\right) \quad \text{where } 0.0 \leq \xi^*_C \leq 1.0 \tag{E.5}$$

Meng et al. (2016)

According to Meng et al. (2016), the concept of approximation is based on two common approaches, considering the error $e = y - y^*$ (where y is the original function and y^* is the linear approximation of the function): (i) least squares approximation and (ii) best uniform approximation. The best uniform approximation, initially introduced by Chebyshev in the 19$^{\text{th}}$ century, relies on a set of linearly independent polynomial functions (Meng et al., 2016). It is applied in the paper to provide a new estimation for the HB–MC fitting procedure. The linear MC criterion is expressed in the $\sigma_1 - \sigma_3$ space, as described by Sofianos and Nomikos (2006):

$$\sigma_1 = k\sigma_3 + C_0 \tag{E.6}$$

In this context, the tunnel support pressure p_i represents the lower limit of the minor stress range, while the upper limit p_e corresponds to the radial stress at the interface between the plastic and elastic regions. By using the best uniform approximation approach, equivalent MC failure envelope inclination and cohesion are then easily determined.

$$k = 1 + \frac{\sigma_{ci}\left[\left(\frac{m_b p_i}{\sigma_{ci}} + s\right)^a - \left(\frac{m_b p_e}{\sigma_{ci}} + s\right)^a\right]}{p_i - p_e}$$

$$C_0 = \frac{(1-k)(\sigma_d + p_i)}{2} + \frac{\sigma_{ci}}{2}\left[\left(\frac{m_b \sigma_d}{\sigma_{ci}} + s\right)^a + \left(\frac{m_b p_i}{\sigma_{ci}} + s\right)^a\right] \tag{E.7}$$

with $$\sigma_A = \frac{\sigma_{ci}}{m_b}\left\{\left[\frac{\sigma_{ci}}{a m_b}\frac{\left(\frac{m_b p_i}{\sigma_{ci}} + s\right)^a - \left(\frac{m_b p_e}{\sigma_{ci}} + s\right)^a}{p_i - p_e}\right]^{\frac{1}{a-1}} - s\right\}$$

F

Appendix F: Numerical modelling results

F.1 Relevant numerical simulations overview

Among the first round of simulations, two key design alternatives are highlighted in this section: the $R = 18\,\text{m}$ non-pillar geometry and the $R = 20\,\text{m}$, $r = 4\,\text{m}$ pillar geometry. These two configurations emerged as the final design candidates for the project and were therefore also utilised in the second round of simulations. Presenting both pillar and non-pillar geometries allows for a clearer comparison of their respective stress and displacement distributions, as well as the magnitude of these values along the excavation contour.

In both simulation rounds, major principal stress distributions are visualised through volumetric averaging (Fig. F.1, Fig. F.3; Fig. F.7, Fig. F.9), which enables a clearer representation of stress contours along the excavation surface. Stress tensors are also plotted (Fig. F.2, Fig. F.4; Fig. F.8, Fig. F.10) to identify peak stress values and localised concentrations, particularly in corners and other critical areas of the excavation.

Translational displacements are displayed (Fig. F.5; Fig. F.11) to evaluate both the magnitude and location of maximum deformations along the excavation boundary. Additionally, the average mechanical ratio is used as a control parameter (Fig. F.6; Fig. F.12) to assess whether numerical convergence is being ensured in each excavation step.

Note: FLAC3D adopts a sign convention where compressive stresses are negative and tensile stresses are positive.

Geometry 1: R = 18 m

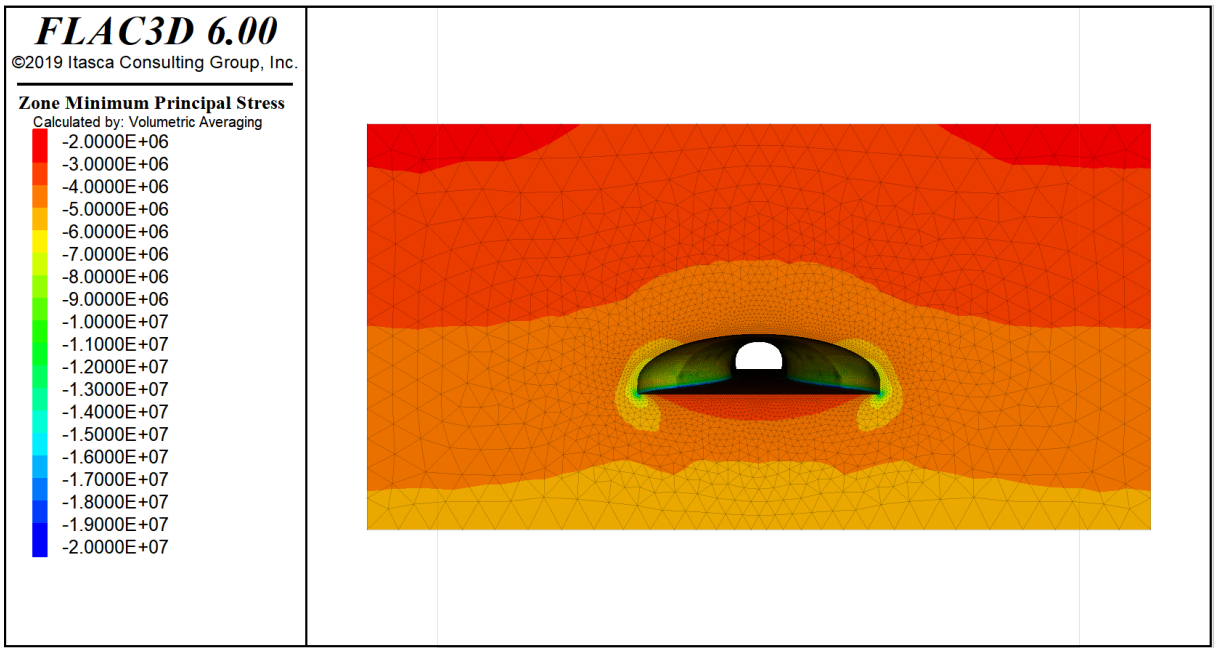


Figure F.1: Overview of major principal stresses (calculated by volumetric averaging) in the R = 18 m cavern excavation.

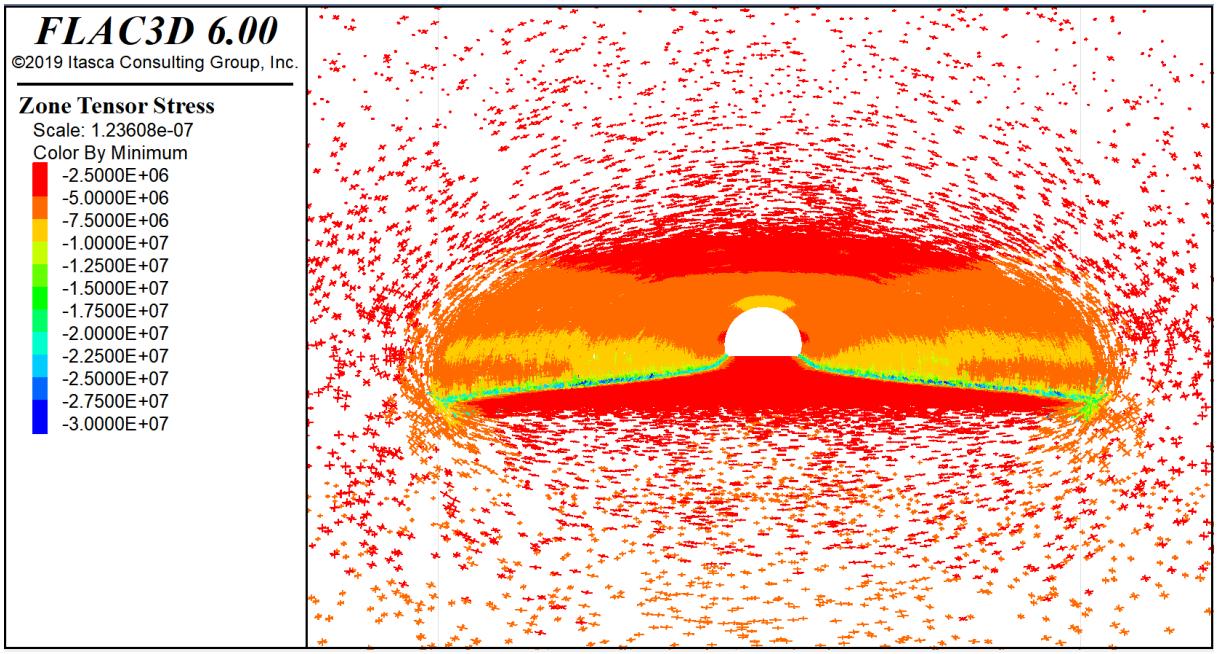


Figure F.2: Overview of major principal stresses tensors in the R = 18 m cavern excavation.

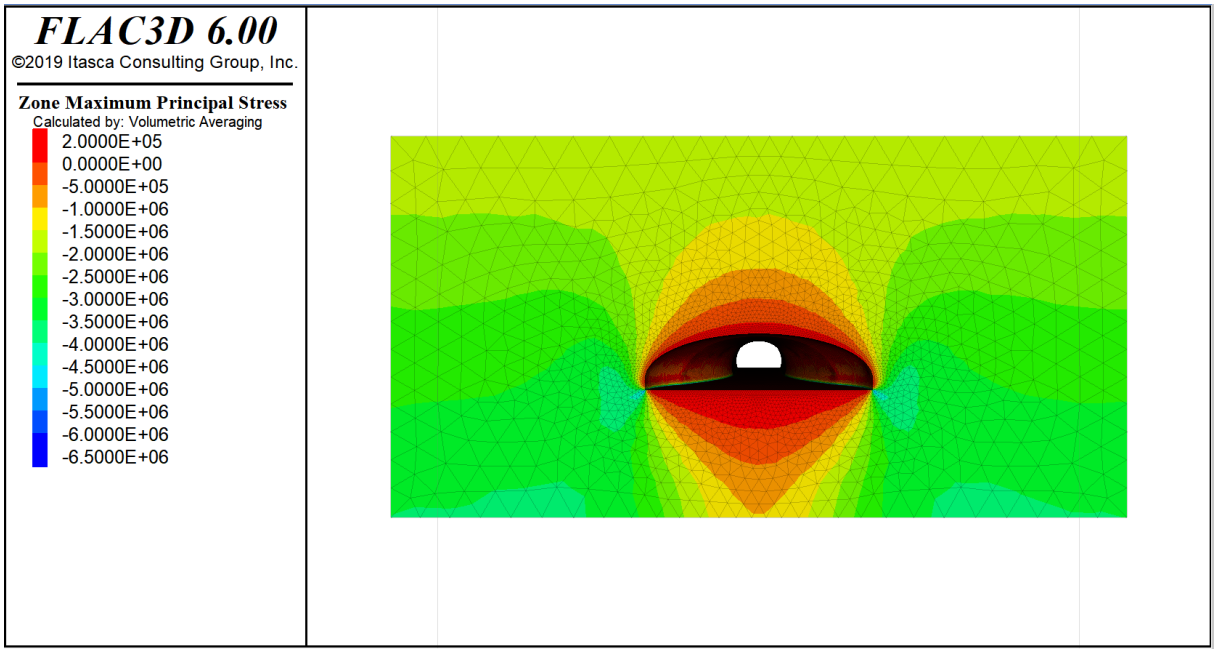


Figure F.3: Overview of minor principal stresses (calculated by volumetric averaging) in the R = 18 m cavern excavation.

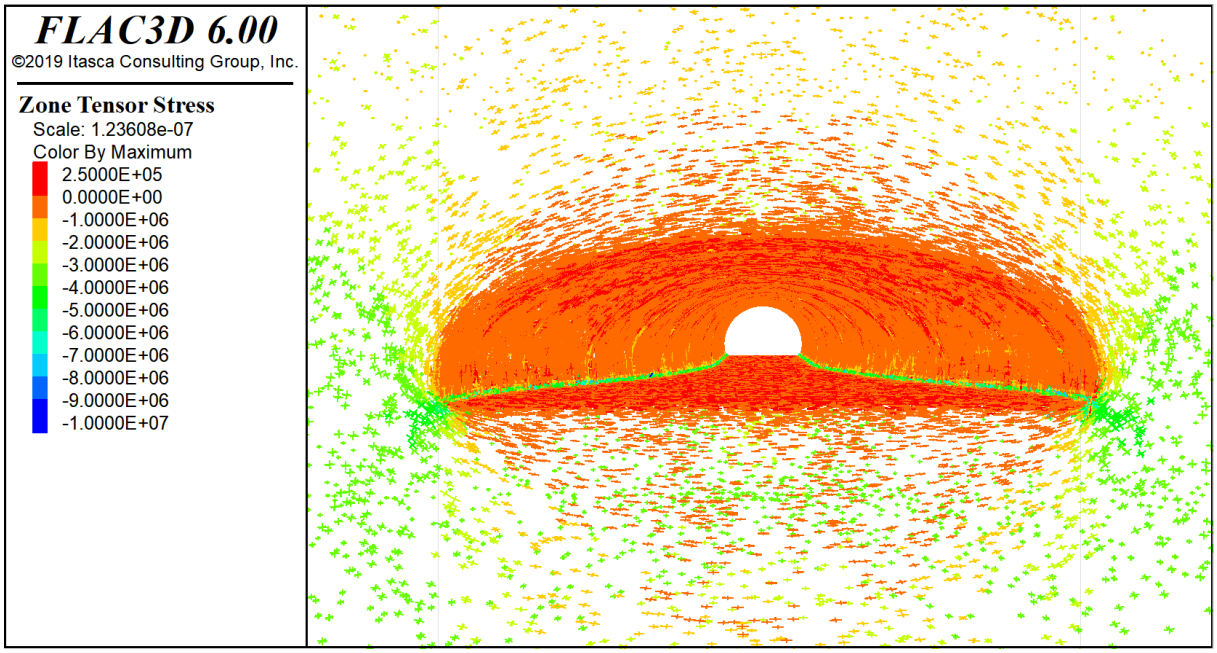


Figure F.4: Overview of minor principal stresses tensors in the R = 18 m cavern excavation.

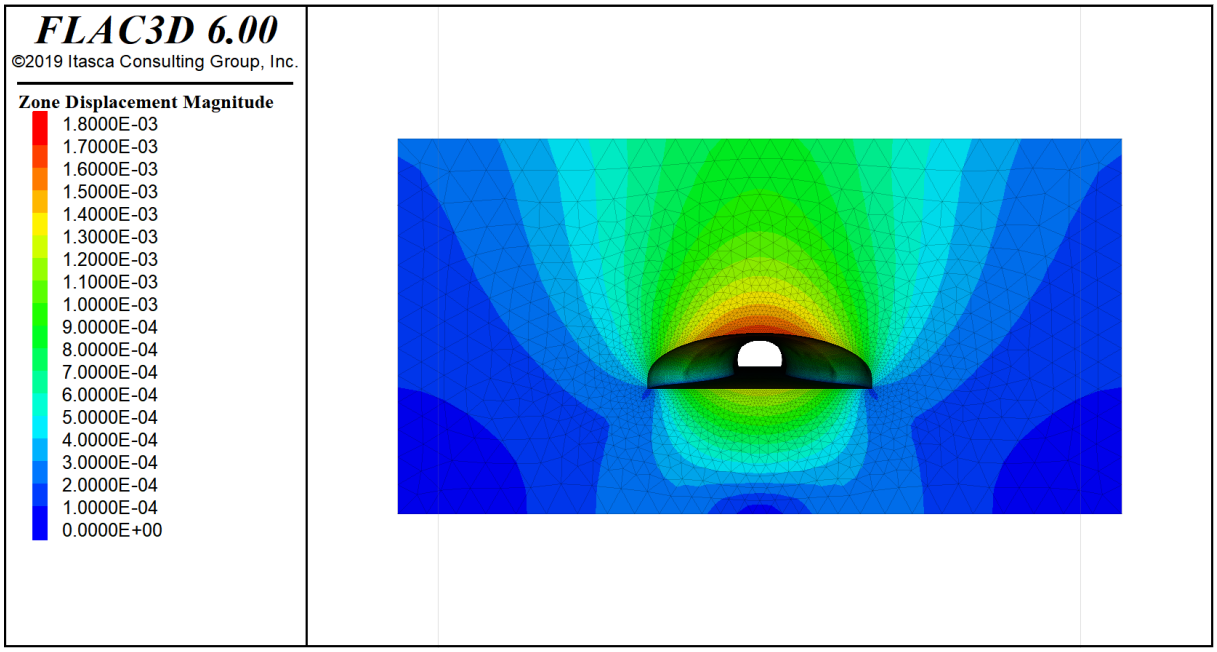


Figure F.5: Overview of translational displacements in the R = 18 m cavern excavation.

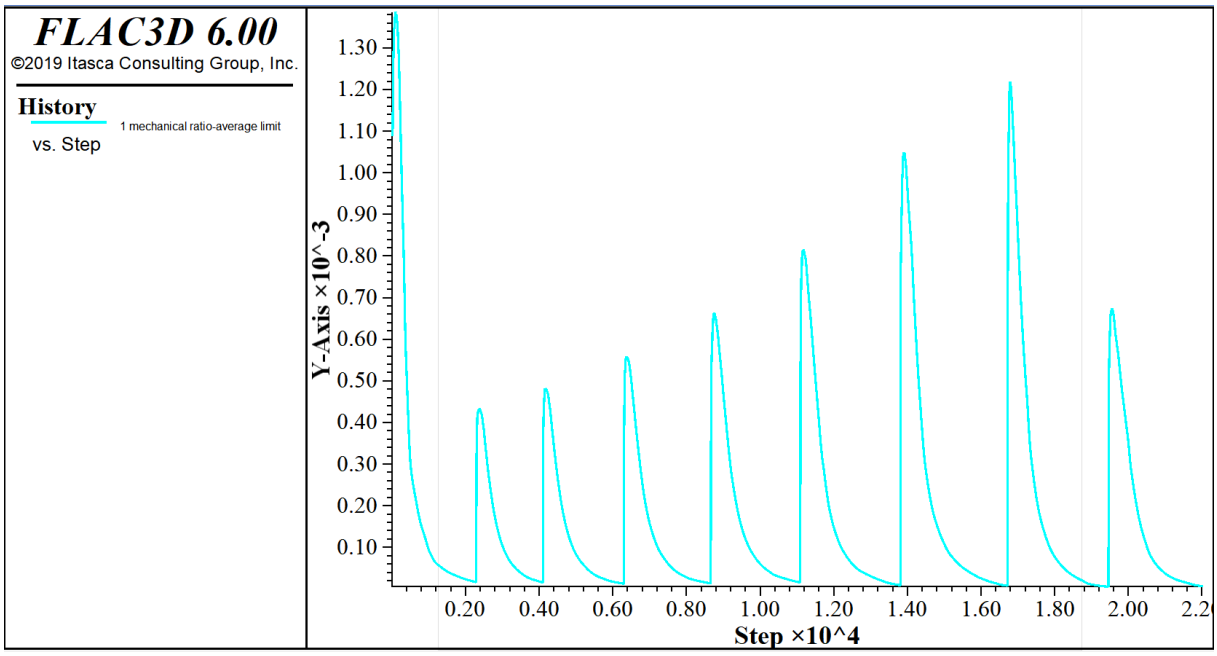


Figure F.6: Mechanical ratio average evolution in the R = 18 m cavern excavation.

Geometry 2: R = 20 m, r = 4 m

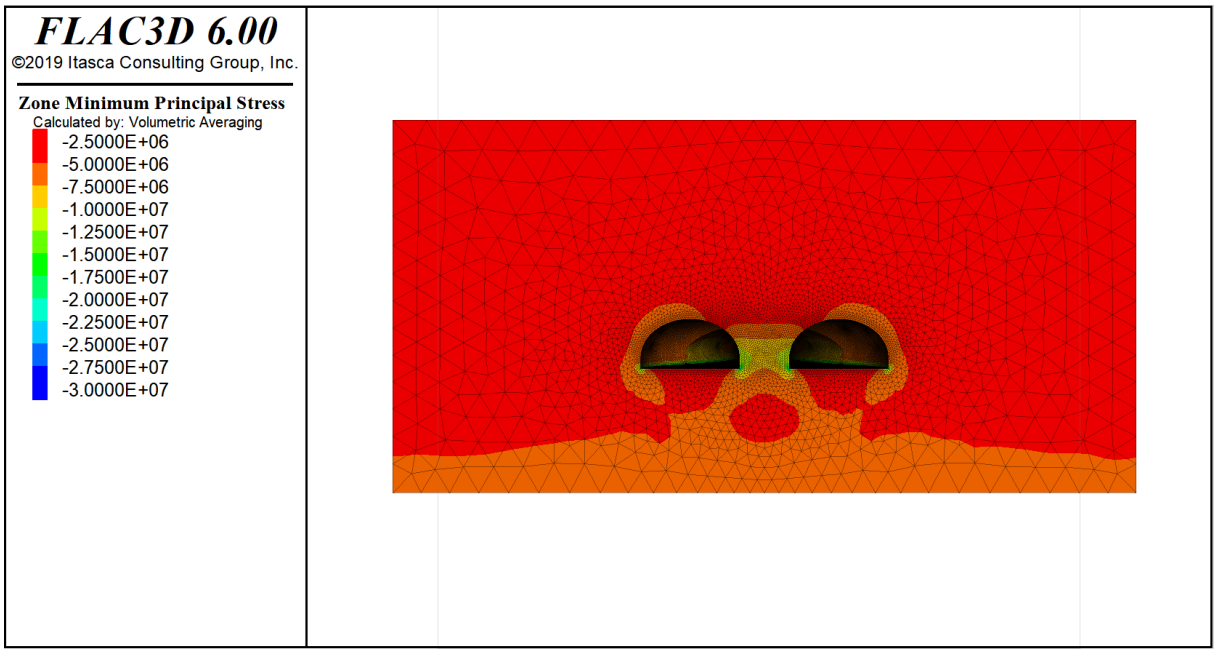


Figure F.7: Overview of major principal stresses (calculated by volumetric averaging) in the R = 20 m, r = 4 m cavern excavation.

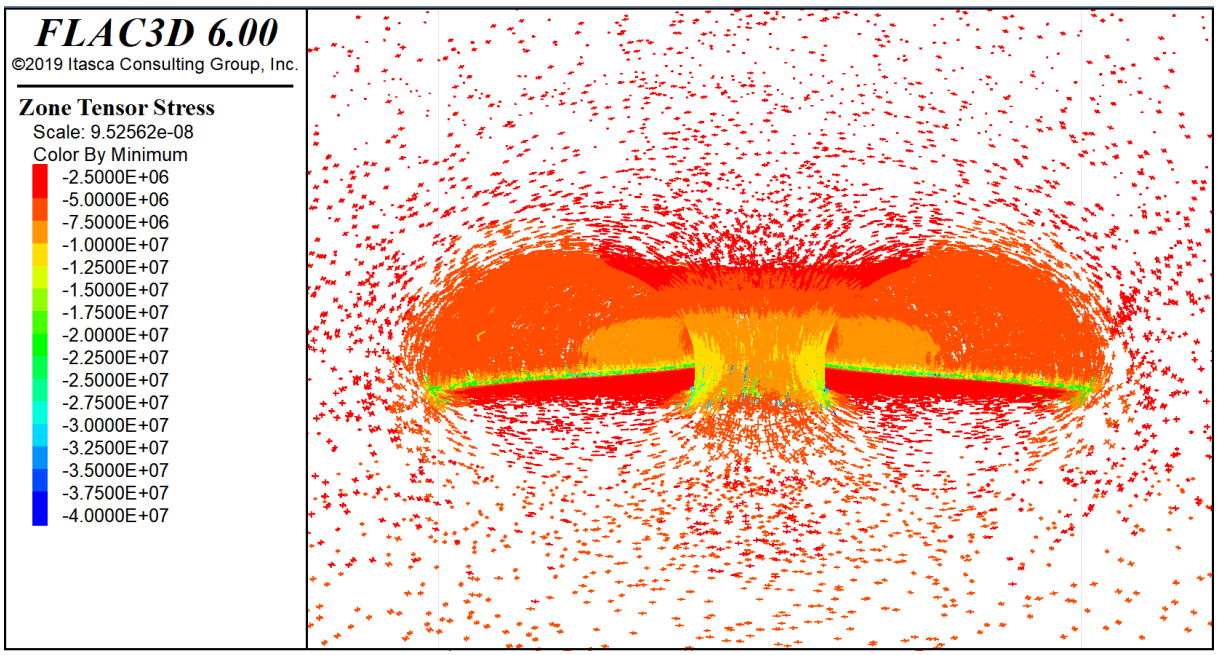


Figure F.8: Overview of major principal stresses tensors in the R = 20 m, r = 4 m cavern excavation.

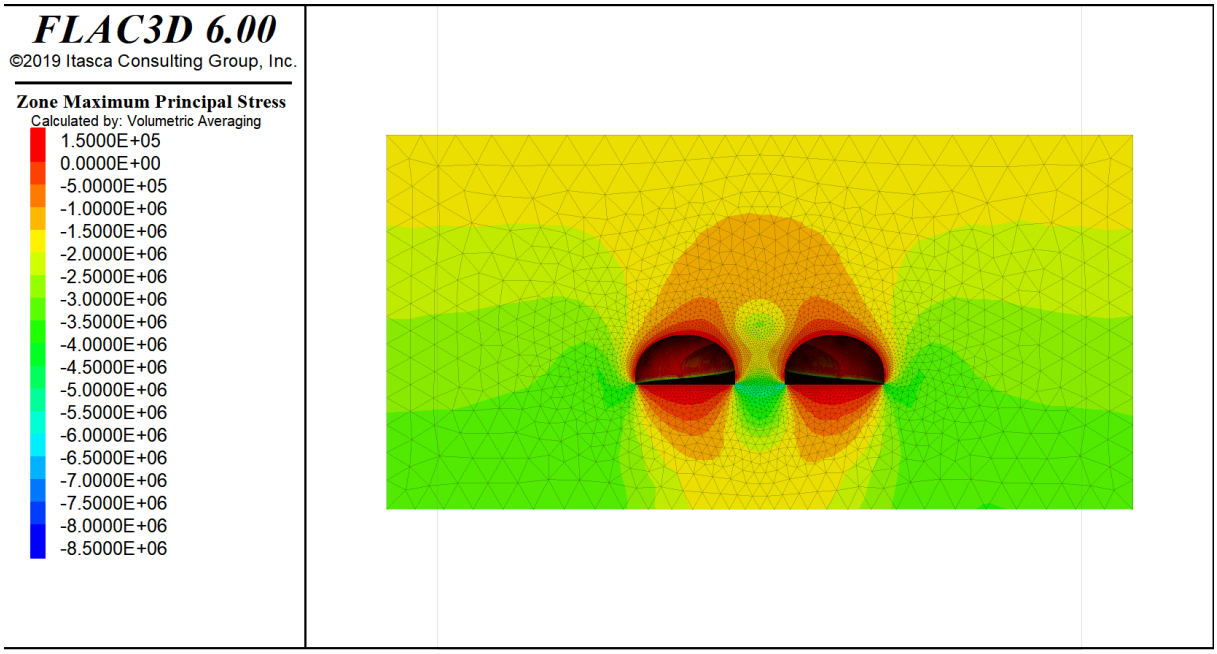


Figure F.9: Overview of minor principal stresses (calculated by volumetric averaging) in the R = 20 m, r = 4 m cavern excavation.

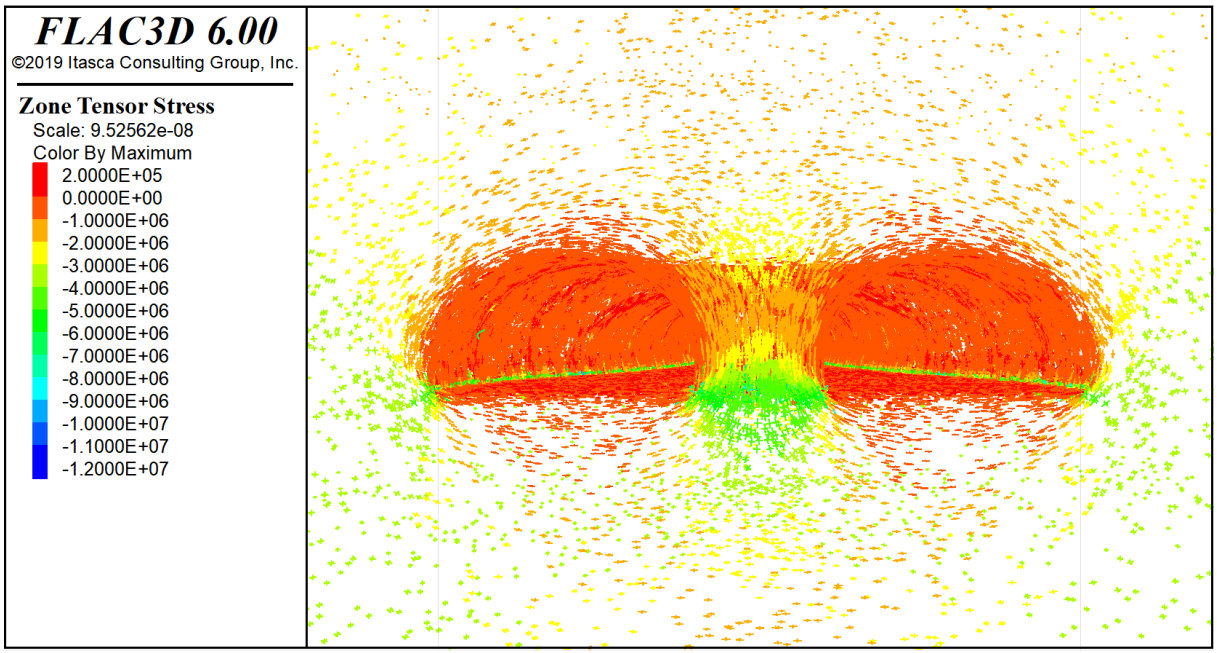


Figure F.10: Overview of minor principal stresses tensors in the R = 20 m, r = 4 m cavern excavation.

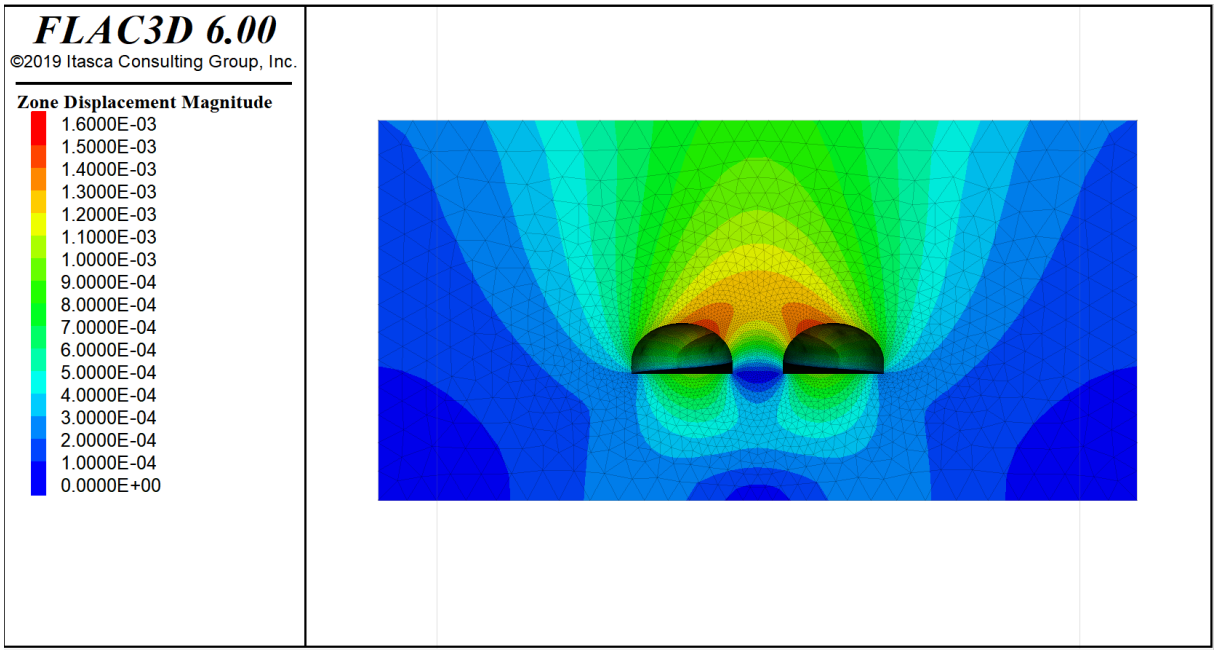


Figure F.11: Overview of translational displacements in the R = 20 m, r = 4 m cavern excavation.

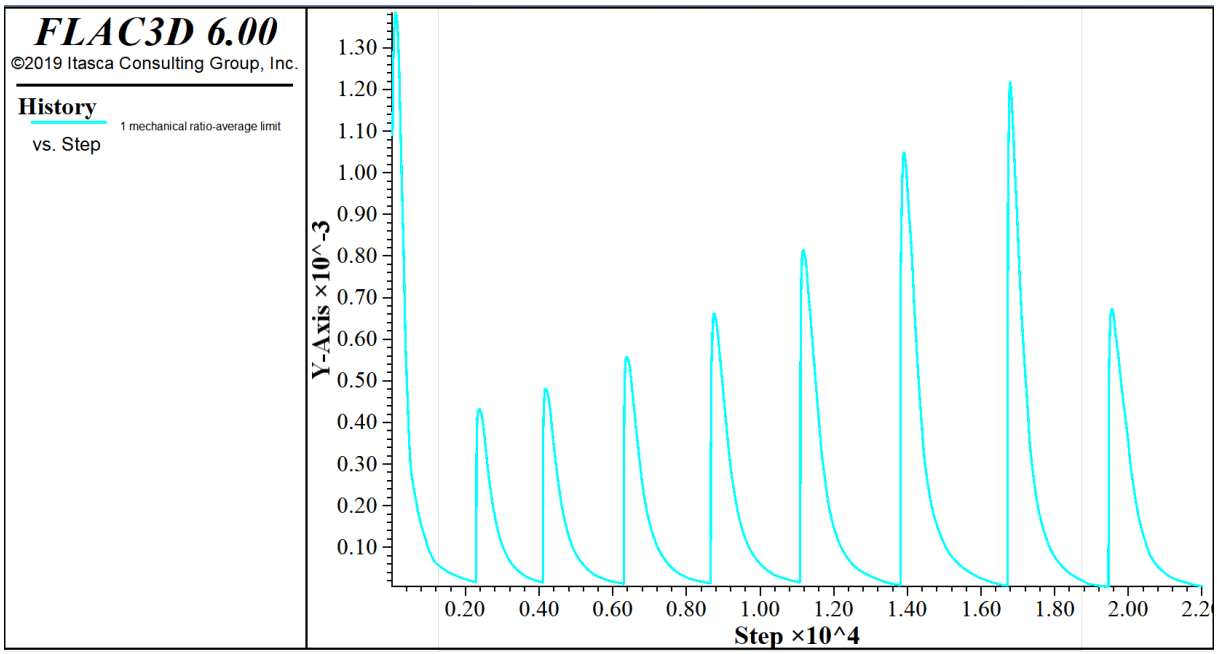


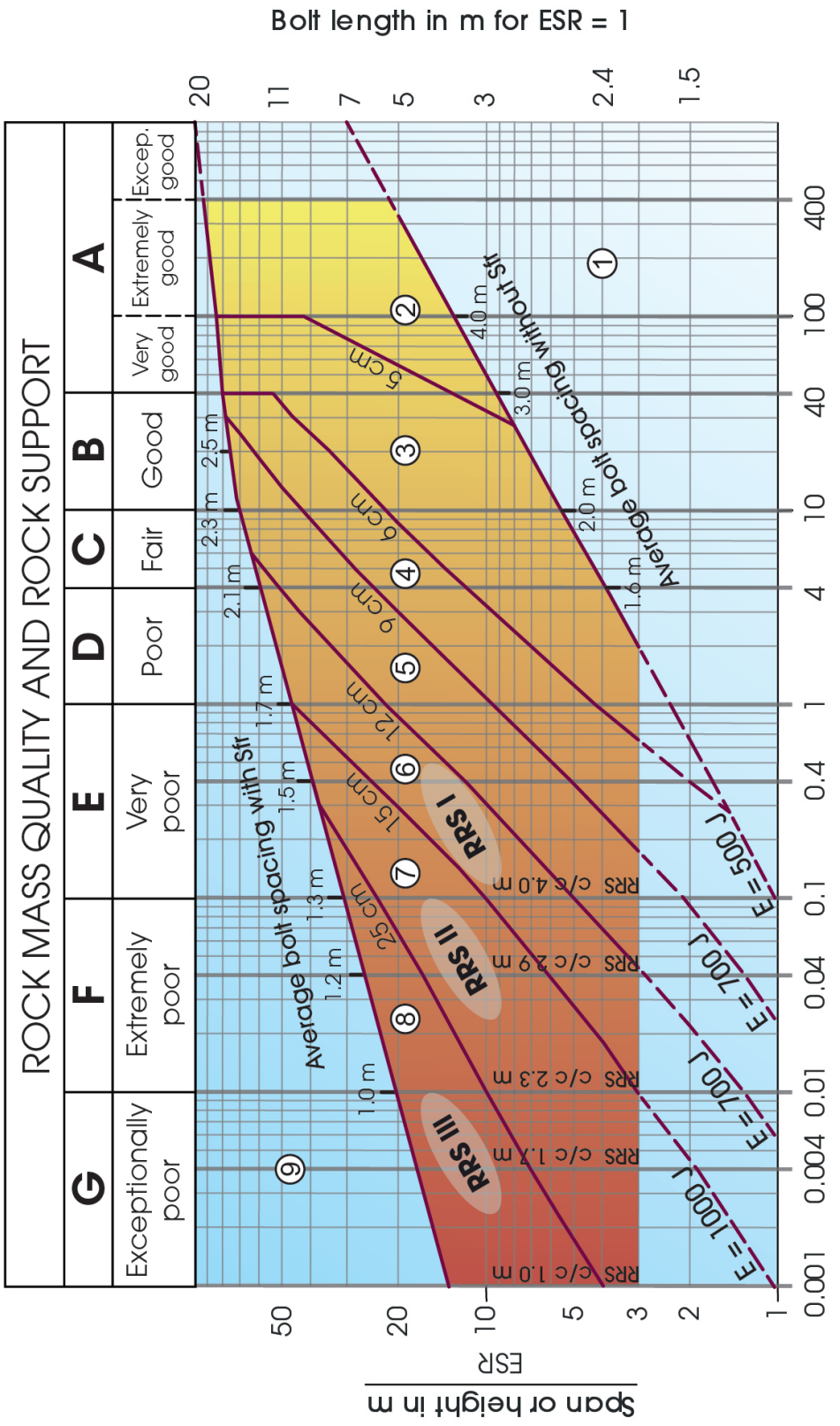
Figure F.12: Mechanical ratio average evolution in the R = 20 m, r = 4.0 m cavern excavation.

F.2 Using the Rock Support Chart and the Revised Support Chart for the Faroe Islands

In this section, the Rock Support Chart (RSC) developed by NGI (Norwegian Geotechnical Institute, 2015) and the Revised Support Chart currently in development by Prof. Grøv and colleagues for the specific Faroese context are included. Additionally, their application in defining appropriate support measures for the two cavern geometries and geotechnical units of this project is illustrated.

Table 7 ESR-values.

7	Type of excavation	ESR
A	Temporary mine openings, etc.	*ca.* 3-5
B	Vertical shafts*: i) circular sections ii) rectangular/square section * Dependant of purpose. May be lower than given values.	*ca.* 2.5 *ca.* 2.0
C	Permanent mine openings, water tunnels for hydro power (exclude high pressure penstocks), water supply tunnels, pilot tunnels, drifts and headings for large openings.	1.6
D	Minor road and railway tunnels, surge chambers, access tunnels, sewage tunnels, etc.	1.3
E	Power houses, storage rooms, water treatment plants, major road and railway tunnels, civil defence chambers, portals, intersections, etc.	1.0
F	Underground nuclear power stations, railways stations, sports and public facilitates, factories, etc.	0.8
G	Very important caverns and underground openings with a long lifetime, ≈ 100 years, or without access for maintenance.	0.5


Bolt length in m for ESR = 1
ROCK MASS QUALITY AND ROCK SUPPORT
G
F
E
D
C
B
A
Exceptionally poor
Extremely poor
Very poor
Poor
Fair
Good
Very good
Extremely good
Excep. good
Average bolt spacing without Str
Average bolt spacing with Str
RRS I
RRS II
RRS III
E = 1000 J
E = 700 J
E = 500 J
Span or height in m
ESR
Rock mass quality Q = RQD/Jn x Jr/Ja x Jw/SRF

Support categories

① Unsupported or spot bolting
② Spot bolting, **SB**
③ Systematic bolting, fibre reinforced sprayed concrete, 5-6 cm, **B+Sfr**
④ Fibre reinforced sprayed concrete and bolting, 6-9 cm, **Sfr (E500)+B**
⑤ Fibre reinforced sprayed concrete and bolting, 9-12 cm, **Sfr (E700)+B**
⑥ Fibre reinforced sprayed concrete and bolting, 12-15 cm + reinforced ribs of sprayed concrete and bolting, **Sfr (E700)+RRS I +B**
⑦ Fibre reinforced sprayed concrete >15 cm + reinforced ribs of sprayed concrete and bolting, **Sfr (E1000)+RRS II+B**
⑧ Cast concrete lining, **CCA** or **Sfr (E1000)+RRS III+B**
⑨ Special evaluation

Bolts spacing is mainly based on Ø20 mm

E = Energy absorbtion in fibre reinforced sprayed concrete

ESR = Excavation Support Ratio

Areas with dashed lines have no empirical data

RRS - spacing related to Q-value

I — **Si30/6 Ø16 - Ø20 (span 10m)**
D40/6+2 Ø16-20 (span 20m)

II — Si35/6 Ø16-20 (span 5m)
D45/6+2 Ø16-20 (span 10m)
D55/6+4 Ø20 (span 20m)

III — D40/6+4 Ø16-20 (span 5 m)
D55/6+4 Ø20 (span 10 m)
Special evaluation (span 20 m)

Si30/6 = Single layer of 6 rebars, 30 cm thickness of sprayed concrete
D = Double layer of rebars
Ø16 = Rebar diameter is 16 mm
c/c = RSS spacing, centre - centre

Figure 7 Permanent support recommendations based on Q-values and span/ESR.

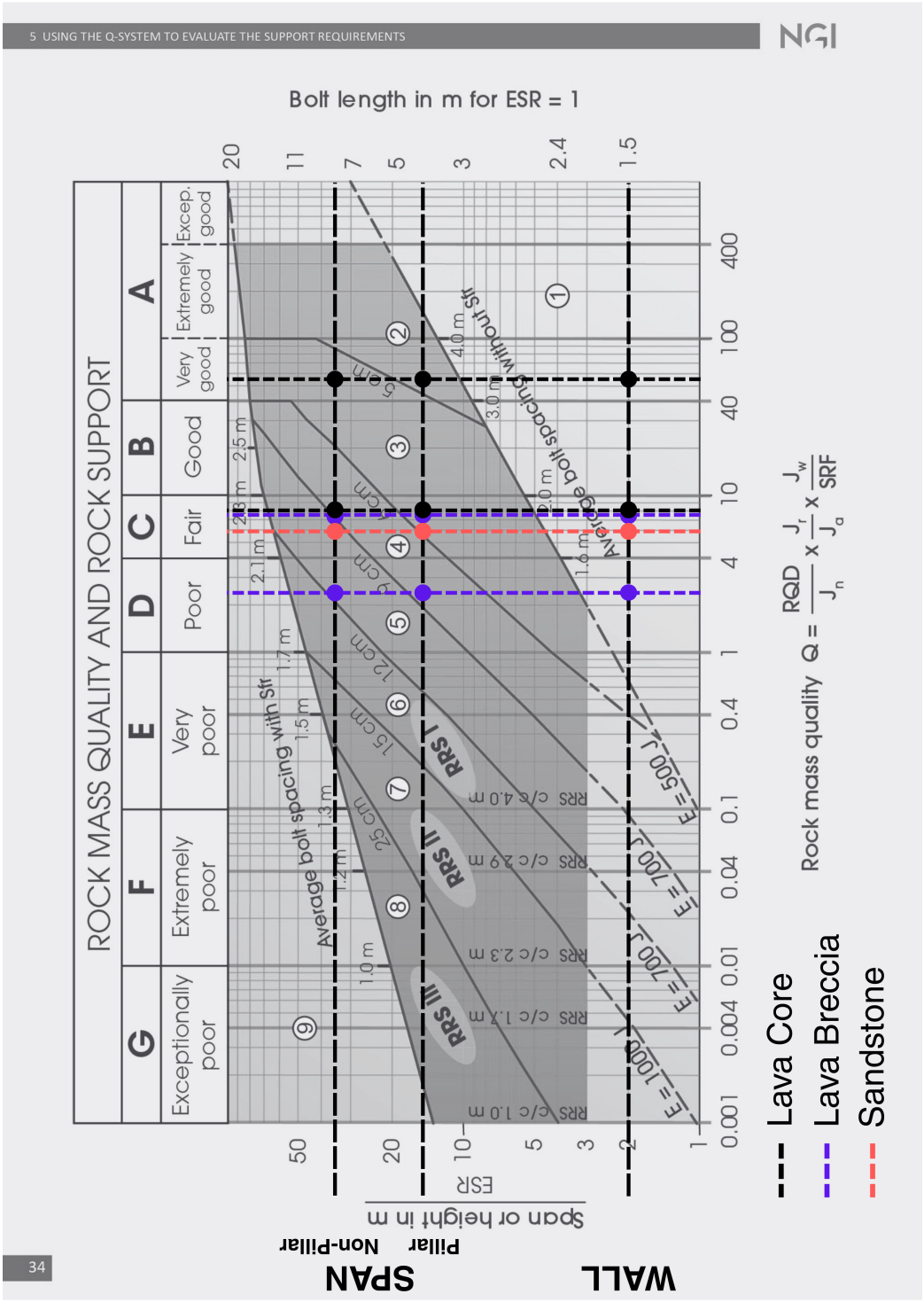


Figure F.13: Employment of RSC for Cavern 1 structural supports.

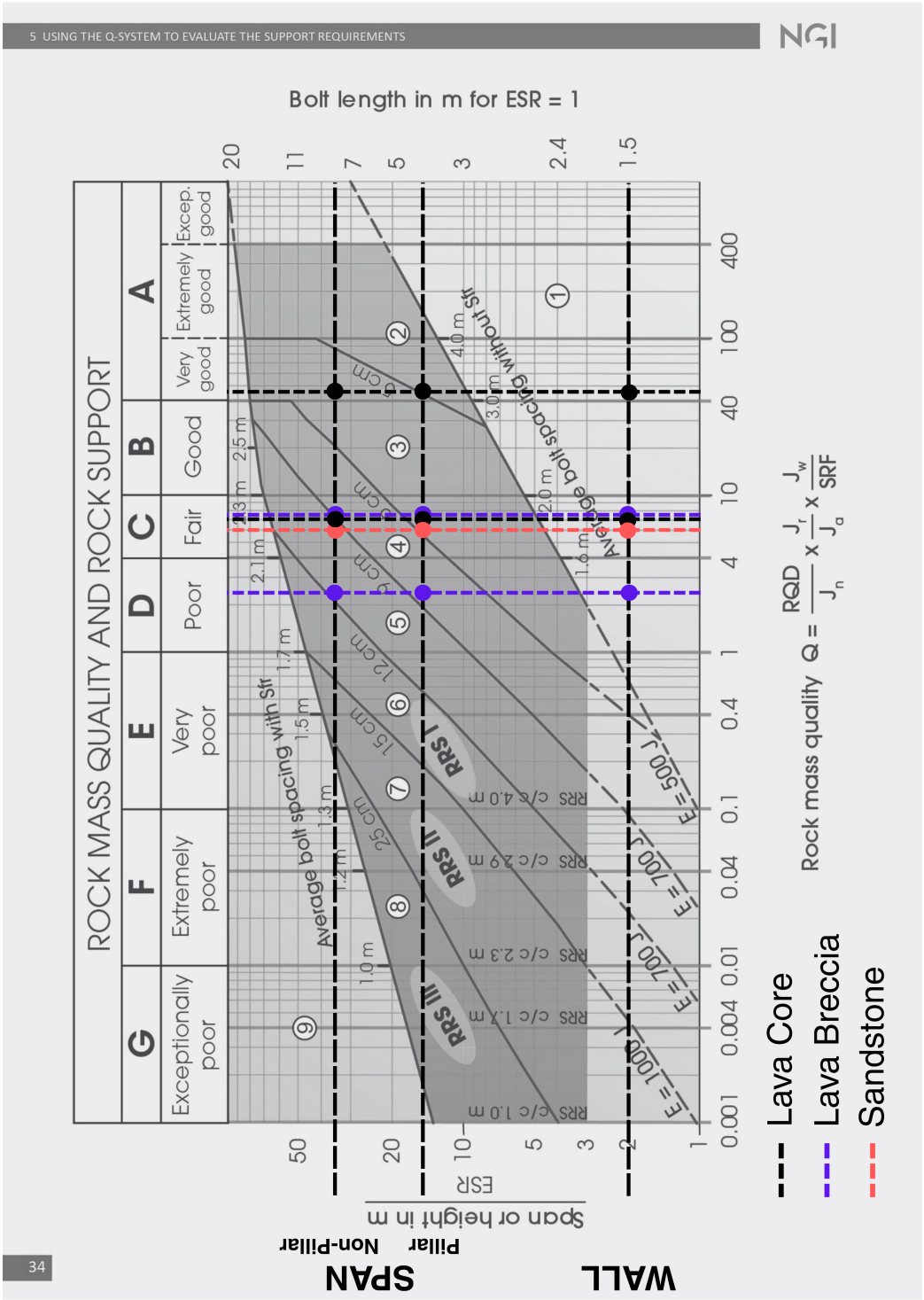
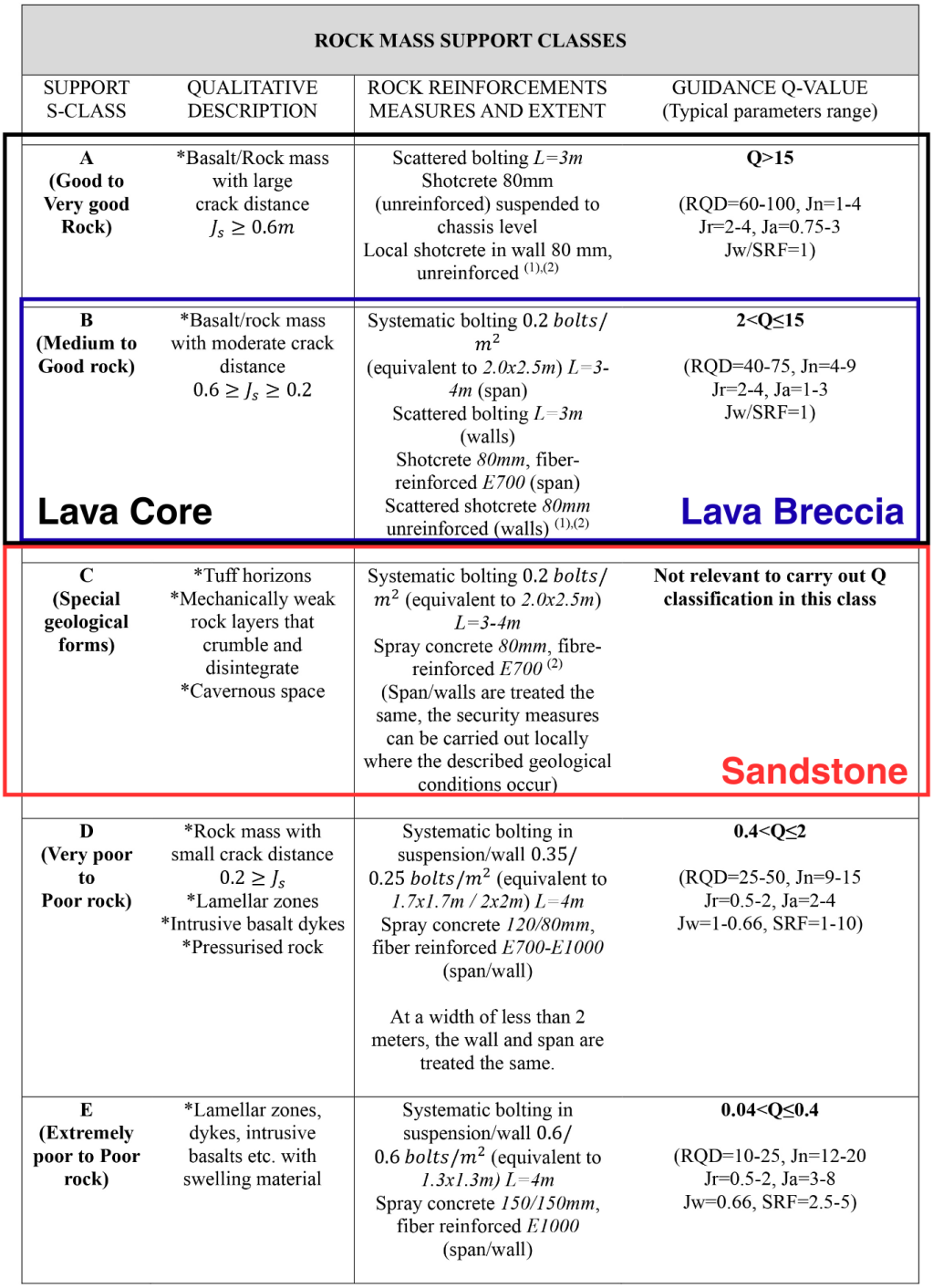


Figure F.14: Employment of RSC for Cavern 2 structural supports.

ROCK MASS SUPPORT CLASSES			
SUPPORT S-CLASS	QUALITATIVE DESCRIPTION	ROCK REINFORCEMENTS MEASURES AND EXTENT	GUIDANCE Q-VALUE (Typical parameters range)
A (Good to Very good Rock)	*Basalt/Rock mass with large crack distance $J_s \geq 0.6m$	Scattered bolting *L=3m* Shotcrete 80mm (unreinforced) suspended to chassis level Local shotcrete in wall 80 mm, unreinforced [(1),(2)]	**Q>15** (RQD=60-100, Jn=1-4 Jr=2-4, Ja=0.75-3 Jw/SRF=1)
B (Medium to Good rock)	*Basalt/rock mass with moderate crack distance $0.6 \geq J_s \geq 0.2$	Systematic bolting 0.2 $bolts/m^2$ (equivalent to *2.0x2.5m*) *L=3-4m* (span) Scattered bolting *L=3m* (walls) Shotcrete *80mm*, fiber-reinforced *E700* (span) Scattered shotcrete *80mm* unreinforced (walls) [(1),(2)]	**2<Q≤15** (RQD=40-75, Jn=4-9 Jr=2-4, Ja=1-3 Jw/SRF=1)
C (Special geological forms)	*Tuff horizons *Mechanically weak rock layers that crumble and disintegrate *Cavernous space	Systematic bolting 0.2 $bolts/m^2$ (equivalent to *2.0x2.5m*) *L=3-4m* Spray concrete *80mm*, fibre-reinforced *E700* [(2)] (Span/walls are treated the same, the security measures can be carried out locally where the described geological conditions occur)	**Not relevant to carry out Q classification in this class**
D (Very poor to Poor rock)	*Rock mass with small crack distance $0.2 \geq J_s$ *Lamellar zones *Intrusive basalt dykes *Pressurised rock	Systematic bolting in suspension/wall 0.35/ 0.25 $bolts/m^2$ (equivalent to *1.7x1.7m / 2x2m*) *L=4m* Spray concrete *120/80mm*, fiber reinforced *E700-E1000* (span/wall) At a width of less than 2 meters, the wall and span are treated the same.	**0.4<Q≤2** (RQD=25-50, Jn=9-15 Jr=0.5-2, Ja=2-4 Jw=1-0.66, SRF=1-10)
E (Extremely poor to Poor rock)	*Lamellar zones, dykes, intrusive basalts etc. with swelling material	Systematic bolting in suspension/wall 0.6/ 0.6 $bolts/m^2$ (equivalent to *1.3x1.3m) L=4m* Spray concrete *150/150mm*, fiber reinforced *E1000* (span/wall)	**0.04<Q≤0.4** (RQD=10-25, Jn=12-20 Jr=0.5-2, Ja=3-8 Jw=0.66, SRF=2.5-5)

F (Extremely bad rock and worse)	*Zones of different types and origins with clay fill and/or crushed material (swelling and non-swelling) and little or absent self-bearing capacity	Systematic bolting in span/wall $0.8 bolts/m^2$ (equivalent to *1.0x1.25m*) *L=4m* Fiber reinforced shotcrete *E1000, 150-250mm* RRS (reinforced ribs of sprayed concrete)	**Q≤0.04** (RQD=10, Jn=15-20 Jr=1, Ja=3-12 Jw=0.66, SRF=5-10)
J_s: Joint spacing (average crack spacing) [(1)] Sealing with shotcrete for locally occurring phenomena that do not require stability reinforcement			
[(2)] For durability considerations, the minimum thickness of shotcrete is 80 mm. An increased minimum thickness may be prescribed if necessary.			



ROCK MASS SUPPORT CLASSES			
SUPPORT S-CLASS	QUALITATIVE DESCRIPTION	ROCK REINFORCEMENTS MEASURES AND EXTENT	GUIDANCE Q-VALUE (Typical parameters range)
A (Good to Very good Rock)	*Basalt/Rock mass with large crack distance $J_s \geq 0.6m$	Scattered bolting *L=3m* Shotcrete 80mm (unreinforced) suspended to chassis level Local shotcrete in wall 80 mm, unreinforced [1),(2)]	**Q>15** (RQD=60-100, Jn=1-4 Jr=2-4, Ja=0.75-3 Jw/SRF=1)
B (Medium to Good rock) Lava Core	*Basalt/rock mass with moderate crack distance $0.6 \geq J_s \geq 0.2$	Systematic bolting 0.2 $bolts/m^2$ (equivalent to *2.0x2.5m*) *L=3-4m* (span) Scattered bolting *L=3m* (walls) Shotcrete *80mm*, fiber-reinforced *E700* (span) Scattered shotcrete *80mm* unreinforced (walls) [1),(2)]	**2<Q≤15** (RQD=40-75, Jn=4-9 Jr=2-4, Ja=1-3 Jw/SRF=1) Lava Breccia
C (Special geological forms) Sandstone	*Tuff horizons *Mechanically weak rock layers that crumble and disintegrate *Cavernous space	Systematic bolting 0.2 $bolts/m^2$ (equivalent to *2.0x2.5m*) *L=3-4m* Spray concrete *80mm*, fibre-reinforced *E700* [2] (Span/walls are treated the same, the security measures can be carried out locally where the described geological conditions occur)	**Not relevant to carry out Q classification in this class**
D (Very poor to Poor rock)	*Rock mass with small crack distance $0.2 \geq J_s$ *Lamellar zones *Intrusive basalt dykes *Pressurised rock	Systematic bolting in suspension/wall 0.35/ 0.25 $bolts/m^2$ (equivalent to *1.7x1.7m / 2x2m*) *L=4m* Spray concrete *120/80mm*, fiber reinforced *E700-E1000* (span/wall) At a width of less than 2 meters, the wall and span are treated the same.	**0.4<Q≤2** (RQD=25-50, Jn=9-15 Jr=0.5-2, Ja=2-4 Jw=1-0.66, SRF=1-10)
E (Extremely poor to Poor rock)	*Lamellar zones, dykes, intrusive basalts etc. with swelling material	Systematic bolting in suspension/wall 0.6/ 0.6 $bolts/m^2$ (equivalent to *1.3x1.3m) L=4m* Spray concrete *150/150mm*, fiber reinforced *E1000* (span/wall)	**0.04<Q≤0.4** (RQD=10-25, Jn=12-20 Jr=0.5-2, Ja=3-8 Jw=0.66, SRF=2.5-5)

Figure F.15: Employment of Revised Support Chart for Cavern 1 and Cavern 2 structural supports.